

Nearshore waves and related wave overtopping in complex estuaries

Oosterlo, P.

DOI

[10.4233/uuid:884cbc96-ebcd-488a-a820-0daae3962bb1](https://doi.org/10.4233/uuid:884cbc96-ebcd-488a-a820-0daae3962bb1)

Publication date

2021

Document Version

Final published version

Citation (APA)

Oosterlo, P. (2021). *Nearshore waves and related wave overtopping in complex estuaries*. [Dissertation (TU Delft), Delft University of Technology]. <https://doi.org/10.4233/uuid:884cbc96-ebcd-488a-a820-0daae3962bb1>

Important note

To cite this publication, please use the final published version (if applicable). Please check the document version above.

Copyright

Other than for strictly personal use, it is not permitted to download, forward or distribute the text or part of it, without the consent of the author(s) and/or copyright holder(s), unless the work is under an open content license such as Creative Commons.

Takedown policy

Please contact us and provide details if you believe this document breaches copyrights. We will remove access to the work immediately and investigate your claim.

NEARSHORE WAVES AND RELATED WAVE OVERTOPPING IN COMPLEX ESTUARIES

This dissertation focuses on the Eems-Dollard estuary in the north of the Netherlands and contributes to the MVED field measurement project in the area. This work considers two main knowledge gaps related to the modelling of wave propagation effects and measuring of (very) oblique wave run-up and overtopping in this complex estuary. A particular aspect of the estuary is that the dike design conditions consist of an offshore-directed wind and very obliquely incident waves, up to 80° relative to the dike normal. Almost no studies have been performed on the estuary and almost no measurements were available inside the estuary.

The first part of this dissertation provides more insight into the physical processes that play a role in the wave propagation in the Eems-Dollard estuary, and the performance of the numerical wave model SWAN in modelling these processes. The results show that the waves indeed become onshore-directed at the dike during design conditions, despite the offshore-directed wind. This is caused by a variety of processes. SWAN performs reasonably well in the estuary, but some limitations of SWAN arise in this highly complex area.

In the second part of this dissertation, an innovative laser scanner system is developed to measure oblique wave run-up and overtopping. Laser scanners have not been applied to measure run-up and overtopping in the field before. A novelty of the system is that two synchronised scanners are used to measure directional information of the waves. The system is flexible and mobile, it can be placed and relocated easily, without having to dig into the dike. The measurements with the system provide more insight in oblique wave run-up and overtopping, such as in the run-up depths of up-rushing oblique waves.

With the results obtained in this dissertation, the uncertainties in the required crest heights of the dikes in the estuary can be reduced. The knowledge gained also contributes to the dike safety assessment framework in the Netherlands, and to the overall knowledge on numerical wave modelling and wave run-up and overtopping.

Patrick Oosterlo

NEARSHORE WAVES AND RELATED WAVE OVERTOPPING IN COMPLEX ESTUARIES

NEARSHORE WAVES AND RELATED WAVE OVERTOPPING IN COMPLEX ESTUARIES



Patrick Oosterlo

NEARSHORE WAVES AND RELATED WAVE OVERTOPPING IN COMPLEX ESTUARIES

WEDNESDAY 8 DECEMBER 2021

PRESENTATION: 12:00

DEFENCE: 12:30

SENAATSAAL
AULA CONFERENCE CENTRE
DELFT UNIVERSITY OF
TECHNOLOGY

MEKELWEG 5
2628 CC DELFT
THE NETHERLANDS

Patrick Oosterlo
patrickoosterlo@gmail.com

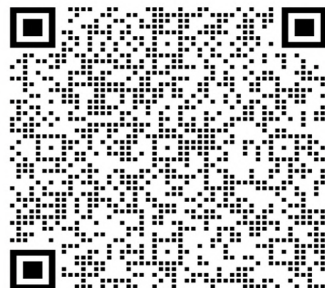


Waterschap NOORDERZIJLVEST



Hoogwaterbeschermingsprogramma

An electronic version of this dissertation is available at:



<https://doi.org/10.4233/uuid:884cb96-ebcd-488a-a820-0daae3962bb1>

ISBN: 978-94-6416-915-7



9 789464 169157 >



Waterschap NOORDERZIJLVEST



Hoogwaterbeschermingsprogramma

Propositions

accompanying the dissertation

NEARSHORE WAVES AND RELATED WAVE OVERTOPPING IN COMPLEX ESTUARIES

by

Patrick OOSTERLO

1. Waves can turn around the corner at the Eemshaven and become onshore-directed at the dike to the north of Delfzijl during design conditions, despite an offshore-directed wind (*this dissertation*).
2. Wave sheltering, wave (de)focusing, wave trapping (reflection), refraction and triad wave-wave interactions are the main wave propagation and transformation processes that play a role in the Eems-Dollard estuary during design conditions (*this dissertation*).
3. Laser scanners can measure wave run-up and overtopping parameters on dikes in the field during storms at least as accurate as conventionally used methods (*this dissertation*).
4. Wave run-up heights of very obliquely incident breaking waves in relatively deep water are Weibull-distributed (*this dissertation*).
5. The Dutch dike safety assessment should only consider the onshore-directed part of the wave spectrum, leading to up to 25% lower design wave heights in the Eems-Dollard estuary.
6. A paradigm shift towards the use of (2D) wave spectra for calibration and validation of numerical wave models is necessary, as bulk wave parameters do not always provide enough information to properly assess the performance of a wave model.
7. A single-blind peer review process is not fitting for a scientific journal.
8. Investments should be made in the further development of alternatives for a meat-based diet, instead of the further reduction of the environmental footprint of animal farms.
9. If Murphy's law is applied on flood safety, measurement instruments provide better protection against flooding than strengthening flood defences; the more instruments you place, the less storms occur.
10. The COVID-19 pandemic has shown that the impact of conspiracy theories on social media can be as large as that of papers in scientific journals.

See e.g. Constantinou, M., Kagialis, A., & Karekla, M. (2021). COVID-19 Scientific Facts vs. Conspiracy Theories: Is science failing to pass its message? *Int. J. Environ. Res. Public Health*, 18, 6343.

These propositions are regarded as opposable and defensible, and have been approved as such by the promotor prof. dr. ir. J.W. van der Meer and the co-promoters dr. ir. B. Hofland and dr. ir. M. Zijlema.

Stellingen

behorende bij het proefschrift

NEARSHORE WAVES AND RELATED WAVE OVERTOPPING IN COMPLEX ESTUARIES

door

Patrick OOSTERLO

1. Golven kunnen tijdens ontwerpcondities bijdraaien om de bocht bij de Eemshaven en aanlandig worden bij de dijk ten noorden van Delfzijl, ondanks een afluiddige wind (*dit proefschrift*).
2. Tijdens ontwerpcondities zijn beschutting, het (ont)-focussen van golven, reflectie ("golfverstrikking"), refractie en de driegolfwisselwerkingen de belangrijkste golfvoortplantings- en golftransformatieprocessen die een rol spelen in het Eems-Dollardestuarium (*dit proefschrift*).
3. Laserscanners kunnen tijdens stormen golfoploop- en golfoverslagparameters op dijken in het veld minstens zo nauwkeurig meten als conventioneel gebruikte methoden (*dit proefschrift*).
4. Golfoploophoogten van zeer schuin invallende, brekende golven in relatief diep water volgen een Weibull-verdeling (*dit proefschrift*).
5. Het Beoordelings- en OntwerpInstrumentarium (BOI) voor de Nederlandse dijken zou alleen het aanlandige deel van het golfspectrum moeten beschouwen, wat leidt tot wel 25% lagere ontwerp golfhoogtes in het Eems-Dollardestuarium.
6. Een paradigmaverschuiving naar het gebruik van (2D-)golfspectra voor kalibratie en validatie van numerieke golfmodellen is noodzakelijk, aangezien integrale golfparameters niet altijd voldoende informatie verschaffen om de prestaties van een golfmodel goed te kunnen beoordelen.
7. Een enkelblinde peerreview past niet bij een wetenschappelijk tijdschrift.
8. Er zou geïnvesteerd moeten worden in het verder ontwikkelen van vleesvervangers en kweekvlees, in plaats van in het verder verkleinen van de ecologische voetafdruk van veehouderijen.
9. Als de wet van Murphy wordt toegepast op de waterveiligheid, bieden meetinstrumenten betere bescherming tegen overstromingen dan het versterken van waterkeringen; hoe meer instrumenten je plaatst, hoe minder stormen er optreden.

10. De COVID-19-pandemie heeft aangetoond dat de impact van complottheorieën op sociale media net zo groot kan zijn als die van artikelen in wetenschappelijke tijdschriften.

Zie bijvoorbeeld Constantinou, M., Kagiialis, A., & Karekla, M. (2021). COVID-19 Scientific Facts vs. Conspiracy Theories: Is science failing to pass its message? *Int. J. Environ. Res. Public Health*, 18, 6343.

Deze stellingen worden opponeerbaar en verdedigbaar geacht en zijn als zodanig goedgekeurd door de promotor prof. dr. ir. J.W. van der Meer en de copromotoren dr. ir. B. Hofland en dr. ir. M. Zijlema.

**NEARSHORE WAVES AND RELATED WAVE
OVERTOPPING IN COMPLEX ESTUARIES**

NEARSHORE WAVES AND RELATED WAVE OVERTOPPING IN COMPLEX ESTUARIES

Proefschrift

ter verkrijging van de graad van doctor
aan de Technische Universiteit Delft,
op gezag van de Rector Magnificus Prof.dr.ir. T.H.J.J. van der Hagen,
voorzitter van het College voor Promoties,
in het openbaar te verdedigen op woensdag 8 december 2021 om 12:30 uur

door

Patrick OOSTERLO

civiel ingenieur, Technische Universiteit Delft, Nederland
geboren te Heerenveen, Nederland

Dit proefschrift is goedgekeurd door de

promotor: Prof.dr.ir. J.W. van der Meer

copromotor: Dr.ir. B. Hofland

copromotor: Dr.ir. M. Zijlema

Samenstelling promotiecommissie:

Rector Magnificus,

Prof.dr.ir. J.W. van der Meer,

Dr.ir. B. Hofland,

Dr.ir. M. Zijlema,

voorzitter

Technische Universiteit Delft & IHE Delft, promotor

Technische Universiteit Delft, copromotor

Technische Universiteit Delft, copromotor

Onafhankelijke leden:

Prof.dr.ir. A.J.H.M. Reniers,

Prof.dr.ir. P. Troch,

Prof.dr.-ing.habil. N. Goseberg,

Dr.ir. H. Steetzel,

Prof.dr.ir. S.N. Jonkman,

Technische Universiteit Delft, Nederland

Universiteit Gent, België

Technische Universität Braunschweig, Duitsland

Arcadis, Nederland

Technische Universiteit Delft, Nederland, reservelid

Dr.ir. G.Ph. van Vledder† heeft als begeleider in belangrijke mate aan de totstandkoming van het proefschrift bijgedragen.



Waterschap NOORDERZIJLVEST



Hoogwaterbeschermingsprogramma

Keywords: Eems-Dollard estuary; field measurements; numerical wave modelling; refraction; diffraction; non-linear interactions; laser scanner; LIDAR; wave run-up; wave overtopping

Printed by: Ridderprint, Alblaserdam, the Netherlands

Front & Back: Timo Hensen, TH Producties

Copyright © 2021 by P. Oosterlo

ISBN 978-94-6416-915-7

An electronic version of this dissertation is available at

<https://doi.org/10.4233/uuid:884cbc96-ebcd-488a-a820-0daae3962bb1>.

To Ana Cristina.

PREFACE

Working on this PhD research for the past five years has been very interesting and highly rewarding, but also challenging and frustrating at times. I feel that I have learnt a lot in the last five years, not just related to the topic of this dissertation or research in general, but also about many aspects of life outside academia. Nevertheless, even after five years of working on this dissertation, the little voice inside remains that says: 'Things can still be better, more thorough and more complete'.

Compared to the original plans, my PhD research was somewhat delayed and the scope of this dissertation significantly changed over time. The original plan for this study was to focus on wave measurements and numerical wave modelling in the Eems-Dollard estuary. The wave measurements would form an important component of analyses and would provide data for calibration and validation of the models.

The shift in scope and delay of this dissertation had several causes. Perhaps this PhD research started somewhat too early in the MVED field measurement project in the Eems-Dollard estuary. No instruments were installed yet in the first two years of the campaign. Since 2018, many instruments were placed in the area. However, it seems that the more instruments you install, the less storms occur. We can plan carefully and control many things, but we cannot control Nature. Hence, during the past years we were often 'waiting for the perfect storm' (see <https://www.tudelft.nl/en/ceg/research/stories-of-science/waiting-for-the-perfect-storm>). So far, one storm was measured (storm Ciara in February 2020), but this storm had a western wind direction, which did not lead to the required wave heights in the estuary. Due to the lack of wave measurements, the laser scanner work was added to this PhD research after two years. Hence, the work for the laser scanners was all done in the last three years, during which we measured one actual storm.

The modelling with the numerical wave model SWASH also influenced the progress, which was especially slow and frustrating in the beginning. Many unforeseen issues arose with compiling the model on the Dutch national supercomputer, on which the model was not used previously. After the successful compilation, difficulties arose related to running the model, keeping the runs stable, generating the right wave conditions and generating the right output. Step by step, in collaboration with (and thanks to) Marcel Zijlema, we solved these issues. Several recommendations for the compiling and running of SWASH on a large computational cluster can be found in Appendix C. Despite the issues, this process allowed me to learn a lot about numerical wave models.

Not only unforeseen circumstances out of my own hands had an influence on this PhD project. Keeping focus is still difficult for me, because I always find too many things too interesting. Meeting someone from the other side of the world, being in a long-distance relationship for two years and managing our way through the Dutch immigration process, had their impact as well. Around the 2-year mark of my PhD, I struggled with illness for some time. On the other side, I feel fortunate that I have made it through the COVID-pandemic relatively easily: physically, mentally, and by being able to continue working on

this dissertation without many problems.

All this certainly does not mean that I have not enjoyed working on my PhD. There is probably no other job where you have as much freedom to focus on what you find interesting and as much time to study one - very specific - topic. Furthermore, I feel lucky that I was able to present my work at several conferences. The days in Baltimore, Hannover and Melbourne were the icing on the cake that was this PhD. The design and set-up of and measurements with the laser scanner system were highly rewarding and fun as well. Performing field measurements already is a great experience in itself. Being able to stand on the dike in the field every once in a while, to see what happens in reality, also really helped me with writing this dissertation (and of course, it is simply a lot of fun).

I would like to thank everyone that contributed in some way to the creation of this dissertation. First of all, I would like to thank the committee members for their thorough reading of this dissertation and their constructive comments, which have significantly improved this dissertation.

I would like to thank my promotor Jentsje van der Meer for everything he has done for me, not just during this PhD, but also in the years before. Your enthusiasm and expertise made me decide to study civil engineering in the first place. I am very grateful for your support and supervision, first with my BSc and MSc theses, and now during my PhD research. Thanks to you, I was able to start this PhD in the first place, and I was able to keep on working on it for a fifth year. Your expertise on wave run-up and overtopping and years of experience with lab and field measurements have been indispensable to this research. Thank you for your help in navigating the paper publication process as well. Our discussions, and your reading of and commenting on all my work, have helped me improve my work immensely. You are someone I admire and look up to, and someone whose opinion I hold in very high regard. I feel lucky to already know you and Betsie for years now, and fondly remember the nice times together on the dike, at conferences and at your house.

I am also grateful to my co-promotor Bas Hofland. Without your help, this dissertation would not look like it looks now. Your help in the addition of the laser scanner work to this dissertation has been vital. Thank you for our discussions and for all the late-night reading of papers, chapters and reports. I always enjoy our discussions a lot. You are always very easy to talk to, willing to help, positive, eager to brainstorm and think outside the box.

I would like to thank my co-promotor Marcel Zijlema as well. You became an official member of the committee at a later stage, but already helped out with many aspects related to numerical wave modelling before that. Thank you for all your assistance, it has improved both my numerical modelling and this dissertation immensely. Also, I am happy that I could aid you with the computational modelling course.

I want to reserve a special place in this acknowledgement for Gerbrant van Vledder. Gerbrant and I first met at the end of 2016, to discuss my PhD research. At that time, he was not officially involved in my research yet, but he joined as co-promotor soon after. It was not necessary for him to do this; he was already very busy with other things, but he did this purely because he found the topic so interesting and fun. Over time I got to know him better, as a very passionate researcher, but above all as an exceptionally friendly man, with an incredible passion for everything he did. He was like a mentor to me and I was able to learn a lot from him about performing research and working with numerical wave models. Over time, our relationship grew from a supervisor-student relationship to more

of a relationship between good colleagues. For example, we always gave each other some sightseeing tips when one of us went on a trip to a new destination. Gerbrant was a source of inspiration for me, in his work as a researcher and as a person outside of work as well. He cared about our planet and tried to have as little impact on the environment as possible. He was always there for me, at any time. I remember the morning after his arrival in Melbourne for the Wave Workshop. He had arrived in the middle of the previous night, with a laptop that broke during his flight. Nevertheless, he was there first thing in the morning, before the start of the conference, to help me with my presentation. Gerbrant introduced me to many people in the field and taught me to get the most out of conferences. I feel privileged that I got to know him.

I would also like to thank my colleagues of the MVED project and Waterschap Noorderz-ijlvest. Marco Veendorp and Jan-Willem Nieuwenhuis, thank you for all the opportunities that you have given me, related to the funding, contracts and of course the field measurements themselves. A special thanks goes out to Maarten Overduin and Gosse Jan Steendam of Infram Hydren, for the very pleasant collaboration with the laser scanner measurements. In relation to the laser scanners, I cannot omit Gerben van der Meer, Frans Roorda and Jan Bakker, for their help in setting up the system and performing the measurements. Some of my fondest memories of the PhD are related to these measurements. We had a lot of fun (and Frisian snacks) during those days, and in those moments you realise what all the hard work is for.

I would like to thank the TU Delft for being a good employer and for all their support, especially at the section of Hydraulic Structures and Flood Risk. I am grateful to Bas Jonkman, who gave me the opportunity to continue working at the university after my MSc graduation. Furthermore, I would like to thank my fellow PhDs Chris Lashley and Su Kalløe and the colleagues who I had the pleasure of sharing an office with, especially Jeroen van den Bos and Arne van der Hout, for the discussions and pleasant collaboration. The same holds for my colleagues Vincent Vuik and Alessandro Antonini. I have had the pleasure to supervise several students during the past years: Ceylan Çete, Akshay Patil, Ineke van der Reijden and Jorick Laan. I enjoyed supervising you and your work has contributed to this dissertation in multiple ways.

I am grateful to the people at Deltares as well, for giving me several opportunities over the past years, from working on my MSc thesis, to helping out with measurements in the Delta Flume, to doing numerical work with OpenFOAM. With respect to the latter, I would specifically like to thank Marcel van Gent and Niels Jacobsen.

Much appreciation goes out to my current employer, Rijkswaterstaat. Most specifically, thank you Cees Henk Oostinga, Robert Slomp and Marcel Bottema, for giving me the chance to work at your department and for your flexibility regarding the finishing of my PhD.

Lastly, I would like to thank my family and friends. First of all, my parents, for always supporting me in every way possible, from my years in primary school until university and now during my PhD. I am forever indebted for your endless support in every aspect of my life. Thank you for all the opportunities you have given me and for never doubting me. I would like to thank my brother Leon as well, specifically for the fun moments we share. I always enjoy them thoroughly and it has helped in distracting me from the stress of the PhD. I also would like to thank my grandmother, for always motivating me to study hard

and have a critical attitude, already from a very young age. Además me gustaría agradecer a mi familia mexicana, por aceptar a este güero en su familia, por su apoyo en nuestra relación y todos los buenos momentos en viajes a México, Holanda o cualquier otro lugar.

I could not have completed this dissertation without the support of my friends, specifically Timo and León. You provided stimulating discussions as well as happy distractions to rest my mind outside of my research. Furthermore, thank you Timo, for creating the cover of this dissertation.

Last but not least, I want to thank you, Cristina. I am forever grateful that I met you. Thank you for bearing with me and coping with everything, no matter how difficult things would get. Thanks for always supporting me and coping with me during these often stressful times, for your interest in my research and your proof-reading of this dissertation. Thank you for your understanding during these - seemingly endless - busy times, and thank you for distracting me from the stress of the PhD during the few less busy moments. I hope I will have more time for us soon again. Thank you for always being there for me, no matter what. I am lucky to have you in my life.

Patrick Oosterlo
Den Haag, August 2021

SUMMARY

This dissertation focuses on the Eems-Dollard estuary in the north of the Netherlands and contributes to the MVED ('Meerjarige Veldmetingen Eems-Dollard') field measurement project in the area. The Eems-Dollard estuary is part of the Wadden Sea, a shallow shelf sea with barrier islands, deep tidal channels, shallow tidal flats and wetlands. The Eems-Dollard estuary is even more complex than the Wadden Sea, because of the deep channels, which run close to the dikes, and the very shallow flats, as well as the funnel shape, which can lead to very high water levels during storms. A particular aspect for this area is that the dike design conditions consist of an offshore-directed wind and very obliquely incident waves, up to 80° relative to the dike normal. Almost no studies have been performed on the estuary and almost no measurements were available inside the estuary.

This dissertation considers two main knowledge gaps, related to the modelling of wave propagation effects and measuring of (very) oblique wave run-up and overtopping, in a complex estuary. First, the performance of the SWAN wave model in predicting the wave conditions in a highly complex area, such as the Eems-Dollard estuary, has not been assessed before. Second, knowledge on and (field) measurements of the extra parameters (such as front velocities) necessary for the cumulative overload method are still scarce. This method considers the overtopping and erosion of the dike cover explicitly. Added to this, the few available (lab) investigations on wave run-up and overtopping during (very) oblique wave attack have not yet led to clear conclusions or guidelines. Therefore, the aim of this dissertation is to gain more insight into the uncertainties related to wave propagation processes and (very) oblique wave run-up and overtopping, which are important for the extreme wave loads on the dikes around the Eems-Dollard estuary.

More specifically, this dissertation regards two characteristic dike locations in the estuary, which protect a large part of the province of Groningen against flooding. One of these dikes was deemed 4 m too low with the last dike safety assessment. This high required crest level seems a result of uncertainties in the design conditions at the dike. These extreme conditions are determined by numerical wave models and overtopping prediction methods, as measurements during such extreme conditions are not available. It is of large importance that these conditions are accurately predicted by the applied methods and models. Applying such models in a highly complex estuary as the Eems-Dollard estuary, might mean reaching or even surpassing the models' limits of applicability.

To this end, the Dutch flood defence safety assessment framework (WBI) is studied and described in more detail first. A summary of the current framework is made, aimed at the knowledge gaps studied in this dissertation. This provides insight in where this dissertation is located in the current Dutch flood protection practices, and serves as background information for the more detailed analyses performed next.

The first part of this dissertation starts with investigating the performance of SWAN in the estuary and the near-dike wave conditions. The SWAN development version gives an up to 30% lower H_s and up to 20% lower $T_{m-1,0}$ at the dike than the assessment version.

Part of these differences are caused more offshore already, mainly at the transition from the North Sea to the Wadden Sea. The main causes for these more offshore differences are differences in the refraction formulations of both SWAN versions.

Next, the mechanisms that potentially turn the waves against the wind direction and around the corner at the port Eemshaven in the estuary are investigated. Simulations with the SWAN, SWASH and REFRAC wave models are performed, using a schematised version of the estuary. The results show that the waves indeed turn around the corner and become onshore-directed at the dike during design conditions, despite the offshore-directed wind. A large number of processes play a role in the estuary and influence the wave conditions at the dike. The main wave propagation processes are wave sheltering, refraction, wave (de)focusing, wave trapping (reflection) and diffraction. Triad wave-wave interactions are the main wave transformation process. The main generative and dissipative processes are depth-induced breaking and wave growth by the wind. These processes create a complex wave field and sometimes directionally multi-peaked spectra at the dike.

Following this, it is studied if the wave conditions as predicted by the SWAN assessment version are accurate or not, if the waves remain as large as the model predicts, and if SWAN can be used safely in this highly complex area. These questions are answered using large-scale simulations with SWAN, SWASH and REFRAC on the Dutch national supercomputer.

Recommended SWAN settings for the modelling of the wave propagation effects are determined. The refraction performance of SWAN mainly depends on the depth difference per grid cell Δd , the turning rate equation, the numerical scheme used to discretise this equation and the number of directional bins. The here determined recommended settings and the assessment settings generally outperform other SWAN settings. Predicted wave heights are lower with the recommended settings. Whether the wave heights as predicted by SWAN for the Dutch dike safety assessment or with the recommended settings are more accurate, depends in a large part on the accuracy of the used wind drag relations. Some limitations of SWAN arise in the complex Eems-Dollard estuary. These limitations are related to the omission of diffraction and non-collinear triad wave-wave interactions in SWAN, the overestimation of the transfer to the super-harmonic by the LTA method for the triads, and the overall worse performance of SWAN for more narrow-spread seas.

A wind direction of 330°N seems to be most relevant for the extreme loads on the dike in the estuary, as a direction of 300°N gives much lower wave heights. For a wind direction of 330°N, 2% - 25% of the wave energy is offshore-directed close to the dike. This energy does not contribute to the loads on the dike. This aspect is not considered in the Dutch dike safety assessment, but may have a large impact on the required crest levels of the dikes in the estuary.

Finally, it is determined where and how the wave conditions should be measured in the estuary, to gain further insight into the wave propagation processes in the area. The preferred measurement locations are determined by studying the wave propagation effects with SWAN. These recommended locations are the corner of the Eemshaven and the transition area from the deeper channel Bocht van Watum towards the shallow areas in front of the dike.

The second part of this dissertation investigates whether laser scanners can be used to measure (very) oblique wave run-up and overtopping on dikes in the field, during severe

winter storms. For this, an innovative system is designed, set-up, calibrated and validated, consisting of two synchronised laser scanners. Laser scanners have not been applied to measure run-up and overtopping in the field before. A novelty of the system is that two synchronised scanners are used to measure directional information of the waves. The system is flexible and mobile, it can be placed and relocated easily, without having to dig into the dike.

To determine the accuracy of the laser technique and the parameters that can be measured, the system is calibrated and validated in the field. The laser scanner technique is highly accurate, provided the correct laser scanner settings are used and a proper calibration of the laser position is performed before the actual measurements are started. Overall, wave run-up and overtopping parameters can be determined as accurately with the laser scanner system as with conventionally used methods.

Wave run-up heights can be determined accurately, for both normally and obliquely incident waves. Run-up depths larger than several centimetres can be measured reliably with the lasers as well. Close to the surf zone, the lasers give too large run-up depths due to foam and spray. Front velocities can be measured accurately for normally incident waves. 2D front velocity components of very oblique waves are difficult to measure. Wave overtopping volumes and discharges based on the laser data agree well with the most commonly used overtopping equations, for normally incident waves. Overtopping volumes and discharges during a storm with very obliquely incident waves agree well with wave overtopping tank measurements. The overtopping equations give larger volumes and discharges than the lasers and tank. These differences mainly stem from a large measured $T_{m-1,0}$ wave period at the toe of the dike. Furthermore, incident peak wave periods can be determined accurately based on the run-up time signals, for both normally and obliquely incident waves. Angles of incidence can be determined accurately for oblique wave attack. For the very oblique waves with $\beta > 65^\circ$ as present during the measured storm, the angle of incidence cannot be determined as well.

Finally, the influence of (very) oblique wave attack on wave run-up and overtopping is studied in more detail, with the verification of the laser scanner system in the field during the observed severe winter storm. For this storm with very obliquely incident waves and $d_{toe}/H_{s,toe} > 2.5$, the run-up is Weibull-distributed with the shape factor $b = 2.1-2.4$. Discrepancies in the $c_{d2\%}$ -values of the most commonly used run-up depth equation, as found in the literature, seem to be caused by the different dike slope angles that were used, rather than differences between small and large-scale tests. The results of the observed storm further suggest that the influence of the wave angle of incidence on the run-up depths is small. Measured front velocity components during the storm are larger than a commonly used front velocity relation. The present results suggest that the influence of oblique incidence on the front velocities is small. b -values of the Weibull distribution of overtopping wave volumes of the laser scanners are smaller than the most commonly used empirical relation, but the trend of the data agrees reasonably well. These differences could be related to the very oblique incidence or the influence of foam, entrained air and spray on the measured run-up depths by the lasers.

The first part of this dissertation provides more insight into the physical processes that play a role in the wave propagation in the Eems-Dollard estuary, and the performance of SWAN in modelling these processes. In the second part of this dissertation, an innovat-

ive laser scanner system is developed. The measurements with the system provide more insight in the influence of oblique wave attack on the run-up and overtopping. This dissertation contributes directly to several of the work packages of the MVED field measurement project in the Eems-Dollard estuary, and to the two main goals of the MVED project. Based on the results obtained in this dissertation, the uncertainties in the required crest height of the dike in the estuary can be reduced. The gained knowledge does not only contribute to the understanding of and reduction of uncertainties in and around the estuary, but at other locations as well. Furthermore, the knowledge gained contributes to the dike safety assessment framework in the Netherlands, and to the overall knowledge on numerical wave modelling and wave run-up and overtopping.

SAMENVATTING

Dit proefschrift richt zich op het Eems-Dollardestuarium in het noorden van Nederland en draagt bij aan het project Meerjarige Veldmetingen Eems-Dollard (MVED) in het gebied. Het Eems-Dollardestuarium maakt deel uit van de Waddenzee, een ondiepe binnenzee met eilanden, diepe getijdengeulen, ondiepe droogvallende platen en wetlands. Vergeleken met de Waddenzee is het Eems-Dollardestuarium nog complexer, vanwege de diepe geulen die vlak langs de dijken lopen, de zeer ondiepe platen, en de trechtersvorm, die bij storm tot zeer hoge waterstanden kan leiden. Een bijzonder aspect van dit gebied is, dat de ontwerpcondities van de dijken bestaan uit een afluende wind en zeer schuin invalende golven, tot 80° ten opzichte van de dijknormaal. Verder zijn er bijna geen studies uitgevoerd over het estuarium en waren er tot voor kort bijna geen metingen beschikbaar in het estuarium.

Dit proefschrift beschouwt twee belangrijke kennisleemten, gerelateerd aan de modellering van golfvoortplantingseffecten en het meten van (zeer) schuine golfoploop en -overslag, in een complex estuarium. Ten eerste is de nauwkeurigheid van het SWAN-golfmodel in het voorspellen van de golfcondities in een zeer complex gebied, zoals het Eems-Dollard estuarium, nog niet eerder onderzocht. Ten tweede ontbreekt er kennis over, en ontbreken er (veld)metingen van de extra parameters die nodig zijn voor de cumulatieve overbelastingmethode (zoals frontsnelheden). Deze methode beschouwt de overslag en erosie van de dijkbekleding expliciet. Ook hebben de enkele (laboratorium)-onderzoeken naar golfoploop en golfoverslag tijdens (zeer) schuine golfaanval die beschikbaar zijn, nog niet geleid tot duidelijke conclusies of richtlijnen. Het doel van dit proefschrift is dan ook meer inzicht krijgen in de onzekerheden met betrekking tot golfvoortplantingsprocessen en (zeer) schuine golfoploop en -overslag, welke van belang zijn voor de extreme golfbelastingen op de dijken in de Eems-Dollard.

Meer specifiek ligt de focus van dit proefschrift op twee karakteristieke dijklocaties in het estuarium, die een groot deel van de provincie Groningen beschermen tegen overstromingen. Een van deze dijken is bij de laatste beoordelingsronde 4 meter te laag bevonden. Deze hoge vereiste kruinhoogte lijkt het gevolg van onzekerheden in de ontwerpcondities bij de dijk. Deze extreme condities worden bepaald met numerieke golfmodellen en overslagformules, omdat metingen tijdens dergelijke extreme omstandigheden niet beschikbaar zijn. Het is van groot belang dat deze condities nauwkeurig worden voorspeld door de toegepaste methoden en modellen. Het toepassen van dergelijke modellen in een zeer complex estuarium als het Eems-Dollard estuarium, zou kunnen betekenen dat de toepasbaarheidsgrenzen van de modellen worden bereikt of zelfs overschreden.

Hiertoe is eerst het Wettelijk Beoordelingsinstrumentarium 2017 (WBI2017), waarmee de Nederlandse dijken worden beoordeeld, in meer detail bestudeerd. Het huidige instrumentarium is samengevat beschreven, gericht op de kennisleemten die in dit proefschrift worden bestudeerd. Dit geeft inzicht in waar dit proefschrift past binnen de huidige Nederlandse hoogwaterbeschermingspraktijk, en dient als achtergrondinformatie voor de

gedetailleerdere analyses die daarna zijn uitgevoerd.

Het eerste deel van dit proefschrift begint met het onderzoeken van de prestaties van het SWAN-golfmodel in het estuarium en de golfcondities bij de dijk. De ontwikkelingsversie van SWAN geeft een tot 30% lagere golfhoogte en tot 20% lagere -periode dan de WBI-versie bij de dijk. Een deel van deze verschillen wordt al verder van de kust veroorzaakt, vooral bij de overgang van de Noordzee naar de Waddenzee. De belangrijkste oorzaken van deze verschillen zijn verschillen in de refractieformuleringen van beide SWAN-versies.

Vervolgens zijn de mechanismen onderzocht, die er mogelijk voor zorgen dat de golven – om de bocht bij de Eemshaven en tegen de wind in – bijdraaien. Hiervoor zijn simulaties met een geschematiseerde versie van het estuarium uitgevoerd, met de golfmodellen SWAN, SWASH en REFRAC. De resultaten laten zien dat de golven tijdens ontwerpcondities inderdaad de hoek om draaien en aanlandig worden bij de dijk, ondanks de aflandige wind. Een groot aantal processen spelen een rol in het estuarium en beïnvloeden de golfcondities bij de dijk. De belangrijkste golfvoortplantingsprocessen zijn beschutting, het (ont)focussen van de golven, reflectie ("golfverstrikking"), refractie en diffractie. De diepgolfwisselwerkingen zijn het belangrijkste golftransformatieproces. Dieptegeïnduceerd breken en golfgroei door de wind zijn de belangrijkste generatie- en dissipatieprocessen. Deze processen creëren een complex golfveld en zorgen voor directioneel dubbel- of zelfs driedubbelgepekte spectra bij de dijk.

Aansluitend is onderzocht of de golfcondities, zoals voorspeld door de WBI-versie (beoordelingsversie) van SWAN, nauwkeurig zijn of niet. Verder is onderzocht of de golven in werkelijkheid zo hoog blijven als het model voorspelt, en of SWAN veilig kan worden gebruikt in dit zeer complexe gebied. Deze vragen worden beantwoord met behulp van grootschalige simulaties met SWAN, SWASH en REFRAC op de nationale supercomputer Cartesius.

Hierna zijn aanbevolen SWAN-instellingen voor het modelleren van de golfvoortplantingseffecten bepaald. De nauwkeurigheid van SWAN op het gebied van de refractie hangt voornamelijk af van het diepteverschil per roostercel Δd , evenals de gebruikte vergelijking voor de draaisnelheid van de golfrichting, het numerieke schema gebruikt voor de discretisatie van deze vergelijking, en het aantal richtingsbins. De hier bepaalde aanbevolen instellingen en de WBI-instellingen presteren over het algemeen beter dan andere SWAN-instellingen. Voorspelde golfhoogten zijn lager met de aanbevolen instellingen. Of de golfhoogten zoals voorspeld door SWAN voor WBI of met de aanbevolen instellingen nauwkeuriger zijn, hangt voor een groot deel af van de nauwkeurigheid van de gebruikte windschuifspanningsrelaties. Een aantal beperkingen van SWAN worden zichtbaar in het complexe Eems-Dollardestuarium. Deze beperkingen zijn gerelateerd aan de omissie van diffractie en de niet-collineaire diepgolfwisselwerkingen in SWAN, de overschatting van de overdracht naar de superharmonische door de LTA-methode voor de diepgolfwisselwerkingen, evenals de algehele slechtere prestaties van SWAN voor meer langkammige zeeën.

Een windrichting van 330°N lijkt het meest relevant voor de extreme belastingen op de dijken in het estuarium, aangezien een richting van 300°N veel lagere golfhoogten geeft. Voor een windrichting van 330°N is 2% - 25% van de golfenergie aflandig gericht bij de dijk. Deze energie draagt niet bij aan de belastingen op de dijk. Dit aspect wordt niet mee-

genomen binnen WBI, maar kan een grote invloed hebben op de benodigde kruinhoogte van de dijken in het estuarium.

Hierna is bepaald waar en hoe de golfcondities in het estuarium moeten worden gemeten, om meer inzicht te krijgen in de golfvoortplantingsprocessen in het gebied. De voorkeurslocaties zijn bepaald door de golfvoortplantingseffecten te beschouwen met SWAN. De aanbevolen locaties zijn de bocht bij de Eemshaven en het overgangsgebied van de diepere geul (de Bocht van Watum) richting de ondiepe delen voor de dijk.

Het tweede deel van dit proefschrift onderzoekt of laserscanners tijdens zware winterstormen kunnen worden gebruikt voor het meten van (zeer) schuine golfoploop en -overslag op dijken in het veld. Hiervoor is een innovatief systeem ontworpen, opgezet, gekalibreerd en gevalideerd, bestaande uit twee gesynchroniseerde laserscanners. Laserscanners zijn nog niet eerder toegepast om oploop en overslag te meten in het veld. Een innovatief aspect van het systeem is dat twee gesynchroniseerde lasers worden gebruikt, om richtingsinformatie van de golven te kunnen bepalen. Het systeem is flexibel en mobiel; het kan gemakkelijk worden geplaatst en verplaatst, zonder in de dijk te hoeven graven.

De nauwkeurigheid van de lasertechniek en de parameters die kunnen worden gemeten, zijn bepaald door het lasersysteem in het veld te kalibreren en te valideren. De laserscannertechniek is zeer nauwkeurig, op voorwaarde dat de juiste instellingen van de laserscanners worden gebruikt en een juiste kalibratie van de laserpositie is uitgevoerd, voordat de daadwerkelijke metingen worden gestart. Globaal gezien kunnen de golfoploop- en overslagparameters net zo nauwkeurig worden bepaald met het laserscannersysteem, als met conventioneel gebruikte methoden.

Golfoploophoogten zijn nauwkeurig te bepalen, voor zowel loodrecht als schuin invallende golven. Laagdiktes groter dan enkele centimeters kunnen betrouwbaar worden gemeten. De lasers geven te grote laagdiktes dicht bij de brandingszone, door schuim op het water en rondvliegende waterdruppels. Frontsnelheden kunnen nauwkeurig worden gemeten voor loodrecht invallende golven. 2D-frontsnelheidscomponenten van zeer schuine golven zijn moeilijk te bepalen op basis van de laserdata. Golfoverslagvolumes en -debieten op basis van de laserdata komen goed overeen met de meestgebruikte overslagformules, voor loodrechte golfaanval. Overslagvolumes en -debieten tijdens een storm met zeer schuine golfaanval komen goed overeen met metingen met een overslagbak. De overslagformules geven grotere volumes en debieten dan de lasers en bak. Deze verschillen komen voornamelijk voort uit een grote gemeten $T_{m-1,0}$ golfperiode aan de teen van de dijk. Verder kan de piekperiode van de inkomende golven nauwkeurig worden bepaald op basis van de tijdsignalen van de golfoploop, voor zowel loodrechte als schuine golfaanval. Hoeken van golfaanval kunnen nauwkeurig worden bepaald voor schuine golfaanval. Voor de zeer schuine golven, zoals tijdens de gemeten storm ($\beta > 65^\circ$), kan de hoek van golfaanval niet goed worden bepaald met de laserscanners.

Tot slot is de invloed van (zeer) schuine golfaanval op de golfoploop en golfoverslag nader bestudeerd, tijdens de gemeten zware winterstorm. Voor deze storm, met zeer schuin invallende golven en $d_{10e}/H_{s,10e} > 2,5$, is de oploop Weibull-verdeeld met vormfactor $b = 2.1-2.4$. Verschillende waarden voor de $c_{d2\%}$ -parameter van de meestgebruikte laagdiktevergelijking zoals gegeven in de literatuur, lijken te worden veroorzaakt door de verschillende dijkellingen die zijn gebruikt, niet door de verschillen tussen labschaal en prototypeschaal. De resultaten van de gemeten storm suggereren verder, dat de invloed van de

hoek van golfaanval op de laagdikte klein is. Tijdens de storm gemeten frontnelheidscomponenten zijn groter dan volgens een veelgebruikte frontnelheidsrelatie. De huidige resultaten suggereren dat de invloed van schuine golfaanval op de frontnelheden klein is. *b*-waarden van de Weibull-verdeling van overslagvolumes, bepaald op basis van de laserscanners, zijn kleiner dan de meestgebruikte empirische relatie, maar de trend van de data komt redelijk goed overeen. Deze verschillen kunnen zijn veroorzaakt door de zeer schuine golfaanval, of door de invloed van schuim op het water, lucht in de waterlaag of rondvliegende waterdruppels.

Het eerste deel van dit proefschrift geeft meer inzicht in de fysische processen die een rol spelen bij de golfvoortplanting in het Eems-Dollardestuarium, en de nauwkeurigheid van SWAN in het modelleren van deze processen. In het tweede deel van dit proefschrift is een innovatief laserscannersysteem ontwikkeld. De metingen met het systeem bieden meer inzicht in de invloed van schuine golfaanval op de golfoploop en -overslag. Dit proefschrift draagt direct bij aan een aantal van de werkpakketten van het MVED-project in het Eems-Dollardestuarium, evenals aan de twee hoofddoelen van het project. Op basis van de resultaten die in dit proefschrift zijn verkregen, kunnen de onzekerheden in de vereiste kruinhoogte van de dijk in het estuarium worden verkleind. De opgedane kennis draagt niet alleen bij aan het beter begrijpen en verminderen van de onzekerheden in en rond het estuarium, maar ook op andere locaties. Verder draagt de opgedane kennis bij aan het beoordelingsinstrumentarium voor de waterkeringen in Nederland en aan de algemene kennis over numerieke golfmodellering en golfoploop en -overslag.

CONTENTS

1	Introduction	1
1.1	Background	1
1.2	Knowledge gaps	5
1.3	Aim and main research questions	5
1.4	Approach, methods, scope and outline	6
1.5	Embedding in field measurement project MVED	10
2	A description of the Dutch flood defence safety assessment framework	15
2.1	Introduction	16
2.2	Offshore forcing and generation of storms	17
2.3	Determination of nearshore loads acting on the dikes	18
2.3.1	Steps 1 & 2: Wind fields	19
2.3.2	Steps 3 & 4: WAQUA simulations	20
2.3.3	Step 5: Boundary conditions	21
2.3.4	Step 6: SWAN simulations	22
2.3.5	Step 7: Interpolation	22
2.4	Determination of loads acting on the dike and probabilistic calculations	23
2.5	Relation of this dissertation to the framework	24
I	Modelling wave propagation effects in coastal waters	27
3	Wave modelling in a complex estuary	29
3.1	Introduction	30
3.2	Locations of interest	32
3.3	Approach	33
3.3.1	Quantification of propagation effects	33
3.3.2	Comparison SWAN assessment and development versions	34
3.3.3	Modelling of area around the corner of the Eemshaven	36
3.4	Results	37
3.4.1	Quantification of propagation effects	37
3.4.2	Comparison SWAN assessment and development versions	40
3.4.3	Modelling of area around the corner of the Eemshaven	45
3.5	Discussion	49
3.6	Conclusions	50
4	Modelling wave propagation effects in a complex estuary	53
4.1	Introduction	54
4.2	Literature review	57
4.3	Refraction and diffraction in SWAN	60

4.4	Methods and model set-up	61
4.4.1	Set-up of academic cases with narrow-spread waves	61
4.4.2	Set-up of academic cases with broad-spread waves	63
4.4.3	Set-up of detailed model cases	63
4.4.4	REFRAC set-up	64
4.4.5	SWAN set-up	64
4.4.6	SWASH set-up	65
4.5	Results of academic cases with narrow-spread waves	66
4.5.1	Results of refraction cases with regular waves	66
4.5.2	Results of diffraction cases with regular waves	73
4.5.3	Results of refraction cases with irregular, narrow-spread waves	74
4.5.4	Results of diffraction cases with irregular, narrow-spread waves	78
4.6	Results of academic cases with broad-spread waves	79
4.6.1	Results of refraction cases with irregular, broad-spread waves	79
4.6.2	Results of diffraction cases with irregular, broad-spread waves	85
4.7	Results of detailed model cases	87
4.7.1	Model verification	87
4.7.2	Model results	89
4.7.3	Discussion and implications for Dutch dike safety assessment	97
4.8	Conclusions	98
II Measuring wave run-up and overtopping on dikes		101
5	Calibration and preparation of field measurements with laser scanners. Part I: Wave run-up and overtopping	103
5.1	Introduction	104
5.2	Approach and system set-up	104
5.3	Data processing	106
5.3.1	Calibration	106
5.3.2	Data quality	107
5.4	Laser scanner settings and environmental conditions	108
5.5	Results and analysis of normally incident waves	109
5.5.1	Wave run-up heights	109
5.5.2	Wave run-up depths	111
5.5.3	Front velocities	112
5.5.4	Wave overtopping volumes and discharges	113
5.6	Outlook obliquely incident waves and other parameters	115
5.7	Conclusions	116
6	Calibration and preparation of field measurements with laser scanners. Part II: Oblique wave run-up and overtopping	119
6.1	Introduction	120
6.2	Approach and system set-up	121
6.3	Data processing and data analysis	124
6.4	Results and analysis of perpendicularly incident waves	126
6.4.1	Wave run-up heights	126

6.4.2	Wave run-up depths	128
6.4.3	Front velocities.	130
6.4.4	Wave overtopping volumes and discharges	131
6.5	Analysis and preparation for obliquely incident wave measurements.	133
6.5.1	Tests with oblique waves generated by the wave run-up simulator.	133
6.5.2	Numerical SWASH simulations	135
6.6	Conclusions.	143
7	Field measurements of very oblique wave run-up and overtopping with laser scanners	145
7.1	Introduction	146
7.2	System set-up.	147
7.3	Measurements during storm Ciara	149
7.4	Methods	152
7.5	Results	155
7.5.1	Wave run-up heights.	155
7.5.2	Wave run-up depths	159
7.5.3	Front velocities.	161
7.5.4	Wave overtopping volumes and discharges	163
7.5.5	Wave periods and angles of incidence	167
7.6	Conclusions.	168
8	Conclusions and recommendations	171
8.1	Conclusions.	172
8.1.1	Part I: Modelling wave propagation effects in coastal waters	172
8.1.2	Part II: Measuring wave run-up and overtopping on dikes	175
8.2	Recommendations	177
8.3	Application to the MVED field measurement campaign.	180
	Bibliography	181
A	Determination of characteristic storms	197
B	Refraction in SWAN	203
C	Guidelines for parallel simulations with SWASH	207
D	SWAN model settings	211
E	Outlook	217
	List of Symbols	231
	List of Figures	237
	List of Tables	247
	Curriculum Vitæ	251
	List of Publications	253

1

INTRODUCTION

*An expert is a person who has made all the mistakes that can be made
in a very narrow field.*

Niels Bohr

1.1. BACKGROUND

There are many low-lying countries, deltas and areas in the world. The Netherlands is one of those areas. In these low-lying areas, flooding is one of the major possible disasters. After the most well-known flood in the Netherlands, the 'Watersnoodramp' of 1953, the Delta Commission was installed, to study the causes of the flood and to develop measures to prevent future disasters. The commission developed the Delta Plan, which consisted of the Delta Works, the construction of several storm surge barriers, dams and locks, and the improvement of the dikes. These Delta Works had to protect the country from future flooding and were completed in 1997. Presently, the Netherlands is protected by 3,800 km of primary flood defences. The Netherlands is now known around the world for their past work and achievements in protecting the land from the water. However, protection from flooding and therefore improvement of the flood defences will always remain necessary, due to e.g. climate change, land subsidence and sea level rise.

This dissertation focuses on the Eems-Dollard estuary in the north of the Netherlands and contributes to the MVED ('Meerjarige Veldmetingen Eems-Dollard') field measurement project in the area. The Eems-Dollard estuary is part of the Wadden Sea, a shallow shelf sea with several barrier islands, deep tidal channels, shallow tidal flats and wetlands, see Figure 1.1. Multiple extensive studies, some including field measurements, were performed before in the Wadden Sea, to gain a more detailed understanding of this complex area (e.g. [Eslami Arab, Van Dongeren, & Wellens, 2012](#); [Groeneweg et al., 2009](#); [Groeneweg, Van Gent, Van Nieuwkoop, & Toledo, 2015](#); [Groeneweg & Van Vledder, 2005](#); [Van der Westhuisen et al., 2012](#); [Van Dongeren et al., 2011](#)). The Eems-Dollard estuary is an even more

complex area than the Wadden Sea, because of the deep channels, which run close to the dike, and the very shallow flats, as well as the funnel shape, which can lead to very high water levels during storms, see Figure 1.2. A particular aspect for this area is that the dike design conditions consist of an offshore-directed wind and very obliquely incident waves, up to 80° relative to the dike normal. Furthermore, almost no studies have been performed on the estuary and almost no measurements were available inside the estuary.

More specifically, this dissertation regards two characteristic dike locations in and around the Eems-Dollard estuary. The main focus lies on the dike section (black line in Figure 1.2) between the port Eemshaven (red area in Figure 1.2) and the town Delfzijl (blue area in Figure 1.2). The second dike section that is considered, is the dike section at Uithuizerwad (UHW), which is part of the Emmapolder dike to the west of the Eemshaven, see Figure 1.2. These dikes are two of the primary flood defences in the north of the Netherlands. The dike between the Eemshaven and Delfzijl protects a large part of the province of Groningen against flooding from the Eems-Dollard estuary.



Figure 1.1: Area of interest. The square indicates the Eems-Dollard estuary. Parts of the North Sea, the Wadden Sea and the north of the Netherlands shown as well. Bathymetrical data from Rijkswaterstaat six-yearly bathymetrical surveys, blue is deeper, yellow is shallower.

Currently, the safety of the primary flood defences in the Netherlands is assessed every six years. The framework of models and methods that is used for the assessment is called the 'Wettelijk BeoordelingsInstrumentarium' (WBI). Chapter 2 provides more information on the set-up of this framework. The last assessment was in 2017. The framework is presently being updated and has been renamed to BOI, 'Beoordelings- en OntwerpInstrumentarium', for the next assessment in 2023. With the change to BOI in 2023, the six-yearly assessment will change as well, to a more continuous check with an assessment every twelve years. The dike at Eemshaven-Delfzijl was rejected with the last assessment, meaning that it has to be improved. This was partly a result of projected sea level rise and land subsidence. Sea level rise and climate change with their accompanying rise in

wind speeds, water levels and wave heights, pose challenges for the flood defences. The IPCC (Oppenheimer et al., 2019) predicts a sea level rise of 0.43 m to 0.84 m this century (medium confidence, depending on the future volume of greenhouse gases emitted). In case of breaching of the flood defence in the Eems-Dollard, the possible damage and loss of life are very large. Veiligheid Nederland in Kaart 2 (Van Reen, 2013) gives estimates of the damage when breaching of the dike occurs, being up to 1 billion euros and up to a thousand lives.



Figure 1.2: Eems-Dollard estuary, with the port Eemshaven (red area), the town Delfzijl (blue area), the deep main tidal channel (number 1), the secondary channel the Bocht van Watum (number 2), the dike section of interest (black line) and the two locations of interest for the field measurements, Uithuizerwad (UHW) and the Twin Dikes (TD). Bathymetrical data from Rijkswaterstaat six-yearly bathymetrical surveys, blue is deeper, yellow is shallower.

The wave conditions at flood protection structures are important in the design and assessment of these structures. Precise and validated data about the extreme (design) conditions that might act on the flood defences are available for most of the Dutch coast, but not for the area around Delfzijl, as the area is highly complex and almost no measurements were available. The dike in the area was deemed 4 m too low with the last assessment. This high required crest level seems a result of uncertainties in the design conditions at the dike. These extreme conditions are determined by numerical wave models and overtopping prediction methods, as measurements during such extreme conditions are not available. It is of large importance that these conditions are accurately predicted by the applied methods and models. Applying such models in a highly complex estuary such as the Eems-Dollard estuary, with a highly irregular bathymetry, very oblique wave attack, and in which no measurements were available for calibration, might mean reaching or even surpassing the models' limits of applicability. Due to these complexities, it is difficult

to determine the wave conditions at the dike section between the Eemshaven and Delfzijl.

Furthermore, the extreme storms in the area tend to start out in the southwest and then turn to the northwest, resulting in an offshore-directed wind at the dike during extreme conditions. Even with this offshore-directed wind, relatively high onshore waves are predicted for this location, potentially due to the presence of the deep main tidal channel in the area (indicated by the number 1 in Figure 1.2), and a secondary channel that runs close to the dike (the Bocht van Watum, number 2 in Figure 1.2).

The phase-averaged numerical wave model SWAN (Simulating WAVes Nearshore, [Booij, Ris, & Holthuijsen, 1999](#)) is used for the dike safety assessment in the Netherlands. SWAN predicts large, onshore-directed waves at the dike, of order $H_s = 2$ m, which turn around the corner at the Eemshaven. Since no measurements are available, the wave boundary conditions are currently predicted without direct validation nearshore. Furthermore, there are indications that the formulations presently implemented in SWAN for e.g. refraction (e.g. [Dusseljee, Klopman, Van Vledder, & Riezebos, 2014](#); [Magne et al., 2007](#); [Van der Reijden, 2020](#)), diffraction (e.g. [Guzman Mardones, 2011](#); [Liu, 2009](#)) and triad wave-wave interactions (e.g. [Eslami Arab et al., 2012](#); [Groeneweg et al., 2015](#); [Salmon, Smit, Janssen, & Holthuijsen, 2016](#)) do not always suffice. This uncertainty in the wave conditions plays a large role in the uncertainty in the required dike crest height and could potentially lead to millions of euros of unnecessary dike reinforcements.

In the past, the required crest heights of dikes were determined by assessing the wave run-up heights. Nowadays, dikes are usually designed using the mean wave overtopping discharge. Typically, wave overtopping is measured in the field using wave overtopping tanks (e.g. [De Rouck, Verhaeghe, & Geeraerts, 2009](#); [Van der Meer et al., 2019](#); [Wenneker, Spelt, Peters, & De Ronde, 2016](#)), but overtopping measurements in the field are scarce, since they are difficult to perform. Furthermore, overtopping tanks are fixed at a certain location and at a fixed elevation. The required crest level of the dikes in the Netherlands is based on the mean wave overtopping discharge as well, using the equations of [Van der Meer \(2002\)](#), later included in [EurOtop \(2007\)](#). Presently, a transition is ongoing towards a cumulative overload method ([Van der Meer, 2011](#); [Van der Meer et al., 2010](#)), whereby erosion of the dike (grass) cover is considered explicitly. Not only measurements of overtopping discharge or volumes, but also of (front) velocities are necessary for calibrating this method. Velocities and depths of run-up and overtopping flows have been measured in the lab and field, but they are difficult to perform, due to turbulence and aeration ([Schüttrumpf & Van Gent, 2004](#); [Van der Meer et al., 2010](#)). The measurements are performed often using resistance type gauges, which require a certain minimum run-up depth, or step gauges, which have a coarse resolution. Recently, laser scanners have been used to measure wave run-up and overtopping in the lab, showing promising results ([Hofland, Diamantidou, Van Steeg, & Meys, 2015](#)). However, this method had not been applied in the field yet.

Much is known already about wave run-up and overtopping of normally incident waves, as quite some research has already been performed on these topics, see [EurOtop \(2018\)](#). Only limited research is available on the influence of oblique wave attack on wave run-up and overtopping. Most of the relevant research was performed on the influence of long-crested waves, only a few investigations are available on the influence of oblique short-crested waves on wave run-up and wave overtopping. This especially holds for very large

angles of wave attack. The few available investigations have not yet led to clear conclusions or guidelines (e.g. [Bornschein et al., 2014](#); [Vieira Leite et al., 2019](#)). As the expected angles of incidence at the dike in the Eems-Dollard estuary are up to 80° , the influence of (very) oblique wave attack on wave run-up and overtopping plays a role in the area of interest as well. Furthermore, it is the uncertainty in this influence which is partly responsible for the large required crest height of the dike.

1.2. KNOWLEDGE GAPS

This dissertation considers two main knowledge gaps, related to the modelling of wave propagation effects and measuring of the related (very) oblique wave run-up and overtopping, in a complex estuary:

1. The performance of SWAN in predicting the wave conditions at the dike in a highly complex area as the Eems-Dollard estuary, consisting of deep tidal channels, shallow flats, and characterised by an offshore wind, has not been assessed before.
2. Knowledge on and (field) measurements of the extra parameters necessary for the transition towards the cumulative overload method, such as (front) velocities, are still scarce. Furthermore, there exists a general lack of knowledge on wave run-up and overtopping during (very) oblique wave attack, as the few available (lab) investigations have not yet led to clear conclusions or guidelines.

1.3. AIM AND MAIN RESEARCH QUESTIONS

The aim of this dissertation is to gain more insight into several uncertainties related to wave propagation processes and (very) oblique wave run-up and overtopping, which are important for the extreme wave loads on the dikes around the Eems-Dollard estuary. These uncertainties contribute to the present large required crest height of the dike in the area. The goals of the first part of this dissertation are to determine which wave propagation processes play a role in the area, to determine how significant their role is, and to gain more insight in the most significant processes. Further goals of the first part of this dissertation are to determine how well SWAN can model these processes and how well the model performs in the estuary. The goal of the second part of this dissertation is to develop a new measurement technique, which can measure (very) oblique wave run-up and overtopping in the field during severe winter storms, and to subsequently determine what the influence of (very) oblique wave attack on wave run-up and overtopping and their related parameters is. Hence, the focus of the first part of this dissertation lies on modelling with the numerical wave model SWAN. The focus of the second part lies on measuring wave run-up and overtopping with laser scanners.

Based on the results obtained in this dissertation, the uncertainties in the required crest height of the dike can potentially be reduced. The gained knowledge can potentially not only contribute to the understanding of and reduction of uncertainties in and around the Eems-Dollard estuary, but at other locations as well. Furthermore, the knowledge gained can contribute to the dike safety assessment framework in the Netherlands, and to the overall knowledge on numerical wave modelling and wave run-up and overtopping.

Six main research questions have been formulated, addressing the two knowledge gaps considered in this dissertation.

Knowledge gap 1, part I of this dissertation, about modelling of wave propagation:

1. What is the cause of the apparent turning of the waves around the corner at the Eemshaven; which processes play a role?
2. How well can SWAN model these processes; how well does the model perform in the estuary?
 - (a) Are the wave conditions as currently predicted by SWAN in the estuary accurate or not?
 - (b) Do the waves remain as large as the SWAN assessment version predicts?
 - (c) Can SWAN be used safely in such a highly complex area, or are the limitations of the underlying modelling concepts of SWAN reached or surpassed?
3. Where and how should the wave conditions be measured in the Eems-Dollard estuary, to gain further insight into the wave propagation processes in the area?

Knowledge gap 2, part II of this dissertation, on measuring wave run-up and overtopping:

4. Can laser scanners be used to measure (very) oblique wave run-up and overtopping in the field during severe winter storms?
5. How accurate is this technique, and can the additional parameters required for the cumulative overload method be measured accurately as well?
6. What is the influence of (very) oblique wave attack on wave run-up and overtopping, and on the related (distributions of) heights, depths, velocities, volumes and discharges?

1.4. APPROACH, METHODS, SCOPE AND OUTLINE

Figure 1.3 presents the outline of this dissertation. First, the Dutch flood defence safety assessment framework is described in more detail, in chapter 2. This chapter summarises the current framework, aimed at the knowledge gaps studied in this dissertation. Therefore, the focus lies on the determination of the wave loads acting on the dikes and the determination of the wave overtopping over the dikes. The chapter provides insight in where this dissertation is located in the current Dutch flood protection practices. Furthermore, this chapter serves as an introduction to and background information for the more detailed analyses performed in the following chapters of this dissertation.

The bulk of this dissertation is split into two parts, where Part I: Modelling wave propagation effects in coastal waters, focuses on the first knowledge gap. Part II: Measuring wave run-up and overtopping on dikes, focuses on the second knowledge gap.

To fill in the first knowledge gap, it is necessary to study whether using the SWAN model in this highly complex area means reaching the limitations of the underlying modelling concepts of the model. Furthermore, it is necessary to study whether the predictions by SWAN in this area are accurate or not, what the cause is of the apparent turning of the

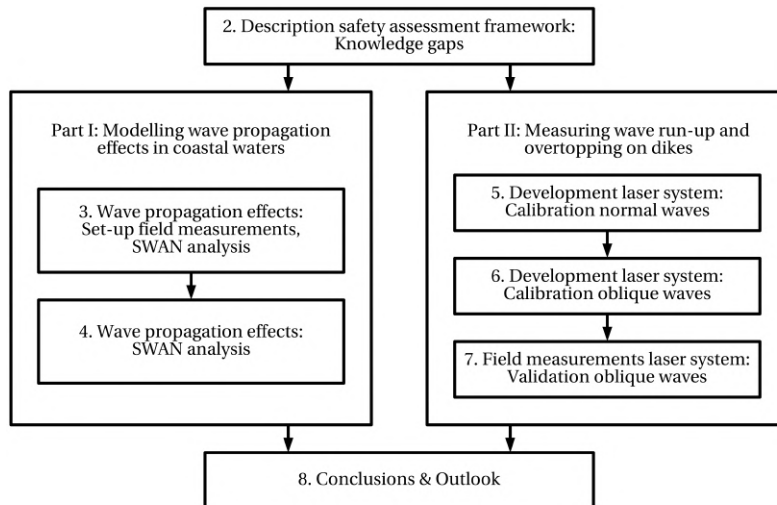


Figure 1.3: Outline of the dissertation. The set-up with two main parts is given, as well as the interactions between the different components.

waves around the corner of the Eemshaven, and whether the waves remain as large as the model predicts in reality as well.

Part I consists of chapters 3 and 4. Chapter 3 focuses on wave propagation effects in the whole of the eastern Wadden Sea and Eems-Dollard estuary. It treats the locations that are most suited for wave measurements in the area, to validate SWAN and to gain more insight in the physics that play a role. For this goal, an analysis of propagation effects is made. Further, the origin of the large predicted onshore-directed wave heights is studied. Lastly, it assesses how SWAN can best be applied in this complex area, by comparing SWAN versions (research questions 1-3).

Chapter 4 focuses on the performance of SWAN related to nearshore wave propagation effects, like refraction effects. The main goals of this chapter are to determine which processes play a role in the estuary and whether SWAN can accurately predict the wave conditions in the area. The performance of the model is assessed with schematised bathymetries of increasing complexity, based on the Eems-Dollard estuary. The results are compared to different numerical wave models, since no measurements were available yet (research questions 1-2).

To fill in the second knowledge gap, it is necessary to measure the wave run-up and overtopping parameters in the area of interest, where very oblique wave attack occurs. Application of a new measurement technique in the estuary could provide more insight in the influence of very oblique wave attack on wave run-up and overtopping, thereby potentially reducing the uncertainties in the required crest level of the dike.

Part II consists of chapter 5, 6 and 7. Chapter 5 focuses on the development of an innovative system to measure wave run-up and overtopping, using two laser scanners. The system measures run-up characteristics of normally and obliquely incident waves on a dike in the field. Furthermore, the wave overtopping volumes and discharges can be

calculated from the measured data. The chapter considers the development of, and first calibration tests with the system in the field, with normally and obliquely incident waves generated by the wave run-up simulator on a grass dike slope, with the main focus on the normally incident waves (research questions 4-5).

Chapter 6 extends this with an analysis of oblique wave attack, with the wave run-up simulator field tests and with simulations with the phase-resolving numerical wave model SWASH (Zijlema, Stelling, & Smit, 2011), to gain more insight in the potential performance of the system under actual oblique waves. This chapter yields insight in the capabilities of the laser scanners in measuring perpendicularly and obliquely incident waves (research questions 4-5).

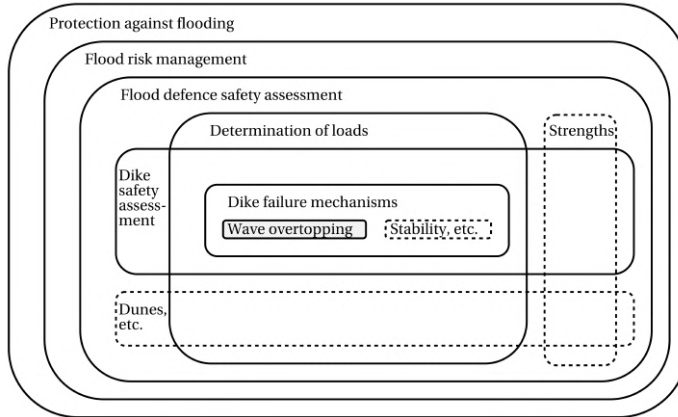
Chapter 7 focuses on the first field measurements with the laser scanner system, during an actual severe winter storm with very oblique wave attack, storm Ciara. The chapter describes the analysis of the run-up and overtopping data obtained during the storm and compares the results with data from more standard measurement techniques and the current knowledge on wave overtopping, to gain possible new insights in the influence of very oblique wave attack (research questions 4-6).

Finally, chapter 8 presents the main conclusions of this dissertation, as well as the limitations and potential applications of the results, and recommendations for future research.

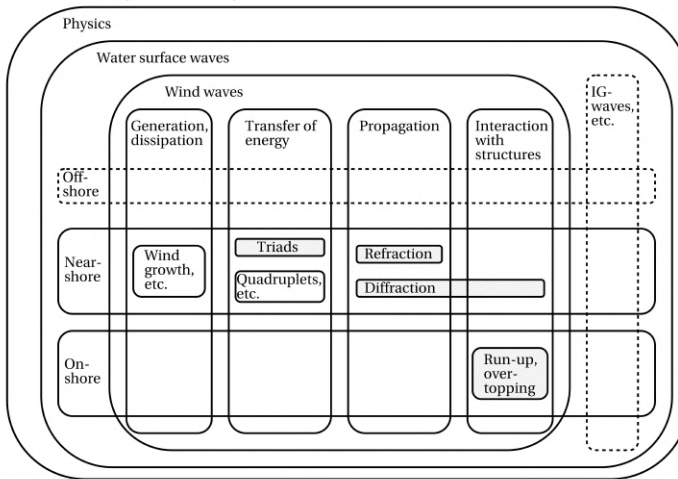
The focus of this dissertation can be shown from three different points of view, being the protection against flooding, the physics of water surface waves and the measuring and modelling of physical processes, see Figure 1.4. The three sub-figures also show the scope and limitations of this dissertation. Regarding the protection against flooding (upper panel of Figure 1.4), the focus lies on the Dutch flood defence safety assessment, more specifically the dike safety assessment. Dunes and structures such as storm surge barriers are not considered here. The focus lies on one location, the Eems-Dollard estuary. The emphasis lies on the side of the loads, the strength of the dikes is not considered in detail. Concerning the loads, the focus lies on the dike failure mechanisms 'erosion of the grass revetment on the outer slope' and 'erosion of the grass revetment on the crest and inner slope'. Failure mechanisms such as stability or piping are not studied in this dissertation.

Regarding the physics of water surface waves (middle panel of Figure 1.4), the main focus lies on wind waves in the nearshore and onshore. Longer waves are included whenever they are relevant, shorter waves – such as capillary waves – are not considered. This dissertation focuses on the energy transfers in the spectrum of wind waves in the nearshore, as well as the propagation of these waves and their interactions with structures. The main focus lies on the propagation effects refraction and diffraction, but energy transfers such as the non-linear triad wave-wave interactions are considered as well. Other energy transfers such as the quadruplet interactions, or generative or dissipative processes such as wind generation or depth-induced breaking, are briefly discussed whenever relevant or of influence. Bragg-scattering is not treated in detail. Regarding the onshore interactions of wind waves with structures, wave run-up and overtopping on dikes are studied in this dissertation. The focus lies on the sea-side of the dikes. Velocities and flow depths on the land-side are not considered, neither is erosion of the inner slope.

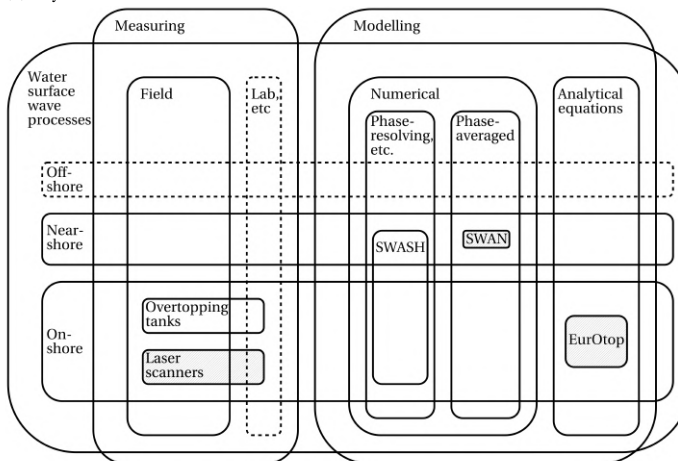
Regarding the measuring of water surface wave processes (lower panel of Figure 1.4), the focus lies on measuring in the field. The main area of interest is onshore measure-



(a) Protection against flooding.



(b) Physics of water surface waves.



(c) Measuring and modelling of water surface wave processes.

Figure 1.4: Dissertation focus from three different points of view. Top: Protection against flooding. Middle: Physics of water surface waves. Bottom: Measuring and modelling of water surface wave processes. Hatched areas are main focuses, dashed areas are outside the scope of the dissertation. Figures inspired by [Vuik \(2019\)](#).

ments of wave run-up and overtopping with laser scanners. Measurements with overtopping tanks are included as well, for comparison with laser scanner data. Regarding the modelling of water surface wave processes, this dissertation focuses on numerical wave models and analytical wave run-up and overtopping equations. The phase-averaged numerical wave model SWAN is mainly studied, simulations with the phase-resolving numerical wave model SWASH and the ray-tracing model REFRAC are included for comparisons. The [EurOtop \(2018\)](#) equations are the run-up and overtopping equations that are considered mainly.

1.5. EMBEDDING IN FIELD MEASUREMENT PROJECT EEMS-DOLLARD ESTUARY

This dissertation contributes to the MVED ('Meerjarige Veldmetingen Eems-Dollard') field measurement project. During the design of the preferred alternative for the improvement of the dike between the Eemshaven and Delfzijl, the impression was obtained that a very conservative result was achieved with respect to the required crest level, due to the use of new safety standards in the Netherlands ([Van der Meer Consulting et al., 2017](#)). As an alternative to a very large raise of the crest level of the dikes, the local water board chose to reduce the design lifetime from 50 years to 25 years. The plan was to use field measurements and further study to determine whether the previously used uncertainties and safeties were indeed too large, and if the proposed dike height will still be safe for the next 50 years. Hence, the 12-year long MVED field measurement campaign was planned, starting in 2018. The aim of the measurement campaign is twofold. First, to understand the processes yielding nearshore wave conditions better, ultimately leading to improved numerical prediction models. Second, to understand the processes related to oblique wave run-up and overtopping better, leading to improved prediction methods. To this end, a combination of numerical modelling and field measurements is used.

The focus of the measurements in the MVED project lies on two locations, Uithuizerwad (UHW) and the Twin Dikes (TD, named after a dike reinforcement project in the area), see [Figure 1.2](#). Uithuizerwad is part of the Emmapolder dike to the west of the Eemshaven, where measurements of water levels and waves were available at an existing measurement pole. The pole is located on the shallow flat in front of the dike. The dike at UHW consists of asphalt on the lower and grass on the upper slope. Refer to [Figure 1.5](#) and the upper panel of [Figure 1.6](#). The Twin Dikes location is part of the dike section of interest, and is located inside the estuary to the south of the Eemshaven. Here, no measurements were available yet. The orientation of the dike normal at TD is approximately 45°N , thus north-east. See [Figure 1.5](#) and the lower panel of [Figure 1.6](#). Both locations are under oblique to very oblique wave attack, but at Uithuizerwad this wave attack is direct and coming from the Wadden Sea, whereas it is indirect at the Twin Dikes. Furthermore, the wave conditions at Uithuizerwad are shallow water conditions, due to the kilometre-long shallow area in front of the dike, located above mean sea level at approximately 0.65 m+NAP ('Normaal Amsterdams Peil', Dutch ordnance level roughly corresponding to mean sea level). The Twin Dikes location lies sheltered from direct wave attack by the corner at the Eemshaven. The wave conditions there are not depth-limited, due to a lower bottom level and higher water levels. The deeper secondary channel the Bocht van Watum runs quite close

to the Twin Dikes location, and there is a shallower area located around mean sea level directly in front of the dike of several hundreds metres wide.

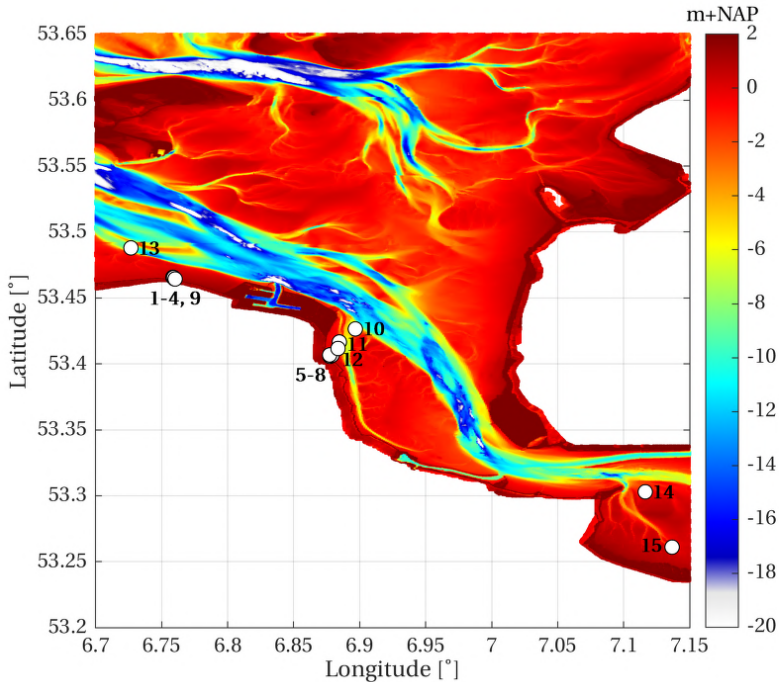


Figure 1.5: Eems-Dollard estuary with measurement instruments as of the end of 2020. See Table 1.1 for the definitions of the numbers and further details on the instruments. Bathymetrical data from Rijkswaterstaat six-yearly bathymetrical surveys.

Water levels and waves are measured by a step gauge and a radar at the existing measurement pole at UHW. Note that these instruments do not provide directional information of the waves. In time, more and more instruments have been installed in the area, of which Figure 1.5 and Table 1.1 give an overview. Waves are measured with directional wave buoys (WaveDroids, see <https://www.obscape.com>) and ADCPs. Wave overtopping is measured with four overtopping tanks built into the dikes, two at each measurement location. Wave run-up and wave overtopping are measured with an innovative system using two terrestrial laser scanners (LIDARs) as well, see Part II of this dissertation (chapters 5, 6 and 7). Waves might be measured with X-band radar in the project in the future. Furthermore, a wind meter will probably be installed in the estuary.

Van der Meer (2018) presents an overview and analysis of historical storms in the area. Appendix A determines the expected wave conditions at UHW and TD, corresponding to storms with several return periods and based on data of the Dutch dike safety assessment framework WBI 2017. Furthermore, overtopping discharges and required crest levels corresponding to these return periods are presented. Based on these conditions, two characteristic storms were determined for the Eems-Dollard estuary, with their characteristic offshore conditions and nearshore conditions at UHW and TD. These characteristic



(a) Uithuizerwad.



(b) Twin Dikes.

Figure 1.6: Top: Dike at Uithuizerwad (UHW), with two of the overtopping tanks and the laser scanner system in the background. Bottom: Twin Dikes location (TD), with two of the overtopping tanks being built into the dike.

storms were used to determine which wave heights and periods can be expected during the measurement campaign, and are used for analyses throughout this dissertation. Two actual storms have been measured within the field measurement campaign so far: the Kroojanusvloed of 9 January 2019 with a northwestern wind direction, and storm Ciara of 10 to 12 February 2020 with a southwestern to western wind direction. This last storm is further discussed in chapter 7.

This dissertation contributes to the design and the two main goals of the field measurement campaign. Regarding the design of the campaign, the dissertation aids with the placement of wave buoys and with performing the laser scanner measurements. Part I directly contributes to the first main goal of the campaign: 'to understand the processes yielding nearshore wave conditions better, which should ultimately lead to improved numerical prediction models'. Part II contributes to the second main goal: 'to understand

the processes related to oblique wave run-up and overtopping better, which should lead to improved prediction methods'.

No. [-]	Instrument	Measurement type	Installed since season [year]	Lon. [°]	Lat. [°]	Usage [-]
1	Tank UHW, 4.4 m+NAP	Overtopping	2018-2019	6.75991	53.46446	U
2	Tank UHW, 5.3 m+NAP	Overtopping	2018-2019	6.75973	53.46446	U
3	ADCP UHW	Waves	2018-2019	6.75916	53.46545	U
4	WaveDroid UHW	Waves	2018-2019	6.75853	53.46569	U
5	Tank TD, 4.0 m+NAP	Overtopping	2019-2020	6.87758	53.40575	NU
6	Tank TD, 4.6 m+NAP	Overtopping	2019-2020	6.87744	53.40579	NU
7	ADCP TD	Waves	2019-2020	6.87722	53.40681	LB
8	WaveDroid TD	Waves	2019-2020	6.87892	53.40653	LB
9	Lasers UHW	Run-up, overtopping	2019-2020	6.76019 ¹	53.46439	D
10	WaveDroid BVW	Waves	2019-2020	6.89670	53.42650	LB
11	WaveDroid BVW	Waves	2019-2020	6.88460	53.41660	LB
12	WaveDroid BVW	Waves	2019-2020	6.88360	53.41170	LB
13	WaveDroid OWEZ	Waves	2020-2021 ²	6.72672 ¹	53.48794	NU
14	WaveDroid DLD	Waves	2020-2021	7.11632 ¹	53.30294	NU
15	WaveDroid DLD	Waves	2020-2021	7.13665 ¹	53.26105	NU
16	Wind pole DLD	Wind	TBD	TBD	TBD	NU
17	X-band radar EMSH	Waves	TBD	TBD	TBD	NU

Table 1.1: Overview of instruments MVED field measurement campaign. See Figure 1.5 for the locations of the instruments in the estuary. BVW indicates the channel Bocht van Watum, OWEZ indicates Oude WesterEems Zuid, the location of a Rijkswaterstaat directional Waverider buoy. The WaveDroid is located next to this buoy for validation. DLD indicates the southern part of the Eems-Dollard estuary, EMSH is the Eemshaven. TBD is To Be Determined. D indicates Developed in this dissertation, LB indicates Location Based on information in this dissertation, U is Used in this dissertation, NU is Not Used. ¹Approximate location. ²WaveDroid might be relocated after the first year.

2

A DESCRIPTION OF THE DUTCH FLOOD DEFENCE SAFETY ASSESSMENT FRAMEWORK

*I learned very early the difference between knowing the name of something
and knowing something.*

Richard Feynman

This chapter summarises the framework that is currently used in the Netherlands to assess the flood defences, for the protection against flooding.¹ This framework consists of probabilistic, numerical and analytical models. This chapter mainly focuses on the aspects of the framework that are relevant for the knowledge gaps studied in this dissertation. Considering the framework itself, the focus lies on the dike safety assessment, with the more specific focus being the determination of the loads acting on the dikes (e.g. water levels, waves), to be used as input for the failure mechanism that considers wave overtopping. Geographically, the focus lies on the protection against flooding in the coastal region, more specifically in the Wadden Sea and Eems-Dollard estuary. This chapter provides insight in where this dissertation is located in the current flood protection practices. Furthermore, this chapter serves as an introduction to and background information for the more detailed analyses performed in the following chapters of this dissertation.

¹This chapter was written based on the framework used for the assessment in 2017 (WBI 2017). By now, the framework has been renamed to BOI and is in the process of being updated for the next assessment in 2023.

2.1. INTRODUCTION

An excellent summary of the history of the Dutch struggle against the sea, as well as the development of the Dutch flood protection practices, can be found in [Battjes and Gerritsen \(2002\)](#). This chapter presents a condensed description of the current Dutch flood defence safety assessment framework, aimed at the topics of this dissertation. [Chbab and De Waal \(2016\)](#); [De Waal \(2018\)](#); [Gautier and Groeneweg \(2012\)](#); [Ministerie van Infrastructuur en Milieu \(2016a, 2016b, 2016c\)](#) give more extensive descriptions of the framework.

Currently, the flood defences in the Netherlands are assessed every six years. The Dutch safety assessment framework, 'Wettelijk BeoordelingsInstrumentarium' (WBI) in Dutch, is a framework consisting of statistical models, numerical models, empirical equations and software tools, which is used to perform the assessment of the primary flood defences in the country. The last assessment was performed in 2017 (WBI 2017). The safety assessment comprises determining the probability of flooding of an area protected by a trajectory of flood defences and comparing this probability of flooding with the norm probability as prescribed by law. These trajectories were defined based on differences in consequences of flooding of the hinterland, physical characteristics of the hinterland, the length of the trajectory and location-specific circumstances.

Before 2017, areas enclosed by flood defences (typically polders, and called 'dike rings') were used instead of trajectories of flood defences. Furthermore, the norm probability of exceedance was defined by law, instead of the probability of flooding. By prescribing a norm probability of flooding, some of the consequences of flooding are taken into account as well, e.g. by setting a stricter probability of flooding for areas with a large population or economic value. Recently, the framework was renamed to BOI ('Beoordelings-en OntwerpInstrumentarium'). Together with this change in name, the six-yearly assessment will change to a more continuous check with an assessment every twelve years, in 2023. With the transition to BOI, the framework will shift more and more from the probability of flooding towards the risk of flooding in the future, taking more of the potential consequences of flooding (economic, loss of life, et cetera) into account as well.

The probability of flooding is estimated from the combined probabilities of sub-processes that contribute to the final event of flooding, taking all relevant elements and associated failure mechanisms and their probabilities into account ([Battjes & Gerritsen, 2002](#)). Thus, the loads corresponding to different failure mechanisms (called assessment tracks in WBI) are compared to the strength of the defences in a certain trajectory. Failure mechanisms are ways in which flooding can occur due to failure of a defence, e.g. erosion, sliding and piping. A trajectory can consist of e.g. dikes, dunes or structures such as storm surge barriers. This chapter focuses on dikes, as the focus of this dissertation lies on a dike section.

Two probabilities of flooding have been prescribed by law for each dike trajectory, a signal value and a lower limit. The lower limit is the norm probability of flooding and is used for the safety assessment. The dike trajectory has to be improved (is rejected), if it has a larger probability of flooding than the limit value. The signal value is a less strict probability of flooding. The ministry needs to be notified if a certain trajectory has a larger probability of flooding than the signal value. The lower limit for the dike trajectory of which the dike at Uithuizerwad is a part is $1,000 \text{ year}^{-1}$. For the dike trajectory of which the Twin Dikes is a part, this is $3,000 \text{ year}^{-1}$ ([Van Reen, 2013](#)). The norm probability depends on the vulnerability, population and economic value of the hinterland.

This chapter mainly focuses on the determination of the loads, which act on the dikes, in the coastal region. The loads are determined by translating the offshore parameters that characterise a storm, such as the wind, to nearshore parameters at the flood defence, viz. water levels and wave conditions. These loads at the flood defences are then translated to the relevant parameters acting on the flood defence for a certain failure mechanism, e.g. a wave overtopping discharge. With respect to the failure mechanisms, the main focus of this chapter lies on the failure mechanisms 'erosion of the (grass) revetment on the outer slope' and 'erosion of the (grass) revetment on the crest and inner slope' of WBI 2017.

Section 2.2 treats the aspects related to the (offshore) forcing and generation of storms, e.g. the wind. The determination of the (nearshore) loads at the dikes (e.g. water levels and waves) are discussed in section 2.3. Section 2.4 treats the (onshore) loads acting on the dikes (e.g. wave overtopping) and the probabilistic calculations. Finally, section 2.5 discusses the relations of this dissertation to the framework.

2.2. OFFSHORE FORCING AND GENERATION OF STORMS

The normative situation for the loads acting on the dikes in the coastal region of the Netherlands is defined by extreme water levels and waves. These water levels and waves are caused by storms with extreme wind velocities. Therefore, the offshore ('base') stochastic variables considered in WBI for the coastal region are the wind direction and wind velocity, as well as the sea water level. The eastern Wadden Sea and Eems-Dollard estuary are part of this coastal region.

The wind direction and velocity are considered as stochastic. The wind direction is treated as a discrete stochastic variable, with 12 discrete wind direction bins. The wind velocity is treated as a continuous stochastic variable, defined by an exponential distribution. The wind direction-dependent exceedance probabilities have been defined at several locations, based on time series of measurements. E.g. for the eastern Wadden Sea, measurement station West-Terschelling was used. The wind velocity variable that is used, is the potential wind velocity U_p [m/s], which is defined as the hourly averaged wind velocity at 10 m above homogeneous open terrain with a roughness length of 0.03 m (De Waal, 2003).

The statistics for the sea water levels were determined for several measurement locations, derived from time series of measurements at these measurement stations. The measured time series of water levels up until 1985 were used to determine the statistics. To account for sea level rise since 1985, a certain robustness value is added to the water levels. For the Eems-Dollard, this robustness value is 7 cm (Chbab & De Waal, 2016). In reality, the water level set-up is partly caused by the wind. This physical relation between wind and water level is not explicitly accounted for in WBI. However, the influence of the wind on the water levels is implicitly included in the statistical series of the measurement stations. The correlation between wind velocity and water level is based on an analytical relation of Vrouwenvelder and Steenbergen (2003). Within the probabilistic model, the statistical uncertainties in the probability distributions of the wind velocity and sea water level are taken into account as well.

2.3. DETERMINATION OF NEARSHORE LOADS ACTING ON THE DIKES

From the offshore forcing, the nearshore loads at the flood defences are determined. As described, these loads consist of water levels and waves for the coastal region. Bulk wave parameters are used to characterise the wave loads, being the significant wave height H_s or H_{m0} [m] (the latter when using SWAN), the peak wave period T_p or spectral wave period $T_{m-1,0}$ [s] and the mean wave direction [$^{\circ}$ N].

The statistics of the sea water level at the dikes in the coastal region are determined based on triangular interpolation, using the sea water level statistics at the measurement stations.

To determine the wave conditions, a combination of the numerical flow model WAQUA ('Water beweging en water QUALity modellering') and the phase-averaged numerical wave model SWAN (Simulating WAVes Nearshore, Booij et al., 1999) were used. These models were run for many (1800 for SWAN, see Table 2.1) combinations of the offshore stochastic variables (wind and water level), to translate each of the combinations to nearshore wave loads close to the dikes. In other words, a relation was determined between the offshore stochastic variables and the local wave loads. Since the focus of a large part of this dissertation lies on the determination of the wave loads with SWAN in the Eems-Dollard estuary, the determination of the wave loads within WBI is treated in more detail here.

For the eastern Wadden Sea and Eems-Dollard estuary, the following steps were performed to determine the local wave conditions:

1. Determine the development in time of the wind direction and wind velocity, based on standard storm development profiles, coupled with a transformation of potential wind velocity to open water wind velocity.
2. Create the (spatially uniform) wind fields for all combinations of wind velocity and wind direction, based on the storm development profiles, to serve as input for the numerical models.
3. Determine the astronomical tide to be applied on the boundaries of the Wadden Sea WAQUA model, based on WAQUA simulations with the larger Continental Shelf Model (CSM) and southern North Sea model (ZUNO, 'Zuidelijke Noordzee').
4. Determine the water level and flow fields in the Wadden Sea using WAQUA, for every combination of wind surge, phase difference between tide and maximum wind velocity (see Table 2.1), and the wind fields of step 2.
5. Determine the offshore wave conditions to be applied on the boundaries of the Wadden Sea SWAN model, based on measured wave conditions at offshore measurement locations.
6. Perform a stationary SWAN simulation for every combination of step 4, using the water level and current fields from WAQUA and the offshore wave conditions as input. These SWAN simulations were performed at five times around the peak of the storm (-2, -1, 0, 1, 2 hour relative to the moment of maximum wind velocity, see Table 2.1).

7. Interpolate the SWAN results at the dikes for every simulation towards the offshore values of wind velocity, wind direction and water level, to incorporate them into the statistical model.

The result is a collection of wave loads at the dikes as a function of the offshore water level, potential wind velocity and wind direction.

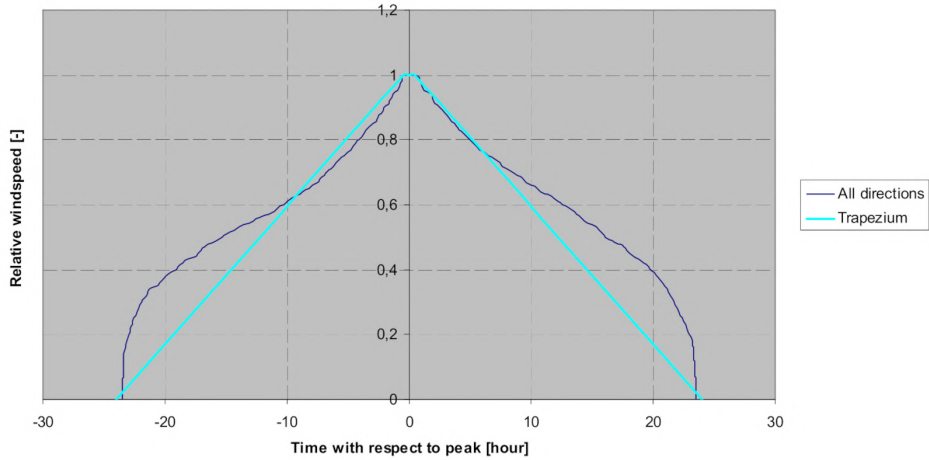
2

Wind velocity U_p [m/s]	Wind direction [°N]	Wind-induced set-up [m]	Phase difference tidal peak & storm peak [hour]	Time relative to storm peak [hour]
20	0	0	0	-2
25	90	2	4	-1
30	180	4	8	0
35	210			1
40	240			2
	270			
	300			
	330			
5	8	3	3	5
Total				1800

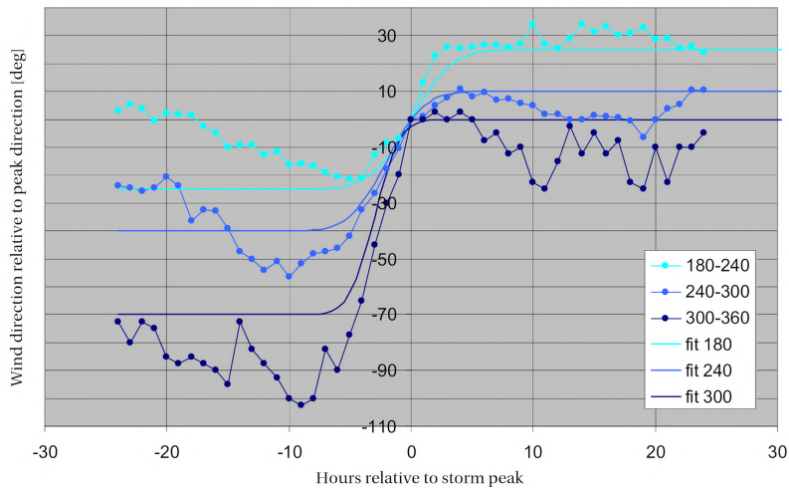
Table 2.1: Combinations of stochastic variables as used in WBI WAQUA and SWAN simulations, to determine the nearshore wave loads for the Wadden Sea. After [Gautier and Groeneweg \(2010\)](#).

2.3.1. STEPS 1 & 2: TRANSFORMATION TO WIND FIELDS WITH SPATIAL AND TEMPORAL DEVELOPMENT

For the wind, a transformation from a potential wind velocity at a measurement location, to an open water wind field in space and time is required. First, the potential wind velocity at the measurement station was transformed to an open water wind velocity. The [Charnock \(1955\)](#) relation was used for the wind drag. Next, the development of the wind in time was considered. [Lopez de la Cruz \(2010\)](#) derived an average storm development profile for the Wadden Sea, which is characterised by the turning of the wind direction in time. The standard time profiles of wind velocity and direction were determined based on measured storms at one of the measurement stations. A trapezoidal shape with a peak duration of 1 hour was deemed to describe the development of the relative wind velocity in time, see the upper panel of [Figure 2.1](#). For the development of the wind direction in time, the average change of the wind direction relative to the direction during the peak of the storm was determined. For western storms, three different sectors were determined, see the lower panel of [Figure 2.1](#). Wind fields were then determined based on these storm development profiles. The wind velocity and direction in these fields are non-stationary, but uniform.



(a) Wind velocity profiles.



(b) Wind direction profiles.

Figure 2.1: Top: Average (indicated by all directions) and schematised (indicated by trapezium) profile for the development of the wind velocity in time (Beckers, Gautier, & Groeneweg, 2009). Bottom: Average (lines with circles) and schematised (solid lines) profiles for the development of the wind direction in time for several directional sectors (after Gautier & Groeneweg, 2012).

2.3.2. STEPS 3 & 4: DETERMINING TIDE, WATER LEVEL AND FLOW FIELDS WITH WAQUA

To determine the tide, water levels and flow fields, simulations with WAQUA were performed. First, the continental shelf model was run, which generated the boundary conditions for the southern North Sea model. In turn, the southern North Sea model generated the tide and storm surge boundary conditions for the Wadden Sea model. The tide and surge were the only boundary conditions imposed on the continental shelf model

and southern North Sea models. No wind was applied. The wind velocities, wind directions, set-up and phase differences of Table 2.1 were then combined into 360 runs with the Wadden Sea model. The wind was imposed on the Wadden Sea model by using the non-stationary, uniform wind fields of steps 1 and 2. Finally, the resulting water level and flow fields were interpolated onto the SWAN Wadden Sea grids.

2.3.3. STEP 5: DETERMINING SWAN OFFSHORE WAVE BOUNDARY CONDITIONS

SWAN was used to determine the nearshore wave conditions at the dikes. More specifically, the WBI version of SWAN was used, version 40.72ABCDE, using the WBI settings (see Appendix D for an overview of these settings).

The SWAN simulations were run on four curvilinear grids, refer to Figure 2.2. The first grid covers part of the North Sea and generates the boundary conditions for the other grids. The second grid covers the whole Wadden Sea. The third grid covers the eastern part of the Wadden Sea and Eems-Dollard estuary. In this grid, the refraction limiter of [Van Vledder and Koop \(2009\)](#) was enabled, to improve the modelling of long wave penetration into the eastern Wadden Sea. This refraction limiter switches off the refraction for the lower frequencies. The third grid determines the wave conditions in the eastern Wadden Sea and Eems-Dollard estuary. The fourth grid was used because of an error in SWAN, where the wave boundary conditions of the second grid did not enter the model domain. Therefore, the fourth grid was used as a partial replacement of the second grid.

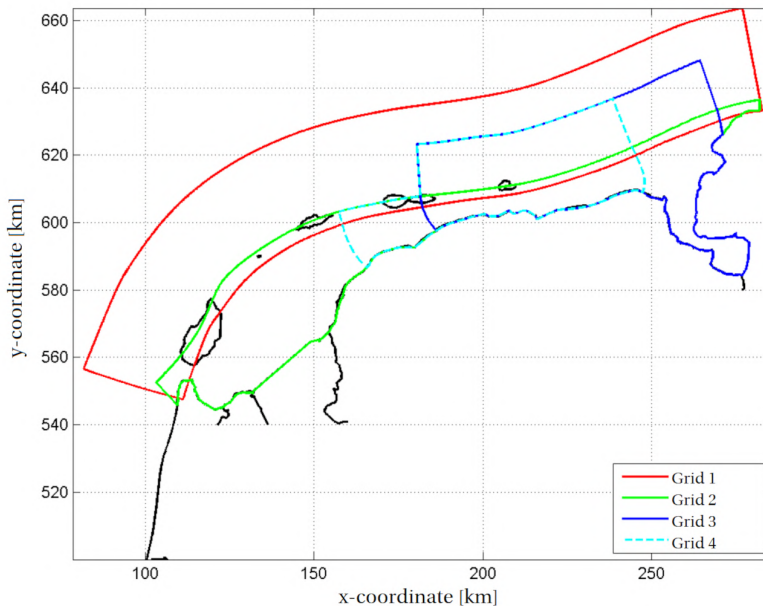


Figure 2.2: Overview of the WBI SWAN grids used to determine the wave conditions in the Wadden Sea (after [Klein & Kroon, 2011](#)).

1.5D spectra (energy density, mean wave direction, directional spreading as a function of frequency) were imposed on the boundaries of the first grid. To determine these 1.5D spectra, the following steps were performed:

- SWAN simulations for all combinations of wind velocity and direction on the southern North Sea grid, which determined the 1.5D spectra at two measurement stations in the North Sea and at the boundaries of the Wadden Sea grid.
- Determining the ratio between the wave parameters as determined by SWAN at the two measurement stations and wave parameters based on measurements at these stations, derived from an analysis of [Stijnen and Kallen \(2010\)](#).
- Correcting the spectra on the boundaries of the Wadden Sea grid, based on the previous step, and then applying the corrected 1.5D spectra on the boundaries of the first (Wadden Sea) grid.

2.3.4. STEP 6: PERFORMING SWAN SIMULATIONS FOR EACH OF THE 1800 COMBINATIONS

Next, a SWAN simulation was performed for every combination of the parameters of Table 2.1. The water level and flow fields from the 360 runs with WAQUA, the offshore wave conditions, and the wind fields were used as boundary conditions. These wind fields were based on the fields as determined in steps 1 and 2. The SWAN simulations were run in stationary mode, with a uniform wind velocity and direction. The temporal variation in wind velocity and direction was accounted for by running the simulations for the five different times around the peak of the storm (-2, -1, 0, 1, 2 hour relative to the peak of the wind velocity, see Table 2.1), resulting in 1800 combinations and runs in total. The processes that were taken into account in the SWAN simulations are:

- Wave growth by the wind;
- White-capping;
- Depth-induced wave breaking;
- Dissipation by opposing currents;
- Bottom friction;
- Triad wave-wave interactions;
- Quadruplet wave-wave interactions;
- Refraction.

Diffraction, reflection and wave set-up were not taken into account. For the exact model settings, see Appendix D. The WBI SWAN settings were determined by calibration and validation in earlier studies, see e.g. [Gautier \(2010\)](#).

2.3.5. STEP 7: INTERPOLATION OF SWAN RESULTS FOR INCORPORATION IN THE STATISTICAL MODEL

The 1800 SWAN simulations produce the wave conditions at the output locations close to the dikes. As described, the offshore stochastic variables for the coastal region in WBI

are the wind velocity, wind direction and water level. The wind velocity and direction as used for the SWAN simulations are non-stationary. Since the SWAN simulations were performed at several moments around the peak of the storm, the wind direction and velocity at the SWAN output locations can also change in time. Furthermore, the calculated wind velocities at the dikes are open water winds. The stochastic offshore wind direction and velocity, which were based on the peak of the storm, are constant in time and this wind velocity is a potential wind velocity. Hence, to be able to use the SWAN output in the statistical model of WBI, the results needed to be interpolated back towards the offshore values of (potential) wind velocity, wind direction and water level. The interpolation procedure reduces the results of the 1800 SWAN simulations to 280 combinations (eight wind directions, with for each direction five wind velocities and seven water levels). Thus, effectively the time relative to the peak of the storm, the storm surge and the phase relative to the tide are eliminated with this interpolation procedure. The full interpolation procedure was described by Nicolai, Klein, Kroon, Kallen, and Verkaik (2011). Finally, this interpolation procedure yields a collection of wave loads at the dikes as a function of the stochastic variables offshore water level, potential wind velocity and wind direction.

2.4. DETERMINATION OF LOADS ACTING ON THE DIKE AND PROBABILISTIC CALCULATIONS

In the next steps of the framework, the water level and wave loads at the dikes are converted to loads acting on the dikes for the different failure mechanisms (assessment tracks). An example of such a load is a wave overtopping discharge, relevant for the failure mechanism erosion of the grass revetment on the crest and inner slope. Depending on the failure mechanism, a semi-probabilistic or probabilistic calculation is performed. Since this dissertation focuses on wave run-up and overtopping, the focus of this section lies on the failure mechanisms erosion of the grass revetment on the outer slope and erosion of the grass revetment on the crest and inner slope. The probabilistic aspects are treated only briefly.

For the probabilistic calculations, model uncertainties in the wave loads at the dikes are used. Model uncertainties are prescribed for the wave heights and wave periods in the coastal region, no model uncertainties are used for the water levels in the coastal region.

The failure mechanism erosion of the grass revetment on the crest and inner slope is an example of a failure mechanism for which a fully probabilistic calculation is performed. For this mechanism, failure has been defined as the moment where 20 cm of the top layer on the crest or inner slope has been eroded, such that the revetment does not protect the subsoil against erosion any longer. The probability distribution of the wave overtopping discharge is compared to the probability distribution of the critical wave overtopping discharge, which has been defined for different possible grass cover qualities (see e.g. Ministerie van Infrastructuur en Milieu, 2016d). The Van der Meer (2002) equations, later implemented in EurOtop (2007), are used to determine the wave overtopping discharge. This results in a probability of flooding for this specific failure mechanism. If the dike does not comply with the norm probability for this mechanism, a more detailed assessment can still be performed. For this assessment, the cumulative overload method can be used. For a description of the method, see e.g. Van der Meer (2011); Van der Meer

et al. (2010). Erosion of the dike (grass) cover is considered explicitly in the cumulative overload method. Therefore, information on overtopping flow velocities and strength of the dike grass cover are necessary for this method.

Once the defences in a trajectory have been assessed for all failure mechanisms, the resulting probabilities are combined into one probability of flooding of the trajectory. Default weighting factors have been prescribed in Jongejan (2013), depending on the type of defence (e.g. dike or dune), giving a relative weight to each failure mechanism in the calculation of the total probability of flooding of the trajectory (the 'failure probability budget'). This probability of flooding is then compared to the norm probability of flooding, after which the trajectory is accepted or rejected. If the trajectory is rejected, it is possible to define custom weighting factors better suited to that specific trajectory, resulting in a 'tighter fitting' assessment for that location.

2.5. RELATION OF THIS DISSERTATION TO THE FRAMEWORK

As described in chapter 1, the knowledge gained in this dissertation can potentially contribute to the Dutch dike safety assessment framework, as both knowledge gaps studied in this dissertation are of importance to the framework.

In the framework, SWAN is used to determine the wave conditions in the coastal region, of which the Eems-Dollard estuary is a part. Accurate and validated data about the extreme conditions that might act on the flood defences are available for most of the coastal region, but not for the estuary, since the area is highly complex and characterised by an offshore wind. Furthermore, almost no measurements were available for calibration. As mentioned, WBI 2017 used the older SWAN version 40.72ABCDE. On the grid that covers the Eems-Dollard estuary, the refraction limiter of Van Vledder and Koop (2009) was used, which was not based on any physics. The newest SWAN version includes different formulations for the physics, which contain the newest insights in the physics, as well as a more accurate and stable implementation of the refraction. Still, there are indications that the formulations implemented in SWAN for e.g. refraction, diffraction and triad wave-wave interactions do not always suffice. This might especially hold for a highly complex area as the Eems-Dollard estuary. Hence, assessing the performance of SWAN in predicting the wave conditions at the dike in such a highly complex area, consisting of deep tidal channels, shallow flats, and characterised by an offshore wind, can be of large importance to the Dutch flood defence safety assessment framework as well.

The wave overtopping equations of Van der Meer (2002), later implemented in EurOtop (2007) were used in WBI 2017. Since then, new and improved equations have become available, in the newest version of the overtopping manual (EurOtop, 2018). Within WBI 2017, the failure mechanism erosion of grass revetment on crest and inner slope was assessed by using the mean wave overtopping discharge q [l/s/m]. This is an integrated parameter, which does not provide much insight in the actual overtopping process. It was possible to use the cumulative overload method in WBI 2017 already, by performing a more detailed assessment. It is expected that this method will completely replace the assessment based on the mean overtopping discharge in the future. Since the erosion of the grass cover is considered explicitly in this method, more information is necessary on the (overtopping) velocities and flow depths, as well as on the strength of the grass cover. Preferably, measurements at full scale in the field should provide such information. Next

to that, the dike section of interest in the Eems-Dollard estuary is characterised by very oblique wave attack. Only limited research is available on the influence of oblique wave attack on wave run-up and overtopping, and this especially holds for very oblique wave attack. The uncertainty in this influence is partly responsible for the uncertainty in the required crest level of the dike in the estuary as well. Hence, increasing the knowledge on wave run-up and overtopping during very oblique wave attack, more specifically on the extra parameters necessary for the cumulative overload method, such as front velocities, can be of large importance to the Dutch flood defence safety assessment framework as well.

Hence, by closing the knowledge gaps considered in this dissertation, the uncertainties in the wave conditions and related wave run-up and overtopping at the dike in the estuary can potentially be reduced. By reducing these uncertainties, a more accurate safety assessment can be performed, leading to less uncertainty in the required crest levels of the dikes.

I

MODELLING WAVE PROPAGATION EFFECTS IN COASTAL WATERS

3

WAVE MODELLING IN A COMPLEX ESTUARY: STUDY IN PREPARATION OF FIELD MEASUREMENT CAMPAIGN EEMS-DOLLARD ESTUARY

The universe does not allow perfection.

Stephen Hawking

This chapter considers the Eems-Dollard estuary in the north of the Netherlands, which is part of the shallow shelf sea the Wadden Sea. This estuary is a highly complex area with tidal flats and deep channels, and is characterised by an offshore-directed wind during extreme conditions, posing a challenge to wave prediction models. As few measurements are available, a measurement campaign was set up to provide field data for verifying and improving these wave models. This chapter mainly focuses on wave propagation effects, in both the eastern Wadden Sea and the Eems-Dollard estuary. The chapter has three main goals. The first is to determine the locations that are most suited for wave measurements in the area, to be able to validate SWAN and gain more insight in the physics that play a role. For this first goal, an analysis of propagation effects is made. The second goal is to gain insight in the reasons why such large and onshore-directed wave heights are predicted by SWAN at the dike and to gain insight in the processes that play a role in the area. The third is to assess the reliability and applicability of SWAN in this highly complex area. To reach these last two goals, a comparison is made between the SWAN version as

This chapter was based on **Oosterlo, P.**, Van der Meer, J.W., Hofland, B., & Van Vledder, G.Ph. (2018). Wave modelling in a complex estuary: Study in preparation of field measurement campaign Eems-Dollard estuary. *Coastal Engineering Proceedings*, 1(36), 66. Baltimore, Maryland: American Society of Civil Engineers. This paper was updated and extended for this dissertation.

used for the Dutch dike safety assessment and the newest version, which is used for development and includes the state of the art formulations of the physics. Large differences occur between the two SWAN versions. These differences are studied in more detail, and the causes of these differences are identified.

3.1. INTRODUCTION

Wave conditions at flood protection structures are important in the design of these structures. These conditions are often determined by using numerical wave models as measured data are not always available. It is of large importance that these wave conditions are accurately predicted by the applied model. Applying such a model in a highly complex estuary, which is part of a shallow sea with tidal flats and wetlands, where the wind acts in an offshore direction, and in which no measurements are available, might mean reaching or even surpassing the model's limits of applicability.

This chapter focuses on the Eems-Dollard estuary in the north of the Netherlands, which is part of the Wadden Sea, a shallow shelf sea with several barrier islands, deep tidal channels, shallow tidal flats and wetlands, see Figure 3.1 and Figure 3.2. Multiple extensive studies, some including field measurements, were performed before in the Wadden Sea, to gain a more detailed understanding of this complex area. Some noteworthy ones are [Eslami Arab et al. \(2012\)](#); [Groeneweg et al. \(2009, 2015\)](#); [Groeneweg and Van Vledder \(2005\)](#); [Van der Westhuysen et al. \(2012\)](#); [Van Dongeren et al. \(2011\)](#). These studies mainly focused on the tidal channels and tidal deltas at the transition from the North Sea to the Wadden Sea. The Eems-Dollard estuary is an even more complex area, see Figure 3.2. The fact that almost no studies have been performed in the estuary and that almost no measurements are available inside the estuary, makes the situation even more complex. More specifically, this study focuses on the dike section between the Eemshaven, the main port in the area, and the town of Delfzijl, as indicated by the black line in Figure 3.2. This dike protects a large part of the province of Groningen from flooding. This study focuses on the extreme conditions, as used for the dike safety assessment. These conditions correspond to return periods of 10,000 to 100,000 years.

Since the area is rather complex, and no measurements were available around the Eemshaven, it is difficult to determine the wave boundary conditions at this dike section. Furthermore, the extreme storms in the area tend to start out in the southwest and then turn to the northwest. Hence, the wind is offshore-directed at the dike during extreme conditions, as indicated by the arrow in Figure 3.2. The offshore-directed wind indicates that wave heights are probably low. Instead, relatively high onshore waves are predicted for this location, probably due to the presence of the deep main tidal channel in the area (indicated by the number 1 in Figure 3.2), and a secondary channel that runs close to the dike (the Bocht van Watum, number 2 in Figure 3.2). The phase-averaged numerical wave model SWAN (Simulating WAVes Nearshore, [Booij et al., 1999](#)) is used for the dike safety assessment in the Netherlands. The version that is used (version 40.72ABCDE, the assessment version) predicts large, onshore-directed waves at the dike, of order $H_s = 2$ m. SWAN predicts that the waves turn around the corner of the Eemshaven and become onshore-directed. However, since there are no measurements available, this means that the wave boundary conditions during (extreme) storms that are currently predicted by SWAN are without direct validation nearshore. This uncertainty in the wave conditions leads to un-

certainties in the required dike crest levels and could potentially lead to millions of euros of unnecessary dike reinforcements.

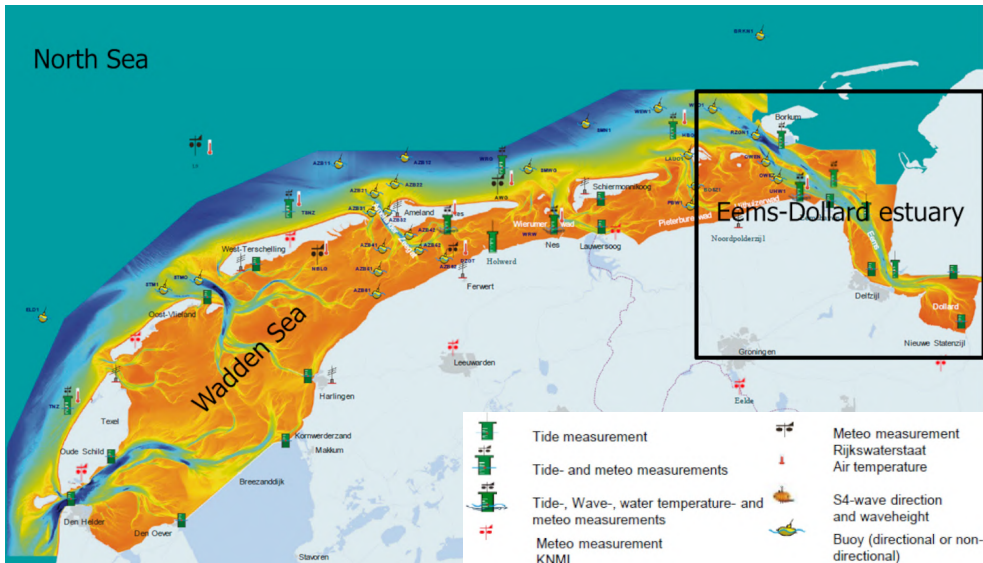


Figure 3.1: Bathymetry of the area of interest. The square indicates the Eems-Dollard estuary. Parts of the North Sea, the Wadden Sea and the north of the Netherlands are shown as well. Blue is deeper, orange is shallower (after Zijderveld & Peters, 2009).

To the authors' knowledge, the performance of SWAN in predicting the wave conditions at the dike in such a complex area, consisting of deep tidal channels, shallow flats, and characterised by an offshore wind, has not been assessed before. Hence, the question is, whether using the model in this highly complex area means reaching the limitations of the underlying modelling concepts of SWAN. Further questions are whether the predictions by SWAN in this area are accurate or not, what the cause is of the apparent turning of the waves around the corner of the Eemshaven, and whether the waves remain as large as the model predicts in reality.

Therefore, this chapter has three main objectives. The first is to determine the locations that are most suited for wave measurements in the area, to be able to validate SWAN and gain more insight in the physics that play a role. For this first objective, an analysis of propagation effects is performed. The second objective is to gain insight in the reasons why such large and onshore-directed wave heights are predicted by SWAN at the dike and to gain insight in the processes that play a role in the area around the corner of the Eemshaven. The third is to assess the reliability and applicability of SWAN in this highly complex area. To reach these last two objectives, a comparison is made between the SWAN version as used for the Dutch dike safety assessment (40.72ABCDE), and the newest version¹, which is used for development (41.10AB) and includes the state of the art formulations of the physics. Simulations are performed for a schematised version of the area

¹Version 41.10AB was the newest version when this chapter was written.

around the corner of the Eemshaven.

This study is part of the preparation of a 12-year long field measurement campaign in the area, which aims to improve the reliability of the wave boundary conditions by improving the models, using a combination of numerical modelling and field measurements. Wind, water levels, currents, waves, wave run-up and wave overtopping will all be measured, by using a large range of instruments, such as wave buoys, X-band radars, ADCPs, wave overtopping tanks and LIDAR.

3

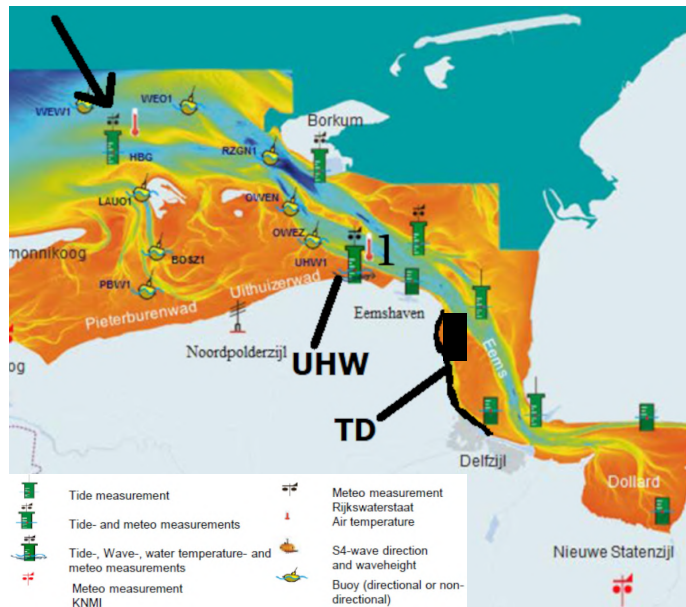


Figure 3.2: Eems-Dollard estuary, with the deep main tidal channel (number 1), the secondary channel the Bocht van Watum (number 2), the dike section of interest (black line), the two locations of interest for setting up the first measurements, Uithuizerwad (UHW) and the Twin Dikes (TD), and the wind direction during extreme conditions (arrow). Blue is deeper, orange is shallower.

3.2. LOCATIONS OF INTEREST

For setting up the first field measurements, the focus is on two locations, Uithuizerwad (UHW) and the Twin Dikes (TD, named after a dike reinforcement project in the area), see Figure 3.2. Uithuizerwad is located to the west of the Eemshaven, where measurements of wind, water levels and waves are available at an existing measurement pole. The Twin Dikes location is part of the dike section of interest, and is located to the south of the Eemshaven. Here, no measurements were available yet. Both locations are under oblique to very oblique wave attack, but at Uithuizerwad this wave attack is direct and coming from the Wadden Sea, whereas it is indirect at the Twin Dikes. Furthermore, the wave conditions at Uithuizerwad are shallow water conditions, due to a kilometre-long shallow area in front of the dike, located above mean sea level. The Twin Dikes location lies sheltered from direct wave attack by the corner at the Eemshaven. The wave conditions there will

not be depth-limited, due to a lower bottom level and higher water levels. The deeper (up to -10 m+NAP, Normaal Amsterdams Peil, Dutch ordnance level roughly corresponding to mean sea level) secondary channel Bocht van Watum runs quite close to the Twin Dikes, and there is a shallower area located around mean sea level directly in front of the dike of several hundreds metres wide.

3.3. APPROACH

3.3.1. QUANTIFICATION OF PROPAGATION EFFECTS

A quantification of propagation effects was made with SWAN. The analysis was performed to determine the locations where waves should be measured, to gain more insight in the physics that play a role in the area, as well as to be able to validate SWAN in more detail in a next step of this study.

The 40.72ABCDE version of SWAN was used for these stationary simulations with constant and uniform wind fields, corresponding to storms occurring on average once every 1, 10 and 100,000 years, the latter corresponding to the design conditions. Table 3.1 gives these conditions. The model settings as used for the WBI (the Wettelijk BeoordelingsInstrumentarium, the Dutch dike safety assessment) were applied, see Table 3.2. These settings were determined and validated in previous studies, e.g. [Gautier \(2010\)](#). The simulations use five telescoping nested curvilinear grids, with the one-way coupling from coarse to higher resolution grids by 2D spectra. Figure 3.3 shows the grids. No wave boundary conditions were applied on the outermost grid as local wave generation is sufficient for the present purposes. This set-up was based on the set-up as used in [Adema, Geleynse, and Telenta \(2014, 2015\)](#). The DCSMv6 model (Delft Continental Shelf Model version 6, [Wenneker & Gautier, 2016](#)) was split into three parts, an outer part (grid 1, blue in left panel of Figure 3.3), an inner part around the United Kingdom and Denmark (grid 2, red), and another refined part around the Dutch coast (grid 3, yellow). Furthermore, a refined version of the Kuststrook model ([Wenneker & Gautier, 2016](#)) was used (grid 4, magenta in right panel of Figure 3.3), and a sixteen times more detailed part of that model in the Eems-Dollard (grid 5, green). This results in minimum grid cell sizes of approximately 10 m by 20 m. The bathymetry was based on the bathymetry of the DCSM and Kuststrook models, as well as on six-yearly bathymetrical survey data, see the left panel of Figure 3.4.

Average return period [year]	1	10	100,000
Wind velocity [m/s]	20	25	35
Wind direction [°N]	300	330	330
Water level [m+NAP]	4	4	6

Table 3.1: Storm conditions as used for quantification of propagation effects.

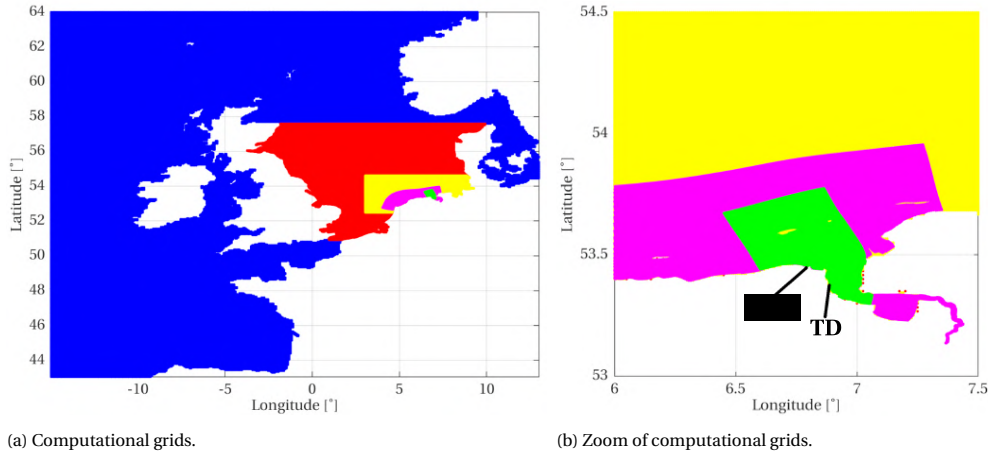


Figure 3.3: Left: The five computational grids as used for the SWAN simulations. Right: Zoom of the most detailed grids. Uithuizerwad (UHW) and the Twin Dikes (TD) indicated in the right panel.

3.3.2. COMPARISON SWAN ASSESSMENT (40.72ABCDE) AND DEVELOPMENT (41.10AB) VERSIONS

To determine why such large and onshore-directed wave heights are predicted by SWAN at the dike, and to gain more insight in the governing physics, a comparison was made between the SWAN safety assessment version 40.72ABCDE using the WBI settings (A cases), and the development version 41.10AB using the default settings (B cases). Furthermore, simulations were performed where the safety assessment version was used for grids 1 to 4, and the development version for grid 5 (C cases). In this way, it is ensured that potential differences in results are purely locally generated. This comparison uses the same model grids and storm conditions as used for the quantification of propagation effects, see Table 3.1. Hence, each case (A, B or C) consists of three different simulations, one for each of the three storm conditions. Table 3.2 gives the WBI settings of SWAN version 40.72ABCDE and the default settings of version 41.10AB.

SWAN version & model settings	SWAN Dutch safety assessment WBI (40.72ABCDE)	SWAN development default (41.10AB)
Directional resolution	36 10° bins	36 10° bins
Frequency resolution	44 bins, 0.015 Hz - 1 Hz	36 bins, 0.03 Hz - 1 Hz
Third-generation mode	Van der Westhuysen et al. (2012) GEN3 WESTH	Komen, Hasselmann, and Hasselmann (1984) GEN3 KOM
Linear wind growth	Cavaleri and Rizzoli (1981) (disabled)	Cavaleri and Rizzoli (1981) (disabled)
Exponential wind growth	Yan (1987)	Komen et al. (1984)
Wind drag formulation	Wu (1982)	Zijlema, Van Vledder, and Holthuijsen (2012)
White-capping	Van der Westhuysen, Zijlema, and Battjes (2007) WCAP WESTH [cds2]=5e-5 [br]=0.00175 [p0]=4 [powst]=0 [powk]=0 [nldisp]=0 [cds3]=0.8 [powfsh]=1	Komen et al. (1984); Pallares, Sánchez-Arcilla, and Espino (2014); Rogers, Hwang, and Wang (2003) WCAP KOM [delta]=1
Quadruplet wave-wave interactions	Explicit DIA per sweep (S. Hasselmann & Hasselmann, 1985; S. Hasselmann, Hasselmann, Allender, & Barnett, 1985) QUAD [iquad]=2	Explicit DIA per sweep (S. Hasselmann & Hasselmann, 1985; S. Hasselmann et al., 1985) QUAD [iquad]=2
Bottom friction	JONSWAP (K. Hasselmann et al., 1973) FRIC JON CON [cfjon]=0.038	JONSWAP (K. Hasselmann et al., 1973) FRIC JON CON [cfjon]=0.038
Depth-induced breaking	Van der Westhuysen (2010) BREA WESTH [alpha]=0.96 [pown]=2.5 [bref]=-1.3963 [shfac]=500	Battjes and Janssen (1978) BREAK CON
Triad wave-wave interactions	OCA LTA (Eldeberky, 1996) TRIAD [itriad]=1 [trfac]=0.1 (in 40.72ABCDE) TRIAD [itriad]=11 [trfac]=0.1 (in 41.10AB)	CCA LTA (Eldeberky, 1996; Salmon et al., 2016) TRIAD [itriad]=1 [trfac]=0.8

Refraction	c_θ based on depth-gradients and using first-order backward differences NUM DIR DEP; Limiter on excessive directional turning based on Tolman (2009) (disabled); Limiter, disabling refraction for low frequencies (Van Vledder & Koop, 2009) (enabled) REFRL 0.2 2	c_θ based on gradient in wave number and using second order central differences (The SWAN team, 2017a) NUM DIR WNUM; Limiter on excessive directional turning based on Dietrich et al. (2013) (disabled)
Quadruplet and action limiter	LIM	LIM
Numerical propagation scheme	SORDUP	SORDUP
Stop criterion	NUM STOPC [dabs]=0.00 [drel]=0.01 [curvat]=0.001 [npnts]=99. STAT [mxitst]=80 [alfa]=0.001	NUM STOPC [dabs]=0.005 [drel]=0.01 [curvat]=0.005 [npnts]=99.5 STAT [mxitst]=50 [alfa]=0.00

Table 3.2: SWAN model settings as used for the Dutch dike safety assessment WBI (version 40.72ABCDE) and default settings of the SWAN development version 41.10AB. Refer to The SWAN team (2017b) for further explanations of the different parameters.

3.3.3. MODELLING OF AREA AROUND THE CORNER OF THE EEMSHAVEN

To analyse the mechanisms and physics that play a role at the corner of the Eemshaven and in turning the waves around the corner in more detail, a schematised model of the area was made. The model measures 1.2 km by 2 km and uses a rectilinear grid with 20 m x 20 m grid cells. Three versions of the model were used, where the first one completely consists of a deep area at -12.5 m+NAP, representing the main tidal channel in the area. The second and third consist of the deep channel in the north and a shallow area at 0 m+NAP in the south, representing the area in front of the dike. A transitional slope of either 1:10 (second model) or 1:30 (third model) was included, roughly corresponding to channel slopes as found in the area. The right panel of Figure 3.4 shows the bathymetry of the second model. The western boundary is partially closed off ($y = 0$ m to $y = 1500$ m), representing the dike. On the western and northern boundaries a JONSWAP spectrum was imposed, with conditions corresponding to the design conditions as given in Table 3.3. These conditions correspond to kd values ranging from 0.9 - 2.1 in the models. Note that the channel-part of the model was rotated by approximately 45° in the counter-clockwise direction compared to reality. Therefore, the boundary conditions were rotated by 45° as well. This analysis mainly focuses on gaining insight in the physics that play a role, e.g. by considering the 2D spectra and source terms.

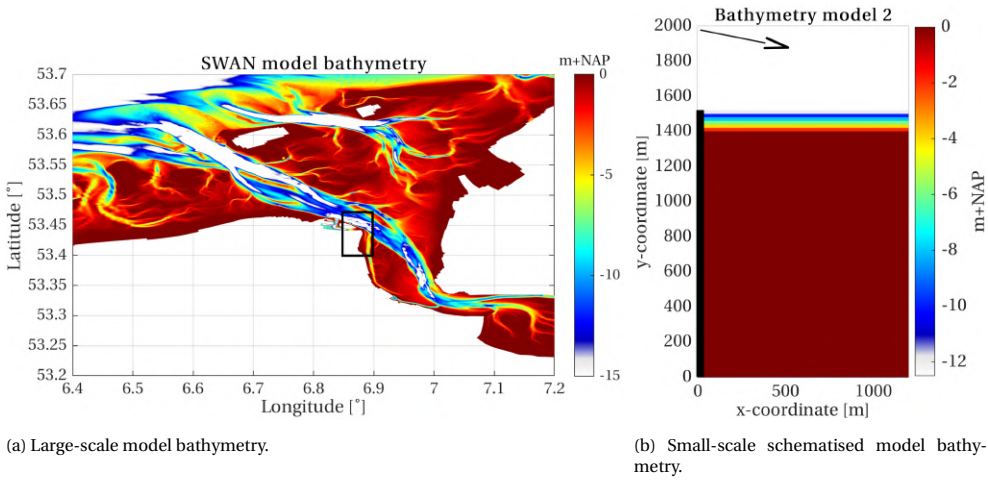


Figure 3.4: Left: SWAN model bathymetry as used for the quantification of propagation effects and the comparison of the two SWAN versions, with the area around the Eemshaven indicated by the rectangle. Right: Bathymetry of the schematised model of the area around the Eemshaven, including the shallow area in front of the dike and a 1:10 slope. The western boundary ($y = 0$ m until $y = 1500$ m) is closed off, representing the dike (thick black line). Mean wave direction indicated with the arrow.

Average return period P [year]	100,000
Wind velocity W_{vel} [m/s]	35
Wind direction (reality) [$^{\circ}$ N]	330
Wind direction (model) W_{dir} [$^{\circ}$ N]	285
Water level h [m+NAP]	6
Significant wave height H_s [m]	3.4
Wave peak period T_p [s]	6
Mean wave direction (reality) [$^{\circ}$ N]	324
Mean wave direction (model) δ [$^{\circ}$ N]	279
Wave directional spreading σ_{δ} [$^{\circ}$]	30

Table 3.3: Design conditions as used in the SWAN simulations with the schematised model of the area around the Eemshaven.

3.4. RESULTS

3.4.1. QUANTIFICATION OF PROPAGATION EFFECTS

The wave parameters at Uithuizerwad and the Twin Dikes resulting from the present simulations with the assessment version agree well with the Dutch dike safety assessment WBI results, with less than 2% difference in the spectral wave period H_{m0} [m] at Uithuizerwad and a maximum of 8% difference in H_{m0} at the Twin Dikes. Hence, the results are largely representative of the WBI situation. Large and onshore-directed waves are found at the Twin Dikes during design conditions. The largest differences between the present simulations and the safety assessment results occur for the spectral wave period $T_{m-1,0}$ [s], with

a maximum difference of 9% at Uithuizerwad and a maximum of 14% at the Twin Dikes. These differences are mainly caused by the different boundary conditions as used in WBI, as well as the exclusion of the effect of flow fields in the present simulations.

The upper left panel of Figure 3.5 shows the mean wave direction vectors for the 1-year condition. The waves become approximately alongshore-directed at the Twin Dikes for this case. The results for the 10-year return period and the design conditions (100,000 years) are very similar. For these last two cases, the waves become obliquely onshore-incident. With the 1-year storm, the mean wave direction turns less towards the dike, because of the more westerly wind direction. However, the trends are similar for all three conditions, where the strongest turning of the mean wave direction occurs around the corner at the Eemshaven, at the transitions from deep channels to shallow areas and at the shallow flats directly in front of the dike.

From the absolute spatial gradient in the mean wave direction (in rad/m), the locations of strongest wave turning can be confirmed. The right panels of Figure 3.5 give these gradients. The behaviour is quite similar for all three storm conditions again. The strongest directional turning occurs around the corner of the Eemshaven and at the transition from the secondary channel to the shallower area in front of the dike. Some directional turning occurs more in the north as well, caused by a shallower area next to the main tidal channel. Furthermore, there is an area more towards the east where turning occurs, which is caused by a deep inlet onto the large shallow flat. The same trends are found when the propagation terms (radiation stresses, SWAN energy propagation terms) are considered (not shown in the figures).

From these results, advice can be given on where to measure waves in the area, to gain more insight in the physics affecting the waves, as well as to validate SWAN in more detail. Since the strongest turning occurs around the corner of the Eemshaven and at the transition from the Bocht van Watum to the shallow areas in front of the dike, it is recommended to measure at these two locations. Figure 3.6 gives these locations. The measurements should preferably be performed with X-band radar, as well as with (arrays of) directional wave buoys, since they provide directional information of the waves.

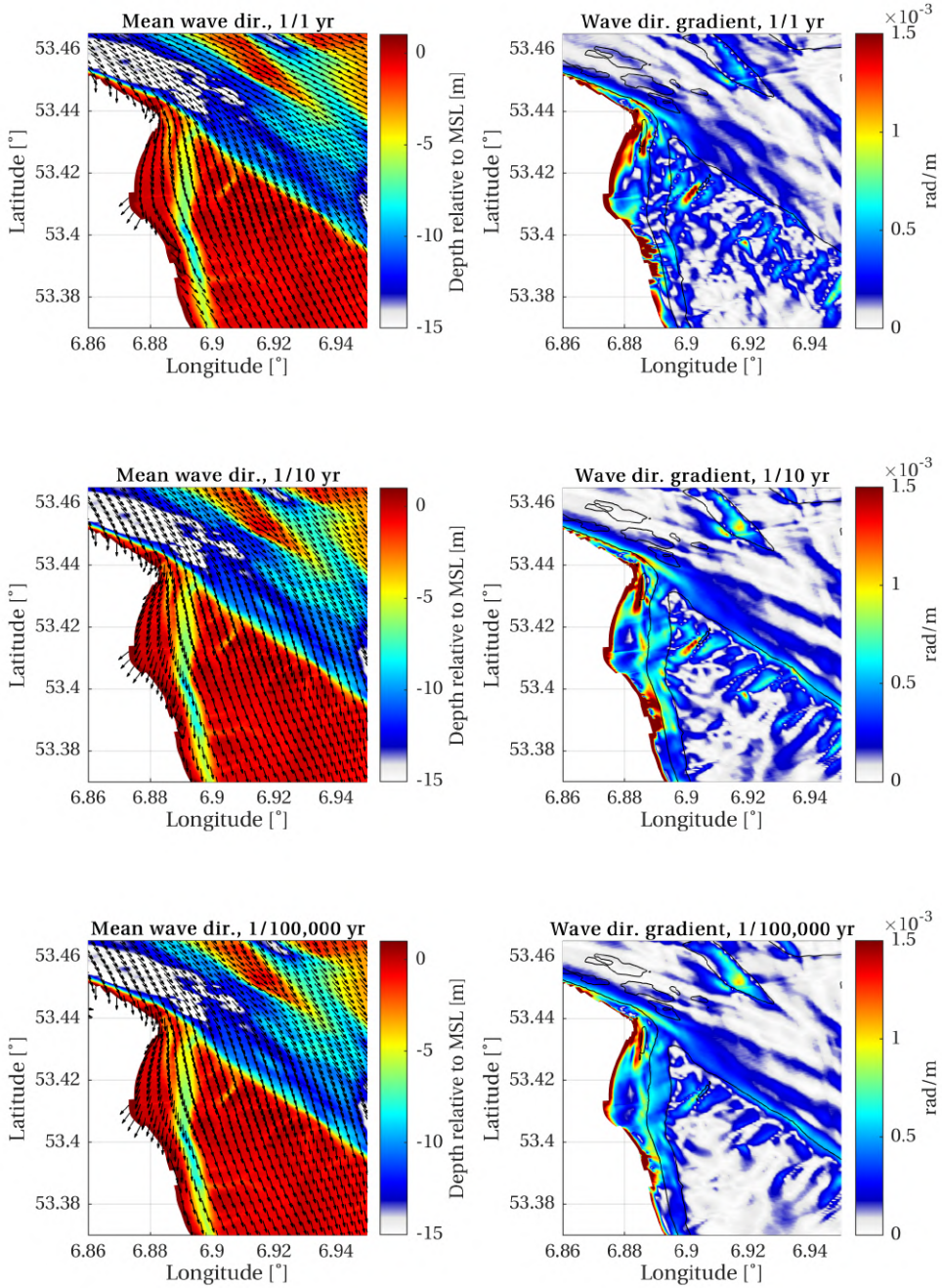


Figure 3.5: Results for return periods of 1 year, 10 years and 100,000 years. Left: SWAN model bathymetry and mean wave direction vectors. Right: Absolute gradient in mean wave direction. Bottom contours drawn at -3 m, -15 m and -25 m.

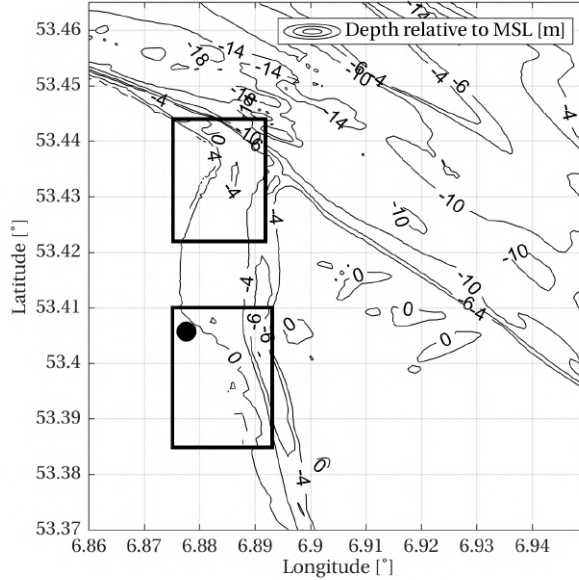


Figure 3.6: Model bathymetry (contours), Twin Dikes location (black dot) and recommended measurement locations (rectangles).

3.4.2. COMPARISON SWAN ASSESSMENT (40.72ABCDE) AND DEVELOPMENT (41.10AB) VERSIONS

Figure 3.7 shows that the bulk wave parameters of both model versions (A and B cases) are largely different. An up to 30% lower H_s is found at Uithuizerwad and the Twin Dikes, as well as an up to 20% lower $T_{m-1,0}$ wave period, when using the development version.

However, these differences could already occur more offshore, and affect the waves already in the North Sea or Wadden Sea, and not necessarily in the estuary itself or close to the dike. The C cases that use the safety assessment version for grids 1 to 4, and the development version for grid 5 (refer to Figure 3.3), provide insight into this. In this way, it is ensured that the local differences in and around the estuary are considered only.

The wave conditions of the C cases are equal to or almost equal to the B cases in large parts of the estuary, see Figure 3.7. The main differences occur in the mean wave direction δ at locations 3 to 5, where the δ of the B and C cases differ by several degrees. The exact causes of these differences are unknown. Otherwise, the bulk wave parameters of the B and C cases are almost identical. However, large differences occur between these cases and the A cases, which use the assessment version on all five grids. The main difference is that more low-frequency energy is able to penetrate into the estuary with the assessment version. Low-frequency energy is defined here as offshore-generated North Sea wind waves with frequencies lower than 0.1 Hz.

The 2D spectral boundary conditions for the boundaries of grid 5, resulting from grid 4, are largely similar for both the development and assessment versions of SWAN for the 1-year and 10-year storms. However, for the design conditions, the boundary conditions are more extreme with the safety assessment version. The northern boundary of grid 5 is

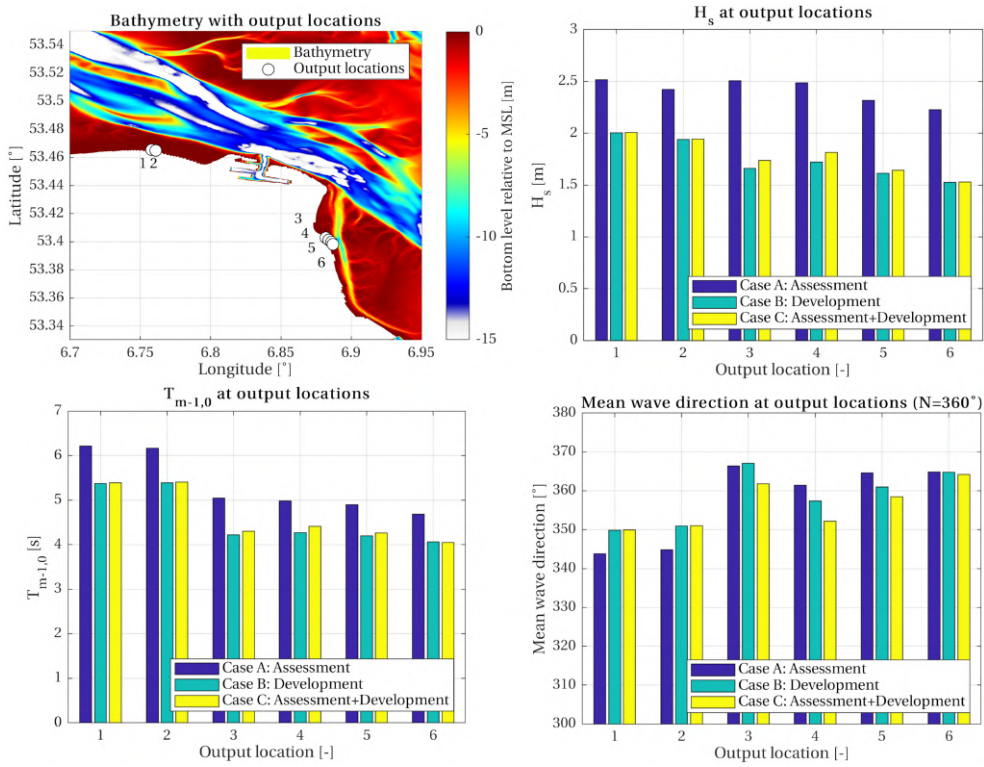


Figure 3.7: In clockwise direction: SWAN bathymetry with output locations around UHW and TD. Significant wave height H_s at the output locations for the three different cases, during design conditions. Mean wave direction (δ , nautical, coming from) at the output locations. Here, north is 360°, northwest<360°, northeast>360°. Spectral wave period $T_{m-1,0}$ at the output locations.

located at deep water in the North Sea. Hence, for the C case with design conditions, the more extreme boundary conditions as found with the assessment version are applied to the boundaries of grid 5, for which the development version is used.

These differences at the boundaries between the B and C cases disappear quickly as the waves propagate into the domain, where both cases already show roughly the same wave heights before the waves reach the Wadden Sea. After this boundary area, cases B and C give largely the same wave conditions. This shows that despite the different boundary conditions, the wave conditions inside the Wadden Sea and Eems-Dollard estuary become largely equal when using the development version on grid 5. Hence, the wave conditions in the Wadden Sea and Eems-Dollard estuary are largely dependent on the model settings as applied on grid 5. The largely different wave conditions for the A case confirms this, even though this case uses the same boundary conditions on grid 5 as the C case.

The 2D wave spectra during design conditions are considered at four locations for the A, B and C cases. Figure 3.8 shows the locations, Figure 3.9 gives the spectra as polar contours using the Nautical convention (coming from) with contour lines at the levels 0.99, 0.9, $1/2$, $1/4$, $1/8$, $1/16$, $1/32$, $1/64$ and $1/128$ times the local maximum variance density. In the North

Sea, at location 1 in Figure 3.8 and Figure 3.9, the differences in wave heights and the spectra are mainly caused by the differences in boundary conditions. Furthermore, differences in wind growth, white-capping and depth-induced breaking occur. The first two are somewhat more pronounced with the assessment version, the last one is somewhat stronger with the development version.

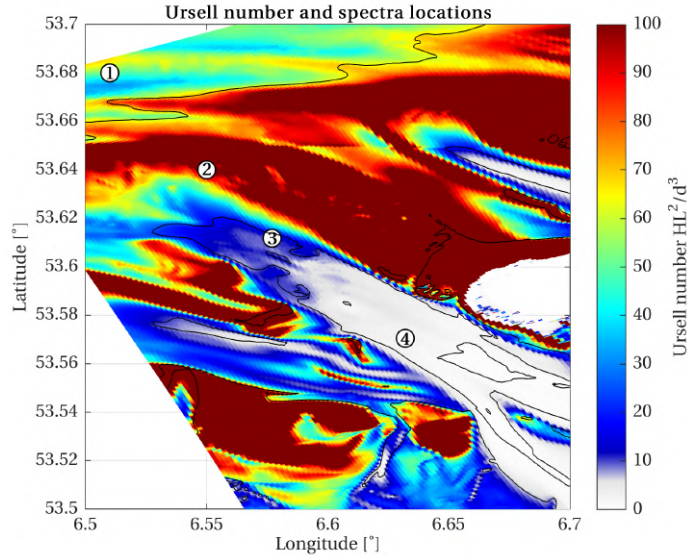


Figure 3.8: Ursell number $U = H_{m0}L_p^2/d^3$ during design conditions and 2D spectra output locations. Location 1 is located in the North Sea, location 2 on the tidal delta, location 3 just behind the tidal delta in the main tidal channel and location 4 is located further inside the main tidal channel. -3 m, -15 m and -25 m depth contours shown as well.

The first differences between the two SWAN versions become visible at the transition from the deeper North Sea to the shallower Wadden Sea, at location 2 in Figure 3.8 and Figure 3.9, where dissipation occurs. The reduction in wave energy is stronger and occurs more rapidly for the development version than for the assessment version. This is caused by the differences in the formulations of the physics, mainly the depth-induced breaking. On the tidal delta, the difference between the two models in significant wave height is already around 1 m. The spectral shape becomes different as well, with more (south)westerly energy and somewhat less north-easterly low-frequency energy for cases B and C.

At the transition from the North Sea to the Wadden Sea over the tidal delta (locations 2 and 3 in Figure 3.8 and Figure 3.9), largely the same behaviour is observed as described by Van Nieuwkoop and Groeneweg (2014). Most of the wave energy travels over the ebb-tidal delta, where the waves refract towards the shallow flats and where energy is dissipated, after which part of the wave energy enters the channel and refracts back. In the main tidal channel, part of the low-frequency energy comes from the (south)west, which means that energy travels around the western side of the tidal delta, bends around the delta due to refraction, and then enters the channel. This westerly wave energy was not observed in

the measurements analysed by [Van Nieuwkoop and Groeneweg \(2014\)](#), but was present in their SWAN results. The measurements had only one spectral peak, with an even distribution of energy on both sides. [Van Nieuwkoop and Groeneweg \(2014\)](#) attribute this to the (2D) non-linear triad wave-wave interactions. These non-linear interactions are described by e.g. [Groeneweg et al. \(2015\)](#). They directionally broaden the spectrum and are not included in SWAN. [Dusseljee et al. \(2014\)](#) observed similar effects. These non-linear interactions likely play a role, as the Ursell number $U = H_{m0}L_p^2/d^3$ is large around the tidal delta and shallow flats, indicating that non-linear effects cannot be neglected, see [Figure 3.8](#).

Inside the main tidal channel, at locations 3 and 4 in [Figure 3.8](#) and [Figure 3.9](#), H_s is 1 m to 1.5 m lower with the development version. More westerly energy is present, because the waves travel around the tidal delta in SWAN. Less of the North Sea low-frequency energy is left with the development version (B and C cases), caused by the differences in the refraction formulations.

The assessment version determines the directional turning rate c_θ based on the depth-gradients and using first-order backward differences. This method of calculating the turning rate can be rather inaccurate for steep bottom slopes on coarse grids. Furthermore, a limiter on excessive directional turning can be applied, based on [Tolman \(2009\)](#). This limiter is disabled by default. Finally, the WBI settings use the limiter of [Van Vledder and Koop \(2009\)](#) that disables the refraction for frequencies < 0.2 Hz. This limiter was included, since too little low-frequency energy could penetrate the channels under certain conditions, compared to measurements ([Van Vledder & Koop, 2009](#)). However, this limiter is not based on any known physics.

The development version determines c_θ based on gradients in the wave number and uses second order central differences ([The SWAN team, 2017a](#)), which is more robust. Furthermore, the development version includes a limiter on excessive directional turning based on [Dietrich et al. \(2013\)](#), which is disabled by default as well. The limiter of [Van Vledder and Koop \(2009\)](#) is not used in the default settings of the development version.

The influence of the refraction limiter of [Van Vledder and Koop \(2009\)](#) is visible in the 2D spectra in the tidal channel, where more low-frequency energy is present than with the development version. If this frequency-dependent refraction limiter is applied in the development version, this same larger penetrative behaviour of the low-frequency energy is found, but does not fully explain the differences between the two models.

Furthermore, the spectrum in the channel is somewhat more symmetrical for cases B and C, with a more even distribution of wave energy on both sides of the peak direction. This high-frequency shape of the spectrum agrees better with the measurements as described in [Van Nieuwkoop and Groeneweg \(2014\)](#), but the larger amount of low-frequency energy in case A (with the refraction limiter that was not based on any known physics) agrees better with the low-frequency part of the spectrum in the measurements.

The apparent underestimation of low-frequency energy in SWAN was studied by [Eslami Arab et al. \(2012\)](#) as well, who tested several hypotheses. Wave-driven currents due to wave breaking on a slope, non-linear effects due to waves steepening on a slope, and too steep bathymetry gradients to model accurately with SWAN all could not explain the differences between SWAN and measurements. [Eslami Arab et al. \(2012\)](#) recommended to study the wave reflection on steep slopes further, as this could be a possible explanation.

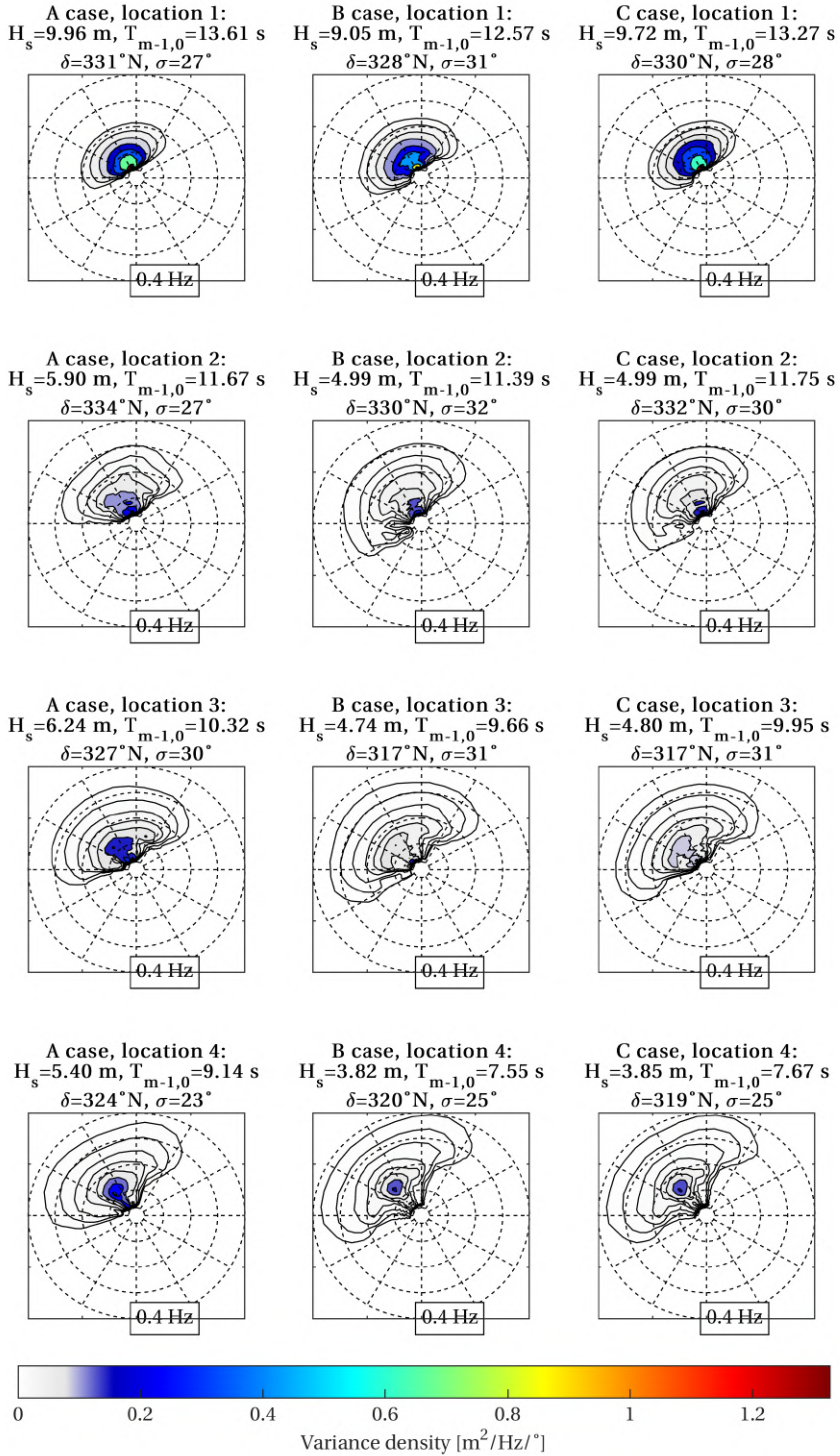


Figure 3.9: 2D variance density spectra at locations of Figure 3.8 during design conditions, as found by SWAN 40.72ABCDE with WBI settings (A cases), SWAN 41.10AB with default settings (B cases), and combination of 40.72ABCDE and 41.10AB (C cases). Contour lines plotted at 0.99, 0.9, $1/2$, $1/4$, $1/8$, $1/16$, $1/32$, $1/64$ and $1/128$ times the local maximum variance density. Spectra plotted using Nautical convention (coming from).

Concluding, the differences in the wave conditions between the two SWAN versions are caused partly offshore already, at the transition from the North Sea to the Wadden Sea. Caution is necessary when applying SWAN in such a complex area, and caution is required when specifying the model settings. The largely different results between the two model versions show that improvements in the understanding of the physics and the implementations of the physics in the model are still necessary. Therefore, the measurement campaign in the area is highly necessary, as well as more detailed modelling of the area (e.g. with SWASH), and validation and application of the most recent developments in SWAN in this area (such as the ST6 physics of Rogers, Babanin, and Wang (2012) and 2D non-linear interactions as described by Groeneweg et al. (2015)). The differences between the SWAN versions are caused partially locally as well, when the waves enter into the Eems-Dollard estuary around the corner at the Eemshaven, and when they travel onto the shallow flats in front of the dike. These effects are studied in the next section.

3.4.3. MODELLING OF AREA AROUND THE CORNER OF THE EEMSHAVEN

To determine the local differences between the SWAN versions and to gain more insight into the mechanisms and physics that play a role in the apparent turning of the waves around the corner of the Eemshaven, the schematised model of this area is used (see the right panel of Figure 3.4).

Differences in bulk wave parameters between the cases without a slope, with a 1:30 slope or a 1:10 slope are generally small. Wave heights in the area close to the dike are approximately 0.8 m to 1 m during design conditions for the model without a slope, using the safety assessment version. The wind is offshore-directed during design conditions. $T_{m-1,0}$ wave periods are between 2.7 s and 4 s. The mean wave direction at the dike is approximately 335°N. This is much smaller than what was found with the large-scale simulations as discussed in the previous sub-section (H_s around 2 m, $T_{m-1,0} = 5$ s - 6 s).

Figure 3.10 gives the wave heights for the case with a 1:10 slope, as well as the spectral output locations. Figure 3.11 presents the 2D spectra of both the assessment and development versions of SWAN. Several effects can be observed from these spectra and the associated source terms. The main process is wave sheltering. The further into the shadow zone behind the dike, the less energy at the original peak frequency is left. Only the energy at the most northern directions can reach this area, the rest is all filtered out by wave sheltering. This directionally narrows the spectra, see Figure 3.11. The wave sheltering and some numerical diffusion cause wave height gradients to appear, which resemble diffraction patterns, even when diffraction is not included in the SWAN model. These processes turn the mean wave direction more towards the north, and cause part of the wave energy to become onshore-directed, even with an offshore wind direction and without diffraction in the model.

The source terms with the largest influence are the wind growth, white-capping and quadruplet wave-wave interactions. These three source terms balance one another and work in cooperation; if the wind is turned off, the influence of the white-capping and quadruplets becomes much smaller as well. The wind adds energy to the whole spectrum and generates high-frequency energy at a broad range of directions around the wind direction (279°N), directionally broadening the spectra. White-capping occurs mainly offshore and at the slope (when a slope is present in the model), where the waves

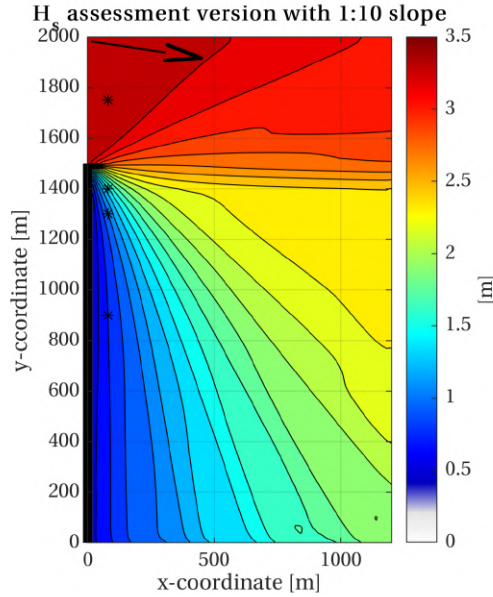


Figure 3.10: Significant wave height H_s during design conditions for the case with a 1:10 slope, using the safety assessment version. Gradients in the wave height occur, resembling diffraction patterns, without inclusion of diffraction in the model. Spectral output locations (asterisks) and mean wave direction (arrow) shown as well.

are steeper. The quadruplet wave-wave interactions redistribute energy, adding energy at frequencies higher than two times the peak frequency f_p . The typical removal of energy above the peak frequency and addition of energy at frequencies lower than the peak frequency does not occur clearly here. These three source terms do not balance each other completely for the present cases. The wind growth has a larger influence than the other two source terms, due to which the high-frequency tail of the spectrum becomes relatively larger in the shadow zone. This imbalance is probably caused by the very large wind velocity. The bottom friction, triad wave-wave interactions and depth-induced breaking do not play a role for the case without a slope, and play a minor role for the cases with a slope.

The role of the refraction is difficult to discern, due to the large influence of the wave sheltering and directional spreading. Directional turning of up to 15° seems to occur on the slope, allowing the somewhat more westerly wave energy at the peak frequency to reach the shadow zone as well, compared to the case without a slope. Differences between the cases with a 1:10 and 1:30 slope in wave direction are negligible, except on the slope itself due to the different slope angles. The combined positive effect of more energy reaching the shadow zone due to refraction and negative effect of the increased white-capping, depth-induced breaking and bottom friction result in wave heights in the shadow zone that are several centimetres larger for the cases with a slope than for the case without a slope. Furthermore, the $T_{m-1,0}$ is 0.2 s larger and the mean wave direction is up to 2° more northerly.

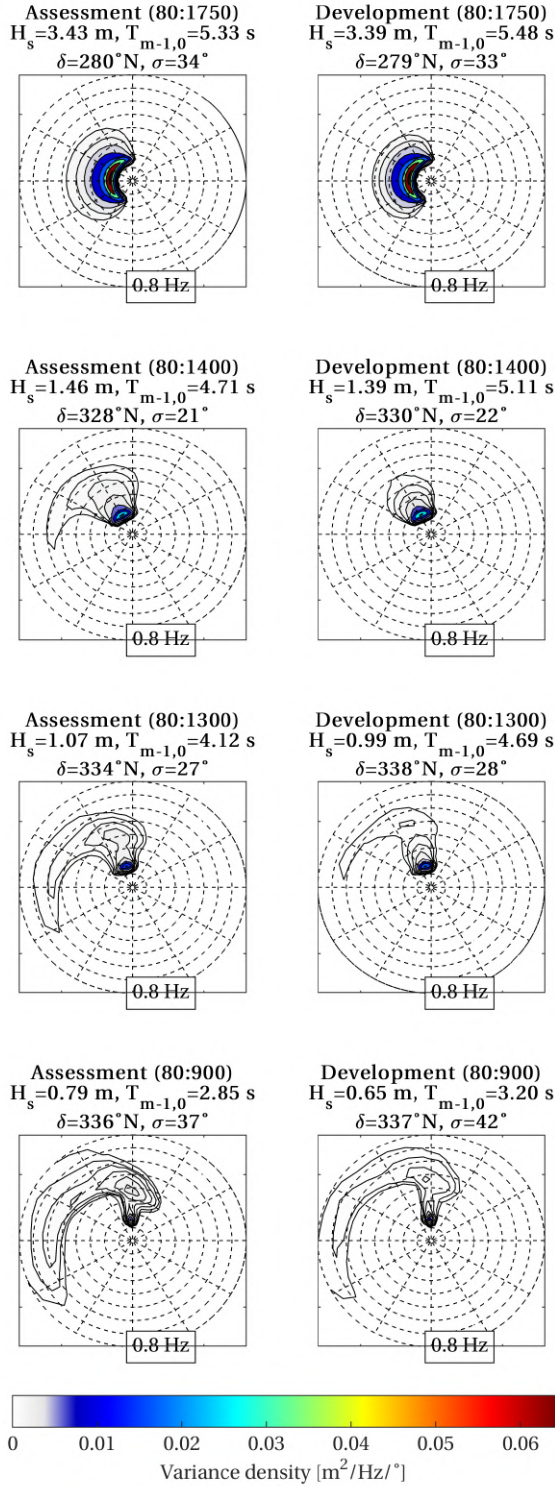


Figure 3.11: 2D spectra for the case with a 1:10 west-east slope, using both the SWAN assessment and development versions.

Largely the same trends hold for locations more offshore, towards the east. The further offshore, the more of the offshore wave energy can reach these areas, as the sheltering by the dike is reduced. This gives larger wave heights, due to which the source terms are larger in absolute sense as well. The larger influence of the source terms increases the local differences around the slope between the cases with and without a slope, at these more eastern locations. However, these differences quickly disappear again more towards the south.

Hence, differences may occur locally between the cases with and without a slope. However, at the dike, these differences are quite small, especially in the bulk wave parameters, since the wave field at these locations is mostly characterised by the wave sheltering and wind growth, which occur regardless of whether a slope is present or not.

The development version gives similar wave heights as the assessment version offshore, but lower wave heights in the shadow zone (up to 15 cm or up to 20% lower), see Figure 3.11. Somewhat more of the energy at the original peak frequency reaches the shadow zone, compared to the assessment version. However, much less energy is present at the higher frequencies. These effects lead to a somewhat larger $T_{m-1,0}$ wave period in the shadow zone and a somewhat more northerly mean wave direction (1° - 3° difference). The larger amount of energy at the peak frequency does not mainly stem from differences in refraction, as differences in directional turning on the slope are minimal for the present cases. However, both the differences in energy at the spectral peak and at the higher frequencies are mainly caused by the smaller influence of the wind growth and white-capping, compared to the assessment version. Since the wind growth, white-capping and quadruplets tend to balance one another, the influence of the quadruplets is somewhat reduced compared to the assessment version as well. Hence, the exponential wind growth of Yan (1987), the white-capping of Van der Westhuysen (2007) and the wind drag coefficient formulation of Wu (1982) as used in the WBI settings of the assessment version are much stronger than the exponential wind growth of Komen et al. (1984), the white-capping of Komen et al. (1984) and the drag coefficient formulation of Zijlema et al. (2012) in the default settings of the development version, for the present cases. The main difference in the wind growth potentially stems from the drag coefficient formulation, as the expression of Wu (1982) gives 10% - 30% larger drag values for wind velocities of 15 m/s to 30 m/s, and over 30% larger values for wind velocities >30 m/s (The SWAN team, 2017a; Zijlema et al., 2012). Compared to the assessment version, the influence of depth-induced breaking is slightly larger with the development version, as well as the influence of the triads.

The development version with and without a slope gives largely similar trends as the assessment version. A somewhat larger H_{m0} of up to 5 cm is found in the shadow zone for the cases with a slope, as well as an up to 0.4 s larger $T_{m-1,0}$ and a 3° to 4° more northerly mean wave direction. As with the assessment version, these differences are mainly caused by the refraction, which allows more energy at the peak frequency to reach the shadow zone.

Thus, the differences in the wave conditions between the two SWAN versions were caused partially offshore already (see previous sub-section), but part of the differences are caused locally as well. These differences occur when the waves enter into the Eems-Dollard estuary around the corner of the Eemshaven and when they travel onto the shal-

low flats in front of the dike. As for the offshore differences, these local differences are caused by the different formulations of the physics in both models.

3.5. DISCUSSION

During the simulations, it was observed that SWAN has difficulties converging in this highly complex area, and that even after the maximum number of 80 iterations as set in the WBI settings, varying numbers of computational points had not yet converged. This mainly influences the mean wave direction and directional spreading, as they converge slower than e.g. the wave height and wave period. Therefore, a stricter stop criterion was applied, where the simulation is stopped when the relative change in H_s from one iteration to the next is less than 0.003 and the curvature of the iteration curve of H_s , normalised with H_s is less than 0.002 in 99.5% of the wet grid points. The maximum number of iterations was set to 160. This new stop criterion improved the convergence sufficiently.

In the simulations comparing the two SWAN versions in the Wadden Sea and Eems-Dollard estuary, another effect was observed in the assessment version results. Spatial alongshore oscillations with a length scale of 1 to 2 kilometre occur in the wave parameters along the dike around Uithuizerwad, mainly in the $T_{m-1,0}$ (up to 10%), but also in the H_s (up to 5%). These oscillations were found in the actual Dutch safety assessment WBI results as well. To find the cause, a schematised model was made of an inlet between two islands in the Wadden Sea, and extending from the North Sea towards the dike. This effect turns out to be related to the sweep mechanism in SWAN that is used for curvilinear grids. With rectilinear/regular grids, this effect does not play a role, and therefore is something to keep in mind when deciding on the use of (curvilinear) grids in these complex areas.

Wave heights as found with the schematised model of the area around the Eemshaven and the Twin Dikes were much lower than with the large-scale model. The mean wave direction did not become onshore-directed either, whereas it did become onshore with the large-scale model and in the WBI results. These differences seem to stem mainly from errors in the rotation of the schematised model compared to reality. Simplifications in the bathymetry could have played a role as well. In a next step of this study, the channel Bocht van Watum, which runs close to the dike, will be included in the models as well.

The Dutch safety assessment (WBI) uses the mean wave direction and total (significant) wave height as input for wave overtopping calculations, to determine the crest levels of the dikes. The 2D spectra of the present simulations show that even if the mean wave direction is onshore-directed, a large part of the wave field may be offshore-directed. Using the total wave height in combination with the mean wave direction may thus lead to overestimations of the overtopping and required crest levels.

The SWAN assessment version uses 36 10° directional bins. This coarse directional resolution might lead to removal of certain wave directions by sheltering, which in reality would still be able to penetrate. This was tested by using 180 directional bins of 2° each, which indeed gives a smoother behaviour of the wave parameters and wave spectra.

By default, SWAN uses the SORDUP numerical scheme for the wave propagation. The BSBT scheme that gives more numerical diffusion, can be used as well. In case this scheme is used, the wave height gradients are smoothed much more, resulting in larger wave heights at the dike. This shows once more that the model settings need to be carefully picked in a highly complex area, such as the one considered here.

Diffraction effects may play a role around the corner of the Eemshaven. A phase-decoupled refraction-diffraction approximation by [Holthuijsen, Herman, and Booij \(2003\)](#) can be applied in SWAN. The approximation is expressed in terms of the directional turning rate of the individual wave components in the 2D wave spectrum and is based on the mild-slope equation for refraction and diffraction, omitting phase information. Using the approximation leads to slightly smoother wave height patterns, but does not lead to largely different wave heights at the dike. However, this does not mean that diffraction does not play a role in reality, since the phase information is missing in the approximation. Simulations with a numerical model such as SWASH (Simulating WAVes till SHORE, [Zijlema et al., 2011](#)), which is able to determine the diffraction effects fully, should be used to determine if diffraction effects play a role in reality. This again shows that the field measurements in the area are highly necessary.

3.6. CONCLUSIONS

This chapter determined the locations that are most suited for wave measurements in the Eems-Dollard estuary, to gain insight in the reasons why large onshore-directed wave heights are predicted by SWAN during offshore-directed winds. It provided information on the processes that play a role in the area around the corner of the Eemshaven and at the tidal inlet as well, and an assessment was made of the reliability and applicability of SWAN in this highly complex area.

The area considered here is highly complex, and no data for validation were available yet. Availability of validation data is highly necessary and will be filled in by the field measurement project. Caution is necessary when applying SWAN in such a complex area, as the complex bathymetry and offshore wind conditions cause the underlying modelling concepts of SWAN to reach their limits. Furthermore, caution is necessary when picking both the settings for the physics and the numerics, because slightly different settings can lead to very different results. One has to be aware of the limits of applicability of the model, in conjunction with the assumptions within the model.

The preferred measurement locations were determined by considering the propagation effects. These preferred locations are the corner of the Eemshaven and the transition area from the deeper channel Bocht van Watum towards the shallow areas in front of the dike.

Quite large differences occurred in the results between the SWAN assessment and development versions. These differences appeared both offshore, at the transition from North Sea to Wadden Sea, as well as more locally inside the estuary, around the Eemshaven and close to the dike. Offshore, these differences were mainly caused by the differences in the refraction formulations. The lack of agreement between both SWAN versions and previous field measurements shows that improvements in the understanding of the physics and improvements in the model formulations are necessary. Inside the estuary, several main effects in turning the mean wave direction around the corner at the Eemshaven were observed: wave sheltering, directional spreading, wind growth, white-capping, wave-wave interactions and some numerical diffusion effects. The nearshore differences between both models were caused by differences in the formulations of these physical processes. The differences between and accuracy of these different formulations are an important aspect for further research. Local diffraction effects likely play a role

in areas with large wave height gradients and strong refraction as well, such as around the corner of the Eemshaven and at the transitions from deep channels to shallow flats. Whether the waves become onshore-directed in reality as well, has to be determined by further study. The field measurements, inclusion of the Bocht van Watum in the SWAN models, and more detailed numerical modelling using SWASH can all aid in this. These aspects will be considered in the next steps of the study.

ACKNOWLEDGEMENTS

This study was supported by Waterschap Noorderzijlvest and the Hoogwaterbeschermingsprogramma.

4

MODELLING WAVE PROPAGATION EFFECTS IN A COMPLEX ESTUARY: PERFORMANCE OF THE NUMERICAL WAVE MODEL SWAN

The use of an extensive computer program often provides more insight into the used computer system than into the program.

Gerbrant van Vledder

This chapter provides more insight into the wave propagation processes that play a role in the Eems-Dollard estuary in the north of the Netherlands, which characterise the extreme wave loads on the dike in the estuary. The dike design conditions in this highly complex estuary are characterised by an offshore-directed wind. Nevertheless, the phase-averaged wave model SWAN (Booij et al., 1999) predicts large, onshore-directed waves at the dike during extreme conditions. The main aim of this chapter is to determine which processes play a role in the estuary and whether SWAN can accurately predict the wave conditions in the area. To this end, simulations with schematised bathymetries of increasing complexity are performed with the numerical wave models REFRAC, SWAN and SWASH, as no measurements were available inside the estuary yet. A variety of processes play a role in the area, which create a complex wave field and cause complex and sometimes directionally multi-peaked spectra at the dike. The models predict that the waves indeed turn around the corner at the Eemshaven and become onshore-directed at the dike during design conditions. SWAN performs reasonably well for the more complex cases based on the bathymetry of the estuary. Still, some limitations of SWAN were identified, related to the omission of diffraction and non-collinear triad wave-wave interactions, the overestimation of the transfer to the super-harmonic by the triad interactions, as well as the overall worse

performance of SWAN for more narrow-spread seas. Whether the wave heights as predicted for the Dutch dike safety assessment are correct, depends in a large part on the accuracy of the different wind drag relations implemented in SWAN. To further validate the results, SWAN and SWASH simulations using the actual bathymetry of the Eems-Dollard estuary should be compared to future buoy measurements and preferably X-band radar measurements in the estuary.

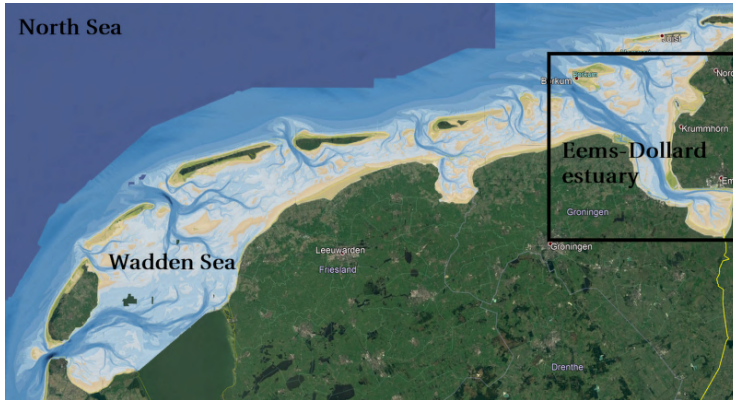
4.1. INTRODUCTION

Wave conditions at flood protection structures are important in the design of these structures. These conditions are often determined by using numerical wave models, since measured data are not always available. It is of large importance that these wave conditions are accurately predicted by the applied model. Applying such a model in a highly complex estuary, which is part of a shallow shelf sea with tidal flats and wetlands, and where the wind acts in an offshore direction, might mean reaching or even surpassing the model's limits of applicability.

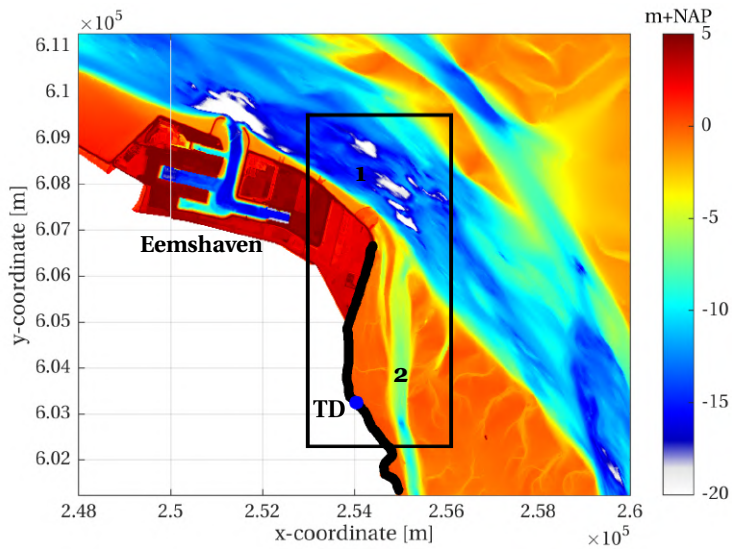
The upper panel of Figure 4.1 shows the area of interest of this study, the Eems-Dollard estuary. The Eems-Dollard estuary is a highly complex estuary in the north of the Netherlands, which is part of the Wadden Sea, a shallow shelf sea. Multiple extensive studies, some including field measurements, have been performed in the Wadden Sea, to gain a more detailed understanding of this complex area. Some noteworthy ones are [Eslami Arab et al. \(2012\)](#); [Groeneweg et al. \(2009, 2015\)](#); [Groeneweg and Van Vledder \(2005\)](#); [Van der Westhuysen et al. \(2012\)](#); [Van Dongeren et al. \(2011\)](#). These studies mainly focused on the tidal channels and tidal deltas at the transition from the North Sea to the Wadden Sea. The Eems-Dollard estuary is even more complex than the Wadden Sea, and consists of deep tidal channels, shallow tidal flats and wetlands, see the lower panel of Figure 4.1. Moreover, almost no studies have been performed in the estuary and almost no measurements are available inside the estuary. The focus of this study lies on the area (black rectangle in lower panel of Figure 4.1) around the dike (black line in Figure) between the Eemshaven, the main port in the area, and the town of Delfzijl. This dike protects a large part of the province of Groningen from flooding.

A particular aspect of this area is that the dike design conditions consist of an offshore-directed northwestern wind and very obliquely incident waves, up to 80° relative to the dike normal. SWAN (Simulating WAVes Nearshore, [Booij et al., 1999](#)), a phase-averaged wave model based on the wave action balance equation, is used for the dike safety assessment in the Netherlands, within the Dutch flood defence safety assessment framework WBI ('Wettelijk BeoordelingsInstrumentarium'). The SWAN version that is used in the framework, version 40.72ABCDE (the assessment version), predicts large, onshore-directed waves at the dike, of order 2 m during design conditions. SWAN predicts that the waves turn around the corner of the Eemshaven, potentially due to refraction and diffraction, and become onshore-directed at the dike in the area.

[Van Nieuwkoop and Gautier \(2015\)](#) found a bias in the predictions of the mean wave direction of up to 20° and of the directional spreading by SWAN at the dikes in the eastern Wadden Sea, leading to differences in the required crest levels of the dikes ranging from 7 cm to 30 cm. However, up until recently, no measurements were available in the Eems-Dollard estuary. This means that the wave conditions during (extreme) storms, which are



(a) North Sea, Wadden Sea and Eems-Dollard estuary.



(b) Area of interest in the Eems-Dollard estuary.

Figure 4.1: Top: Area of interest. The square indicates the Eems-Dollard estuary. Parts of the North Sea, the Wadden Sea and north of the Netherlands shown as well. Bathymetrical data from Rijkswaterstaat 2014 bathymetrical survey. Bottom: Area of interest around the Eemshaven in the Eems-Dollard estuary (rectangle), with the deep tidal channels (1 and 2) and shallow flats clearly visible. The black line indicates the dike of interest. TD (Twin Dikes) indicates the overtopping measurement location in the area of interest.

currently predicted by SWAN, are without direct validation nearshore. This uncertainty in the wave conditions leads to uncertainties in the required crest level of the dikes and could potentially lead to millions of euros of unnecessary dike reinforcements.

To gain more insight in the wave conditions, an extensive field measurement project is being performed in the estuary for a period of 12 years. The measurements started in 2018, measuring wind, water levels, waves and wave run-up and overtopping. One of the wave overtopping measurement locations is indicated by TD ('Twin Dikes') in the lower panel of Figure 4.1. The aim of the measurements is twofold: First, to understand the processes yielding nearshore wave conditions better, ultimately leading to improved numerical prediction models. Second, to understand the processes related to oblique wave run-up and overtopping better, leading to improved prediction methods.

The main purpose of this chapter is to gain more insight into the wave propagation processes that play a role in the area, which characterise the extreme wave loads on the dike in the estuary. The focus mainly lies on nearshore wave propagation effects, like refraction and diffraction. Other processes, e.g. triad wave-wave interactions, will be considered whenever relevant or of influence. The aim of this chapter is to answer the following research questions:

1. What is the cause of the apparent turning of the waves around the corner at the Eemshaven; which processes play a role?
2. How well can SWAN model these processes; how well does the model perform in the estuary?
 - (a) Are the wave conditions as currently predicted by SWAN in the estuary accurate or not?
 - (b) Do the waves remain as large as the SWAN assessment version predicts?
 - (c) Can SWAN be used safely in such a highly complex area, or are the limitations of the underlying modelling concepts of SWAN reached or surpassed?

To the best of the authors' knowledge, the performance of SWAN has not been assessed in such a highly complex estuary before. At present, no measurements of storms are available for the area yet. Hence, a direct comparison with measured data is not possible. Therefore, this chapter compares SWAN to the REFRAC and SWASH models for bathymetries of increasing complexity, based on the area of interest. Increasing the complexity of these cases step by step allows for detailed insight into the relevant processes. REFRAC (REFRACTION, [The REFRAC team, 2019](#)) is a ray-tracing model based on Snell's law that provides insight in wave refraction. SWASH (Simulating WAVes till SHore, [Zijlema et al., 2011](#)) is a non-hydrostatic wave-flow model (a phase-resolving wave model), which solves the non-linear shallow water equations.

The outline of this chapter is as follows. First, the relevant literature is discussed briefly. After that, section 4.3 gives a short description of how SWAN accounts for refraction and diffraction. The next section discusses the methods and model set-up. Section 4.5 presents the results of the refraction and diffraction cases with waves with a narrow directional spreading. These academic cases provide more insight in the relevant processes and the performance of SWAN. Next, section 4.6 gives the results of the cases with more realistic

broad-spread waves. Section 4.7 presents the results with a more detailed model, based on the area of interest. This section provides insight into the processes that play a role in the area of interest, as well as the performance of SWAN in the area. The final section gives the conclusions and presents an outlook on the next steps in this study.

4.2. LITERATURE REVIEW

The computation of the directional turning in SWAN is based on Snel's law. Snel's law (or the geometrical optics approximation) holds for parallel depth contours and situations without currents. It does not account for diffraction effects. It is given by:

$$\frac{\sin \theta}{c} = \text{constant} \quad (4.1)$$

where θ [°] is the angle between the wave ray and the normal to the depth contours and c [m/s] is the wave phase velocity. Using linear wave theory, refraction is based on the phase velocity, which is related to the wave number by the dispersion relation. Hence, a longer wave will refract more.

Using Snel's law for a wave travelling from shallower to deeper water, a critical angle θ_{crit} can be determined. This critical angle is defined as the angle relative to the normal to the depth contours, for which the direction of the refracted wave becomes parallel to the depth contours. In this way, the wave cannot enter the deeper water any longer. This critical angle is defined according to the left panel of Figure 4.2 and can be determined by:

$$\theta_{\text{crit}} = \sin^{-1} \left(\frac{c_{\text{shallow}}}{c_{\text{deep}}} \right) \quad (4.2)$$

Note that this critical angle does not depend on the bottom slope.

When the refraction of waves around a deep channel is considered, three refraction modes can occur, see e.g. Zwamborn and Grieve (1974) and the right panel of Figure 4.2:

1. When the waves propagate (almost) parallel to the channel axis, they refract on the slopes of the channel and propagate out of the channel, reducing the wave height in the channel (wave defocusing or wave reduction). The refracted waves interact with the waves unaffected by the channel, which leads to a local increase of wave energy outside of the channel (wave focusing, wave concentration or wave amplification), see e.g. Misra et al. (2008); Ris, Holthuijsen, and Booij (1999).
2. When the angle between the channel axis and wave propagation is larger, the critical angle is of importance. If the angle of incidence is smaller than the critical angle, waves can enter the channel. When the waves enter the channel, they refract, when they leave the channel, they refract back.
3. When the angle between waves and the normal to the depth contours is larger than the critical angle, the waves will not cross the channel, but will mainly concentrate at the channel's wave-ward slope and attune to the channel edge. The waves then travel parallel to the channel and cause an increase in local wave height, see e.g. Dusseljee et al. (2014); Magne et al. (2007).

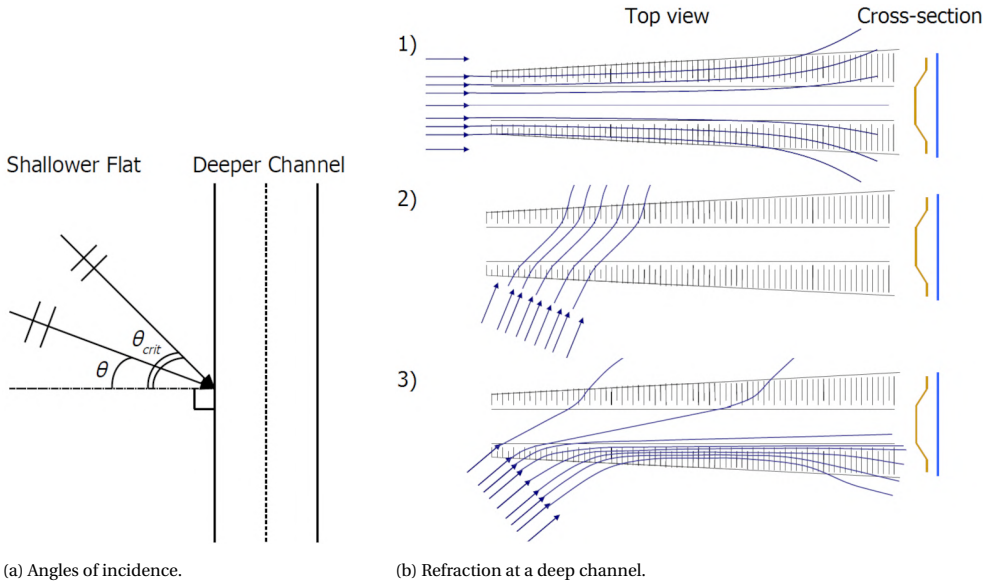


Figure 4.2: Left: Definition of incident angle θ [°] and critical angle θ_{crit} [°], relative to the normal to the depth contours, based on Snell's law. The dashed line is the channel axis. Right: Waves propagating in three different directions over a channel. Longitudinally (1), at an angle smaller than the critical angle (2) and at the critical angle (3). Figure after [Guzman Mardones \(2011\)](#); [Zwamborn and Grieve \(1974\)](#).

In reality, Snell's law is not always valid. Non-parallel depth contours (local bathymetrical changes), currents, directional spreading, frequency spreading, wave non-linearities, evanescent waves or wave tunnelling and diffraction can influence the directional turning as well. SWAN can account for the first four. The influence of wave non-linearities and evanescent waves on the directional turning is not taken into account, as SWAN assumes linear waves. Furthermore, SWAN does not account for the scattering of waves by bathymetrical features smaller than the wavelength (Bragg scattering). SWAN includes an approximation for the diffraction, see section 4.3.

Directional and frequency spreading allow more penetration into a channel compared to unidirectional, monochromatic waves, due to the range of frequencies and directions present in a broader spectrum, see e.g. [Zwamborn and Grieve \(1974\)](#). In shallower water, linear wave theory might not be valid any longer and non-linear effects might start to play a role. These non-linear effects, such as triad wave-wave interactions or waves steepening on the slope, can influence the directional turning.

In situations with waves attuning to the channel edge (situation 3 in the right panel of Figure 4.2), evanescent waves or wave tunnelling can occur. Evanescent waves and wave tunnelling are different names for the same phenomenon. Evanescent waves are waves that are transmitted into the channel in situations where this is not possible according to Snell's law. Hence, evanescent waves enter the channel even for angles of incidence larger than the critical angle. Evanescent waves decay exponentially from the interface. Here, the process will be referred to as evanescent waves, as the name describes the phenomenon

more clearly (evanescent = tending to vanish). Evanescent waves can be considered a diffraction effect, as it prevents a sharp spatial variation in wave amplitude by a leakage of wave energy into areas 'forbidden' by Snell's law (Magne et al., 2007).

Groeneweg et al. (2009) found that SWAN significantly underpredicted the low-frequency energy at shallow up-wave locations next to a tidal channel. The differences between measured and modelled values were attributed to non-linear refraction and diffraction effects, currently not included in SWAN. Dusseljee et al. (2014); Magne et al. (2007) observed transmission of energy, attributed to evanescent waves, for situations where this transmission could not occur according to Snell's law. Furthermore, they found that including diffraction in a phase-averaged model could improve the results related to this transmission. Dusseljee et al. (2014) also found that SWAN performed much better for irregular, directional waves than for regular, unidirectional waves for these kinds of situations. Guzman Mardones (2011); Liu (2009) showed that enabling the diffraction approximation in SWAN could be beneficial under certain conditions. However, they also found that the diffraction approximation of SWAN does not always work properly, resulting in uncertainty whether the observed effects were physical or caused by the approximation method itself. Guzman Mardones (2011) determined that diffraction effects could not be excluded for channel slopes steeper than 1:20. Liu (2009) concluded that in its current state, it was not beneficial to enable the diffraction process in SWAN for waves with a directional spreading larger than a certain limit value, and recommended to study and solve the numerical instabilities in the diffraction implementation of SWAN.

Guzman Mardones (2011) found that differences between SWAN and SWASH were related to the approximations of the quadruplet and triad wave-wave interactions in SWAN. Groeneweg et al. (2015) showed that 2D non-linear triad interactions broaden the spectrum in frequency and directional space, yielding more energy at angles smaller than the critical angle, thus allowing more energy to enter a channel. The present 1D approximations for the triad interactions in SWAN do not include these interactions, and therefore underestimated the energy in the channel. At present, SWAN includes the 1D LTA (Lumped Triad Approximation, Eldeberky, 1996) and the 1D SPB (Stochastic Parametric Boussinesq model, Becq-Girard, Forget, & Benoit, 1999). The LTA only considers the self-self interactions, and only accounts for the generation of super-harmonics. The SPB takes all (1D) interactions into account, thus allows for the generation of both super-harmonics and other (e.g. lower) harmonics. However, the method is limited to very small changes in the bi-spectra. The implementation of these models is based on the collinear approximation, where it is assumed that directional components are isolated, and each direction is treated as an independent wave field (Salmon et al., 2016). This means that energy transfer only occurs between (almost) collinear waves (waves travelling in the same direction), whereas energy may be transferred between non-collinear components in more realistic, directional situations. Salmon et al. (2016) further showed that the Original Collinear Approximation (OCA) of the triad source term, which was used in previous SWAN versions as the one used for the Dutch dike safety assessment WBI, overestimates the energy transfers in the unidirectional limit and underestimates the transfers in short-crested seas. They proposed a Consistent Collinear Approximation (CCA) which remains well-behaved for both unidirectional and directional wave fields. Furthermore, both Groeneweg et al. (2015) and Salmon et al. (2016) recommended to implement more advanced and prefer-

ably 2D triad formulations, such as the 1D formulation of Toledo and Agnon (2012), which accounts for bottom changes and all interactions, the combined SWAN and SAM1D model as considered by Van der Westhuysen (2007), which can model both the resonant and near-resonant interactions exactly, the Distributed Collinear Triad Approximation (DCTA) of Booij, Holthuijsen, and B nit (2009), a 2D formulation with a flat-bottom assumption (Eldeberky, 1996), the 2D directional SPB of Becq, Benoit, and Forget (1998), or the 2D formulation with flat-bottom assumption of P. A. E. M. Janssen (2009). Implementation of a better representation for the evolution of the bi-spectrum, such as T. T. Janssen (2006); Smit and Janssen (2016); Vrecica and Toledo (2016, 2019) was also recommended.

4.3. REFRACTION AND DIFFRACTION IN SWAN

Booij (1998) already found that the SWAN model can give inaccurate results related to refraction, where the directional turning rate per unit distance is over- or underestimated. This can have several causes, related to the grid resolution, to the equation used to calculate the directional turning, or to the numerical scheme used to determine this directional turning.

Different SWAN versions include differences in the equation used to determine the directional turning rate, in the numerical scheme used to determine this turning rate, and in the limiter to prevent excessive directional turning. E.g. version 40.72ABCDE as used for WBI, estimates the directional turning rate c_θ based on depth differences, which it approximates using first-order backward differences, and includes limiters of Booij (1998) (not enabled by default) and Van Vledder and Koop (2009) (enabled for the WBI simulations of the region of interest). On the other side, the newest SWAN version 41.31 estimates c_θ based on the celerity (wave number), approximating it with central differences, and includes the limiter of Dietrich et al. (2013) (not enabled by default). For a more extensive description of the implementation of refraction in SWAN, see appendix B.

Van der Reijden (2020); Zijlema (2020) found that the directional turning rate can indeed be overestimated for waves propagating from deeper to shallower water. Table 4.1 shows this as well, comparing the directional turning rate according to Snell's law with the SWAN turning rate equation based on the water depths (Equation B.7) and based on the wave numbers (Equation B.9), see appendix B. Table 4.1 also shows that the directional turning can be underestimated for waves travelling from shallower to deeper water. The SWAN results are worse for a larger difference in water depth between two grid points, Δd [m]. Note that the accuracy is not dependent on the spatial resolution (grid cell size) or the steepness of the bottom slope alone, but on the balance between the two. A coarse grid resolution may still give accurate results if the bottom slope is gentle; a high grid resolution may still give inaccurate results if the bottom slope is very steep. With large Δd , the errors may become exceptionally large, so that wave energy may turn over more than one directional bin in SWAN. Table 4.1 shows that the equation based on the wave numbers (Equation B.9) gives better results than that based on the water depths (Equation B.7).

Phase information is required for the calculation of diffraction. This phase information is something that is not included in phase-averaged wave models. SWAN includes a phase-decoupled refraction-diffraction approximation of Holthuijsen et al. (2003) to determine the diffraction (not enabled by default). The approximation is expressed in terms of the directional turning rate of the individual wave components in the 2D wave

spectrum. The approximation was based on the mild-slope equation for refraction and diffraction, omitting phase information. Therefore, it does not permit coherent wave fields in the computational domain. The necessary spatial resolution is $1/5^{\text{th}}$ to $1/10^{\text{th}}$ of the wavelength. The approximation has its limitations, and should not be used for obstacles covering significant parts of the down-wave view, for small distances to the obstacle, for coherent reflection off the obstacle, or for obstacles with a significant reflection (The SWAN team, 2019a).

Δx [m]	d_1, d_2 [m]	Δd [m]	$\Delta\theta_{\text{Snel}}$ [°]	$\Delta\theta_{\text{SWAN,DEP}}$ [°]	$\Delta\theta_{\text{SWAN,WNUM}}$ [°]
<i>Deeper to shallower</i>					
150	20 m to 5 m	15	13.79	46.16	26.18
80	20 m to 12 m	8	5.71	9.09	7.14
20	20 m to 18 m	2	1.21	1.34	1.26
5	20 m to 19.5 m	0.5	0.29	0.30	0.29
1	20 m to 19.9 m	0.1	0.06	0.06	0.06
<i>Shallower to deeper</i>					
150	5 m to 20 m	-15	-33.6	-8.60	-14.61
80	5 m to 13 m	-8	-19.57	-8.23	-11.35
20	5 m to 7 m	-2	-5.69	-4.26	-4.73
5	5 m to 5.5 m	-0.5	-1.51	-1.39	-1.43
1	5 m to 5.1 m	-0.1	-0.31	-0.30	-0.30

Table 4.1: Directional turning rates for a 1:10 slope and a wave with $T = 10$ s and initial $\theta = 30^\circ$. Results for several grid cell sizes according to Snel's law, SWAN Equation B.7 (based on the water depths) and SWAN Equation B.9 (based on the wave numbers). Δx [m] is the grid cell size, d_1 and d_2 [m] are water depths, Δd [m] is the difference in water depth over one grid cell, $\Delta\theta_{\text{Snel}}$ [°] the directional turning rate according to Snel's law, $\Delta\theta_{\text{SWAN,DEP}}$ [°] the SWAN turning rate using Equation B.7 and $\Delta\theta_{\text{SWAN,WNUM}}$ [°] the SWAN turning rate using Equation B.9.

4.4. METHODS AND MODEL SET-UP

To reach the goals of this study (see section 4.1), simulations were performed with SWAN, REFRAC and SWASH. Since no measurements were available in the area of interest yet, REFRAC and SWASH were used as the benchmark for SWAN. REFRAC provides insight in the refraction behaviour according to Snel's law, whereas SWASH gives detailed insight in the different physical processes. The model simulations were split into three parts with increasing complexity.

4.4.1. SET-UP OF ACADEMIC CASES WITH NARROW-SPREAD WAVES

The first part consists of simulations with academic refraction and diffraction models with regular and irregular narrow directionally-spread waves. These academic cases allow for isolation of the refraction and diffraction processes, to be able to study their relevance (research question 1, see section 4.1) and the performance of SWAN in modelling them (research question 2). Furthermore, sensitivity analyses were performed, to determine the

recommended SWAN settings for the modelling of refraction and diffraction of narrow-spread waves. The sensitivity analyses were structured according to Cavaleri et al. (2018): first the influence of changes in the boundary conditions was studied, then the influence of the numerical settings and effects, followed by the influence of different formulations for the source terms.

The main focus of this part was on waves with angles of incidence close to and above the critical angle relative to a channel, since this likely plays a role in the area of interest. Furthermore, the focus was on diffraction behind a land mass, since this likely plays a role around the Eemshaven, the port in the area.

Two different refraction models were used, see the first two panels of Figure 4.3. The waves travel from deeper towards shallower water in the first model, and from shallower towards deeper water in the second model. The models measure 800 m by 2000 m (in deep water wavelengths L roughly $14L$ by $36L$ for $T = 6$ s) and consist of a shallow flat at 0 m+NAP, a 1:5 slope and a deeper channel at -12.5 m+NAP (Normaal Amsterdams Peil, Dutch ordnance level). These bottom levels roughly correspond to the heights of the shallow flats in front of the dike and the main tidal channel in the area of interest. The water level was set to 6 m+NAP, approximately the design water level in the estuary.

A semi-infinite breakwater model was used for the diffraction cases, see the third panel of Figure 4.3. The model has the same size as the refraction model, but with a flat bottom at -12.5 m+NAP. Note that this domain is larger than the well-known diffraction diagrams of Goda, Takayama, and Suzuki (1978). The western boundary is partially closed off by the semi-infinite breakwater (from $y = 0$ m - 1500 m), representing the dike and the Eemshaven. The water level was set to 6 m+NAP as well.

The wave height was set to 1 m for the regular waves case, to minimise the influence of wave non-linearities and source terms on the refraction and diffraction. The significant wave height H_s was set to 3 m for the irregular waves cases. This wave height corresponds to the design conditions in the main tidal channel in the area. The (peak) wave period T_p was set to 6 s, the directional spreading σ_θ to 1° . The regular waves were modelled with a delta spectrum, the irregular waves with a standard JONSWAP spectrum (K. Hasselmann et al., 1973). Angles of incidence relative to the normal to the depth contours θ of 30° , 48° , 48.42° , 49° and 60° (300°N , 318°N , 318.42°N , 319°N and 330°N , nautical direction, coming from) were used for the refraction cases. The critical angle according to Snell's law is 48.42° for the conditions considered here. The wave direction was set to $\theta = 0^\circ$ (270°N) for the diffraction cases. No wind was imposed on the models. The wave boundary conditions were applied to the western boundary for the refraction cases and on the western and northern boundaries for the diffraction cases.

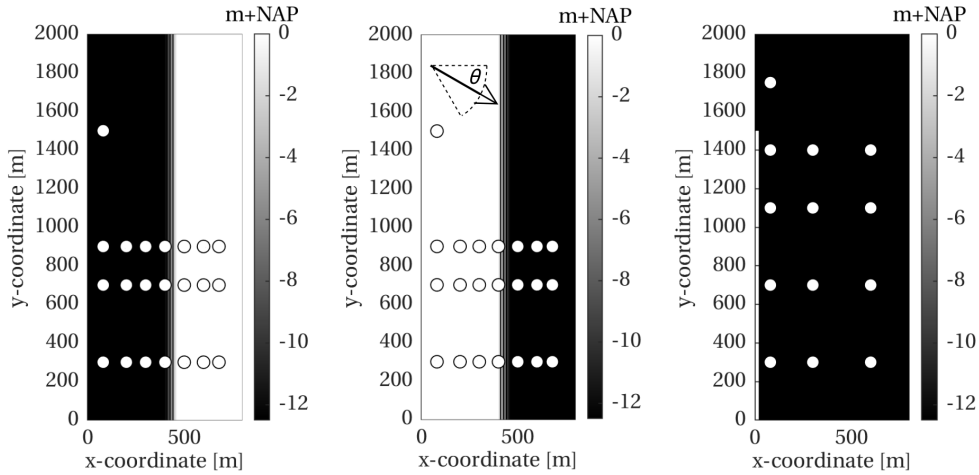


Figure 4.3: Bathymetries of the academic refraction (first two panels) and diffraction (third panel) models. Model (2D spectra) output locations shown with circles, range of angles of incidence θ shown in middle panel.

4.4.2. SET-UP OF ACADEMIC CASES WITH BROAD-SPREAD WAVES

The second part consists of simulations with the academic refraction and diffraction models (Figure 4.3), with irregular broad-spread waves. With these cases, the performance of SWAN in modelling refraction and diffraction of more realistic broad-spread seas was assessed (research question 2). Sensitivity analyses were performed again, to assess the performance of several different versions of the SWAN third generation physics. These settings are the recommended settings as determined based on the cases with narrow-spread waves, the WBI settings (Dutch dike safety assessment settings, based on [Van der Westhuysen et al., 2012](#)), the SWAN default settings (based on [Komen et al., 1984](#)), and the SWAN ST6 settings ([Rogers et al., 2012](#)), the international state of the art, with the parameter values according to [Gautier, Van Nieuwkoop, and De Ridder \(2018\)](#). Note that the newest SWAN version (41.31) was used for all simulations, except for the simulations with the WBI settings. Version 40.72ABCDE (the 'assessment version') had to be used for these simulations, since these settings are not included in the newest SWAN version any longer. Tables [D.1](#) and [D.2](#) in appendix [D](#) give an overview of the exact model settings for these different versions of the third generation physics.

A JONSWAP spectrum with $H_s = 3$ m, $T_p = 6$ s and $\sigma_\theta = 30^\circ$ was applied, to model the broad-spread seas. The same angles of incidence were studied as for the narrow-spread cases. In cases where wind was imposed on the models, a wind direction of 330° N and velocity of 35 m/s were used. These values correspond to the design conditions in the Eems-Dollard estuary.

4.4.3. SET-UP OF DETAILED MODEL CASES

The final part consists of simulations with a more detailed model based on the bathymetry of the area of interest, see Figure [4.1](#) and [4.4](#). These simulations bring all aspects considered in the previous steps together, and were used to determine the causes of the

apparent turning of the waves around the corner at the Eemshaven (research question 1) and how well SWAN models these processes and performs in the estuary (research question 2). Hence, these simulations were used to determine if the wave conditions as currently predicted by SWAN in the estuary are accurate or not, if the waves remain as large as the SWAN assessment version predicts, and if SWAN can safely be used in such a complex area. To answer these questions, SWAN simulations were performed with both the WBI settings and the recommended settings based on the academic cases.

The model consists of a part of the deep main tidal channel in the estuary, the secondary channel that runs close to the dike, and the shallow flat in front of the dike. The size of the model is 1200 m by 2000 m (roughly $21L$ by $36L$). The bottom levels of the deeper and shallower areas were set to -12.5 m+NAP and 0 m+NAP respectively, the channel slopes to 1:5. The design conditions as used in the academic cases with broad-spread waves were used here as well. Wind and wave directions of 300°N and 330°N were studied. The wave boundary conditions were imposed on the western and northern boundaries.

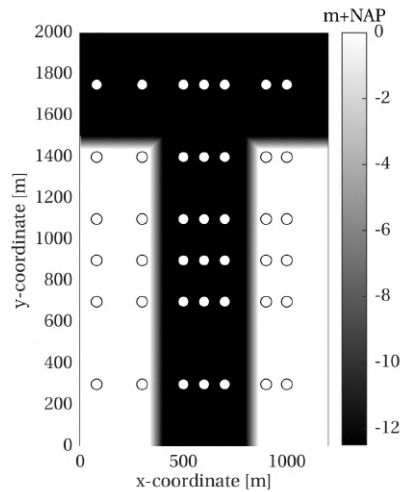


Figure 4.4: Detailed model, schematised based on the area of interest (see lower panel of Figure 4.1). The model includes the main tidal channel, the secondary channel Bocht van Watum and the shallow flats. Model output locations indicated as well (circles).

4.4.4. REFRAC SET-UP

REFRAC version 20.02 was used. The computational and bathymetrical grid cell sizes were set to 5 m. The integration step for the computation of the wave rays, a fraction of the wavelength, was set to 0.01. Parallel wave ray output was requested, with an initial spacing between the rays of 20 m. The Bouws and Battjes (1982) computation was used to determine the wave heights, with averaging over 4 grid cells.

4.4.5. SWAN SET-UP

The computational and bathymetrical grid cell sizes were set to 5 m, a relatively fine resolution, as WBI uses smallest grid cell sizes of approximately 20 m x 80 m. The applied

settings for e.g. the directional resolution, frequency resolution and stop criterion can be found in appendix D. SWAN was used in the stationary mode. The bin-spectrum option was used to model the regular waves. The JONSWAP option was used for the irregular waves. Output was requested in the form of tables with bulk wave parameters, 1D and 2D wave spectra, as well as bulk wave parameter and source term output over the whole computational domain. The semi-infinite breakwater (or dike) in the diffraction cases was modelled with a column of so-called 'exception values'. These points are regarded as permanently dry.

4.4.6. SWASH SET-UP

Sufficient computational resources were necessary for the SWASH simulations. Therefore, the simulations were run on the Dutch national supercomputer Cartesius. Cartesius consists of 47,776 computational cores and 132 GPUs, giving a theoretical peak performance of 1.843 Pflop/s (see <https://userinfo.surfsara.nl/systems/cartesius>). This was the first time that the SWASH model was applied on such a large cluster. SWASH version 7.01ab was used for the final simulations. Version 5.01, 6.01 and 7.01 were used initially, but some issues were encountered while running SWASH on Cartesius. These issues were solved and implemented in temporary versions 7.01a and 7.01ab and finally in the official version 7.01A. These issues, some of the experiences of the authors with respect to the use of the model on a supercomputer, and guidelines on parallel simulations with SWASH can be found in appendix C.

SWASH was run in the non-stationary 2D mode with two equidistant vertical layers for accurate dispersion. A background viscosity of 10^{-5} m²/s was applied for the coupling of the vertical layers. A grid cell size of 2 m was used. The boundary conditions were applied in the same way as in SWAN, with the addition of 100 m wide sponge layers on the northern, southern and eastern boundaries for the academic refraction cases, and on the southern and eastern boundaries for the academic diffraction and detailed model cases. Porous grid cells were used to model the dike in the diffraction cases. The porosity was set to 0.01 to model full reflection (see [The SWASH team, 2019b](#), for the definition).

A default Manning bottom friction value of 0.019 was set, a constant horizontal eddy viscosity was applied and depth-induced breaking was enabled. For the numerics, the default Keller-box scheme was applied. Furthermore, the default explicit time integration was used with a minimum CFL number for the time step control of 0.1 and a maximum of 0.5. The initial time step was set to 0.04 s. After some spin-up, the models were run for a duration of 250 wave periods. Output was requested in the form of multiple tables with water levels at nine grid points per table for the determination of 2D wave spectra, as well as tables with bulk wave parameters and snapshots of the model output over the whole computational domain.

The wave height as applied on the boundary (the target wave height) showed a sudden drop near the boundary. This is known behaviour of the time-domain model SWASH, mainly caused by the forcing of linear wave theory on the boundary, whereas the boundary usually is in the weakly non-linear regime ([De Wit & Reniers, n.d.](#)). It was determined that the wave height became more or less constant after a distance of 80 m from the boundary. Therefore, the wave height at $x = 80$ m was assumed to represent the incident wave height in SWASH. To reduce the influence of such model and boundary effects,

and for ease of comparison between different models, the relative wave heights $H_{rel} = H_{s,local}/H_{s,incident}$ [-] were considered for all models, where for all models a representative incident wave height near the boundary was chosen as being unity. The 2D wave spectra were determined with the BDM method (Bayesian Direct Method, Hashimoto & Kobune, 1988), using the DIWASP (Directional WAVE SPECTRA, Johnson, 2002) MATLAB toolbox.

SWAN was compared to REFRAC and SWASH for the academic refraction and detailed model cases. SWAN was compared to SWASH and the analytical solutions of Penney et al. (1952) (based on Sommerfeld, 1896) and Goda et al. (1978) for the academic diffraction cases.

4.5. RESULTS OF ACADEMIC CASES WITH NARROW-SPREAD WAVES

This section considers the simulations with the academic refraction and diffraction models with regular and irregular narrow-spread waves, refer to Figure 4.3. These cases are used to study the relevance of refraction and diffraction (research question 1, see section 4.1) and the performance of SWAN in modelling them (research question 2). Sensitivity analyses are performed as well, to determine the recommended SWAN settings for the modelling of refraction and diffraction of narrow-spread waves. A wave height of 1 m is used for the regular waves cases, $H_s = 3$ m is applied for the irregular waves, the latter corresponding to the design conditions in the area of interest. $T_p = 6$ s, $\sigma_\theta = 1^\circ$, θ values of 30° , 48° , 48.42° , 49° and 60° were used for the refraction cases, $\theta = 0^\circ$ was used for the diffraction cases. No wind was imposed yet. The default SWAN settings were used for the physics, unless stated otherwise.

4.5.1. RESULTS OF REFRACTION CASES WITH REGULAR WAVES

WAVES TRAVELLING FROM DEEPER TOWARDS SHALLOWER WATER

The academic refraction cases with waves travelling from deeper towards shallower water are treated first. SWAN agrees well with REFRAC and SWASH for these cases. The waves refract towards the normal to the depth contours, whereby H_{rel} becomes somewhat smaller on the shallower flat due to de-shoaling and refraction. REFRAC gives $H_{rel} = 0.75$ on the shallow flat, SWAN $H_{rel} = 0.80$, SWASH $H_{rel} = 0.82$, for an angle of incidence $\theta = 60^\circ$. For this case, REFRAC gives a wave angle relative to the normal to the depth contours of 40° (310°N) on the shallow flat, in agreement with Snell's law. SWAN gives 41° (311°N), SWASH gives 39° (309°N). Contrary to what was found in Table 4.1, SWAN underestimated the refraction compared to Snell's law for all considered angles of incidence. Note that Table 4.1 only accounted for a difference in grid resolution and turning rate equation, hence Equation B.7 or B.9. Other aspects, such as the numerical scheme with which the turning rate equation is approximated, were not included.

The cause of this underestimation of the refraction in SWAN was studied further, by determining the influence of the grid resolution, directional turning equation, numerical scheme used for this equation and the rescaling of negative action density. Negative action densities can occur due to large action density gradients in frequency or directional space. By default, such negative values are removed from the spectrum by setting these values equal to zero and rescaling the remaining positive values such that the frequency-

integrated action density per spectral direction is conserved (Booij et al., 1999). This rescaling can be turned off with the command `OFF RESCALE`.

Table 4.2 gives the results. As expected based on Table 4.1, a coarser grid resolution (with the same bottom slope, thus an increase in Δd per grid step) leads to worse results. Both the directional turning equation based on the water depths (Equation B.7) and based on the wave numbers (Equation B.9) perform almost equal for the present cases. However, note that Δd was quite small here. For larger Δd , Equation B.9 will perform better, see Table 4.1. The numerical scheme and rescaling have quite a large influence on the refraction. Central and backward differences perform roughly equal, where central differences often result in underestimations of the directional turning and backward differences result in overestimations of the directional turning. Turning off rescaling improves the results with central differences, but worsens the results with backward differences. The best results are achieved with a combination of central differences and no rescaling. Turning off rescaling yields less (artificial) directional spreading, improving the refraction results. However, turning off rescaling may lead to negative variance or energy densities in the wave spectra produced by SWAN.

Hence, not only the bottom slope and grid resolution (combined into Δd) are important, but the choice of the directional turning equation, numerical scheme for the turning rate and rescaling of negative action density as well. Values of $\Delta d \leq 5$ m are recommended for narrow-spread waves travelling from deeper towards shallower water, combined with the equation based on the wave numbers (Equation B.9), especially for large Δd , and using central differences. Central differences can be combined with turning off the rescaling to improve the refraction results, but may lead to negative energy in the spectra. Therefore, rescaling was left enabled for the simulations performed in this study. These settings correspond to the default settings of SWAN version 41.31. Since SWAN performed well for these cases, both in predicting the directional turning and wave heights, the simulations with waves travelling from deeper towards shallower water will not be treated further here.

WAVES TRAVELLING FROM SHALLOWER TOWARDS DEEPER WATER

Different angles of incidence yield largely different behaviour when the waves travel from shallower to deeper water, contrary to the previous cases. The three models agree well below the critical angle (30° , 300°N), where the waves refract towards the channel axis and penetrate into the channel. Refer to <https://youtu.be/bgEo1MBDSKU> for a short animation of the SWASH simulation.

Close to the critical angle, for $\theta = 48^\circ$, $\theta = 48.42^\circ$ and $\theta = 49^\circ$ (318°N , 318.42°N and 319°N), much larger differences arise between the different models. Figure 4.5 presents the results for $\theta = 48^\circ$ and $\theta = 60^\circ$. Refer to <https://youtu.be/1CHiErRWckg> for a short animation of the 48° case using SWASH. REFRAC shows that most energy accumulates in a narrow band around the channel slope for $\theta = 48^\circ$, just below the critical angle. This agrees with Snell's law and results in a strong increase in H_{rel} on the channel slope ($H_{rel} > 2.5$). SWASH shows partial reflection off the channel slope in the southern part of the domain, resulting in a local increase in H_{rel} on the shallow flat. SWASH also predicts an increase in wave height on the channel slope ($H_{rel} = 2$), though not as extreme as REFRAC. SWAN shows partial reflection as well (15% versus 10% with SWASH), and $H_{rel} = 1.5$ on the channel slope.

Δx [m]	Δd [m]	Turning rate Eq.	Numerical scheme	Rescaling	$\Delta\theta_{SWAN}$ [°]	$\Delta\theta_{SWAN} - \Delta\theta_{Snel}$ [°]
5	1	Eq. B.9	Central	On	19	-1
5	1	Eq. B.9	Central	Off	20	0
5	1	Eq. B.7	Central	On	19	-1
5	1	Eq. B.7	Central	Off	20	0
5	1	Eq. B.7	Backward	On	20	0
5	1	Eq. B.7	Backward	Off	22	+2
20	4	Eq. B.9	Central	On	17	-3
20	4	Eq. B.9	Central	Off	21	+1
20	4	Eq. B.7	Central	On	18	-2
20	4	Eq. B.7	Central	Off	18	+1
20	4	Eq. B.7	Backward	On	22	+2
20	4	Eq. B.7	Backward	Off	26	+6

Table 4.2: Directional turning rate $\Delta\theta_{SWAN}$ [°] as calculated by SWAN, relative to the incident wave direction and relative to the directional turning rate as calculated by Snel's law, for several combinations of grid cell size Δx [m] or depth difference per grid step Δd [m], turning rate equation, numerical scheme used to discretise this equation and rescaling of negative action density.

SWAN underestimates the directional turning with approximately 5° compared to REFRAC (Snel's law), even for a 5 m grid cell size. This behaviour is in agreement with Table 4.1. A coarser grid resolution of 20 m yields an even larger underestimation of the directional turning (15° less than REFRAC), due to which less energy is trapped on the shallow flat. This gives less reflection, a larger underestimation of H_{rel} on the channel slope and more energy in the channel. Thus, the influence of the grid resolution is large for cases where waves travel from shallower to deeper water. Table 4.1 shows this as well. Therefore, a maximum of $\Delta d = 1$ m is recommended for cases with narrow-spread waves travelling from deeper towards shallower water. This keeps the errors in the refraction limited to approximately 10° with the present conditions. For the relatively fine grid resolution employed here, only minor differences occur when applying Equation B.7 instead of Equation B.9. Once again, the differences are expected to increase if the grid resolution is decreased, and Equation B.9 is recommended. The same holds for first-order backward differences. If the grid resolution is high, then backward differences perform roughly equal to central differences, but for a coarser grid resolution the performance of backward differences quickly deteriorates. Thus, central differences are recommended once more. As for refraction from deeper towards shallower water, turning off rescaling improves the refraction results, but may lead to negative energy in the spectra.

The three models give largely different results for $\theta = 60^\circ$ as well, above the critical angle. Refer to <https://youtu.be/YkCACZc8HLs> for a short animation of the 60° case using SWASH. All three models show that the waves turn towards 360°N on the channel slope. However, REFRAC traps all waves on the shallow flat for angles larger than the critical angle. SWASH still gives wave energy ($H_{rel} = 0.1$) in the channel for this case. SWAN traps almost all energy on the shallow flat as well and gives $H_{rel} = 0.01$ in the channel with

rescaling. All energy is trapped on the shallow flat when rescaling is turned off.

SWASH showed that energy was still able to cross the channel slope, even for angles of incidence above the critical angle. Due to the absorbing northern boundary, through which no wave energy enters the domain, diffraction effects occur close to the northern boundary, see the last two panels of Figure 4.5. This leads to somewhat more westerly wave directions in the northern part of the domain. Potentially, part of the energy in the channel was caused by these diffracted waves. SWASH simulations using porous grid cells in the northeastern part of the domain showed that the influence of diffraction caused by the northern boundary is small in the southern part of the domain (differences in H_{rel} up to 10%) and cannot explain the wave energy that was found in the channel.

Next, it was determined if the energy in the channel was a result of evanescent waves. SWASH shows that waves start to attune to the channel slope, where the wave direction becomes 360° N. Dusseljee et al. (2014) and Magne et al. (2007) observed the same behaviour. Diffraction-like behaviour occurs in the channel, where waves that are initially northerly-directed, turn more towards the west as they propagate further down-wave in the channel. Dusseljee et al. (2014) and Magne et al. (2007) refer to these waves as evanescent waves or wave tunnelling. Evanescent waves exponentially decay, and thus die out quickly. The present results show a decreasing wave height in the channel as well, but the waves do not die out. Hence, evanescent waves cannot fully explain the wave penetration into the channel either, meaning that other mechanisms allow transfer of energy across the channel slope as well.

To gain further insight in these potentially non-linear mechanisms, simulations were performed with a wave height of 0.1 m instead of 1 m. These lower waves adhere to linear wave theory. Several differences occur between the 1 m and 0.1 m cases. These differences are present for all angles of incidence, but can be seen most clearly in the results of the 48° case. Figure 4.6 presents the 2D SWASH spectra with weakly non-linear waves ($H_s = 1$ m, top row), linear waves ($H_s = 0.1$ m, middle row) and SWAN with weakly non-linear waves (bottom row), for $\theta = 48^\circ$ and at three locations. The variance density of each model was normalised and colour-scaled with the maximum variance density at the off-shore (80,1500) location.

SWASH shows directional broadening of the spectra on the shallow flat and in the channel for both the non-linear and linear waves, due to diffraction (first two rows of Figure 4.6). Diffraction is a linear process. However, the spectra with non-linear waves are directionally broader than the spectra with linear waves. This was caused by the (2D) triad wave-wave interactions, which cause a transfer to the super-harmonic at twice the peak frequency on the shallow flat, as well as further directional broadening. Triad interactions are a non-linear process, thus do not play a role in the cases with linear waves. Both transfers by the triads allow more energy to enter the channel ($H_{rel} = 0.12$ for the non-linear $\theta = 60^\circ$ case versus $H_{rel} = 0.10$ for the linear case, not shown), as both shorter waves and waves at smaller angles of incidence can more easily penetrate into the channel. Furthermore, the bi-spectra (not shown) indicate that some recurrence occurs over the channel slope, where the triads transfer energy back from $2 * f_p = 0.33$ Hz to 0.15 Hz and 0.18 Hz. However, this effect is relatively minor.

The SWAN spectra (bottom row of Figure 4.6) are narrower than the SWASH spectra for both non-linear and linear waves. This is due to the omission of diffraction in SWAN.

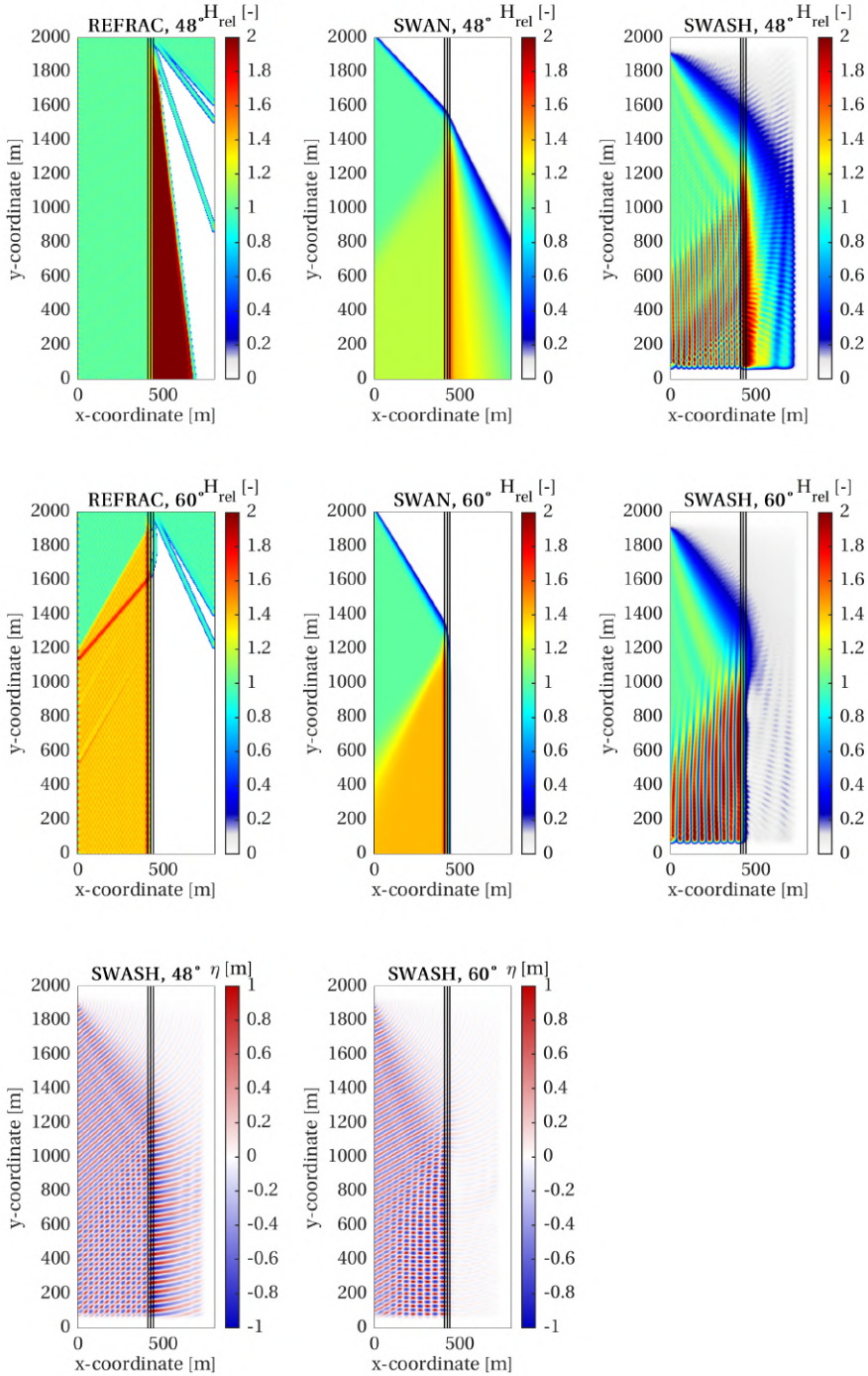


Figure 4.5: First two rows: Relative wave heights H_{rel} [-] of REFRACT, SWAN and SWASH for waves travelling from shallower towards deeper water, with $\theta = 48^\circ$ and $\theta = 60^\circ$ (318°N and 330°N). Bottom row: SWASH surface elevation η [m] for both angles of incidence.

No transfer to the super-harmonic occurs, as the triads (and other source terms) were turned off for the present cases. As a result, SWAN gives much less energy in the channel for the $\theta = 60^\circ$ case ($H_{rel} = 0.01$, not shown) than SWASH. The poor performance of SWAN in predicting the propagation of regular waves is not surprising, since the phase-averaged SWAN model was not developed for such conditions. The processes observed here are in agreement with [Guzman Mardones \(2011\)](#) and [Groeneweg et al. \(2015\)](#), who showed that diffraction effects cannot be excluded for slopes steeper than 1:20, and that 2D triad interactions can directionally broaden the spectra, allowing more energy to penetrate into areas forbidden by Snel's law.

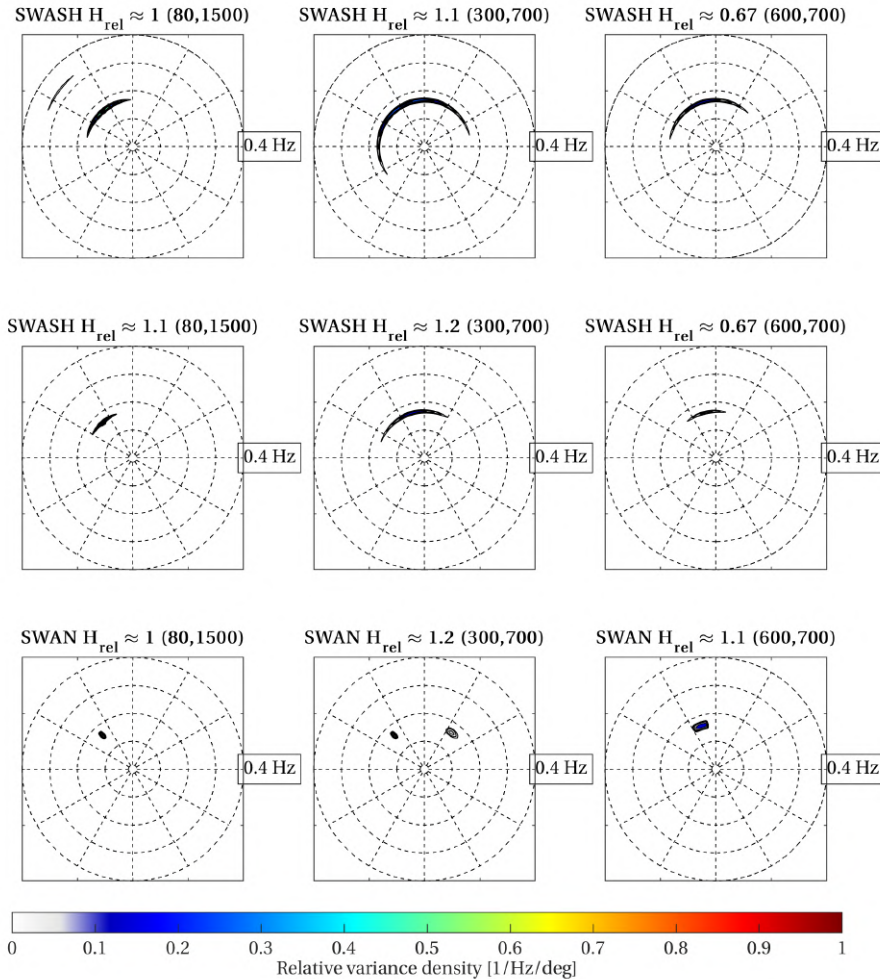


Figure 4.6: 2D spectra at three locations for regular waves travelling from shallower to deeper water with $\theta = 48^\circ$ (318°N). Top row: SWASH with non-linear waves ($H_S = 1$ m). Middle row: SWASH with linear waves ($H_S = 0.1$ m). Bottom row: SWAN with non-linear waves ($H_S = 1$ m). Variance density of each model normalised and colour-scaled with the maximum variance density at the offshore (80,1500) location.

SWAN SENSITIVITY ANALYSES

SWAN sensitivity analyses were performed to determine the recommended settings for the modelling of refraction of regular waves. Only the most relevant cases were selected for further analysis, being the cases for which SWAN performed the worst: the refraction cases with waves travelling from the shallower flat to the deeper channel, with $\theta = 48^\circ$ and $\theta = 60^\circ$.

To study the influence of a change in the wave boundary conditions, simulations were performed with a wave period of 4 s or 12 s instead of 6 s, as well as for a slight change in the directional spreading, $\sigma_\theta = 2^\circ$ instead of $\sigma_\theta = 1^\circ$. As expected, a change in the wave period has a very large influence. A small change in directional spreading has a negligible influence. Note that a larger change in directional spreading may have a much larger influence, as this leads to a broader range of wave directions, due to which more of the wave energy will approach the channel slope at angles smaller than the critical angle.

The influence of changes in several numerical aspects (grid cell size, directional turning equation, numerical scheme used for this equation and rescaling of negative action density) were already treated. The influence of the directional resolution (number of directional bins) was assessed as well, by using 36 10° directional bins instead of 360 1° bins. 36 directional bins are the default SWAN setting and are used within WBI as well. For the present cases, almost no energy enters the domain with a smaller number of directional bins. This is caused by the small directional spreading of 1° , combined with a large directional bin size of 10° . Therefore, the wave energy is spread over the 10° bin, decreasing the total energy entering the domain and introducing artificial directional spreading. This reduces the performance of SWAN strongly: the directional turning is underestimated, yielding an underestimation of the reflection off the channel slope and H_{rel} on the slope ($H_{rel} = 1.3$ versus $H_{rel} = 1.5$ with 360 bins, $H_{rel} = 2$ with SWASH) for the 48° case, and an overestimation of the energy in the channel ($H_{rel} = 0.5$ versus $H_{rel} = 0.01$ with 360 bins, $H_{rel} = 0.1$ with SWASH) for the 60° case. This highlights the importance of using a directional resolution that matches the directional spreading, especially for narrow-spread seas.

The same behaviour occurs when the BSBT (Backward in Space Backward in Time) numerical scheme for the wave propagation is applied, instead of the default SORDUP (Second OrDer UPwind) scheme. The ST6 SWAN settings use the BSBT scheme. The numerical diffusion introduced by the BSBT scheme gives similar patterns as a smaller number of directional bins: smoothing of gradients, leading to an underestimation of the directional turning and wave height on the channel slope ($H_{rel} = 1.4$ versus $H_{rel} = 1.5$ with SORDUP) for the 48° case, and an overestimation of the energy in the channel ($H_{rel} = 0.2$ versus $H_{rel} = 0.01$ with SORDUP) for the 60° case. Hence, the default SORDUP scheme is recommended.

A strict stop criterion with a maximum number of iterations of 160 was used for the present simulations, see appendix D. This stop criterion was applied to ensure that all grid points were converged at the end of the simulation. A maximum number of 50 iterations is default, WBI uses a maximum of 80. The influence of applying the default stop criterion was assessed, but did not have an influence for the present cases, as convergence was reached quickly (<10 iterations) for these cases with the source terms still disabled. With more complex bathymetries or more physical processes enabled, many more iterations

can be necessary, see e.g. chapter 3 and Oosterlo, Van der Meer, Hofland, and Van Vledder (2018).

Finally, the influence of changes in the formulations for the physics was assessed. No energy enters the domain in the present cases, when the diffraction approximation is enabled. The same holds for simulations with the diffraction approximation and a larger or smaller wave height, an increase in the grid resolution, a change in the number of directional bins, or a change in the $[\text{alfa}]$ parameter for the under-relaxation. Only a decrease in the grid resolution to 20 m allows energy to enter the domain, but these simulations do not converge and are therefore not treated further here. The expectation is that a reliable, converging diffraction approximation may aid in directionally broadening the spectra and improving the results. However, the limitation on the grid resolution and lack of convergence mean that the present diffraction approximation is not reliable, nor generally applicable, for narrow-spread seas. Guzman Mardones (2011) and Liu (2009) also drew similar conclusions.

To gain insight in the influence of the different physical processes, simulations were performed with the SWAN default settings for the physics, see appendix D. The quadruplet wave-wave interactions and action limiter were left disabled, since no wind was imposed on the model yet (see The SWAN team, 2019b). As described in sub-section 4.4.1, the present wave height of 1 m was chosen to minimise the influence of the source terms. This is indeed the case, as all source terms either have a minimal influence or are not active.

4.5.2. RESULTS OF DIFFRACTION CASES WITH REGULAR WAVES

Figure 4.7 shows the SWASH (left) and SWAN (middle) results for the diffraction cases with regular waves. The figure compares the models to the analytical solution of Penney et al. (1952); Sommerfeld (1896) (black dashed lines). Refer to <https://youtu.be/40UX6BbIjF8> for a short animation of the SWASH simulation. SWASH is able to reproduce the main features of the wave propagation into the area well. Even for narrow-spread waves, some energy is able to enter the shadow zone behind the dike. SWAN was not able to reproduce the wave penetration, showing very large and unrealistic wave height gradients, underestimating the wave energy in the shadow zone of the dike. This is due to the fact that SWAN, a phase-averaged model, does not include the phase information necessary to determine diffraction.

SWAN SENSITIVITY ANALYSES

SWAN sensitivity analyses were performed for the diffraction cases as well. Since the present cases concern relatively deep water, the diffraction is directly dependent on the wavelength, where longer waves are affected more by diffraction. However, SWAN gives the same results with a wave period of 6 s, 4 s or 12 s, since SWAN does not account for diffraction (without the diffraction approximation enabled). Hence, SWAN is unable to model the diffraction of narrow-spread, regular waves, as the model was not developed for such conditions. An increase in the directional spreading from 1° to 2° yields slightly more energy in the shadow zone behind the dike. This is not caused by diffraction, but by the larger directional spreading. Hence, a larger increase in directional spreading is expected to have a large influence on the results.

Neither a smaller grid cell size, nor a larger grid cell size influence the results much,

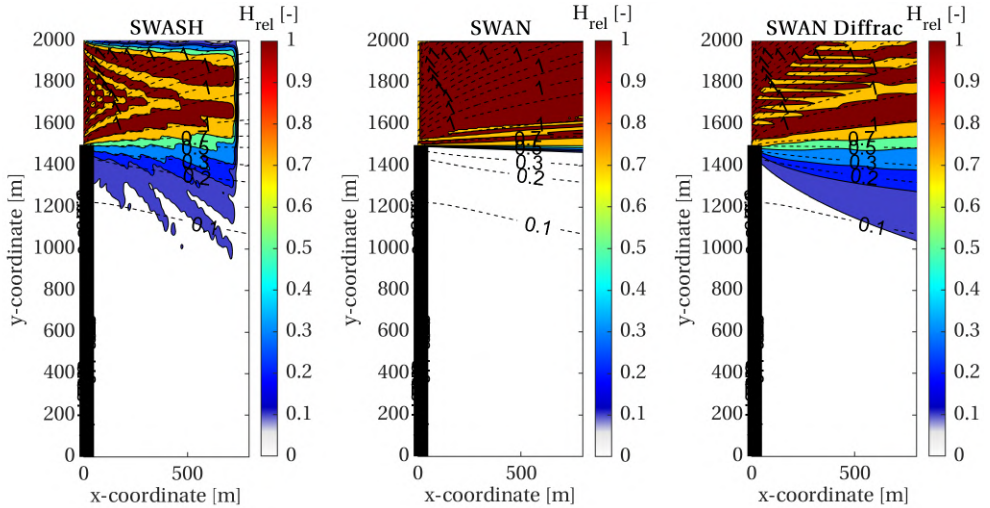


Figure 4.7: Diffraction for semi-infinite breakwater case with regular waves coming from 270°N. SWASH (left), SWAN (middle) and SWAN with diffraction approximation enabled (right), compared to analytical solution of Penney et al. (1952); Sommerfeld (1896) (black dashed lines). The thick black line indicates the dike.

contrary to the refraction cases. The same holds for rescaling. Decreasing the number of directional bins to 36 10° bins yields almost no energy entering the domain again. Applying the BSBT scheme for the wave propagation introduces some numerical diffusion, but the overall influence on the results is negligible. Changes in turning rate equation and stop criterion do not influence the results either.

As was found for the refraction cases, only a low grid resolution of 20 m allows energy to enter the domain when the diffraction approximation is enabled. This simulation agrees much better with SWASH and the analytical solution (right panel of Figure 4.7), but the simulation does not fully converge (95% of the grid points converged, with 99.5% required). Hence, the present diffraction approximation can seemingly improve the results for the diffraction of narrow-spread, regular waves, but has a grid resolution limitation and is not reliable. Since the boundary conditions were chosen such that the influence of other physical processes was minimal, the source terms are not treated further here.

4.5.3. RESULTS OF REFRACTION CASES WITH IRREGULAR, NARROW-SPREAD WAVES

Next, the irregular waves cases are studied. A typical JONSWAP spectrum with $H_s = 3$ m, $T_p = 6$ s and $\sigma_\theta = 1^\circ$ was imposed, see sub-section 4.4.1. No wind was imposed on the model yet. The main focus lies on the cases where the waves travel from shallower towards deeper water, with $\theta = 48^\circ$ and 60° . Refer to <https://youtu.be/Qgnj0JZw020> for a short SWASH animation of the 60° case. The recommended SWAN settings for the numerics (as determined in the previous sub-sections) and the default settings for the physics were used (see appendix D). The source terms potentially play a larger role in these cases, due to the larger wave height and increased wave non-linearity.

Figure 4.8 gives the 2D spectra of SWASH (upper panels) and SWAN (middle panels), for $\theta = 48^\circ$. Both SWAN and SWASH predict that more energy enters the channel than for regular waves, due to the spectral shape. With the applied JONSWAP spectrum, more high-frequency energy is present, which can penetrate into the channel more easily. Depth-induced breaking and the triads are the only source terms that play a role, mainly on the shallow flat. Depth-induced breaking is limited to a narrow band directly at the western boundary of the domain and does not influence the refraction. Therefore, it is not considered further here. The triads are studied in more detail, since they can influence the penetration of the waves into the channel.

The first two panels of Figure 4.8 show that the SWASH spectra become directionally broader on the shallow flat, similar as for the cases with regular waves. This is caused by diffraction and 2D triad interactions on the shallow flat. At the first location (first panel of Figure 4.8), SWASH shows quite some energy at the super-harmonic at 0.33 Hz. The bi-spectra (not shown) show a main transfer from the spectral peak (0.16 Hz) to this super-harmonic. Further onto the shallow flat (second panel of Figure 4.8), the peak at the super-harmonic has been reduced. The triads are still active, mainly transferring energy from the super-harmonic back to the main spectral peak. The cause of this behaviour is unknown. Furthermore, a secondary transfer redistributes energy from 0.025 Hz and 0.125 Hz to 0.15 Hz. The first transfer results in the reduction in the peak at the super-harmonic, the second transfer causes a slight shift of the main spectral peak from 0.16 Hz to 0.15 Hz. In the deeper channel (third panel of Figure 4.8), the low-frequency energy below the spectral peak does not penetrate into the channel and disappears from the spectrum. Furthermore, the triad interactions reduce in the deeper water.

The overall performance of SWAN is better than for the cases with regular waves. However, the SWAN spectra (second row in Figure 4.8) are still much narrower than the SWASH spectra, since SWAN does not account for diffraction, and since the CCA version (Consistent Collinear Approach, [Salmon et al., 2016](#)) of the 1D LTA (Lumped Triad Approximation, [Eldeberky, 1996](#)) does not account for non-collinear interactions. Furthermore, the LTA only accounts for transfers to the super-harmonic. Nevertheless, SWAN still overestimates the energy in the channel for $\theta = 48^\circ$ ($H_{rel} = 0.87$ versus $H_{rel} = 0.79$ with SWASH), because SWAN underestimates the directional turning (see 4.5.1) and because SWAN overestimates the transfer to the super-harmonic. SWAN still underestimates the energy in the channel for the case with $\theta = 60^\circ$ ($H_{rel} = 0.49$ versus $H_{rel} = 0.55$ with SWASH), since the omission of diffraction and 2D triad interactions does not lead to broadening of the spectra. As a result, SWAN predicts that the main spectral peak at 0.16 Hz disappears in the channel, while some energy at this frequency still penetrates into the channel according to SWASH.

Hence, one has to be cautious when applying SWAN to narrow-spread seas, whether they consist of regular or irregular waves, at locations where the waves refract at steep channel slopes. The main weaknesses of SWAN lie in the estimation of the directional turning, the omission of diffraction, and the omission of certain (2D) triad interactions, which are currently estimated by the LTA, a 1D formulation which only accounts for collinear interactions and the transfer to the super-harmonic.

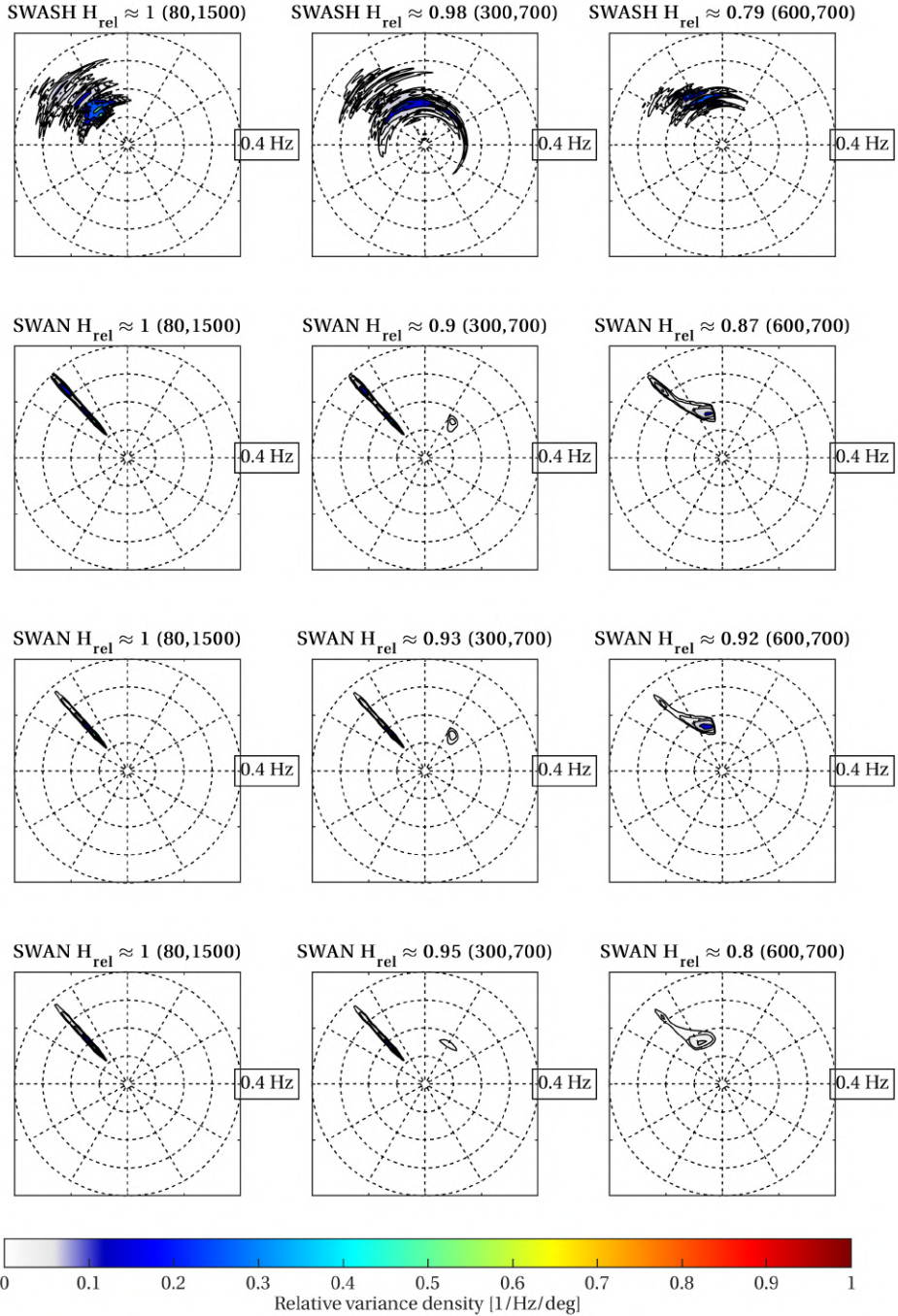


Figure 4.8: 2D spectra at three locations for irregular, narrow spread waves travelling from shallower to deeper water with $\theta = 48^\circ$ (318°N). Top row: SWASH. Second row: SWAN with the recommended settings for the numerics (see sub-section 4.5.1 and appendix D) and the default settings for the physics (see appendix D). Third row: SWAN with the same settings, but with $\alpha = 0.05$ instead of $\alpha = 0.8$. Bottom row: SWAN with the same settings, $\alpha = 0.05$, 20 m grid cells and the diffraction approximation enabled. Variance density of each model normalised and colour-scaled with the maximum variance density at the offshore (80,1500) location.

SWAN SENSITIVITY ANALYSES

The influence of changes in the formulation for the triads and the application of the diffraction approximation were studied in more detail, as these processes had the largest influence on the results. In this way, the recommended SWAN settings for diffraction and triad interactions can be determined, for the modelling of refraction of narrow-spread, irregular seas.

As was found here, [Salmon et al. \(2016\)](#) found that the LTA typically overestimates the transfer to self-self interaction frequencies, for waves with a narrow directional spreading. Therefore, α (`[trfac]` in SWAN), the calibration coefficient of the LTA, should ideally be calibrated for each specific application and amount of directional spreading. [Salmon et al. \(2016\)](#) recommended $\alpha = 0.52$ for unidirectional, irregular waves. Note that this value is essentially the same as the default value of $\alpha = 0.8$ in SWAN. SWAN uses `[cutfr] = 2.5`, which controls the maximum frequency that is considered in the LTA computation ($f_{max} = [cutfr] * f_{m0,1}$), whereas [Salmon et al. \(2016\)](#) calibrated α without any cut-off frequency.

Simulations were performed with the CCA LTA with α values of 1, 0.8, 0.5, 0.1 and 0.05. Generally, a lower value of α will reduce the strength of the transfer. $\alpha = 1$, $\alpha = 0.8$ and $\alpha = 0.5$ give approximately the same results and overestimate the transfer to the super-harmonic. The transfer is reduced for $\alpha = 0.1$ and even more for $\alpha = 0.05$, showing better agreement with SWASH with respect to the transfer to the super-harmonic.

Application of the OCA (Original Collinear Approximation) LTA was tested as well, with the same α values as for the CCA. [Salmon et al. \(2016\)](#) showed that the OCA is highly sensitive to the directional spreading, mainly due to α . If α is calibrated for broader-spread seas, exaggerated energy transfers occur when this value is applied in wave fields with narrower directional spreading than for which it was calibrated. [Salmon et al. \(2016\)](#) found $\alpha = 0.04$ for unidirectional, irregular waves. $\alpha = 0.05$ is the default value for the OCA LTA, WBI uses $\alpha = 0.1$. The OCA can be applied by setting `[itriad] = 1` in SWAN version 40.72ABCDE and `[itriad] = 11` in version 41.31.

The OCA gives approximately the same results for all α values, except for $\alpha = 1$, which causes instabilities. The OCA gives approximately the same strength of the transfer as the CCA with $\alpha = 0.5 - 1$ at the first location (80,1500). However, the OCA gives transfers that lie in between the CCA with $\alpha = 0.05$ and $\alpha = 0.1$ further onto the shallow flat (300,700). The cause of this behaviour is unclear.

The SPB (Stochastic Parametric Boussinesq) method ([Becq-Girard et al., 1999](#)) was considered as well. The SPB does account for all 1D interactions, but comes at an increased computational cost. However, the simulations with the SPB did not converge and the results were unreliable. Hence, for the present cases the SPB cannot be considered a valid alternative to the LTA.

Overall, the CCA with $\alpha = 0.1$ or $\alpha = 0.05$ performs best. Both these values yield an underestimation of the energy at the super-harmonic at the offshore location, where $\alpha = 0.1$ performs somewhat better. Further onto the shallow flat and in the channel, the reduced energy at the super-harmonic with $\alpha = 0.05$ agrees better with SWASH. Therefore, the CCA with $\alpha = 0.05$ is recommended for the present cases. The third row of [Figure 4.8](#) gives the results with these settings. Note that the influence of α on the wave height is small (compare the second and third row). Furthermore, note that this recommendation

is based on the present simulations with narrow-spread waves, and that a different α value may yield the best results for more broad-spread seas. Finally, this recommendation is for lack of a better alternative, as the 1D LTA only accounts for collinear transfers to the super-harmonic, whereas other (non-collinear) interactions play a role as well.

Again, only a decrease in the grid resolution to 20 m allows energy to enter the domain when the diffraction approximation is enabled. The bottom row of Figure 4.8 presents the results. The main difference between the case without diffraction approximation is that the directional turning is predicted much worse, due to the lower grid resolution. As a result, the wave height in the channel is seemingly predicted better, see the titles of the different panels of Figure 4.8. However, SWAN is actually 'more right for the wrong reasons', as this increased wave height is not a result of a better prediction of the physics, but a result of the worse prediction of the directional turning. This shows that bulk parameters such as the (significant) wave height and wave period should not only be used as characteristics for the performance of a wave model, but that more detailed insight is often necessary, e.g. into wave directions, 1D and 2D spectra and the first four moments of the directional distribution (see also Cavaleri et al., 2018; Dabbi et al., 2015; Rogers & Van Vlededer, 2013). Furthermore, the diffraction approximation does not directionally broaden the spectra. Hence, the diffraction approximation does not improve the results and the limitation on the grid cell size is a severe one for situations where an accurate prediction of the directional turning is necessary.

4.5.4. RESULTS OF DIFFRACTION CASES WITH IRREGULAR, NARROW-SPREAD WAVES

Figure 4.9 shows the H_{rel} results of SWASH (left panel), SWAN with the previously determined recommended settings (middle panel) and SWAN with the recommended settings, diffraction approximation and 20 m grid cells (right panel), for the semi-infinite breakwater case with irregular, narrow-spread waves. See <https://youtu.be/jdNf4tujKe4> for a short animation of the SWASH simulation. The Penney et al. (1952); Sommerfeld (1896) solution (black dashed lines) is only marginally different for irregular than regular waves, with slightly less energy entering the shadow zone behind the breakwater (the shorter waves are less affected by diffraction). SWASH underestimates the energy in the shadow zone somewhat, but the overall performance is still quite good. SWAN was again unable to reproduce the wave penetration into the area, showing unrealistic wave height gradients and a large underestimation of wave energy in the shadow zone. The source terms do not influence the results, as the water depth is relatively large and no wind was imposed.

SWAN SENSITIVITY ANALYSES

Only the influence of the diffraction approximation was assessed, since the source terms did not influence the results. Enabling the diffraction approximation improves the results, even though the grid resolution had to be decreased to 20 m again. Around the tip of the dike, SWAN performs as well as SWASH. Deeper into the shadow zone, SWAN underestimates the penetration of energy. As for the diffraction cases with regular waves, the diffraction approximation is able to improve the results, but the restriction on the grid cell size poses a severe limitation, especially for an accurate estimation of the directional turn-

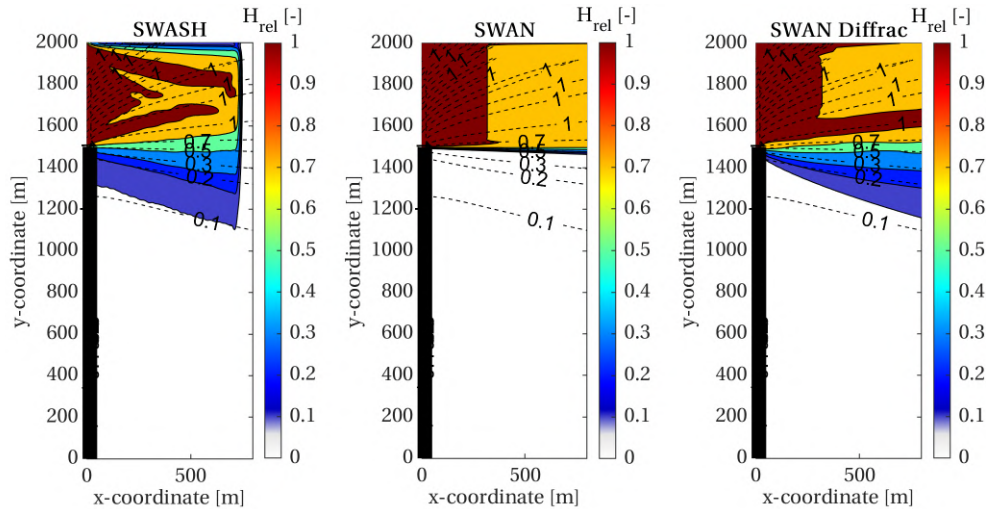


Figure 4.9: Diffraction for semi-infinite breakwater case with irregular, narrow-spread waves coming from 270°N. SWASH (left), SWAN with recommended settings (middle) and SWAN with recommended settings, diffraction approximation and 20 m grid cells (right), compared to analytical solution of Penney et al. (1952); Sommerfeld (1896) (black dashed lines). The thick black line indicates the dike.

ing. Hence, application of the diffraction approximation is only recommended for certain specific diffraction cases, where refraction plays a minor or negligible role.

4.6. RESULTS OF ACADEMIC CASES WITH BROAD-SPREAD WAVES

The second part consists of simulations with the academic refraction and diffraction models (Figure 4.3), with more realistic irregular, broad-spread waves, to assess the performance of SWAN related to refraction and diffraction. A JONSWAP spectrum with $H_s = 3$ m, $T_p = 6$ s and $\sigma_\theta = 30^\circ$ was used to model the broad-spread seas. The same angles of incidence were studied as for the narrow-spread cases. In cases where wind was imposed on the models, a wind direction of 330°N and velocity of 35 m/s were used, corresponding to the design conditions in the area of interest. The previously determined recommended SWAN settings for the numerics and physics were used, see appendix D.

4.6.1. RESULTS OF REFRACTION CASES WITH IRREGULAR, BROAD-SPREAD WAVES

The results of both SWASH and SWAN are consistent for the considered angles of incidence again. Therefore, mainly the 48° case is treated (refer to <https://youtu.be/jNk5ETX60C0> for a short SWASH animation of the 60° case). Figure 4.10 gives the 2D spectra for the 48° case, of SWASH (upper panels), SWAN without wind imposed on the model (middle panels) and SWAN with wind imposed (lower panels). Both models give more energy in the channel compared to the cases with narrow-spread waves. This is a result of the larger directional spreading, due to which waves at a broader range of directions are present. Hence, the directional spreading is relatively more important for the penetration of the waves into the channel than the frequency spreading as discussed in sub-

section 4.5.3. Diffraction and triad wave-wave interactions broaden the spectra again, although their relative influence is smaller for these cases. With wind imposed on the model, the wind growth, quadruplet wave-wave interactions and white-capping play a role as well.

The SWASH spectra directionally broaden on the shallow flat (compare the first and second panel of Figure 4.10), due to diffraction and 2D triad interactions, in agreement with the previously considered cases. However, their influence is smaller compared to the influence of the directional spreading and no clear peak at the super-harmonic arises. The bi-spectra (not shown here) show a transfer of energy from 0.16 Hz to 0.33 Hz, as well as a transfer from 0.30 Hz to 0.15 Hz, on the shallow flat. This somewhat narrows the spectral peak in frequency space. In the deeper channel (third panel of Figure 4.10), some of the high-frequency energy disappears due to recurrence by the triads, and the main spectral peak becomes somewhat broader in frequency space once more.

SWAN performs much better for these cases than for narrow-spread waves, both in predicting the spectral shape and the amount of energy that enters the channel ($H_{rel} = 0.87$ with SWASH, $H_{rel} = 0.84$ with SWAN without wind, $H_{rel} = 0.92$ with wind, for the 48° case). This is in agreement with what e.g. [Dusseljee et al. \(2014\)](#) and [Groeneweg et al. \(2015\)](#) found. Nevertheless, SWAN overestimates the reflection of wave energy at angles larger than the critical angle, as was found in section 4.5. The improved overall performance of SWAN is mainly a result of the larger influence of the directional spreading and the related reduced influence of the directional turning, diffraction and triads. Due to the larger directional spreading, errors in the directional turning and the omission of non-collinear triad interactions and diffraction have become much less pronounced in the results. However, these omissions still yield SWAN spectra that are directionally narrower at the peak frequency than the SWASH spectra. Furthermore, the CCA LTA with $\alpha = 0.05$ overestimates the peak at the super-harmonic somewhat on the shallow flat. This peak (and thus overestimation) persists in the channel, since the LTA does not account for recurrence of energy back to the spectral peak. Note that a higher value for α would yield even larger overestimations.

Some differences occur when wind is imposed on the SWAN model (lower panels of Figure 4.10). The main spectral peak is predicted quite similarly, whether wind is imposed on the model or not. SWAN predicts this main spectral peak well. With wind imposed on the model, the peak at the super-harmonic is less pronounced, but the total amount of energy at the high-frequency tail is larger, as the wind adds energy to these higher frequencies. The increase in high-frequency energy allows more wave energy to penetrate into the channel. This high-frequency tail does not appear in the SWASH results, since SWASH does not account for the wind growth.

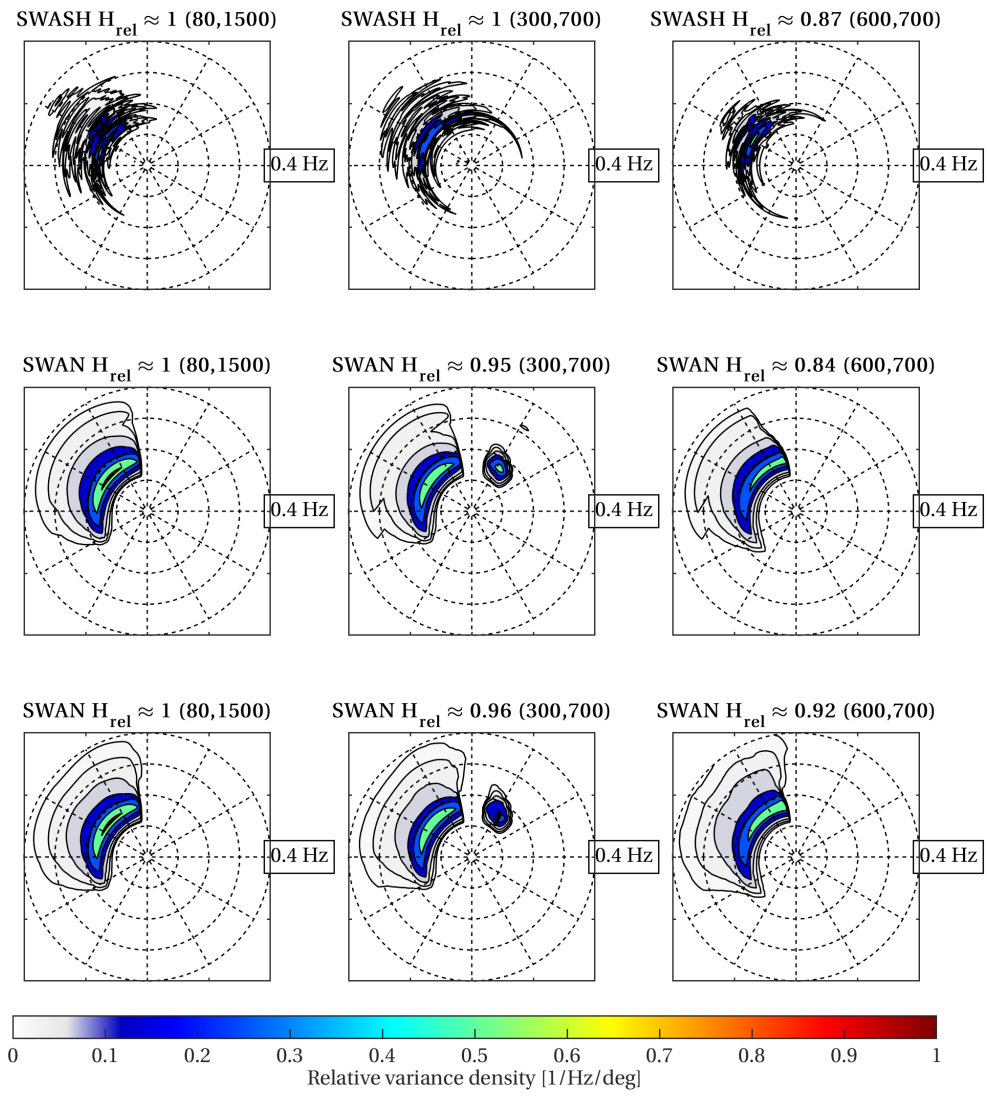


Figure 4.10: 2D spectra at three locations for irregular, broad-spread waves travelling from shallower to deeper water with an angle of incidence of 48° (318°N). Top row: SWASH. Middle row: SWAN with the recommended settings, with no wind imposed on the model. Bottom row: SWAN with the same settings, but with a 35 m/s wind coming from 318°N imposed. Variance density of each model normalised and colour-scaled with the maximum variance density at the offshore (80,1500) location.

SWAN SENSITIVITY ANALYSES

Sensitivity analyses were performed to assess the performance of several different versions of the SWAN third generation physics: the previously determined recommended settings, the WBI settings, the SWAN default settings, and the SWAN ST6 settings with the parameter values according to [Gautier et al. \(2018\)](#) (see appendix D).

The main difference between the recommended settings and the SWAN default settings (first row of Figure 4.11) is the larger overestimation of the peak at the super-harmonic with the default settings, a result of the larger $\alpha = 0.8$. Other than that, both the spectra and wave heights are quite similar to the ones as predicted with the recommended settings. Hence, the smaller number of directional bins (36 versus 360) has a much smaller influence for these cases than for the cases with narrow-spread waves. This confirms once more that the directional spreading has a much larger influence on the wave penetration into the channel than other processes for these cases. The different stop criterion used by the default settings did not have any influence either, as convergence was reached fast (<20 iterations).

The second row of Figure 4.11 shows the results with the WBI settings. The OCA LTA with $\alpha = 0.1$ gives similar results as the CCA LTA with $\alpha = 0.05$, for the present cases. Note that α would ideally be recalibrated for the broad-spread seas as modelled in these cases. The WBI settings estimate the directional turning rate c_θ based on the depth differences (Equation B.7), approximated using first-order backward differences. As was shown in sub-section 4.5.1, this may produce worse results for the directional turning. However, the influence was small here, because of the high grid resolution that was used and because of the relatively larger influence of the directional spreading. The (uncapped) [Wu \(1982\)](#) wind drag formulation that is used with the WBI settings gives more energy at the high-frequency tail of the spectrum compared to the [Zijlema et al. \(2012\)](#) formulation, which places a limit on the drag coefficient for wind velocities >30 m/s. The limit on the wind drag of [Zijlema et al. \(2012\)](#) seems to be physically correct, but the data on which the expression of [Zijlema et al. \(2012\)](#) was based contains a considerable spread. Which expression yields better results cannot be determined based on the present simulations. Finally, the refraction limiter of [Van Vledder and Koop \(2009\)](#), which turns off the refraction for frequencies <0.2 Hz, does not have a large impact on the wave penetration into the channel. However, it does result in a more westerly wave direction at the peak frequency inside the channel. Even though this limiter was not based on any physics, the wave direction at the peak frequency agrees better with SWASH.

The ST6 settings (third row of Figure 4.11) predict directionally narrower spectra than the other settings. The spectral shape in frequency space is predicted better than with the other settings and follows SWASH quite well on the shallow flat. However, the energy at the peak frequency is underestimated and the energy at the super-harmonic is overestimated in the channel. The exact cause of this behaviour is unclear, but it was found that the white-capping was extremely large for the cases with wind imposed on the model. Note that the ST6 parameter values of [Gautier et al. \(2018\)](#) were used here. [Gautier et al. \(2018\)](#) calibrated the ST6 settings for the Dutch North Sea and Wadden Sea, for daily conditions. Further calibration of the ST6 settings for the extreme conditions considered here is still required and may yield improved results.

The lower panels of Figure 4.11 give the results of SWAN with the recommended set-

tings, with the diffraction approximation enabled and 20 m grid cells. Simulations with the diffraction approximation and smaller grid cell sizes do not converge. Use of the diffraction approximation only minimally influences the spectral shape and leads to a slightly different H_{rel} in the channel. This has two reasons. First, the relative influence of diffraction is much smaller than the influence of the directional spreading for these cases, as described above. Second, the diffraction approximation (and LTA) is not effective in directionally broadening the spectra. These results also show that the influence of the grid cell size on the results is much smaller for broad-spread seas than for narrow-spread seas, and that the limitation on Δd as determined in section 4.5 is not as strict for broad-spread seas. Nevertheless, application of the diffraction approximation does not improve the results for broad-spread seas and is unstable for finer grid resolutions.

Hence, the influence of the refraction, diffraction and (non-collinear) triad interactions becomes much smaller for broad-spread seas, since the influence of the directional spreading becomes relatively much more important. This means that the choices for the equation and numerical scheme to estimate the directional turning, the grid cell size, the formulation for the triads and use of the diffraction approximation become less important as well. The overall result is an increase in the performance of SWAN for cases with broad-spread, irregular waves. SWAN performs well with the recommended settings, but the reflection of energy at angles larger than the critical angle and the energy at the super-harmonic in the channel are both still overestimated. The default settings perform similarly to the recommended settings, but show a larger overestimation of the energy at the super-harmonic. The WBI settings perform roughly equal to the recommended settings as well, but the performance related to the wind growth is uncertain. Furthermore, these settings are not available in the newest SWAN version any longer. The ST6 settings predict the spectral shape on the shallow flat better than the other settings, but worse inside the channel. However, further calibration for more extreme conditions may improve the results with the ST6 settings. The recommended settings and WBI settings were compared for the more detailed model in the next section, as these settings performed best for the present cases.

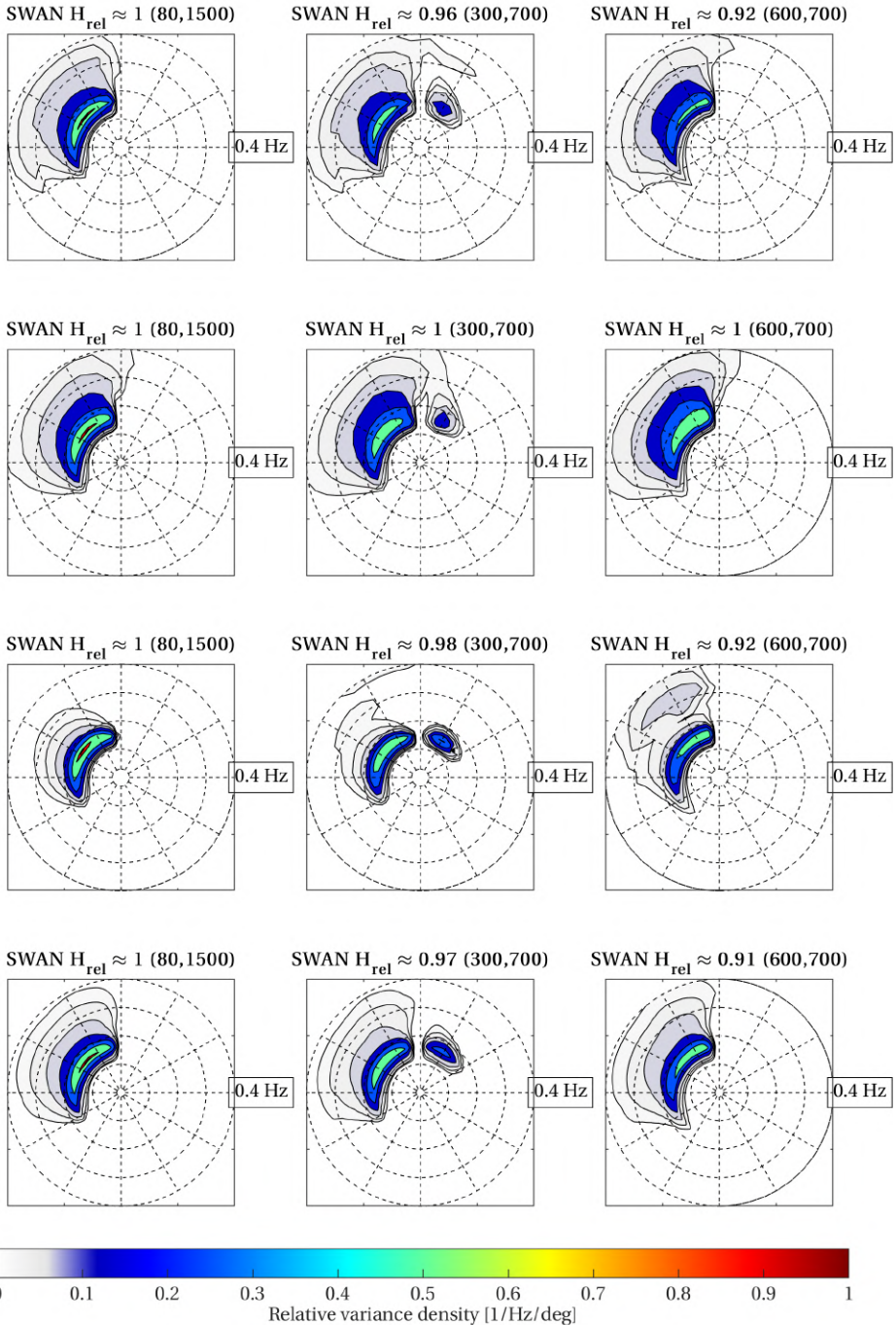


Figure 4.11: 2D spectra at three locations for irregular, broad-spread waves travelling from shallower to deeper water with an angle of incidence of 48° (318°N) and a 35 m/s wind coming from 318°N imposed. Top row: SWAN with default settings. Second row: SWAN with WBI settings. Third row: SWAN with ST6 settings. Bottom row: SWAN with recommended settings, with 20 m grid cells and the diffraction approximation enabled. Variance density of each model normalised and colour-coded with the maximum variance density at the offshore (80,1500) location.

4.6.2. RESULTS OF DIFFRACTION CASES WITH IRREGULAR, BROAD-SPREAD WAVES

Figure 4.12 presents the H_{rel} results of SWASH (left panel), SWAN with the recommended settings without wind (middle panel) and SWAN with these settings with a 35 m/s wind coming from 270°N (right panel), for the semi-infinite breakwater case with irregular, broad-spread waves. The figure shows the analytical solution of Goda et al. (1978) as well. Refer to <https://youtu.be/0ahXrhbpRtE> for a short animation of the SWASH simulation. Much more energy enters the shadow zone behind the breakwater (dike) compared to the cases with narrow-spread waves, due to the broader directional spreading. However, note that the wave heights at the dike are still quite low.

SWASH agrees quite well with the analytical solution around the tip of the dike, but underestimates the wave heights deeper into the shadow zone somewhat. The exact cause of the differences is unknown, but might be explained by omission of e.g. depth-induced breaking or bottom friction in the analytical solution, as well as a potentially different representation of the reflecting breakwater in the analytical solution than in SWASH.

SWAN performs much better for these broad-spread seas and agrees very well with SWASH. The improved performance of SWAN arises from the relatively much larger influence of the directional spreading in these cases. The directional spreading allows much more energy to penetrate into the shadow zone behind the dike, and has a larger influence on the results than diffraction and the source terms, which were found to have a negligible influence.

The wind does influence the results (compare the middle and right panels of Figure 4.12). Note that the analytical solution of Goda et al. (1978) does not account for the wind. Around the tip of the dike, the differences are quite small. The main differences occur deeper into the shadow zone, close to the dike. Without wind imposed on the model, H_{rel} is small at the dike. The local waves have a direction of roughly 0°N and a very narrow directional spreading of only a few degrees, due to the sheltering effect of the dike. Only the waves with increasingly northerly directions are able to reach the dike further into the shadow zone. The wind seems to allow more energy to penetrate into the shadow zone behind the dike, but the waves at the dike are actually locally generated, due to the wind. These locally generated waves are offshore-directed, with a direction centred around the wind direction (270°N) and with a broad directional spreading of up to 50°. This again highlights the importance of not only considering the bulk wave parameters, but the 2D spectra as well.

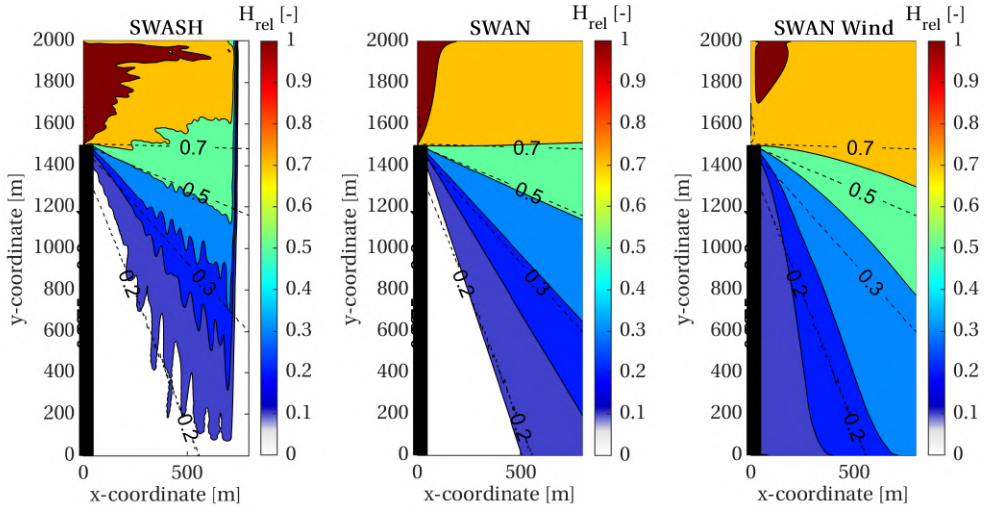


Figure 4.12: Diffraction for semi-infinite breakwater case with irregular, broad-spread waves coming from 270°N. SWASH (left), SWAN (without diffraction approximation) without wind imposed on the model (middle) and SWAN with wind imposed (right), compared to analytical solution of Goda et al. (1978) (black dashed lines). The thick black line indicates the dike.

SWAN SENSITIVITY ANALYSES

The performance of the different SWAN settings was assessed for the diffraction model as well. SWAN with the default settings (not shown) gives approximately the same results as SWAN with the recommended settings, showing that the directional spreading has a much larger influence on the results than e.g. the number of directional bins.

The differences between SWAN with the recommended settings, WBI settings (left panel of Figure 4.13) and ST6 settings (middle panel) mainly occur close to the dike, and are a result of the different wind drag and wind growth formulations that the different settings use. The other source terms have a negligible influence. The wind drag expression of Wu (1982) as used in the WBI settings adds more energy than the expression of Zijlema et al. (2012), as was found for the refraction cases. The expression of Hwang (2011) as used in the ST6 settings yields smaller H_{rel} values close to the dike. Advice on the wind drag and wind growth formulations cannot be given based on the present simulations.

The influence of diffraction is much smaller than the influence of the directional spreading for these broad-spread seas, as indicated by the small differences between the cases without (right panel of Figure 4.12) and with diffraction approximation and 20 m grid cells (right panel of Figure 4.13). Apparently, the same holds for the the grid resolution. Hence, application of the diffraction approximation is not beneficial for these cases with broad-spread seas.

Overall, SWAN performs much better for these cases with broad-spread, irregular waves. It can be concluded that the influence of other processes becomes much smaller for broad-spread seas, due to the large influence of the directional spreading. The same was found for the refraction cases. Hence, the choices for the number of directional bins, grid cell size and use of the diffraction approximation become less important for these conditions.

Results of simulations with the different formulations for the physics mainly differed due to the different wind drag and wind growth formulations. Overall, the recommended and WBI settings seem to perform best again. Advice on the recommended wind drag formulation cannot be given based on the present simulations alone and further research is required.

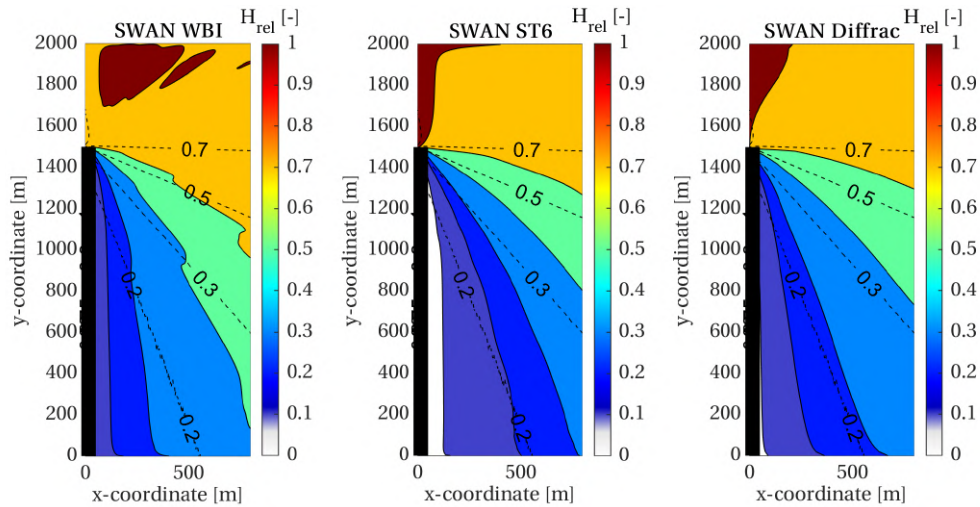


Figure 4.13: Diffraction for semi-infinite breakwater case with irregular, broad-spread waves. SWAN with WBI settings (left), SWAN with ST6 settings (middle) and SWAN with recommended settings, diffraction approximation and 20 m grid cells (right). The black dashed lines indicate the analytical solution of Goda et al. (1978), the thick black line indicates the dike.

4.7. RESULTS OF DETAILED MODEL CASES

This section considers the simulations with the detailed model based on the schematised bathymetry of the area of interest, see Figure 4.1 and 4.4. These cases combine all aspects considered in the previous sections and are used to determine the causes of the apparent turning of the waves around the corner at the Eemshaven (research question 1) and how well SWAN models these processes and performs in the estuary (research question 2). The boundary conditions correspond to the design conditions, being $W_{vel} = 35$ m/s, $W_{dir} = 330^\circ$ N, $h = 6$ m+NAP, $H_s = 3$ m, $T_p = 6$ s, $\delta = 330^\circ$ N and $\sigma_\delta = 30^\circ$. Both the settings optimised in section 4.5 and 4.6 and WBI SWAN settings were used, see appendix D.

4.7.1. MODEL VERIFICATION

The model was verified to ensure that it is representative of the actual area of interest and that it incorporates the same wave processes. The verification compares SWAN results obtained from the Dutch dike safety assessment framework (WBI) database with results from the present model. Figure 4.14 shows 2D variance density spectra obtained from the database for a simulation with design conditions (left panel of Figure 4.14), at the Twin Dikes overtopping measurement location in the area of interest (TD in the lower panel of

Figure 4.1) and at a location approximately 800 m to the southeast of TD (middle panel of Figure 4.14). The shallow flat in front of the dike is approximately 500 m narrower at this location.

The right panel of Figure 4.14 gives the spectrum at (80,700) in the present model, using the WBI settings. The bulk wave parameters agree quite well for all three plotted spectra, see the titles of the three panels. The spectral shape obtained with the present model is more representative of the second location in the database, with two directional peaks, roughly around 0°N and 30°N . A few differences can be observed. The spectra from the database contain low-frequency energy <0.1 Hz, potentially due to the penetration of longer North Sea waves. The WBI SWAN simulations consist of five nested grids, covering the entire European continental shelf. This low-frequency energy is not present in the current model, since a JONSWAP spectrum was applied at the more nearshore boundaries of the present model domain. Furthermore, the spectra from the database show high-frequency energy generated by the wind at a broader range of directions than the present model. This is a result of more offshore wind generation, for which the present model is too local as well. Nevertheless, the model can be considered quite representative of the actual area of interest.

4

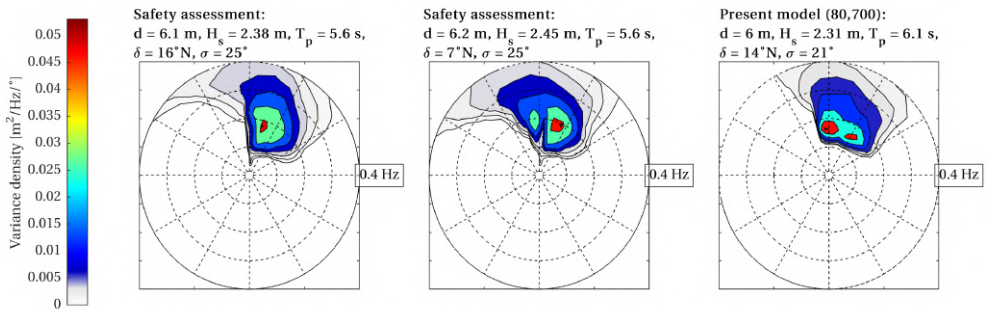


Figure 4.14: 2D variance density spectra ($\text{m}^2/\text{Hz}/^\circ$) from Dutch dike safety assessment WBI database at the Twin Dikes (TD) overtopping measurement location in the area of interest (left panel), at a location several hundred metres to the southeast of TD (middle panel), and from the present SWAN model using the WBI settings (right panel). Water depth d [m], significant wave height H_s [m], wave peak period T_p [s], wave direction δ [$^\circ\text{N}$] and directional spreading σ [$^\circ$] given as well.

The wave propagation effects in the model can be estimated, based on the refraction and diffraction effects observed in the previous sections. Figure 4.15 shows the expected wave ray behaviour during design conditions, based on REFRAC. The mean wave direction and 30° directional spreading are represented by wave rays coming from 330°N , 315°N and 345°N . Waves with more northerly directions, which are more or less aligned with the normal to the depth contours, propagate relatively unaltered onto the two shallow flats, only slightly refracting (wave rays 2 and 6 in Figure 4.15). These waves become approximately alongshore-directed at the dike, with an angle of incidence close to 90° . Waves with more northerly directions that enter the channel, propagate relatively unaltered in the channel (wave ray 5). Waves on the channel slopes refract out of the channel, due to wave defocusing (wave ray 4), also see the right panel of Figure 4.2. These waves increase the wave height on the shallow flat and are onshore-directed at the dike. Waves

with more westerly directions that enter the channel, refract out of the channel and onto the eastern shallow flat, becoming westerly-directed (wave ray 3). Waves with more northerly directions, which refract onto the slope in front of the dike, might (partially) reflect off the channel slope, becoming more easterly-directed (wave ray 1). These waves are (partially) trapped, since their angle of incidence is larger than the critical angle. These waves become onshore-directed at the dike. Furthermore, wave diffraction and sheltering effects will occur, due to the dike (the Eemshaven and land mass of the province of Groningen). Since these effects are not modelled by REFRACT, they are not included in Figure 4.15. Hence, the wave field at the toe of the dike is potentially highly complex, and characterised by an alongshore-directed component, an easterly component caused by waves refracting out of the channel, and an easterly component caused by waves reflecting off the channel slope.

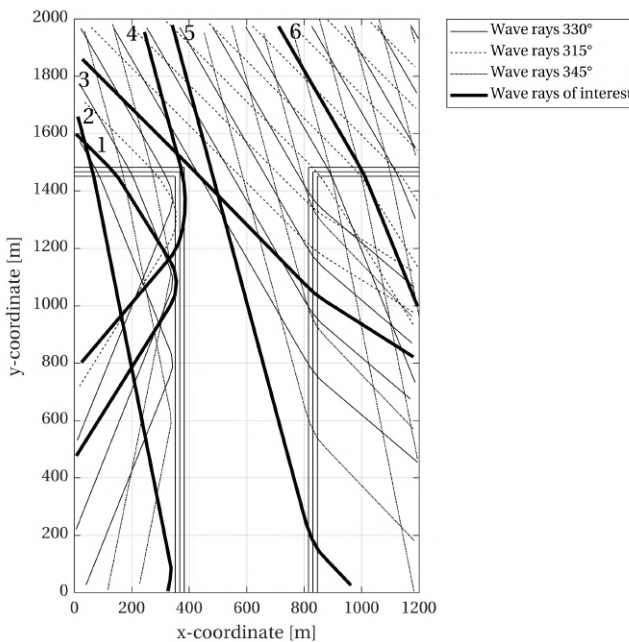


Figure 4.15: REFRACT wave rays for the detailed model. The mean wave direction and 30° directional spreading are represented by wave rays from 330°N, 315°N and 345°N. Several wave propagation effects occur: Relatively unaltered propagation onto shallow flats (2 and 6), relatively unaltered propagation into channel (5), wave defocusing on channel slopes (4), refraction out of channel (3), and wave reflection off the channel slope or wave trapping (1).

4.7.2. MODEL RESULTS

The left panel of Figure 4.16 presents a snapshot of the SWASH steady-state surface elevation, with the depth contours (solid lines) and four areas of interest (dashed rectangles) indicated. The right panel gives the H_{rel} and δ values along three transects. Figure 4.17 gives the spectra at several locations. Refer to <https://youtu.be/SmzK1IpnDXs> for a short animation of the SWASH simulation. The SWASH results show that the estimated

behaviour based on REFRAC describes what happens in the area quite well, with the addition of wave sheltering and diffraction. With these SWASH results, the causes of the apparent turning of the waves around the corner at the Eemshaven can be determined (research question 1).

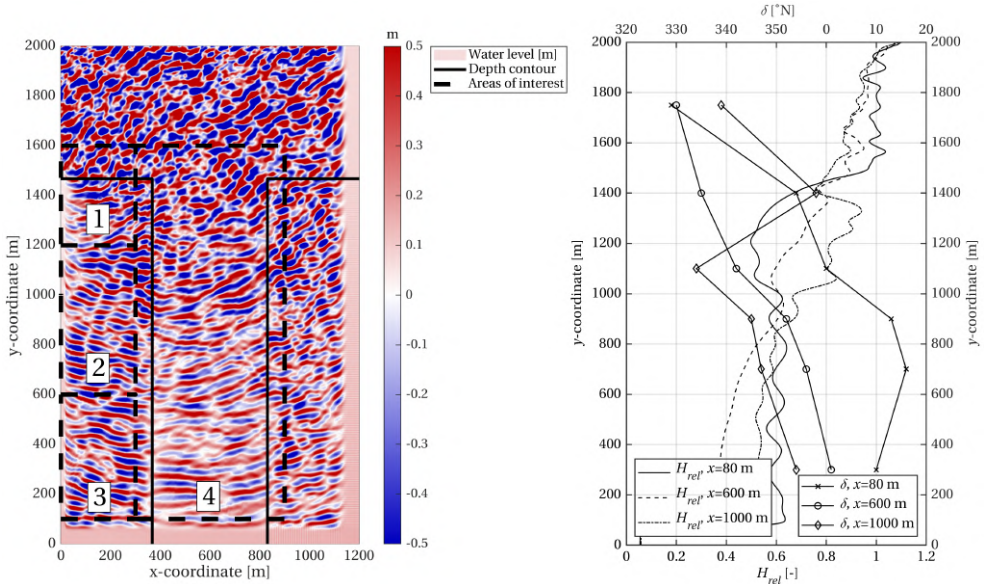


Figure 4.16: Left: SWASH snapshot of steady-state surface elevation and four areas of interest. Directional narrowing and reduction of wave energy, due to wave sheltering, diffraction, depth-induced breaking and refraction from the deep channel to the shallow flat (1). Directional narrowing and slight increase of wave energy, due to wave sheltering, wave (de)focusing and wave reflection or trapping (2). Reduction in wave sheltering, diffraction and wave (de)focusing (3). Directional narrowing and reduction in wave energy, due to wave (de)focusing (4). Right: Relative wave height H_{rel} [-] and mean wave direction δ [°N] along three y -transsects at $x = 80$ m, $x = 600$ m and $x = 1000$ m.

Several processes occur in area 1, see the first two panels of Figure 4.17. The dike causes wave sheltering, which prevents waves with more westerly directions to reach the shadow zone behind the dike. This reduces the directional spreading (width of the spectra) and wave heights more and more, further into the shadow zone. As a result, the mean wave direction turns towards the north. Diffraction plays a role around the corner, which yields a more northerly mean wave direction as well, in agreement with sub-section 4.6.2. Depth-induced breaking and refraction on the channel slope at $y = 1500$ m reduce the wave height and also turn the waves towards the north. The bi-spectra (not shown) show that the triads mainly transfer energy from $2^*f_p = 0.33$ Hz to f_p in the deeper channel (80,1750). On the shallow flat (80,1400) the main transfer is the opposite. Further into the shadow zone (onto the shallow flat), the strength of the triad interactions reduces and a balance occurs between both transfers. The overall result in area 1 is a reduction of the directional width, a reduction in wave height and a more northerly mean wave direction in the shadow zone of the dike.

Wave sheltering further reduces the wave height and directional width of the spectra

in area 2, see the third panel of Figure 4.17. Furthermore, wave (de)focusing and (partial) wave reflection (trapping) occur. Waves that refract out of the secondary channel (wave defocusing) increase the wave height on the shallow flat. Waves that travel on the shallow flat with angles larger than the critical angle, reflect off the channel slope and propagate back towards the dike (wave trapping). These processes allow energy at angles larger than 30°N at frequencies up until f_p to appear. Energy at f_p at angles larger than approximately 48°N has to be the result of wave (de)focusing. This energy cannot be caused by wave trapping on the shallow flat, as the critical angle at the peak frequency is approximately 318°N . Energy at angles larger than 48°N , but at frequencies lower than f_p , can be caused by either process, as these longer waves become trapped at smaller angles of incidence. Easterly energy at angles smaller than 48°N at f_p could have been caused by either process as well. Both wave (de)focusing and trapping turn the mean wave direction more towards the east, and increase the wave height in the southern part of area 2 again (at 80,700, fourth panel of Figure 4.17). Diffraction seems to have a minor influence in this area. The overall result in area 2 is an increase in easterly energy, causing directionally multi-peaked spectra with a significant amount of easterly energy.

The effects of wave sheltering and diffraction become less noticeable in area 3, since this area is located far into the shadow zone of the dike. See the fifth panel of Figure 4.17. Wave defocusing gradually makes the wave field more long-crested, further down-wave in the channel (see area 4 in Figure 4.16). Therefore, the wave (de)focusing effect itself gradually reduces further into the channel as well, somewhat reducing the easterly energy in area 3. Wave trapping effects are still visible in area 3, where waves with (almost) northerly directions reflect off the channel slope and reach the dike. The overall result in area 3 is a directionally single-peaked spectrum, with a more northerly mean wave direction compared to area 2.

A directional filtering effect occurs in area 4, inside the channel (sixth panel of Figure 4.17). A reduction in short-crestedness and wave energy occurs, due to wave defocusing. This produces more long-crested waves, and reduces the directional width and wave height in the channel. On the shallow flat, the wave (de)focusing causes an increase in the wave height, see area 2.

The number of spectral peaks seems to depend on the area in the domain and the processes playing a role in this area. More specifically, the directional multi-peakedness seems to be related to the distance to the deeper channel, as SWASH gives directionally multi-peaked spectra at locations close to the channel slope ($x = 300$ m). The single-peaked SWASH spectra at (80,700) and (80,300) are similar to the WBI spectrum at TD (first panel of Figure 4.14). The multi-peaked SWASH spectra at (80,1100) and (300,700) (not shown) are similar to the WBI spectrum at the more south-easterly location (second panel of Figure 4.14), a location where the shallow flat is narrower and thus closer to the channel. The SWASH spectra do not contain the high-frequency tail in the wind direction of the WBI spectra, since SWASH does not account for the wind growth. SWASH shows that the mean wave direction becomes onshore-directed at the dike, with δ between 355°N in the northern and 15°N in the southern part of the domain, see the right panel of Figure 4.16. This is a directional turning of 25° to 45° compared to the offshore wave and wind direction. $H_{rel} = 0.5 - 0.6$ at the dike, which corresponds to $H_s = 1.3$ m - 1.6 m, as the offshore $H_s = 2.6$ m within the SWASH model.

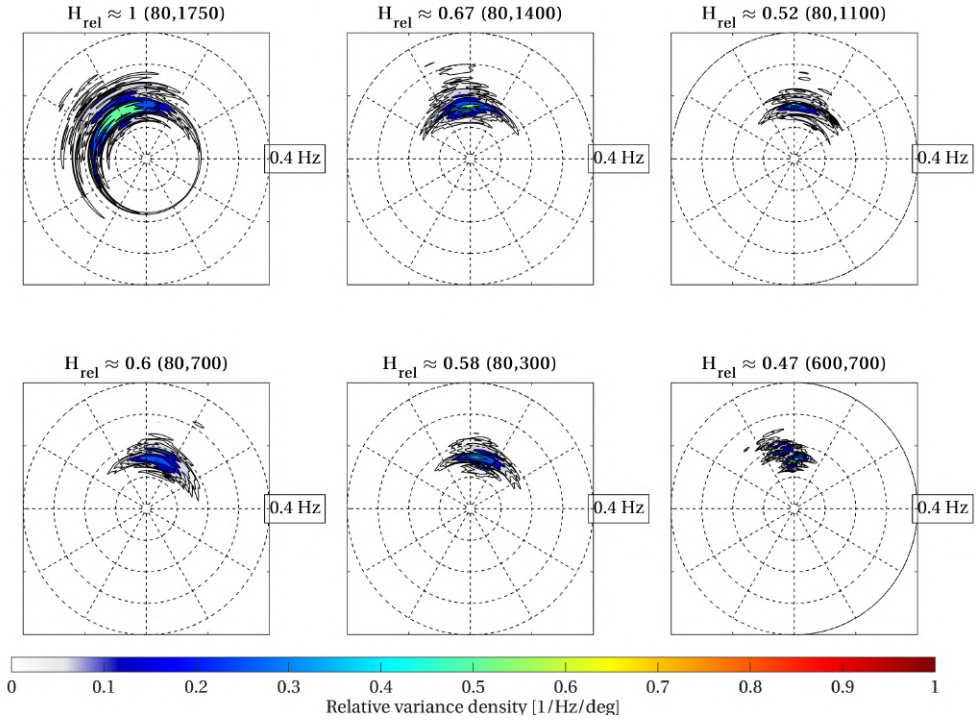


Figure 4.17: SWASH 2D spectra at several locations. Variance density normalised and colour-scaled with the maximum variance density at the offshore (80,1750) location.

Figure 4.18 gives the results of SWAN with the recommended settings, without wind imposed on the model. SWAN performs reasonably well, the largest deviation in H_{rel} being of the order of $\pm 20\%$. The source terms with the largest influence are depth-induced breaking and triads, which act mainly on the channel slopes and shallow flat.

The reduction in wave energy and directional width, and turning of the mean wave direction to the north in area 1 (second panel of Figure 4.18), due to wave sheltering, refraction and depth-induced breaking, is predicted quite well by SWAN. However, the spectrum is directionally narrower than according to SWASH, due to the omission of diffraction and non-collinear triad interactions. The CCA LTA with $\alpha = 0.05$ overestimates the transfer to the super-harmonic and does not account for recurrence. This is in agreement with what was found in sub-section 4.6.1.

Wave sheltering reduces the directional width of the spectra and wave heights even more in area 2, see the third and fourth panel of Figure 4.18, as was found with SWASH. The energy at the super-harmonic is overestimated by the LTA. Nevertheless, the energy at angles larger than $30^\circ N$ and mean wave direction are predicted quite well. This would indicate that both the wave (de)focusing and wave trapping are represented quite well by SWAN. It is difficult to separate both processes, but an estimate can be given based on the results of sub-sub-section 4.5.1, sub-section 4.6.1, the sixth panel of Figure 4.18 and Groeneweg et al. (2015). In sub-sub-section 4.5.1, it was found that SWAN predicts re-

fraction from deeper towards shallower water quite well. However, the sixth panel of Figure 4.18 shows that the wave height in the channel (in area 4) is overestimated compared to SWASH, due to the overestimation of the transfer to the super-harmonic by the LTA. These higher frequencies are affected less by refraction, yielding less wave (de)focusing. Added to this, sub-section 4.6.1 and Groeneweg et al. (2015) found that SWAN overestimates the trapping of wave energy on the shallow flat for angles of incidence above the critical angle, due to the omission of 2D triad interactions and diffraction, which directionally broaden the spectrum. Hence, it is expected that SWAN underestimates the wave (de)focusing and overestimates the wave trapping. The combined effect is an overestimation of H_{rel} at (80,1100) and a slight underestimation at (80,700). Contrary to SWASH, the different spectral peaks remain distinguishable at (80,700). This behaviour persists in area 3 (80,300), see the fifth panel of Figure 4.18. This indicates that the 'merging' of the peaks in SWASH may be related to diffraction or non-collinear triad interactions. Furthermore, this may be related to the more long-crested wave field in the southern part of the domain, for which section 4.5 showed that SWAN performs less well.

Similar results are obtained when wind is imposed on the SWAN model (bottom two rows of Figure 4.18). The spectral shape around f_p is very similar to the case without wind imposed, as are the mean wave directions. Differences mainly occur for the higher frequencies, where energy is added by the wind in a broad range of directions. With wind imposed on the model, the peak at the super-harmonic due to the LTA becomes less pronounced, but the total amount of energy in the high-frequency tail is larger. Therefore, larger H_{rel} values are found as well.

Hence, SWAN performs reasonably well for this more complex and realistic case. SWAN predicts that the mean wave direction eventually becomes onshore at the dike, with δ between 350°N in the northern part of the domain and 20°N in the southern part of the domain. These mean wave directions agree quite well with SWASH, with differences of at most 5° . Furthermore, $H_{rel} = 0.5 - 0.6$ along the dike, as was found with SWASH. This corresponds to $H_s = 1.5 \text{ m} - 1.8 \text{ m}$, with an offshore $H_s = 3 \text{ m}$ within the SWAN model. Still, some limitations of SWAN arise with this complex case. These limitations are related to the omission of diffraction and non-collinear triad wave-wave interactions, the overestimation of the transfer to the super-harmonic by the LTA, as well as the overall worse performance of SWAN for more narrow-spread seas. The result is an underestimation of the wave (de)focusing and an overestimation of the wave trapping, which produce overestimations of the wave height at some locations and underestimations at others, of up to order $\pm 20\%$ in H_{rel} . Furthermore, SWAN predicts that directionally multi-peaked spectra persist at the dike, whereas SWASH predicts that the spectra become more single-peaked at larger distances from the channel and further down-wave in the domain.

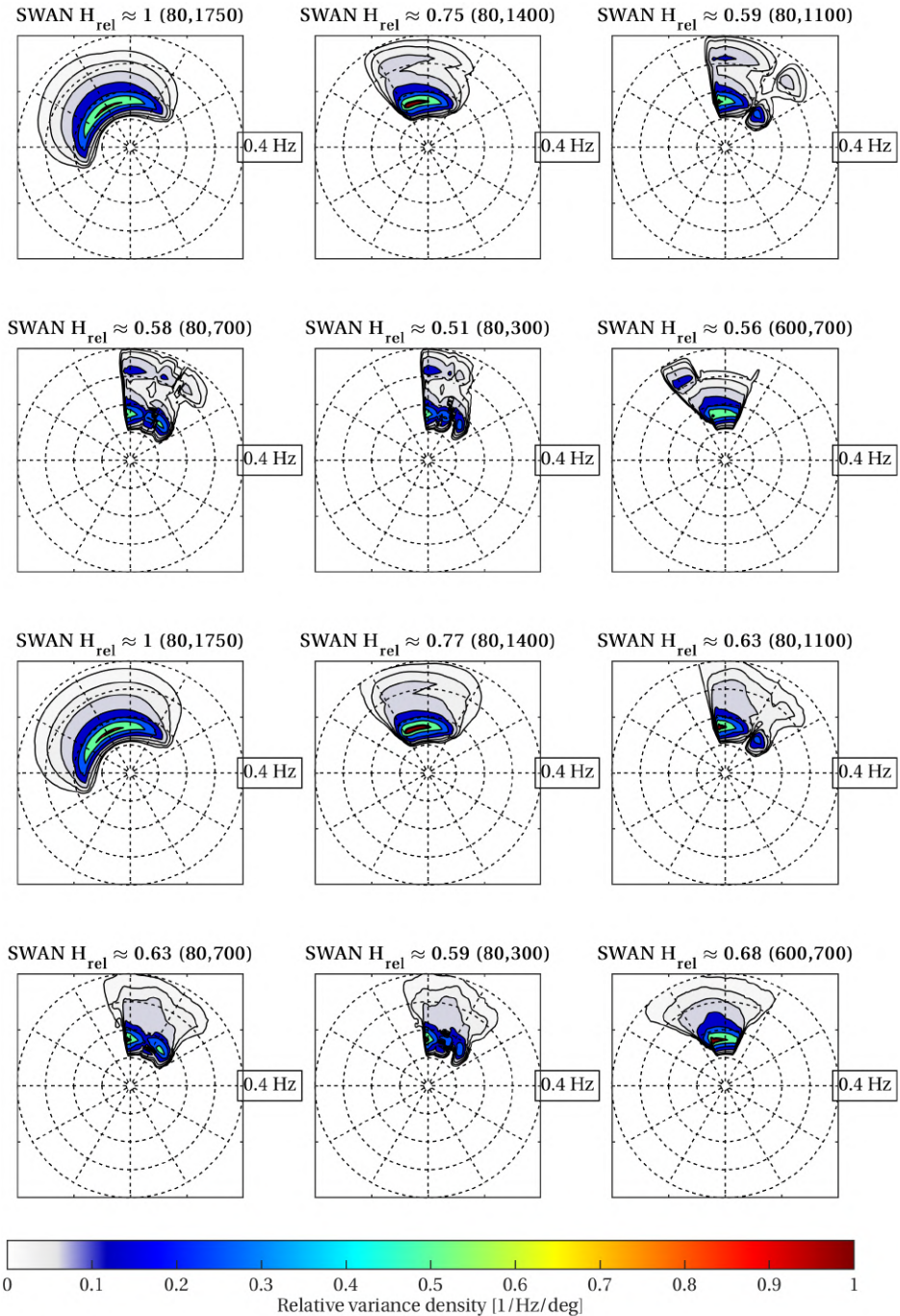


Figure 4.18: 2D SWAN spectra at several locations. First two rows: SWAN with recommended settings, without wind imposed. Bottom two rows: SWAN with recommended settings, with wind. Variance density normalised and colour-scaled with the maximum variance density at the offshore (80,1750) location.

SWAN SENSITIVITY ANALYSES

The sensitivity analysis compares the performance of different versions of the SWAN third generation physics (recommended settings versus WBI settings) and SWAN without and with diffraction approximation (using the recommended settings). Wind was imposed on the model for all cases.

The WBI settings produce less smooth wave height patterns and less detailed 2D spectra, due to the smaller number of directional bins. See the first two rows of Figure 4.19. The depth-induced breaking formulations of [Van der Westhuysen \(2010\)](#) and [Battjes and Janssen \(1978\)](#) give approximately the same results for the present case. The OCA LTA with $\alpha = 0.1$ transfers somewhat less energy to the super-harmonic, which gives slightly better results than the CCA LTA with $\alpha = 0.05$ for this case. The different equation and numerical scheme used to determine the directional turning rate c_θ do not influence the results much, as the grid resolution is high.

Without the refraction limiter of [Van Vledder and Koop \(2009\)](#), SWAN with the WBI settings overestimates the wave heights at the dike, whereas the wave heights in the channel are underestimated (not shown). Too much wave energy refracts out of the channel due to defocusing, likely a result of the smaller number of directional bins as well. The refraction limiter turns off the refraction for frequencies lower than 0.2 Hz, which reduces the wave (de)focusing, but also reduces the wave trapping. This improves the wave heights at the dike, but comes at the cost of a worse representation of the physics. Therefore, it seems preferable to increase the number of directional bins first, before the refraction limiter is chosen as a mitigation measure.

Another difference between the recommended settings and WBI settings is related to the wind growth. The [Wu \(1982\)](#) wind drag formulation adds much more energy to the higher frequencies and in a broader range of directions than the relation of [Zijlema et al. \(2012\)](#). As described in sub-section 4.6.1, it cannot be determined which related yields better results based on the present simulations and further research is necessary.

The bottom two rows of Figure 4.19 present the results of SWAN with the recommended settings, diffraction approximation and 20 m grid cells. The diffraction approximation itself only minimally influences the results. The differences that occur, are mainly a result of the lower grid resolution, which produces less smooth wave height patterns and less detailed spectra. Furthermore, the directional turning is estimated less accurately. This causes an overestimation of the wave (de)focusing, see Table 4.1. The reflection off the channel slope is underestimated. The combined influence on the wave height is small, as the influence of the first process counteracts the influence of the second process, but the representation of the physics is worse than for a higher grid resolution. Hence, the value for the depth difference per grid cell Δd does not influence the results as much as for the cases with narrow-spread seas (see section 4.5), but more than for the cases with broad-spread seas (section 4.6). Therefore, the grid resolution should still be sufficient and $\Delta d \leq 5$ m is recommended. In agreement with the previous sections, application of the diffraction approximation does not improve the results and is unstable for finer grid resolutions.

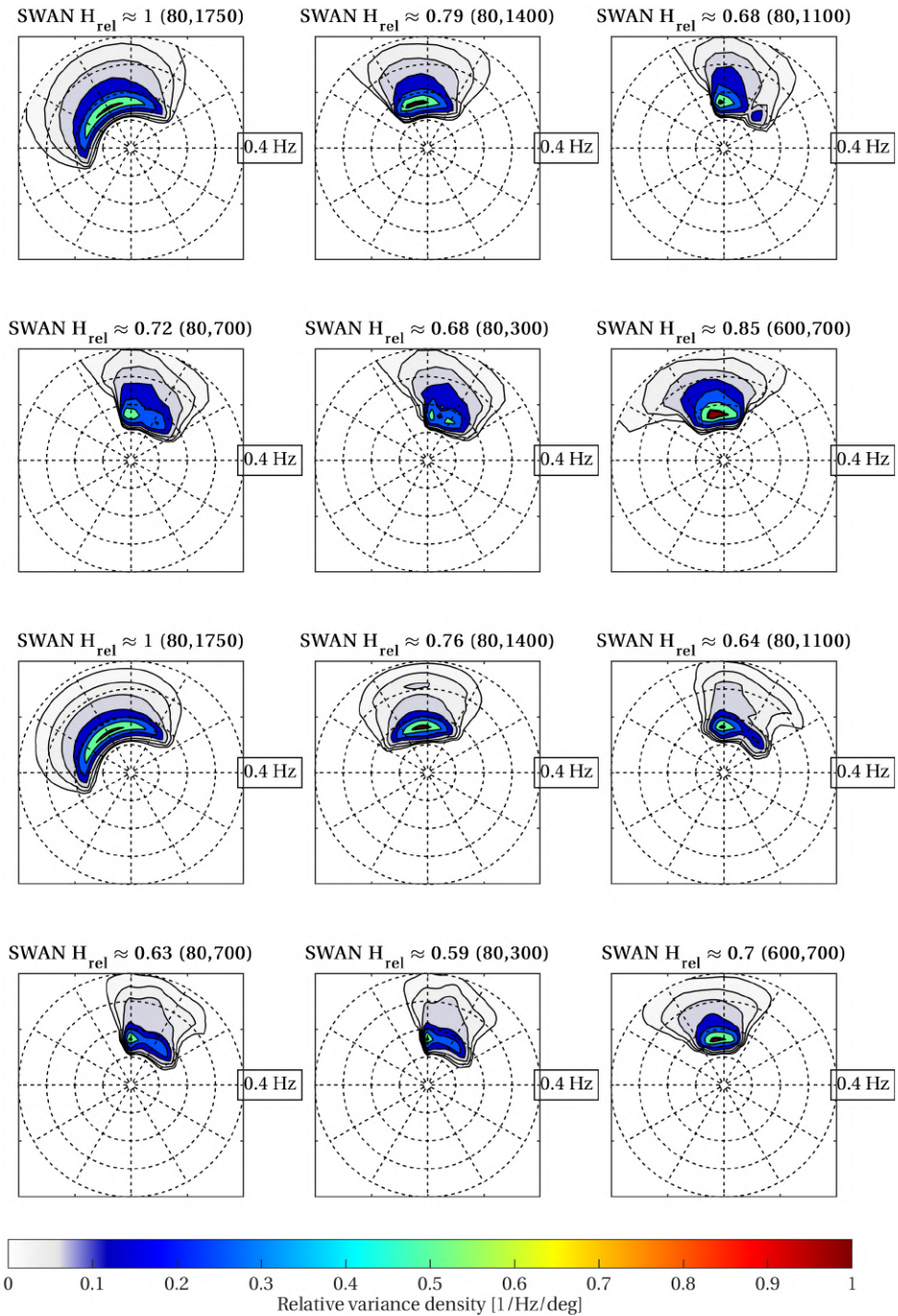


Figure 4.19: 2D SWAN spectra at several locations. First two rows: SWAN with WBI settings, with wind imposed. Bottom two rows: SWAN with recommended settings, diffraction approximation, 20 m grid cells and with wind. Variance density normalised and colour-scaled with the maximum variance density at the offshore (80,1750) location.

4.7.3. DISCUSSION AND IMPLICATIONS FOR DUTCH DIKE SAFETY ASSESSMENT

Research questions 2a and 2b can now be answered and the implications for the Dutch dike safety assessment WBI determined. SWASH predicts that the waves become predominantly onshore-directed at the dike, with mean wave directions $\delta = 355^\circ\text{N} - 15^\circ\text{N}$, a directional turning of 25° to 45° compared to the wind direction. SWAN predicts the mean wave direction at the dike quite well (deviations $<5^\circ$), and the onshore-directed waves as found within the Dutch dike safety assessment can thus be considered reliable.

SWAN also predicts the relative wave heights quite well. An estimate of the influence of the wind can be obtained by subtracting the wave heights from the simulations without wind imposed from the ones with wind. This effect is 0.2 m - 0.3 m for the recommended settings with the Zijlema et al. (2012) drag relation, but 0.5 m - 0.75 m for the WBI settings with the relation of Wu (1982). As a result, $H_s = 1.75\text{ m} - 1.95\text{ m}$ with the recommended settings, and $H_s = 2.15\text{ m} - 2.3\text{ m}$ with the WBI settings. The values with the WBI settings agree with the values obtained from the WBI database, see Figure 4.14. Hence, whether the wave heights as predicted by the Dutch dike safety assessment are correct, depends in a large part on the accuracy of the wind drag relation of Wu (1982). The relation of Zijlema et al. (2012) gives smaller values for the drag coefficient, but which relation is more accurate cannot be determined based on the present results and further research is recommended.

Only a wave and wind direction of 330°N were considered for the detailed model thus far. The WBI database gives $H_s = 1.5\text{ m}$ and 1.6 m , $T_p = 4.1\text{ s}$ and 4.6 s , $\delta = 2^\circ\text{N}$ and 351°N at the two locations of Figure 4.14, for a wind direction of 300°N . Hence, these wave heights are much lower and the mean wave directions more northerly than for a wind direction of 330°N . The same occurs with the present model, where wave heights at the dike are 0.4 m - 0.8 m lower with SWASH, 0.4 m - 0.6 m lower with SWAN with the recommended settings and 0.4 m - 0.8 m lower with SWAN with the WBI settings, for a wind and wave direction of 300°N . These smaller wave heights can be explained with REFRAC, similarly as was done for 330°N in Figure 4.15. With a more westerly wind and wave direction, the influence of both the trapping of wave energy on the shallow flat and wave (de)focusing will be much smaller, and the effect of wave sheltering will increase. Hence, a wind direction of 330°N seems to be most relevant for the dike in the estuary during design conditions.

An aspect that is not considered in the Dutch dike safety assessment, is the amount of energy that is offshore-directed at the dike. This energy does not contribute to the loads on the dike. In the present model, up to 25% of the energy is offshore-directed at the dike for a wind and wave direction of 330°N . In the WBI database results at the Twin Dikes, this is only 2%. This is caused by the dike orientation at TD. The orientation of the dike normal is 45°N at TD, whereas it is 90°N in the present model. Therefore, results were taken from the WBI database at locations in the estuary that have a more north-south orientation as well. There, 3% to 11% of the energy is offshore-directed. For a wind direction of 300°N , 10% of the energy is offshore-directed at TD, 12% - 28% at more north-south oriented locations in the estuary, and up to 28% in the present model. With $H_s = 2\text{ m}$, 10% of the energy is 0.2 m, but 25% is already 0.5 m. Hence, a significant amount of the energy predicted by SWAN may not actually contribute to the loads on the dike, and the omission of this aspect in WBI may have a large impact on the calculated required crest levels of the dikes in the estuary.

4.8. CONCLUSIONS

This chapter provided more insight into the wave propagation processes that play a role in the Eems-Dollard estuary in the north of the Netherlands, which characterise the extreme wave loads on the dike in the estuary. The focus mainly was on nearshore wave propagation effects, like refraction and diffraction. Simulations with the numerical wave models REFRAC, SWAN and SWASH were performed to determine what the cause of the apparent turning of the waves around the corner at the Eemshaven is, which processes play a role in the area, and how well SWAN performs in this highly complex estuary.

SWAN performed well for the refraction of narrow-spread waves travelling from deeper towards shallower water, if the grid resolution was sufficient. The same holds for the refraction of waves that travel from shallower to deeper water, below the critical angle according to Snell's law. Close to and above the critical angle, large differences occurred between SWAN and SWASH, especially for regular waves. SWAN overestimated the energy in the channel just below the critical angle and underestimated it above the critical angle. The main cause is not the omission of evanescent waves or wave tunnelling (as described in [Dusseljee et al., 2014](#); [Magne et al., 2007](#)), but diffraction and non-collinear triad wave-wave interactions (as described in [Groeneweg et al., 2015](#); [Guzman Mardones, 2011](#); [Liu, 2009](#)). Furthermore, SWAN did not perform well for the diffraction of narrow-spread seas, as the model was not developed for such conditions.

SWAN performed well for the refraction and diffraction of broad-spread waves, as was found by e.g. [Dusseljee et al. \(2014\)](#); [Groeneweg et al. \(2015\)](#) as well. The improved performance compared to cases with narrow-spread seas, mainly arose from the larger influence of the directional spreading and reduced influence of the directional turning, diffraction and triad interactions. Nevertheless, SWAN still produced spectra that were directionally narrower than SWASH, due to the omission of diffraction and non-collinear triad interactions in SWAN.

Simulations with a more realistic model based on the area of interest showed that a variety of processes play a role in this highly complex estuary and influence the wave conditions at the dike. The main processes are wave sheltering, refraction, wave (de)focusing, wave trapping, triad interactions, diffraction, depth-induced breaking and wave growth by the wind. These processes create a complex wave field and cause complex and sometimes directionally multi-peaked spectra at the dike.

SWAN performed reasonably well for the more complex and realistic case, predicting the bulk wave parameters quite well. Still, some limitations of SWAN were identified, related to the omission of diffraction and non-collinear triad wave-wave interactions, the overestimation of the transfer to the super-harmonic by the LTA, as well as the overall worse performance of SWAN for more narrow-spread seas. As a result, SWAN underestimated the wave (de)focusing, overestimated the wave trapping and predicted directionally multi-peaked spectra, even at larger distances from the channel.

The models predict that the waves indeed turn around the corner at the Eemshaven and become onshore-directed at the dike to the north of Delfzijl during design conditions. With the used bathymetry, the mean wave directions became $\delta = 355^\circ\text{N} - 15^\circ\text{N}$ at the dike (angles of incidence $\beta = 75^\circ - 95^\circ$ with the present model), a directional turning of 25° to 45° compared to the wind direction.

Whether the wave heights as predicted by the Dutch dike safety assessment are correct,

depends in a large part on the accuracy of the wind drag relation of [Wu \(1982\)](#). The relation of [Zijlema et al. \(2012\)](#) gives smaller values for the drag coefficient and therefore less wind growth and wave heights that are 0.4 m lower during design conditions. Which relation is more accurate cannot be determined based on the present results and further research is recommended.

An aspect that is not considered in the Dutch dike safety assessment, is the amount of energy that is offshore-directed at the dike. 2% - 28% of the wave energy was found to be offshore-directed at the dike, indicating that a significant amount of the energy may not actually contribute to the loads on the dike. This may have a large impact on the calculated required crest levels of the dikes in the estuary.

A wind direction of 330°N seems to be most relevant for the extreme loads on the dike in the estuary, as it was found that a direction of 300°N gave wave heights that were 0.4 m - 0.8 m lower than for 330°N. This was mainly caused by a reduction of wave trapping and wave (de)focusing and an increase of the effect of wave sheltering for more westerly directions.

The here determined recommended SWAN settings and the Dutch dike safety assessment (WBI) settings generally performed best for the present cases (see appendix D for an overview). Regarding the numerics, the recommended settings seem to be an improvement over the WBI settings. Regarding the physics, further validation with measurements in the area is necessary, to determine which version of the settings performs better.

The performance of SWAN related to the directional turning depends on the depth difference per grid cell Δd , as well as the used directional turning equation, numerical scheme used for this equation and number of directional bins. For narrow-spread waves travelling from deeper towards shallower water, $\Delta d \leq 5$ m is recommended, for waves travelling from shallower towards deeper water, $\Delta d \leq 1$ m is recommended. For the refraction of broad-spread seas, the value of Δd seems to be less relevant. Nevertheless, $\Delta d \leq 5$ m is recommended based on the simulations with the more detailed model. Furthermore, the turning rate equation based on the wave numbers (Equation B.9) and central differences are recommended for the discretisation. Turning off the rescaling of negative action density may improve the estimation of the directional turning, but may produce negative energy in the spectra. The default SORDUP numerical scheme for the wave propagation is recommended, as it gives less numerical diffusion than the BSBT scheme. A high directional resolution is especially relevant for narrow-spread seas, but a resolution of 1° also outperformed 10° for broad-spread seas. The refraction limiter of [Van Vledder and Koop \(2009\)](#) seems to improve the prediction of the wave heights at the dike, but comes at the cost of a worse representation of the physics. Therefore, it seems preferable to increase the number of directional bins first, before the refraction limiter is chosen as a mitigation measure.

The depth-induced breaking formulations of [Van der Westhuysen \(2010\)](#) and [Battjes and Janssen \(1978\)](#) gave approximately the same results for the present cases and were not studied in detail. The CCA LTA with $\alpha = 0.05$ and OCA LTA with $\alpha = 0.1$ performed roughly equal, but the first is recommended, as the CCA remains bounded in the unidirectional asymptote. Both the OCA and CCA LTA performed better with smaller α values, but still tended to overestimate the transfer to the super-harmonic. α should ideally be calibrated for each individual case. Application of the diffraction approximation can improve the

results in certain cases, but the approximation is unreliable, unstable and has a grid cell size limitation, so it is currently not recommended to enable the approximation.

The main weaknesses of SWAN still lie in the omission of diffraction, collinear triad interactions other than to the super-harmonic, and non-collinear triad interactions. Implementation of more advanced triad formulations (e.g. Becq et al., 1998; Booij et al., 2009; Eldeberky, 1996; P. A. E. M. Janssen, 2009; Toledo & Agnon, 2012; Van der Westhuysen, 2007) or better representations for the evolution of the bi-spectrum (e.g. T. T. Janssen, 2006; Smit & Janssen, 2016; Vrecica & Toledo, 2016, 2019) may significantly improve the results, but come at an increased computational cost.

The field measurement campaign in the estuary will run for nine years still. To further validate these results, model simulations using the actual bathymetry of the Eems-Dollard estuary should be compared to future buoy measurements and preferably X-band radar measurements, during storms in the area.

ACKNOWLEDGEMENTS

This study was made possible by the inspiring input of the late Gerbrant van Vledder. This chapter was immensely improved by his knowledge, dedication and guidance. This study was supported by Waterschap Noorderzijlvest and the Hoogwaterbeschermingsprogramma.

II

MEASURING WAVE RUN-UP AND OVERTOPPING ON DIKES

5

CALIBRATION AND PREPARATION OF FIELD MEASUREMENTS WITH LASER SCANNERS. PART I: WAVE RUN-UP AND OVERTOPPING

Somewhere, something incredible is waiting to be known.

Carl Sagan

Wave overtopping is commonly measured with overtopping tanks. This chapter develops an alternative system using two laser scanners. It measures wave run-up heights, as well as run-up depths and front velocities, both during normally and obliquely incident waves on a dike in the field. The chapter considers the first field validation tests with the system, with normal and oblique waves generated by the wave run-up simulator on a grass dike slope. The main focus of this chapter lies on the tests with normally incident waves. The run-up is determined from the measured distance and reflection, and agrees well with the observed run-up. Run-up depths and front velocities are determined reliably with the laser scanners. The (virtual) wave overtopping discharge can be calculated as well, which agrees well with the most commonly used overtopping equations.

This chapter has been published as **Oosterlo, P.**, Hofland, B., Van der Meer, J. W., Overduin, M., Steendam, G. J., Nieuwenhuis, J. W., Van Vledder, G. Ph., Steetzel, H., & Reneerkens, M. (2019). Measuring (Oblique) Wave Run-Up and Overtopping with Laser Scanners. In *Proc. Coastal Structures* (pp. 442–452). Hannover, Germany: Bundesanstalt für Wasserbau. Different error metrics were used here, to make the chapter consistent with the rest of the dissertation, and some minor textual changes were made with respect to the paper.

5.1. INTRODUCTION

The Eems-Dollard estuary in the north of the Netherlands is a highly complex estuary with deep channels and tidal flats, which is part of the Wadden Sea. A particular aspect for this area is that the dike design conditions consist of very obliquely incident waves, up to 80° relative to the dike normal. Since the reliability of the models as used for the Dutch dike safety assessment is unknown for such conditions, an extensive 12-year long field measurement project is performed in this estuary. The measurements started in 2018, measuring wind, water levels, currents, waves and wave run-up and overtopping.

In the project, wave overtopping is measured with four innovative wave overtopping tanks built into two dikes. This is a robust method to measure wave overtopping, but fixed in one place.

An alternative and possibly more flexible solution than a fixed overtopping box is being developed using two terrestrial laser scanners (LIDARs) to measure wave run-up heights, depths and front velocities at a dike in field situations with oblique wave attack. The virtual wave overtopping can be calculated from these measurements at any virtual crest level. The present chapter describes the design, set-up and processing, analysis and validation with physically simulated normally and obliquely incident waves on an actual grass dike slope. The next section presents the approach and system set-up, as well as the validation tests set-up. After that, the post-processing and analysis methods are described. The following section validates the measured parameters. The next section gives an outlook on the next steps in this study. The final section presents the conclusions and recommendations. If the validation is positive, the system will be placed on a dike for 3 years to measure wave run-up and to calculate the overtopping for severe winter storms, additional to the measurements with overtopping tanks.¹

5.2. APPROACH AND SYSTEM SET-UP

Laser scanners are often used for terrestrial measurements, but have been used to measure the water surface or waves as well (Allis, Peirson, & Banner, 2011; Blenkinsopp, Mole, Turner, & Peirson, 2010; Streicher, Hofland, & Lindenbergh, 2013), and were used recently to measure wave run-up as well (Hofland et al., 2015; Vousdoukas et al., 2014). The present system uses two SICK LMS511pro HR laser scanners, a commonly used and cheap laser scanner that uses a near-infrared (905 nm) laser beam. The system set-up was based on Hofland et al. (2015), but now with two synchronised laser scanners instead of one, attached to an easily relocatable pole. See Figure 5.1 for the validation set-up at a dike in Friesland, the Netherlands. The laser scanners measure the distance (R) to a surface by measuring the time that the reflection of a laser pulse takes to reach the scanner again. The reflected signal intensity (RSSI) is also measured, which provides information on the type of surface, e.g. wet or dry. The scanners measure the development of the water surface profile in time with 50 Hz and a resolution of 0.333°, providing an accurate temporal profile evolution. The two laser scanners each scan along a line at a certain distance from each other, in this case running from the dike toe to the crest (blue and red lines in right panel of Figure 5.1). The system uses two laser scanners, to measure directional information of the waves efficiently. To this end the scanners are synchronised. The height of the

¹The system was placed on the dike in the Eems-Dollard estuary in October 2019.

laser scanners and the distance between both scanned lines are adjustable.

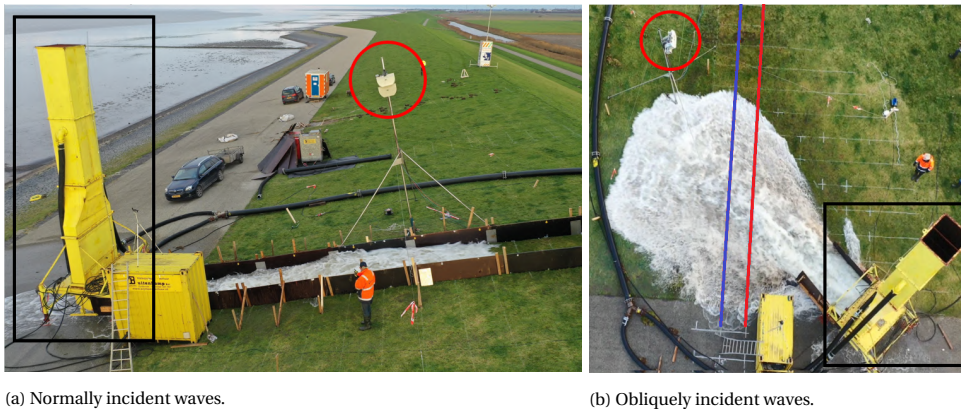


Figure 5.1: Left: Laser scanner system (red circle) and run-up simulator (black rectangle) during tests with normally incident waves. Right: Top view during obliquely incident waves. Scan lines indicated by blue and red lines.

The first system tests were performed with waves generated by the wave run-up simulator (Van der Meer, 2011) on the grass slope of the dike. The laser scanners were placed perpendicular to the local slope at heights of 5.17 m and 5.50 m above the slope. Complicating factors compared to the previous laboratory research on concrete or wooden slopes are, e.g. the convex shape of the dike slope, wave-induced erosion of the grass slope, the blades of grass, which might obfuscate a thin layer of water, as well as water infiltrating into the slope.

Multiple tests were performed for this first system validation. Incident 'waves' (released volumes, hereafter referred to as waves) were simulated with the wave run-up simulator. The simulator is a vertical tank filled with water to a certain level. By quickly opening the bottom of the tank, the tank drains simulating an individual wave running up the slope.

First, tests were performed for normally incident waves (tests 1 to 13), where 7 different waves (volumes) were repeated three times to obtain increased statistical reliability. Hence, in total 21 waves were simulated by using the different filling levels of the wave run-up simulator (1 m to 7 m). With these normally incident waves, the influence of a large range of environmental conditions (e.g. producing artificial wind and rain), as well as laser scanner parameters were tested and calibrated. A test with 100 normally incident random volumes was performed as well, called test 1a. Test 1a was used to assess the performance of the system in e.g. predicting the wave run-up and overtopping. The filling level time series of the simulator were derived from a nearshore significant wave height of 2 m and a peak period of 5.7 s.

After that, the wave run-up simulator was placed under an angle with the dike normal. With this set-up, obliquely incident waves under an angle of 45° were generated and tests were performed to determine the ideal distance between the scanned lines, as well as the ideal distance from the simulator to the scanned lines. Tests 14 to 17 were used, which

contain 3 times 6 waves (filling levels from 2 m to 7 m). Test 17a again consisted of 100 randomly generated waves, to assess the system for oblique run-up and overtopping.

A relation between the filling level of the simulator and the resulting run-up height was determined for the validation, from several visually observed run-up heights at this location. This relation determines the theoretical run-up level for each filling level. Run-up heights and front velocities were determined from videos as well. Run-up depths and velocities near the ground were measured with 'surf boards', floaters that measure the run-up depth, and paddle wheels, impellers that measure the velocities near the ground (see e.g. [Van der Meer et al., 2010](#)).

5.3. DATA PROCESSING

5.3.1. CALIBRATION

Before the start of the tests, the exact laser scanner positions were determined by noting all the system dimensions and determining the exact laser line locations with an alignment bar. This is a bar with several infrared detectors and LEDs, which light up when infrared light is detected. Several scans were made with two wooden beams at known locations on the dike slope, to calibrate the lasers before the actual measurements.

The first step in the data processing converts the raw data files to the format of MATLAB, the software used for the analysis. The relevant data are the scanner serial number, the start angle at which the laser scanner starts measuring, the angular resolution, the time, the measured distance R in polar coordinates of the first, last or all five echoes and the RSSI (Received Signal Strength Indicator) values of the first, last or all five echoes. The laser scanners give the RSSI as a dimensionless value between 0 and 255. After that, the orientation of the lasers was determined and the measured distances in polar coordinates were converted to x - and z -coordinates in metre, see Figure 5.2. Therefore, it was important that the laser scanners were placed perpendicular to the slope and that the local slope angle at the pole location was known accurately, since the slope angle differs along the slope. Using the calibration data with the known locations of the wooden beams, the exact laser scanner locations were determined. The maximum difference between the known x -coordinates of the wooden beams and the x -coordinates of the beams according to the laser scanners was 5 cm, which is the same order of magnitude as the scan resolution and laser footprint. The laser data were corrected for this. Next, the dry slope resulting from the laser scanners was compared to the slope as measured with measurement tape and GPS. Here, the maximum difference in z -coordinate was 5 cm as well, which is highly accurate, because of the convex dike slope and the grass blades.

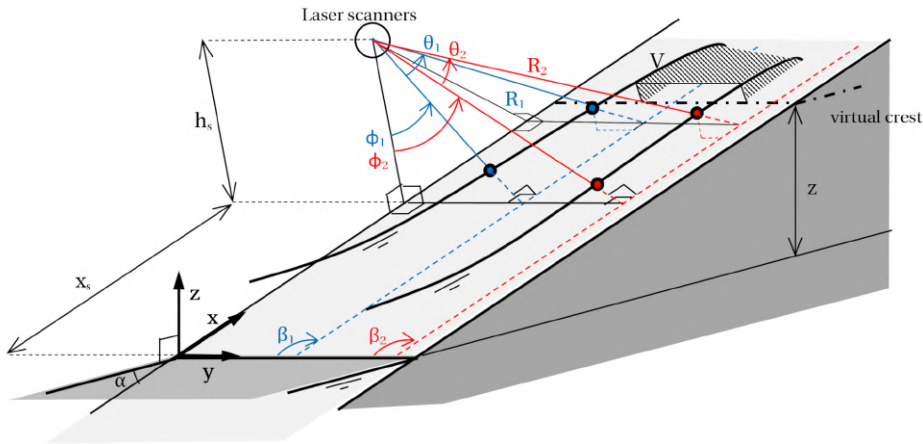


Figure 5.2: Schematised set-up with two laser scanners. Set-up based on Hofland et al. (2015), but with two laser scanners. Scan lines (blue and red dashed lines), scanned points on water surface (blue and red dots) indicated. R [m] is the scanned distance, θ [°] the scan angle, ϕ [°] the slant angle, β [°] a correction in case the scanned line does not run straight along the slope. h_s [m] the laser scanner heights, x_s [m] the x -coordinate of the laser scanners, α [°] the slope angle. V [m³/m] is a virtual overtopping volume.

5.3.2. DATA QUALITY

The data were then further processed. In case all five echoes were recorded, the maximum distance of all echoes was taken, as well as the maximum RSSI value, to filter out e.g. rain or fog, as these give smaller distances and different RSSI-values. If no clear reflection was detected by the scanner, a NaN (Not a Number) was recorded. The percentage of valid measurements at a certain location gives an indication of the measurement quality. The minima of these percentages were high (>99%) for all tests. The data were then filtered in space and time by a five-point median filter, to remove outliers. The percentage of data points that change more than 1 cm or more than 5 cm due to the filtering both indicate the measurement quality. Over all tests the maximum percentage of points that changed more than 1 cm was around 10%, the maximum percentage of points that changed more than 5 cm was in the order of 1%.

Then, the data were interpolated in space, with the constant spacing being the densest laser data spacing, 3 cm in this case. The dry slope was determined for each test separately by taking the first ten seconds of a test, since erosion started to occur directly in front of the wave run-up simulator. Next, the run-up depth was determined by subtracting the dry slope from the measured slope at a certain moment. These data were corrected by removing negative run-up depths, as well as run-up depths larger than 1.5 m, to filter out rain or a person standing in the laser beam. Next, the run-up depth was filtered further by removing large (>0.5 m) local (in 1 time or space step) differences in run-up depth, which were e.g. caused by raindrops. Run-up depths smaller than a certain threshold were removed to remove noise from the signal and prevent the detection of unrealistically high run-up values. This threshold was determined separately for each test and is another indicator of the measurement quality. Finally, if a valid run-up depth >20 cm occurred higher on the slope after more than 40 straight NaN-values, these values were removed as well, as they were

caused by someone or something standing in the laser beam. A similar procedure was followed for the RSSI: a large difference (>100) in one time or space step was removed, and for each test a different threshold value was used to prevent unrealistically high run-ups. Valid values after 40 or more NaNs were removed as well. The run-up could then be determined from the resulting run-up depth and RSSI time series by finding the highest location on the slope where $z_{\text{run-up}} - z_{\text{dry}} > z_{\text{threshold}}$ and $RSSI_{\text{run-up}} - RSSI_{\text{dry}} > RSSI_{\text{threshold}}$.

The root-mean-square error (RMSE) and the from the RMSE derived normalised root-mean-square error and scatter index are used often to evaluate the performance or reliability of some measurement or model. However, [Mentaschi, Besio, Cassola, and Mazzino \(2013\)](#) showed that the RMSE and its variants give smaller values for models affected by negative bias. Hence, these indicators are not always reliable to assess the accuracy of models or measurements. They showed that the HH-indicator as proposed by [Hanna and Heinold \(1985\)](#) provides more reliable information on the accuracy of models or measurements. This HH-indicator is used to assess the laser scanner performance in the present chapter and is defined as:

$$HH = \sqrt{\frac{\sum_{i=1}^N (M_i - O_i)^2}{\sum_{i=1}^N M_i O_i}} \quad (5.1)$$

where M_i is the i th modelled data, O_i is the i th observation and N is the total number of observations. The HH is dimensionless.

5.4. RESULTS AND ANALYSIS OF LASER SCANNER SETTINGS AND ENVIRONMENTAL CONDITIONS

The percentage of valid measurements, the percentage of points that changed more than 1 or 5 cm by the median filters, the chosen run-up depth threshold and RSSI threshold all indicate the measurement quality. They are used here to assess the influence of different environmental conditions and the performance of different laser scanner settings during these different environmental conditions.

The minimum percentage of valid measurements at a certain location was high (larger than 99%) for all tests (thus all different environmental conditions and laser settings). Hence, generally the data can be considered reliable. Of the tests without rain or vibrations, the tests with the first echo, last echo and particle filter seemed to give the best results, as they had the smallest percentages of filtered points, being $<6\%$ for 1 cm change and $<0.4\%$ for 5 cm change. Furthermore, these tests use the lowest run-up depth and RSSI thresholds, of 0.01 m and 5, respectively. This low threshold value of 1 cm shows that the grass blades did not influence the measurements. During the tests it was observed that the grass blades were flattened immediately by the up-rushing waves as well. The fog filter and recording of all echoes also gave decent results, as these settings do not influence the results much during dry weather conditions. However, the tests with a higher frequency and higher resolution gave much worse results, because the higher frequency of 100 Hz comes at the cost of interlacing and a coarser resolution (0.667°). This coarser resolution was not sufficient to capture the run-up peaks accurately. The same holds for the higher resolution (0.167°), which is also achieved by interlacing.

Rain was simulated with two garden sprinklers placed on top of the 'flume' walls, see

Figure 5.3. In general, the rain deteriorated the data quality, resulting in larger percentages of filtered out points and larger threshold values. Drops of water tended to not be visible, nor influence the data, only the strong and continuous beam of water close to the sprinkler was visible in the results. This indicates that normal rain would influence the results only slightly or not at all. Using the first echo led to more detection of rain, as the beam sometimes reflected off a raindrop. Using the last echo or all echoes improved the results, as these later echoes did come from behind the raindrops. Using the particle filter seemed to remove some of the raindrop echoes from the data as well. Using the fog filter during rain led to much worse results, possibly by too strong filtering, and is not recommended. The last echo provides the best results during rain. A combination of the last echo and particle filter or all echoes could be used as well, but the latter will lead to five times larger data files.

Wind-induced vibrations were simulated by manually shaking the guywires, with which the pole was secured, see Figure 5.3. There was still some slack on the lines for this temporary set-up, and they could be secured more tightly when the system is placed for a whole storm season. The translations and rotations of the laser scanners were recorded with an accelerometer, as visible in Figure 5.3. Even with the slacking lines and strong movements of the lines, the resulting displacement of the laser line in any direction was not more than 5 cm and did not significantly influence the data quality or run-up results. With a more permanent placement during a storm season, the lines could be tightened more, and vibrations should be largely eliminated. However, it would still be good to attach the accelerometer, to be able to correlate possible outliers during a storm with potentially occurring vibrations.

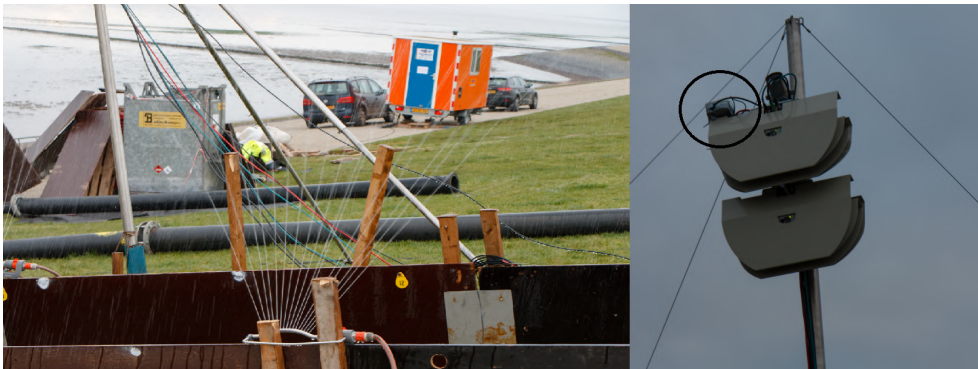


Figure 5.3: Left: Simulation of rain with garden sprinklers. Right: Laser scanners with guywires and accelerometer (circle).

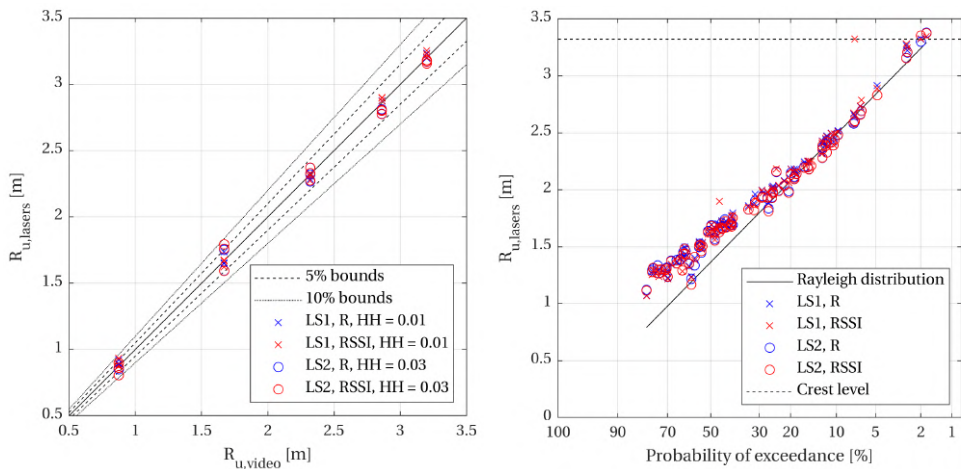
5.5. RESULTS AND ANALYSIS OF NORMALLY INCIDENT WAVES

5.5.1. WAVE RUN-UP HEIGHTS

The left panel of Figure 5.4 shows the run-up heights for test 1 from both laser scanners and based on both the measured distance R and laser reflectance RSSI data, plotted against the visually observed run-up heights taken from videos. 15 out of 21 waves are vis-

ible, as waves with a filling level of 6 m and 7 m overtopped the dike. The data agree well, most data lie within the 5% bounds and all data lie within the 10% bounds. The run-up was simulated in a robust manner, as the run-up levels for each set of three waves with the same filling level lie within a few centimetre of one another. The data of both laser scanners lie quite closely together, with laser scanner 2 giving a somewhat larger HH of 0.03 compared to the observed data. Determining the run-up based on the distance and RSSI gave almost equal results for this case. This is an improvement compared to what Cete (2019); Hofland et al. (2015) found, where the RSSI performed better. This can be explained by the lower run-up depth threshold of 1 cm that was used here, which arose from calibrating the system extensively. The differences that do occur between both laser scanners and between the lasers and video were caused by the variability over the width of the front of the up-rushing wave, since the average run-up height of the front was taken from the video data, and since the laser data give the run-up at two specific locations along the front. The variability in the 2% run-up height $R_{u2\%}$ over the width of the flume (excluding wall effects) was determined as on average 7% of the $R_{u2\%}$ for tests in the Delta Flume (Cete, 2019). Although smaller, the videos of the present tests also showed differences over the width.

5



(a) Run-up heights, test 1.

(b) Run-up heights, test 1a.

Figure 5.4: Left: Run-up data for test 1 from both laser scanners and based on both distance and *RSSI* versus run-up heights from video data. Right: Run-up data for test 1a from both laser scanners and based on both distance and *RSSI*, as well as Rayleigh distribution from wave run-up simulator filling level formula. The *x*-axis on Rayleigh scale, the dike crest level is indicated with the horizontal dashed line.

The right panel of Figure 5.4 gives the results for test 1a, with 100 randomly generated waves. Of this test, only 81 waves could be used, as someone blocked the laser beam during the last waves of the test. No video recording was available for this case. Therefore, the laser data were compared against the Rayleigh-distributed relation between the run-up height and the filling level of the simulator, as determined for this location. The *x*-axis is given on Rayleigh scale such that deviations from the Rayleigh distribution for the higher run-up are recognised easily. The data agree quite well with the Rayleigh distribution for the higher run-up

levels. One outlier is visible in the RSSI-values of laser 1. A more horizontal behaviour was found for the highest few run-up levels. Since the largest waves overtopped the dike, the maximum measured run-up level was the dike crest level (dashed line). The lowest run-up levels were larger than what was expected according to the Rayleigh distribution. The equation was fitted based on visual observations of the 3*7 different waves during a calibration test. During the test with the laser scanners, it was observed that the run-up was higher than during the test on which the relation was based as well. Furthermore, some uncertainty exists in the amount of water in the tank, as the waves were generated at the moment that a person at the run-up simulator saw that the required filling level was reached.

5.5.2. WAVE RUN-UP DEPTHS

As mentioned before, the run-up depth was measured by five surf boards or floaters as well. The left panel of Figure 5.5 compares the maximum run-up depths of the different waves as measured by the laser scanners at a height of $z = 1.42$ m on the slope with the surf board at this same location, as well as with visually estimated run-up depths. These results are also compared to a slightly adjusted version of the linear equation of Van der Meer (2011), being $d = c_d (R_u - z)$. Here, d [m] is the run-up depth, c_d [-] a coefficient, in this case being 0.25 for a 1:5 slope, R_u [m] the run-up height, and z [m] an arbitrary height on the slope. The line is curved here, since the equation was not plotted against the run-up level, but the corresponding filling level of the simulator.

At this location, the data agree quite well, with $HH = 0.32$ between the surf board and the visually estimated values, see the legend of the left panel of Figure 5.5. Here, the HH -values between visually estimated values and laser scanners are 0.23 and 0.15 (see legend). At this location and higher on the slope, the lasers seem to measure the run-up depth accurately, as the data agree quite well with the visually estimated and surf board data. At this location, the laser scanners record a somewhat larger run-up depth than the surf board data, and for some of the filling levels a somewhat smaller run-up depth than the visually observed data. The laser scanners scan the surface of the foam, which the surf boards do not. Furthermore, it was observed that the surf boards slightly sink into the water and do not record the smallest run-up depths, explaining the somewhat lower run-up depths and the zero values for a filling level of 2 m. The shape of the linear equation agrees quite well, but it overestimates the values. The relation could be used as an upper bound. These trends also hold for locations higher on the slope.

Different results were found closer to the simulator, where larger run-up depths occurred. There, also larger differences between the different measurement techniques occurred. At these locations the water was highly turbulent, and a lot of spray and foam were present. The visually estimated run-up depths lie around 60 cm or 65 cm for the largest waves, close to the simulator. As the lasers measure the foam and spray, this led to overestimated run-up depths, with values >1 m close to the simulator for the largest waves. Due to their mounting in the present set-up, the surf boards could not measure a run-up depth larger than approximately 50 cm, and thus gave an underestimation close to the simulator.

The right panel of Figure 5.5 shows the run-up depth in time for a wave with a filling level of 7 m at the same location on the slope ($z = 1.42$ m), for both laser scanners and the surf board. Visible is that the time signals agree quite well, but that the lasers give a

somewhat larger maximum run-up depth. The same holds for the other waves of the test.

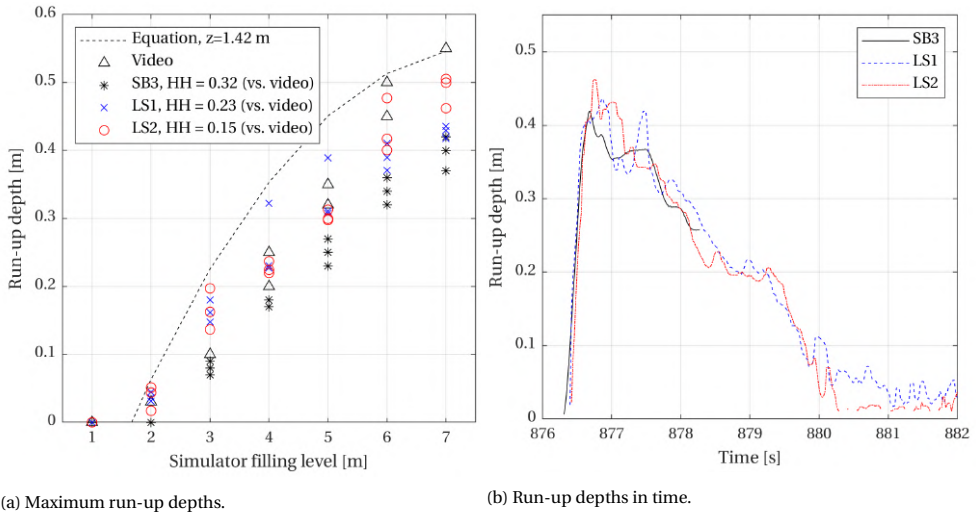


Figure 5.5: Left: Run-up depths at $z = 1.42$ m for test 1 as measured with both laser scanners, a surf board and from visual estimations, compared with equation from Van der Meer (2011). Right: Run-up depth in time at the same location for a filling level of 7 m and for both laser scanners and the surf board.

5.5.3. FRONT VELOCITIES

The front velocity can be determined by taking the distance the front travels along the slope in a certain period of time or by determining the time derivative of the front displacement. First, the displacement along the slope was smoothed by a median filter with a 0.2 s window and a mean filter with a 0.6 s window, which seemed to give the best results. After that, the time derivative was taken and the maxima were determined, giving the maximum front velocities during each wave. The maximum front velocities were determined from the videos as well; by taking the minimum number of video frames it took the front to travel 1 m.

A few outliers occur for these maximum front velocities, but most values fall within the 10% bounds. The HH-values were calculated as well. The data points of both laser scanners lie reasonably close together (HH=0.08), closer than the laser and video data to one another (HH=0.12). The deviations can be explained by the limited framerate of 30 fps with which the videos were recorded. This limited framerate leads to inaccurate results for large front velocities.

Front velocities were determined from the videos and the paddle wheel signals using a different method as well, by determining the time it took the front to travel on the slope from one paddle wheel to the next. In the same way, this velocity can be determined from the laser data. The left panel of Figure 5.6 shows the results. The data lie closely together, with most data within the 10% bounds. Once again, the HH-values were calculated. The data of both lasers lie closer together (HH=0.06) than the video and the paddle wheel data to one another (HH=0.07), giving confidence in the performance of the lasers.

The right panel of Figure 5.6 shows the run-up and front velocity time signals of one of the laser scanners and the front velocity time signal from the video analysis for a wave with a simulator filling level of 5 m of test 1. Both the development in time and the maximum front velocity agree well with one another. The dotted lines indicate percentages of the maximum run-up level. According to Van der Meer (2011), a front velocity close to the maximum velocity is found starting at 15% of the maximum run-up level. This velocity is then more or less constant until 75% of the maximum run-up level. The real maximum front velocity is reached between 30%-40% of the maximum run-up level. As visible in Figure 5.6, the highest front velocities indeed occur within the range of 15%-75% of the maximum run-up level. In this case, the actual peak front velocity is reached just after the 40% line. This also holds for the other waves of this test. This difference in peak front velocity location can be explained by the fact that the analysis of Van der Meer (2011) was based on real waves instead of waves generated by the wave run-up simulator. Despite this deviation in peak location, the wave run-up simulator seems to simulate the development of the front velocity of a wave properly. The erratic development of the run-up signal during the run-down of the wave can be explained by the small run-up depths that occur during the run-down, which lie around the used threshold value for the run-up depth.

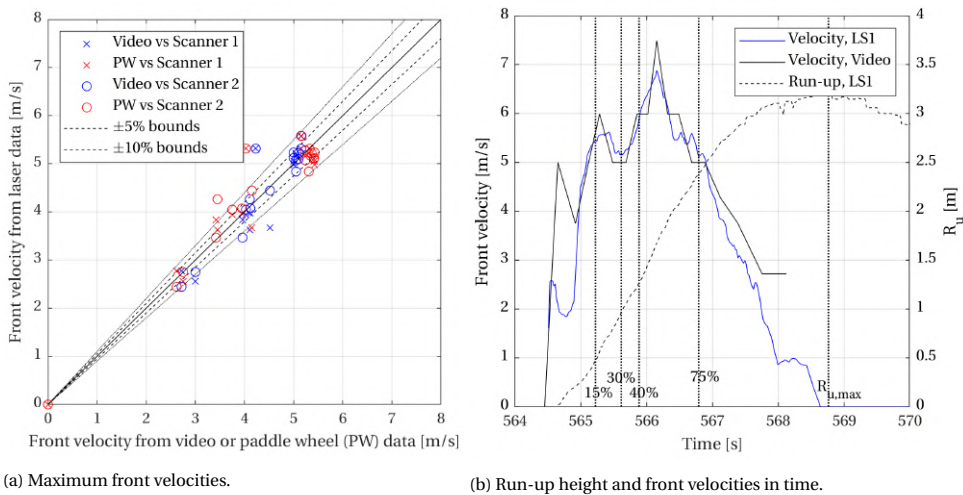


Figure 5.6: Left: Front velocities from laser data compared to video and paddle wheel (PW) data. Right: Run-up and front velocity time signals of one of the laser scanners and front velocity time signal from video analysis for a wave with a filling level of 5 m of test 1. Dotted lines indicate percentages of the maximum run-up level.

5.5.4. WAVE OVERTOPPING VOLUMES AND DISCHARGES

The (virtual) wave overtopping volumes and mean discharges can be calculated at different virtual crest levels, by determining the volume above this crest level by integrating the run-up depth. The overtopping volumes can then be found by taking the maximum values of these volumes during each wave. It was thus assumed that these maximum volumes per wave corresponded to the actual overtopping volumes. Then, the mean overtopping discharge q , in m^3/s per m width, was found by taking the sum of the volumes and divid-

ing by the test duration, $q = \sum_N V_{peak} / D$, with N [-] the number of waves, V_{peak} [m^3/m] the maximum volumes above the virtual crest level and D [s] the test duration. The virtual overtopping discharges at several virtual crest heights were calculated by multiplying the front velocity time series with the run-up depth time series as well. Here, the assumption was made that the front velocity corresponded to the flow velocity at the virtual crest. The left panel of Figure 5.7 shows the results for test 1a and compares them with the [EurOtop \(2018\)](#) wave overtopping equations.

Visible is that the discharges based on the maximum volumes agree well with the [EurOtop \(2018\)](#) equations. [Cete \(2019\)](#); [Hofland et al. \(2015\)](#) also achieved good results by determining the overtopping using the sum of the volumes above a virtual crest for wave flume tests, but the method had not been applied to an actual dike before.

The method of multiplying front velocity with run-up depth has not been applied before. Even though the assumption of local velocity equals front velocity was used, for this case results were found that lie mostly within the 90% bounds. However, the results clearly deviate from the mean line.

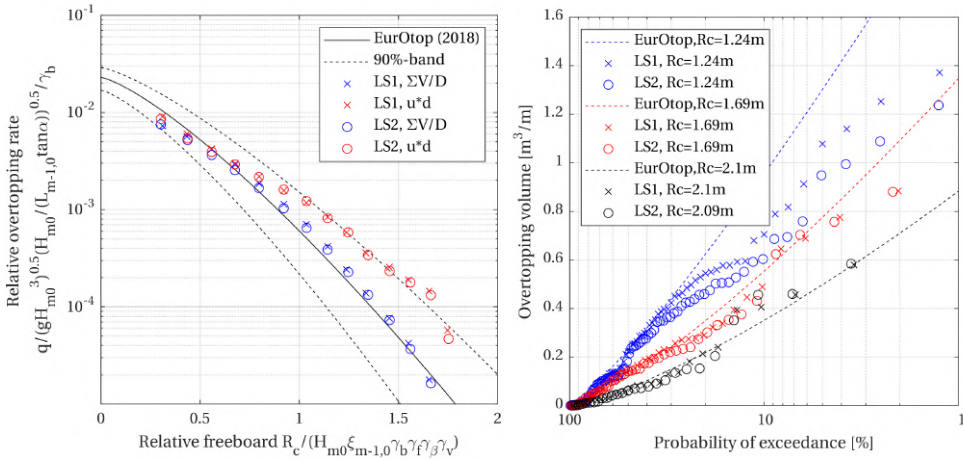
The results agree well with the [EurOtop \(2018\)](#) equations, even though these results were based on only 81 waves, and usually much larger numbers of waves are used. Furthermore, even though the wave run-up simulator is calibrated on run-up levels and not on overtopping volumes or discharges, the results for this case agree well with the most commonly used overtopping equations.

The differences could have several causes. One cause could be that the laser scanners detect a too large run-up depth, caused by foam on top of the water. The overtopping analysis was run again, now removing 10% of the local run-up depth, assuming this was foam and water aeration. This did not change the overall results significantly, but could be of influence for the lower freeboards, as there was a lot of foam and aeration close to the simulator. Another likely cause is that only filling levels larger than 0.7 m were simulated, which means that the smallest waves were omitted. This can explain the slightly lower discharges that were found for the lowest crest freeboards, as these small waves would contribute to the overtopping for these low freeboards.

The results of both laser scanners lie closely together. Only for the largest crest freeboards slight deviations occur, because these overtopping discharges were based on only a few waves. As mentioned before, there was variability in the run-up height over the width of the test section. If a wave surpasses the crest height at the scan transect of laser scanner 1, but barely reaches the crest at laser scanner transect 2, this quickly results in a different overtopping discharge for these high freeboards.

The right panel of Figure 5.7 shows the distribution of (virtual) overtopping volumes, compared with the [EurOtop \(2018\)](#) equations, which give the overtopping volume for a certain probability of exceedance. The volumes agree quite well for the medium and high crest level. The data also agree well for the lower crest level, for the larger probabilities of exceedance. However, for the smaller probabilities (larger volumes), the volumes are lower than according to the equation. A large virtual overtopping volume for these low freeboards, means that a large run-up depth was present over a large area of the slope. If there is any bias or error in the run-up depth as determined by the laser scanners, this error starts to weigh more heavily for these low freeboards and large volumes, because of the large surface that is integrated. Furthermore, the run-down, which does not occur

with an overtopping tank, could play a role. As mentioned before, the limited number of waves in the record could also be of influence.



(a) Relative overtopping rate at different virtual crest levels.

(b) Distribution of individual overtopping volumes.

Figure 5.7: Left: Relative overtopping rate for several virtual crest levels for test 1a and based on maximum volumes or run-up depth multiplied with front velocity, compared to EurOtop (2018) equations. Right: Distribution of individual overtopping volumes, compared to EurOtop (2018). R_c [m] is the crest freeboard, $\xi_{m-1,0}$ [-] is the breaker parameter, the different γ parameters [-] are influence factors, see EurOtop (2018).

5.6. OUTLOOK OBLIQUELY INCIDENT WAVES AND OTHER PARAMETERS

In next steps of the study, the data of all tests with normally incident waves will be analysed in more detail, as well as the data of the tests with oblique waves. Figure 5.8 shows a snapshot of both laser scanners during oblique wave attack. The time lag and different maximum run-up levels are visible. Potentially the 2D front velocity and direction, and the overtopping volumes and discharges can be determined from the cross-correlation between the two measured signals.

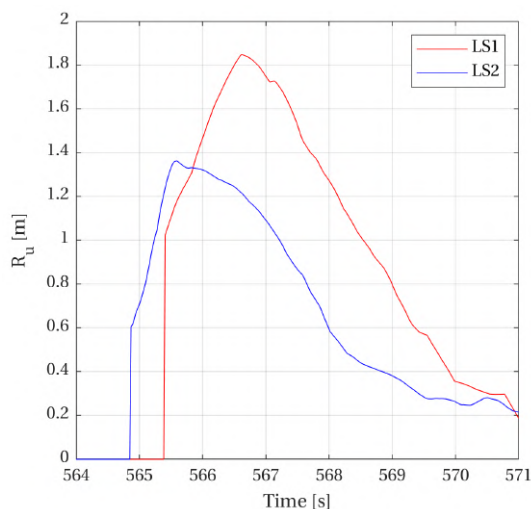


Figure 5.8: Snapshot of run-up level in time for both laser scanners during oblique wave attack. The time lag and different maximum run-up levels are visible.

5.7. CONCLUSIONS

This chapter presents the successful implementation of an innovative system to measure wave run-up and calculate overtopping using two coupled laser scanners at a field site. The system can determine the run-up depths and front velocities on a dike. The chapter considers the first tests with the system, with normal and oblique waves generated by the wave run-up simulator on a grass dike slope. A range of environmental conditions was simulated, to determine their influence on the measurements.

The ideal laser scanner settings were determined for both dry and rainy conditions. Using the last echo gave the best results and is especially important during rainy conditions. The influence wind vibrations of the laser scanners on the data quality and run-up results was small. With a more fixed system placement during a storm season, vibrations should be largely eliminated. However, it would still be good to attach an accelerometer to be able to correlate possible outliers during a storm with potentially occurring vibrations.

The resulting run-up heights agreed well with the visually observed run-up, with differences of only a few centimetre, both for the run-up based on measured distance and based on laser reflectance. Run-up depths were determined as being reliable with the laser scanners as well as with a commonly used method (surf boards) for locations higher on the dike slope. Closer to the simulator, the lasers gave too large and unreliable run-up depths due to foam and spray. The advantage compared to the surf boards is that the run-up depth can be determined over the whole slope, not just at a few locations.

The front velocities were determined as being reliable from the laser scanner data, as well as based on video and paddle wheel data. The average front velocities between two paddle wheels based on the different instruments agreed quite well with one another. Furthermore, the development in time and the front velocity maxima based on the laser scanners agreed well with the video results.

The wave overtopping volumes and discharges were calculated at several virtual crest levels. The overtopping discharges based on maximum volumes agreed well with the [Eur-Otop \(2018\)](#) equations, although more research is recommended. The discharges based on run-up depths multiplied with front velocities agreed less well, although with most values within the 90% bounds of the overtopping equations.

The wave run-up heights, depths and front velocities could be determined as accurately with the laser scanner system as with the conventionally used methods. Since the system is mobile, it can measure at several dike locations by moving the system every few years.

The goals for the next steps in this study are to determine the 2D front velocity and direction and to calculate the overtopping volumes during oblique wave attack, by considering the correlations between the two measured laser signals.

ACKNOWLEDGEMENTS

We would like to thank the POV Waddenzeedijken for the use of the wave run-up simulator, as well as Gerben van der Meer, Jan Bakker and Frans Roorda for their help with the wave run-up tests. This study was supported by Waterschap Noorderzijlvest and the Hoogwaterbeschermingsprogramma.

6

CALIBRATION AND PREPARATION OF FIELD MEASUREMENTS WITH LASER SCANNERS. PART II: OBLIQUE WAVE RUN-UP AND OVERTOPPING

*An experiment is a question which science poses to Nature,
and a measurement is the recording of Nature's answer.*

Max Planck

Wave overtopping is typically measured in the field using overtopping tanks. In this chapter, an alternative system is developed that uses two laser scanners. The system also measures wave run-up, as well as run-up depths and velocities, both during perpendicular and oblique waves on a dike in the field. The chapter considers the first calibration tests with the system in the field, with perpendicular and oblique waves generated by the wave run-up simulator on a grass dike slope. This chapter summarises the results for normally incident waves of chapter 5 and [Oosterlo et al. \(2019\)](#) and extends it with an analysis of oblique wave attack, with the field tests with the wave run-up simulator and with simulations with the phase-resolving numerical wave model SWASH (Simulating WAVes till SHore, [Zijlema et al., 2011](#)). The simulations with the SWASH model are performed to gain more insight in the potential performance of the system during actual oblique wave attack during a storm. The main goal of this chapter is to gain full insight in the capabilities of the laser scanners in measuring both perpendicularly and obliquely incident waves. The run-up is determined from the measured elevation and reflection intensity, which agrees well with

This chapter has been published as [Oosterlo, P., Hofland, B., Van der Meer, J.W., Overduin, M., & Steendam, G.J. \(2021\). Calibration and preparation of field measurements of oblique wave run-up and overtopping on dikes using laser scanners. *Coastal Engineering*, 167, 103915.](#)

the visually observed run-up. Run-up depths and front velocities can be determined accurately as well. The (virtual) wave overtopping discharge can be calculated from the data, which agrees well with the most commonly used overtopping equations for perpendicularly incident waves. Finally, from the simulated run-up data of obliquely incident waves, it is concluded that an estimate can be obtained of the incident wave period and wave angle of incidence at the toe of the structure.

6.1. INTRODUCTION

In the past, the required crest height of dikes was determined by assessing the wave run-up height. Wave run-up heights and run-up depths (layer thicknesses, flow depths) and velocities were measured in the lab and field often in the past, but the latter measurements are difficult because of turbulence and aeration (Schüttrumpf & Van Gent, 2004; Van der Meer et al., 2010). The measurements are performed often using resistance type gauges, which require a certain minimum run-up depth, or step gauges, which have a coarse resolution. Other techniques that have been used are e.g. stereo-photogrammetry (e.g. De Vries, Hill, de Schipper, & Stive, 2011) and ultrasonic altimeters (e.g. Matias, Blenkinsopp, & Masselink, 2014). Nowadays, dikes are usually designed using the mean wave overtopping discharge. Typically, wave overtopping is measured in the field using wave overtopping tanks (e.g. De Rouck et al., 2009; Van der Meer et al., 2019; Wenneker et al., 2016), but overtopping measurements in the field are scarce. Overtopping tanks are a robust method to measure wave overtopping, but fixed at a certain location and at a fixed elevation.

An alternative and more flexible solution was developed in Oosterlo et al. (2019) based on Hofland et al. (2015), using two terrestrial laser scanners or LIDARs. Laser scanners are used often for terrestrial measurements, either from a plane (see Guenther, Cunningham, LaRocque, & Reid, 2000; Vosselman & Maas, 2010) or (autonomous) car (e.g. Spore, Brodie, & Swann, 2014; Wübbold, Hentschel, Vousedoukas, & Wagner, 2012). More recently, they were applied in coastal engineering applications, to measure morphological changes caused by waves (Almeida, Masselink, Russell, & Davidson, 2015; Vousedoukas et al., 2014) and the water surface or waves in the field (Blenkinsopp et al., 2010; Maslov, Fadeev, & Lyashenko, 2000) or in a flume (Allis et al., 2011; Blenkinsopp, Turner, Allis, Peirson, & Garden, 2012; Streicher et al., 2013). Several studies have also used laser scanners to measure wave run-up, in the field (e.g. Brodie, Slocum, & McNinch, 2012) or in a flume (Hofland et al., 2015; Vousedoukas et al., 2014). However, the studies that measured wave run-up in the field generally used a lower scan frequency, thus not obtaining the instantaneous water surface and not being able to measure the wave run-up with a high temporal resolution.

The system as developed in Oosterlo et al. (2019) can measure the wave run-up, front velocities and run-up depths of up-rushing waves on a dike in field situations. The virtual wave overtopping can be calculated at any elevation from these measurements as well. The present chapter summarises the work of Oosterlo et al. (2019) and extends it with an analysis of oblique wave attack, with field tests with the wave run-up simulator, and with simulations with the phase-resolving numerical wave model SWASH, Simulating WAVes till SHore (Zijlema et al., 2011).

The goal of this chapter is to gain full insight in the capabilities of the laser scan-

ners in measuring both perpendicular and obliquely incident waves. To this end, the present chapter describes the analysis and calibration with perpendicular and oblique waves physically simulated with the run-up simulator on an actual grass dike slope, as well as numerical simulations of obliquely incident waves with the SWASH model. This chapter compares the data as measured by the laser scanners with data from video recordings, 'surf boards' (floaters), paddle wheels and the SWASH model. Furthermore, the results are compared to the most commonly used wave run-up and overtopping equations (EurOtop, 2018). If this calibration is successful, the laser scanner system will be placed next to two overtopping tanks on a dike in the Eems-Dollard estuary in the north of the Netherlands, to measure the wave run-up and overtopping during actual severe winter storms.

The outline of this chapter is as follows. Section 6.2 describes the approach and set-up of the system, based on Oosterlo et al. (2019). After that, section 6.3 gives a short summary of the post-processing and data analysis. For the full description, the reader is referred to Oosterlo et al. (2019). The validation of the measured parameters follows in section 6.4, first for perpendicular wave attack as previously described in Oosterlo et al. (2019). Section 6.5 presents the results for obliquely incident waves. The section that treats the oblique wave attack not only discusses the field tests, but also gives a description of the numerical analysis of the system for the interaction with an actual oblique wave field. Furthermore, the section discusses the optimisation of the laser scanner system. Finally, section 6.6 gives the conclusions and presents an outlook on the next steps in this study.

6.2. APPROACH AND SYSTEM SET-UP

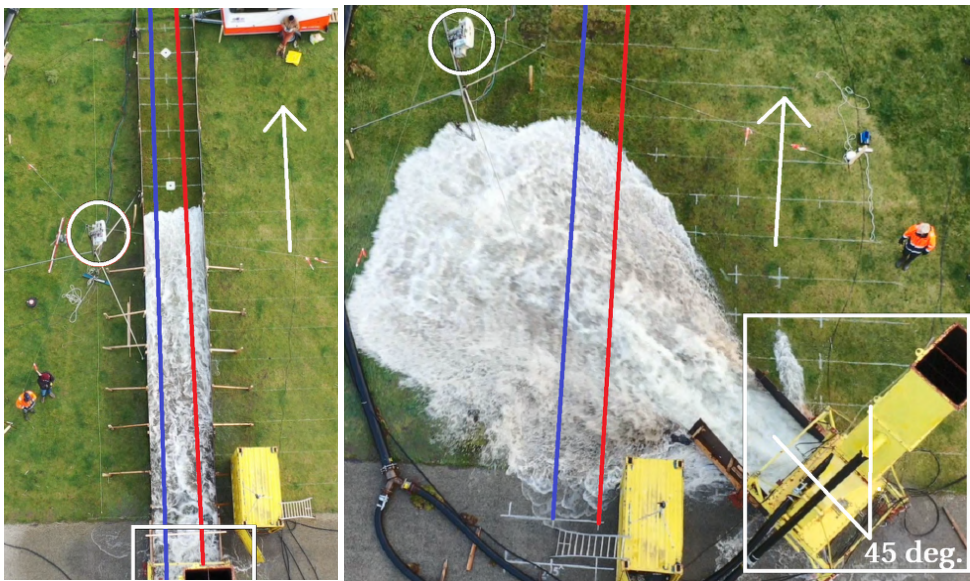
The laser scanner system was tested with waves generated by the wave run-up simulator (Van der Meer, 2011) on a dike in Friesland, the Netherlands. The wave run-up simulator is a 7 m-tall vertical tank, which can be filled with water to a certain level. By quickly opening the bottom of the tank, the tank drains, thereby simulating an individual 'wave' running up the slope. After the tank has drained, the bottom of the tank is closed again, and the tank is filled with water by pumps once more. The time series or steering file of filling levels of the simulator are derived from a Rayleigh distribution with an assumed nearshore significant wave height H_s of 2 m and a peak period T_p of 5.7 s, see also Steendam, Van der Meer, Van Hoven, and Labrujere (2017).

Refer to the left panel of Figure 6.2 for the system set-up and instrumentation on the dike slope. The dike slope consists of basalt blocks until 4.16 m+NAP (Normaal Amsterdams Peil, Dutch ordnance level), asphalt until 6.34 m+NAP and grass until the crest at 9.49 m+NAP. The tests were performed on the upper slope consisting of grass, with the mean slope being approximately 1:5. The wave run-up simulator was placed just below the transition from asphalt to grass, at 6 m+NAP. For tests with the simulator, the modelled storm water level is considered to be located at the same location as the outlet of the simulator. Therefore, the origin of the coordinate system was placed at the simulator as well, with x -coordinates being horizontal, z -coordinates being vertical and y -coordinates being in the lengthwise direction of the dike, see the left panel of Figure 6.2 and Figure 6.3. Complicating factors compared to the previous (lab) research on concrete or wooden slopes are the convex dike slope, wave-induced erosion of the grass slope dur-

ing testing, the blades of grass, which might obfuscate a thin layer of water, as well as water infiltrating into the slope.

The present laser scanner system uses two SICK LMS511pro HR laser scanners, a cheap laser scanner with a near-infrared (905 nm) laser beam, which is the newest version of a commonly used laser scanner in previous research (e.g. in Hofland et al., 2015; Streicher et al., 2013). Figure 6.1 shows the calibration set-up at the dike. The system consists of two laser scanners, attached to an easily relocatable pole placed perpendicular to the dike slope. The laser scanners were mounted at heights of 5.17 m and 5.50 m above the slope. The laser scanners measure the distance R to a surface by measuring the time that the reflection of a laser pulse takes to reach the laser again. The reflected signal intensity RSSI (Received Signal Strength Indicator, a dimensionless value between 0 and 255) is measured as well, which provides information on the type of surface. The run-up heights and depths, front velocities, and wave overtopping volumes and discharges can be determined from the R and RSSI data. The scanners have a sampling frequency of 50 Hz and are synchronised. The two laser scanners each scan a line parallel to one another, running from the dike toe to the crest, as indicated by the blue and red lines in Figure 6.1. The height of the laser scanners and the distance between both scan lines are adjustable.

6



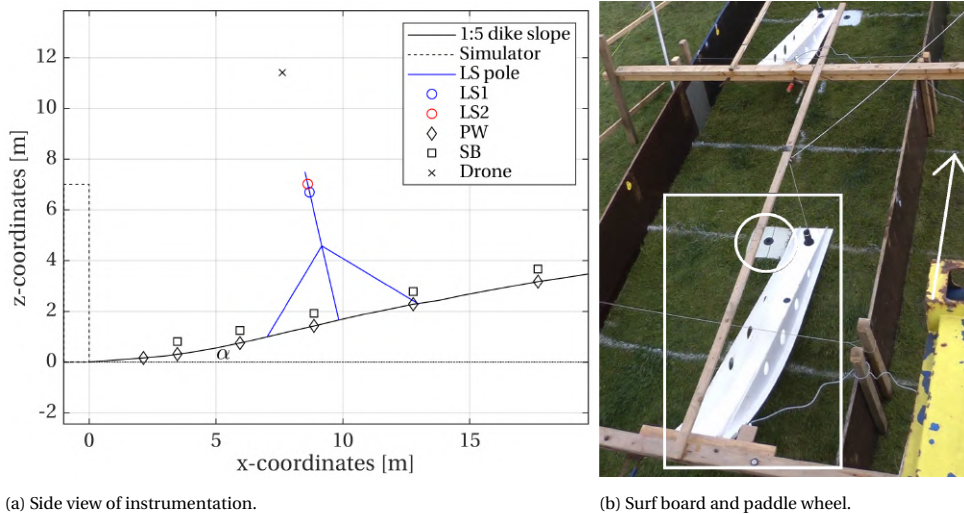
(a) Perpendicular incident waves.

(b) Obliquely incident waves.

Figure 6.1: System overview during perpendicular (left panel) and obliquely (right panel) incident waves. Laser scanners (white circle), run-up simulator (white rectangle), laser scanner scan lines (blue and red lines), up-slope direction (arrows) and 45° angle indicated.

The left panel of Figure 6.2 shows the locations of all the instruments. For the calibration, the laser data were compared with data obtained by the other instruments. Run-up heights and front velocities were determined from videos recorded by a drone flying above the system. Five 'surf boards' measured the run-up depths. The surf boards are curved

boards, which are hinged about 1 m above the slope and which float on top of the flowing water. The rotation at the hinge is measured and gives the run-up depth, see e.g. [Van der Meer et al. \(2010\)](#). Six paddle wheels or impellers measured the velocities near the ground. The right panel of Figure 6.2 shows two of the surf boards and paddle wheels. Note that the surf boards were mounted only during separate tests where the laser scanners were not used, since they block the view for the laser scanners. An accelerometer was attached to the upper laser scanner, to correlate possible outliers with potentially occurring vibrations. Finally, a relation between the filling level of the simulator and the resulting run-up height was determined from several visually observed run-up heights at this location.



(a) Side view of instrumentation.

(b) Surf board and paddle wheel.

Figure 6.2: Left: Side view of system set-up and instrumentation. x -coordinates horizontal, z -coordinates vertical, y -coordinates perpendicular to the figure. α [$^\circ$] is the slope angle. LS pole is the laser scanner pole, LS1 the lower laser scanner, LS2 the upper laser scanner. PW are the 6 paddle wheels; SB the five surf boards. Right: Example of surf board (white rectangle) and paddle wheel (white circle). Up-slope direction indicated by the arrow.

First, tests were performed for perpendicularly incident waves, where for each test seven different known run-up levels (simulator filling levels from 1 m to 7 m) were repeated three times (21 waves in total) to obtain increased statistical reliability, see also <https://youtu.be/KCfflQ-TPtk>. Filling levels of 1 m - 5 m correspond to run-up levels of 0.88 m - 3.2 m. Filling levels of 6 m and 7 m overtopped the dike. With these generated run-up levels, the influence of a large range of environmental conditions, e.g. producing artificial wind and rain, and laser scanner parameters were tested and calibrated, see [Oosterlo et al. \(2019\)](#). Next, a test was performed with 100 random run-up levels as derived from the Rayleigh distribution, to be able to assess the performance of the system in measuring the wave run-up and overtopping. After that, the wave run-up simulator was placed under an angle of 45° with the dike normal. With this set-up, obliquely incident waves were generated, see also https://youtu.be/RMy1Ah8bU_0. For the first tests with oblique waves, 3 times 6 up-rushing waves were generated (simulator filling levels from 2 m to 7 m, 18 waves in total). During these tests, several different distances between the

laser scanner scan lines were tested, being 1.3 m, 2.5 m and 3.4 m. The last test with oblique waves again consisted of 100 randomly generated up-rushing waves, to assess the performance of the system in measuring the oblique run-up and overtopping.

6.3. DATA PROCESSING AND DATA ANALYSIS

Before the start of the tests, the system had to be calibrated, where the exact positions of the laser scanners and laser lines had to be determined. For the full calibration procedure, refer to Oosterlo et al. (2019). The main step in the data processing procedure consists of converting the measured distances R_1 and R_2 in polar coordinates to cartesian x (horizontal) and z (vertical) coordinates in metre, taking into account the positions and angles of the laser scanners, see Figure 6.3. For a full description of the coordinate transformation and data analysis procedures, see Oosterlo et al. (2019). The dry slope was determined from the first 10 s of a test. Next, the run-up depths were determined by subtracting the dry slope from the measured slope at a certain moment. Depths smaller than a threshold value of 0.01 m were removed to remove noise from the signal and prevent the detection of unrealistically high run-up values. Note that this threshold is smaller than what was used in previous research (Cete, 2019; Hoffland et al., 2015), and could be used here because of the generally larger run-up depths that occurred during these field tests than with the previous lab flume research. The run-up height could be determined from the resulting run-up depth and RSSI time series by finding the highest location on the slope where $z_{\text{runup}} - z_{\text{dry}} > z_{\text{threshold}}$ and $RSSI_{\text{runup}} - RSSI_{\text{dry}} > RSSI_{\text{threshold}}$, as shown in Figure 6.4 for the run-up depth. The check on RSSI is performed to detect water layers that are thinner than the noise level of the direct distance measurement of the laser scanner.

6

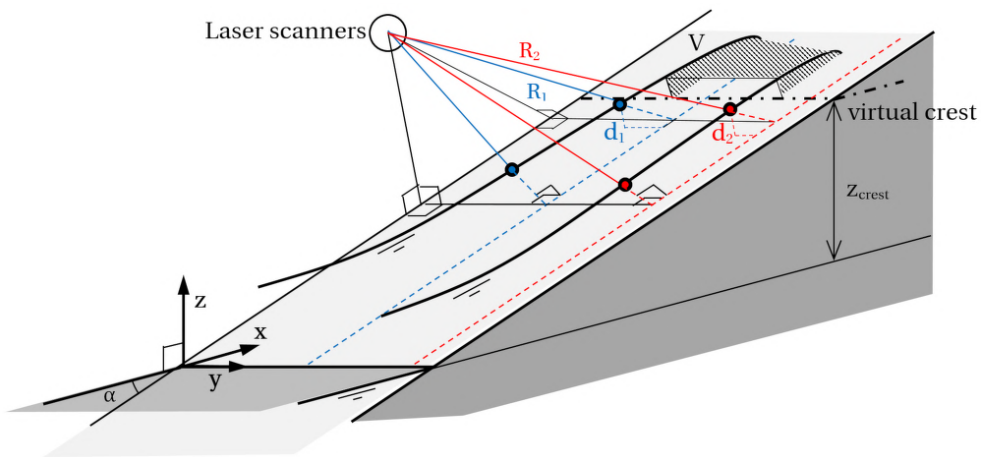


Figure 6.3: System set-up as used for the conversion of measured distances (R_1 [m] and R_2 [m], blue and red lines) in polar coordinates to cartesian x , y , z -coordinates [m] according to the coordinate system as shown. Dike slope α [°], laser scan lines (blue and red dashed lines), scanned points on water surface (blue and red dots), virtual crest level z_{crest} [m], run-up depths d_1 [m] and d_2 [m], and virtual overtopping volume V [m³] indicated.

The front velocities of the up-rushing waves could be determined from the temporal change in run-up level. To this end, first the time signal of the instantaneous front posi-

tion was smoothed by applying a median filter with a 0.2 s window, followed by a moving average with a 0.6 s window. After that, the time derivative was taken and the maxima were determined, giving the maximum front velocities during each wave. The maximum front velocities were determined from the videos as well; by taking the minimum number of video frames it took the front to travel 1 m on the slope.

The (virtual) wave overtopping volumes and mean discharges could be calculated from the laser data at different virtual crest levels. Figure 6.4 shows for three different waves the largest overtopping volume of each wave, at three virtual crest levels. The overtopping volumes were determined by integrating the depicted instantaneous run-up depth above the virtual crest level (shaded areas in Figure 6.4). Then, the overtopping volumes were found by taking the maximum values of these volumes during each wave. Hereby it was assumed that these maximum volumes per wave correspond to the actual overtopping volumes. The mean overtopping discharge q , in m^3/s per m width, was found by taking the sum of these peak volumes and dividing by the test duration, $q = \sum_N V_{peak} / D$, with N [-] the number of waves, V_{peak} [m^3/m] the maximum volumes above the virtual crest level and D [s] the test duration. The virtual overtopping discharge was calculated by multiplying the front velocity time series with the run-up depth time series at several virtual crest heights as well. Here, the assumption was made that the front velocity, which changes in location on the slope, corresponded to the flow velocity at the virtual crest.

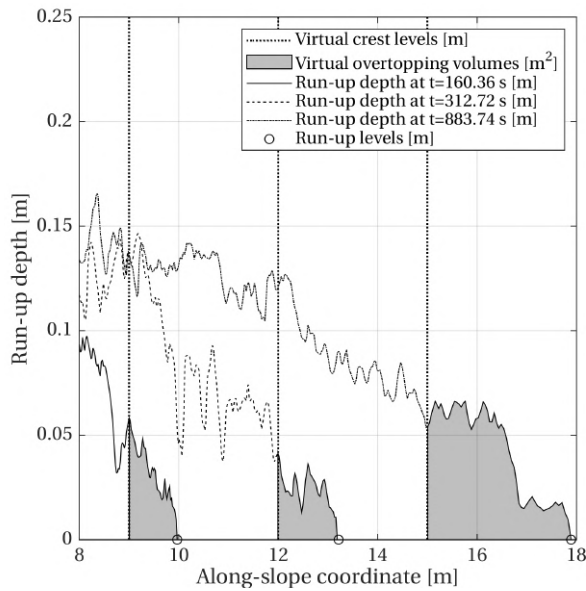


Figure 6.4: Determination of run-up levels R_u [m] (circles) and virtual overtopping volumes V [m^3/m] (shaded regions) based on the run-up depths d (solid, dashed and dash-dot lines), for three different waves and at three different virtual crest levels (dotted lines). The waves are plotted for the moment that the volume above the virtual crest line (the shaded area) is maximum for that specific wave. The assumption is that this would be the overtopped volume that would have overtopped if the crest was located at this virtual level.

Another important step in the data processing procedure was the filtering out of disturbances like rain or a person standing in the laser beam. As described in Oosterlo et al. (2019), using the right laser scanner settings, i.e. the last echo and without any additional filtering, the influence of such disturbances on the results was small. When the first echo was used during rain, this led to more detection of rain, as the laser beam sometimes reflected off a raindrop. The last echo gave good results during dry conditions and improved the results during rain, as this echo did come from behind the raindrops. Waves were removed from the signal if a person was standing in the laser beam.

The percentage of invalid measurements at a certain location indicates the quality of the measurement. An invalid measurement means that the magnitude of the laser reflection was too small. For all tests, these percentages were very small ($\approx 0.1\%$). Finally, from the accelerometer data, it was determined that the influence of vibrations due to the wind on the data quality was small.

Commonly, the root-mean-square error (RMSE) and the from the RMSE derived normalised root-mean-square error and scatter index are used to evaluate the performance or reliability of some measurement or model. However, Mentaschi et al. (2013) showed that the RMSE and its variants give smaller values for models affected by negative bias. Hence, these indicators are not always reliable to assess the accuracy of models or measurements. They showed that the HH-indicator as proposed by Hanna and Heinold (1985) provides more reliable information on the accuracy of models or measurements. This HH-indicator is used to assess the performance of the laser scanners in the present chapter and is defined as:

$$HH = \sqrt{\frac{\sum_{i=1}^N (M_i - O_i)^2}{\sum_{i=1}^N M_i O_i}} \quad (6.1)$$

where M_i is the i th modelled data, O_i is the i th observation and N is the total number of observations. Furthermore, the Normalised Bias Indicator is used:

$$NBI = (\overline{M} - \overline{O}) / \overline{O} \quad (6.2)$$

Both the HH and NBI are dimensionless.

6.4. RESULTS AND ANALYSIS OF PERPENDICULARLY INCIDENT WAVES

6.4.1. WAVE RUN-UP HEIGHTS

The left panel of Figure 6.5 shows the run-up heights for a test with perpendicularly incident waves (seven waves, three times repeated) from both laser scanners, and based on both the measured distance R and laser reflectance RSSI. The results were plotted against the run-up heights derived from video recordings. Only 15 out of 21 waves are visible, as waves with a simulator filling level of 6 m and 7 m overtopped the dike. The data agree well, with most data within the ± 0.05 m bounds and all except one data point within the ± 0.10 m bounds. The run-up was simulated in a robust manner, as the run-up levels for each set of three waves with the same filling level lie within a few centimetres of one another.

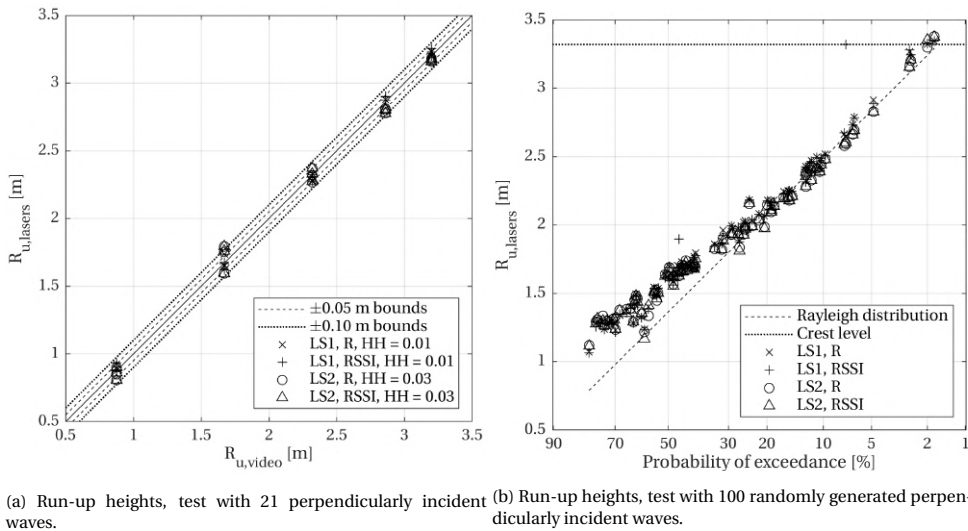


Figure 6.5: Left: Run-up heights derived from both laser scanners (LS1 and LS2), based on distance (R) and laser reflectance ($RSSI$), compared with run-up heights from videos, for a test with 21 perpendicularly incident waves. The HH-indicator values are shown as well. Right: Run-up heights for test with 100 randomly generated perpendicularly incident waves for both laser scanners, as well as Rayleigh distribution derived from wave run-up simulator filling level formula (dashed line). The horizontal axis is plotted on Rayleigh scale, the dike crest level is indicated with the horizontal dotted line.

The data of both laser scanners agree well, where laser scanner 2 gave a somewhat larger HH-value relative to the observed data. NBI values were close to zero (<0.01), being positive for laser scanner 1 and negative for laser scanner 2. Determining the run-up based on the measured distance and RSSI gave almost equal results. This is an improvement compared to what Cete (2019); Hofland et al. (2015) found, where the RSSI performed better. This can be explained by the lower run-up depth threshold of 0.01 m, which could be used here. The differences that occurred between the laser scanner and video run-up heights arose from the variability over the width of the front of the up-rushing wave. The average run-up height of the front was taken from the videos, but the lasers give the run-up at two distinct locations along the front. Variabilities in the 2% run-up height $R_{u2\%}$ over the width of the flume, excluding wall effects, were on average 7% of the $R_{u2\%}$ for tests in the Delta Flume at Deltares, the Netherlands (Cete, 2019). Although smaller, such oscillations over the width of the front also occurred during the present tests.

The right panel of Figure 6.5 presents results for a test with 100 randomly generated perpendicularly incident waves. Of this test, only 81 waves could be used, as a person was standing in the laser beam during the last waves of the test. Since no video recording was available for this test, the laser data were compared against the theoretical run-up heights according to the Rayleigh distribution as simulated by the wave run-up simulator. The run-up simulator generates the wave run-up according to a Rayleigh distribution, which was calibrated based on visual observations of the 3*7 different waves during a calibration test. The dashed line in the right panel of Figure 6.5 represents this Rayleigh distribution.

The horizontal axis was plotted on Rayleigh scale such that deviations from the Rayleigh scale can easily be recognised. Note that the measurements are no real exceedance plot, as the run-up levels for a certain probability of exceedance were created deterministically. The data agree well with the theoretical Rayleigh distribution for the higher run-up levels, with one outlier in the RSSI values of laser 1. This outlier indicates that for this wave, the measured run-up level based on the RSSI did not agree with the theoretically simulated run-up level as derived from the Rayleigh distribution. The highest few run-up levels also deviate somewhat from the distribution. This can be explained as follows; since the largest waves overtopped the dike, this means that the maximum measured run-up level was the dike crest level (dotted line). The lowest run-up levels were higher than expected according to the Rayleigh distribution as used for the run-up simulation, which was confirmed visually during the test as well.

6.4.2. WAVE RUN-UP DEPTHS

The run-up depth is defined as the water depth of the up-rushing wave at a certain location, see Figure 6.3. These run-up depths were measured not only by the laser scanners, but also by five surf boards or floaters. The locations of the surf boards were given in the left panel of Figure 6.2. The left panel of Figure 6.6 shows the maximum run-up depths of the different waves as measured by the laser scanners at approximately halfway up the slope ($z = 1.42$ m, crosses and circles). Furthermore, the figure shows the depths as measured by the third surf board at this same location (asterisks), and visually estimated run-up depths (diamonds). These visually estimated depths came from hand-held video recordings, by determining the water level at the side boards. The left panel of Figure 6.6 also shows the linear equation of Van der Meer (2011) (dashed line):

$$d = c_d (R_u - z) \tag{6.3}$$

where d [m] is the run-up depth, c_d [-] a coefficient, in this case being 0.25 for a 1:5 slope, R_u [m] the run-up height, and z [m] an arbitrary height on the slope. Note that the line is curved here, since the equation was not plotted against the run-up height, but the corresponding filling levels of the simulator.

Table 6.1 gives HH and NBI values for the run-up depths, comparing the depths as measured by the different instruments. Reasonable agreement was found between the data, with the largest differences occurring between the surf board and the visually from video estimated values. The laser scanners generally gave larger values than the surf board, but slightly smaller values than the visually estimated ones. This can be explained as follows; the laser scanners scan the surface of the foam, which the surf boards do not. It was observed that the surf boards slightly sink into the water and do not record the smallest run-up depths, explaining the generally smaller values and the zero values for a filling level of 2 m. The visually estimated values were larger for the largest waves. Since the visually estimated depths were determined at the side boards, they might have been slightly overestimated, as most spray also occurred at the side boards. The shape as obtained from the equation agrees quite well, but it overestimates the depths. These trends also hold for locations higher on the slope. Hence, it can be concluded that at this location and higher on the slope, the lasers accurately measure the run-up depths.

Different results were found closer to the simulator. In front of the simulator, larger

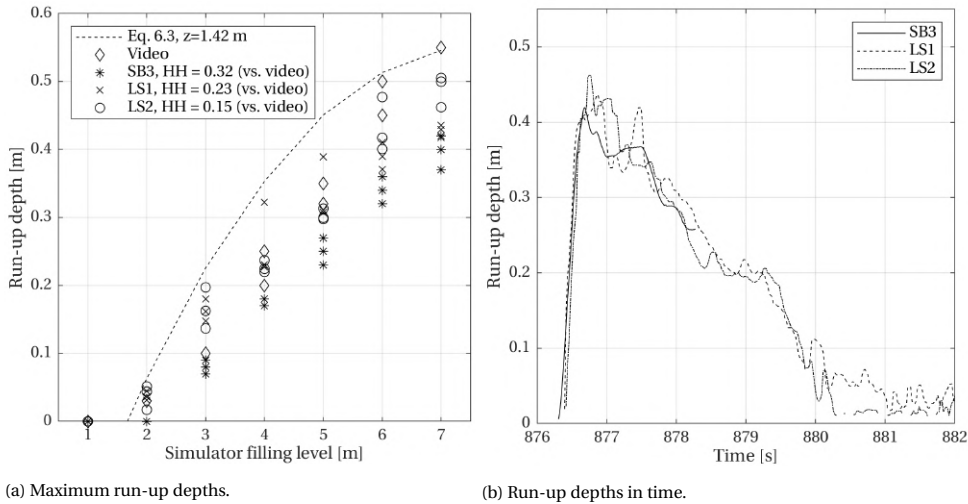


Figure 6.6: Left: Run-up depths as measured with both laser scanners (LS1 and LS2), the third surf board (SB3) and as estimated from videos at $z = 1.42$ m, compared with the relation of [Van der Meer \(2011\)](#) (Equation 6.3). Right: Run-up depths in time at the same location for a single wave, for both laser scanners and the third surf board.

run-up depths occurred, the water was highly turbulent, and a lot of foam and spray were present. Larger differences between the different measurement techniques were found at those locations. The visually estimated run-up depths were around 0.60 m or 0.65 m in front of the simulator for the largest waves. Due to the mounting, the surf boards could not measure a run-up depth larger than approximately 0.50 m, and thus gave an underestimation close to the simulator. Since the laser scanners measure the foam and spray, this led to overestimations of the run-up depths close to the simulator for the largest waves, where values >1 m were found.

The right panel of Figure 6.6 shows the run-up depth in time for a wave with a simulator filling level of 7 m at the same location on the slope ($z = 1.42$ m), for both laser scanners and the third surf board. The time record agrees quite well, but the lasers again gave a somewhat larger maximum depth. The same holds for the other waves of the test. Note that the surf board signal ends at a depth of approximately 0.25 m. The surf boards need to be lifted out of the water before the run-down starts, as they would break otherwise. Hence, another advantage of the laser scanners is that the whole run-up depth time signal can be measured, including the smaller depths and the run-down.

Run-up depths		
Instruments	HH [-]	NBI [-]
SB3 vs. Video	0.32	-0.28
LS1 vs. SB3	0.26	+0.30
LS2 vs. SB3	0.27	+0.33
LS1 vs. Video	0.23	-0.06
LS2 vs. Video	0.15	-0.04

Table 6.1: HH and NBI values, comparing the run-up depths as measured by different instruments. SB3 is the third surf board, LS1 is laser scanner 1, LS2 is laser scanner 2.

6.4.3. FRONT VELOCITIES

Comparing the maximum front velocities based on the laser scanner data with the velocities based on the video analysis, a few outliers were found, but most data points were located within the ± 0.5 m/s bounds. The data points of both laser scanners agree well (HH = 0.08, NBI = 0.02), better than the laser and video data (HH = 0.12, NBI = -0.05), but overall the deviations were small. The deviations that did occur can be explained by the limited framerate of 30 fps of the videos, which led to less accurate results for larger front velocities.

6

Front velocities were determined from the paddle wheel records as well, by determining the time it took the front to travel on the slope from one paddle wheel to the next. See the left panel of Figure 6.2 for the paddle wheel locations. The velocity was determined by dividing the travelled distance by this measured time delay. Hence, the paddle wheels were used as wave detectors. Such front velocities were determined from the laser data and videos as well. The left panel of Figure 6.7 plots these laser data against the video and paddle wheel data. The data agree quite well, with most data within the ± 0.5 m/s bounds and the data of all but one wave within the ± 1 m/s bounds, giving confidence in the laser analysis and results. The data of both laser scanners agree well (HH = 0.07, NBI = 0.01), the same agreement as was found between the video and paddle wheel data (HH = 0.07, NBI = 0.01).

The right panel of Figure 6.7 gives the run-up and front velocity time signals of one of the laser scanners and the front velocity time signal from the manual video analysis for one wave. Both the development in time and the maximum front velocity for both techniques agree well. The dotted vertical lines indicate percentages of the maximum run-up level. According to Van der Meer (2011), front velocities close to the maximum front velocity are found between 15% and 75% of the maximum run-up level, being approximately constant in this range. The actual maximum front velocity is reached between 30% and 40% of the maximum run-up level. Here, the highest front velocities indeed occurred within the range of 15%-75% of the maximum run-up level. However, the actual peak of the front velocity was reached at around 50% of the maximum run-up level for this case. The same behaviour was found for the other waves of this test. This difference in location of the peak front velocity can be explained as follows; the analysis of Van der Meer (2011) was based on real waves instead of waves generated by the wave run-up simulator. Despite this deviation in peak front velocity location, the wave run-up simulator seems to simulate the

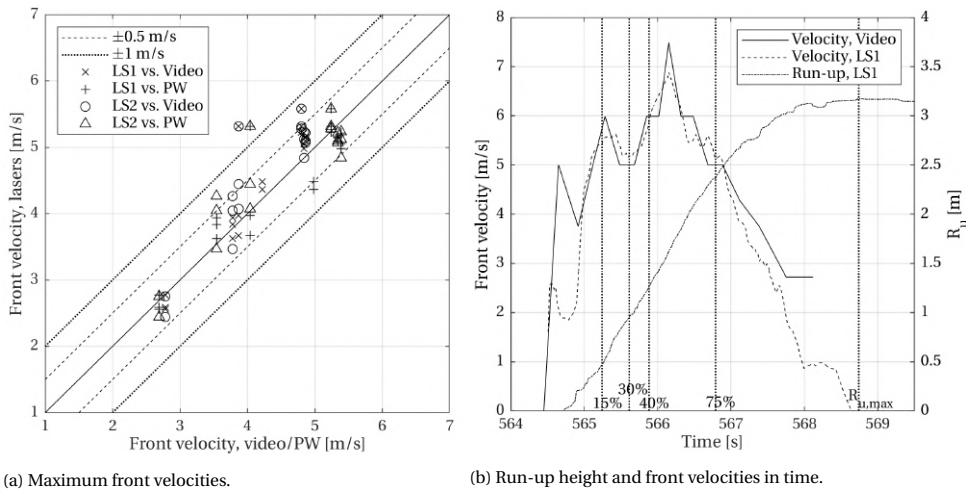


Figure 6.7: Left: Front velocities determined from laser scanner data versus paddle wheel (PW) and video data. Velocities based on front travelling from one paddle wheel to the next. Right: Run-up (dash-dot) and front velocity (dashed) time signals of laser scanner 1 and front velocity time signal (solid line) from video analysis for a single wave. The dotted vertical lines indicate percentages of the maximum run-up level.

development of the front velocity of a wave properly, and the laser scanners can be used to locate the front velocity over the slope automatically and accurately.

6.4.4. WAVE OVERTOPPING VOLUMES AND DISCHARGES

The left panel of Figure 6.8 shows the overtopping discharges as determined based on both maximum volumes above the virtual crest and run-up depth multiplied with front velocity (see section 6.3) for the test with 100 randomly generated waves, and compares them with the *EurOtop* (2018) wave overtopping equations. 81 out of 100 waves of this test could be used, due to a person standing in the laser beam.

The discharges based on the maximum volumes above the virtual crest agree well with the *EurOtop* (2018) equations. *Cete* (2019); *Hofland et al.* (2015) achieved good results for wave flume tests, by determining the overtopping using this method. However, the method had not been applied to an actual dike before. Results based on run-up depth multiplied with front velocity lie mainly within the 90% bounds of the overtopping equations, but deviate from the mean line. This overestimation mainly stems from the assumption that the front velocity around the virtual crest equals the flow velocity at the virtual crest. Since the results based on maximum volumes performed better, this method is recommended for future research.

The virtual overtopping volumes are similar to, but not the same as overtopping volumes as measured by a tank. With the virtual volumes, a pressure gradient from the run-up volume above the virtual crest is present still, which would not be present with an overtopping tank. Despite these differences, still good results were achieved here based on the maximum virtual volumes. Furthermore, the results agree well with the equations, despite the fact that these results were based on only 81 waves. Overtopping discharges

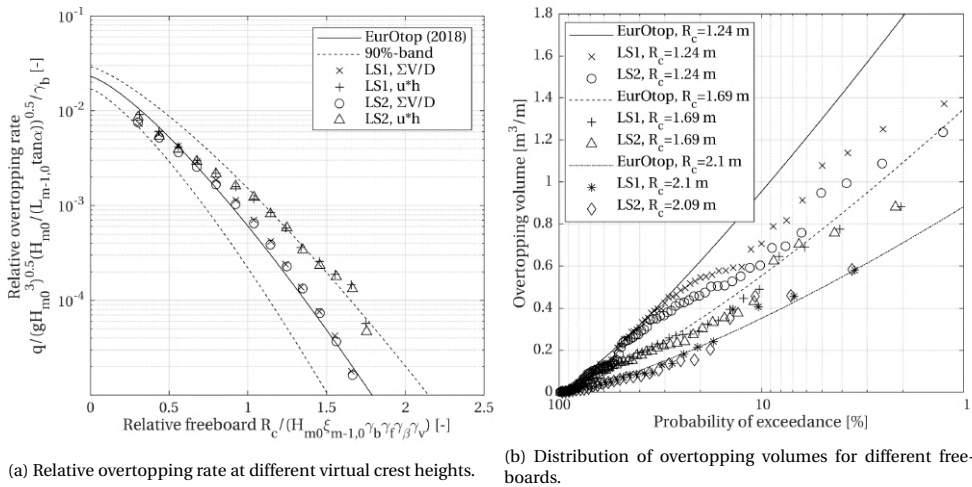


Figure 6.8: Left: Relative overtopping rate at different virtual crest heights based on maximum volumes (crosses, circles) or run-up depth multiplied with front velocity (pluses, triangles) for a test with 100 random perpendicularly incident waves, compared to [EurOtop \(2018\)](#) equations (solid and dashed lines). Right: Distribution of overtopping volumes for three different crest freeboards, compared to [EurOtop \(2018\)](#). R_c [m] is the crest freeboard, $\xi_{m-1,0}$ [-] the breaker parameter, the different γ parameters are influence factors, see [EurOtop \(2018\)](#).

6

are usually based on much larger numbers of waves. The results show that the simulator apparently simulates the correct overtopping volumes and discharges, even though the wave run-up simulator is calibrated on run-up levels and not on overtopping volumes or discharges.

Both laser scanners gave almost equal results. Only for the largest virtual crest freeboards slight differences occur, because these discharges were based on only a few waves. As mentioned before, variability in the run-up height over the width of the test section occurred. If a wave surpassed the virtual crest level at the scan line of laser scanner 1, but only barely reached the virtual crest at the scan line of laser scanner 2, this quickly results in a different mean overtopping discharge for these large freeboards. The slightly smaller discharges that were found for the lowest crest freeboards were likely caused by the fact that only simulator filling levels larger than 0.7 m were simulated, which means that the smallest waves were omitted. These smallest waves would contribute to the overtopping discharge for these small freeboards in reality.

The right panel of Figure 6.8 compares the distributions of virtual overtopping volumes with the [EurOtop \(2018\)](#) equations, which give the overtopping volume for a certain probability of exceedance, for three different freeboards. The volumes agree reasonably well for the medium and high crest levels. For the lower crest level, the results also agree reasonably well for the larger probabilities of exceedance, but for the smaller probabilities (larger volumes) the measured volumes were smaller than according to the equations. For these small freeboards, a large virtual overtopping volume means that a large run-up depth was present over a large area of the slope. If there was any bias or error in the depths as determined by the laser scanners, this bias starts to weigh stronger for these large volumes

and small freeboards, because of the large surface that is integrated. The previously mentioned pressure gradient and the run-down, which do not occur with an overtopping tank, could also have influenced the results. Finally, the limited number of waves that were simulated could have played a role.

6.5. ANALYSIS AND PREPARATION FOR OBLIQUELY INCIDENT WAVE MEASUREMENTS

The laser setup will be employed in an area with very oblique wave attack. Waves during storms are expected to arrive at angles up to 80° to the dike normal. By using two parallel laser lines, the time lag between the two measurements can give information about the obliquity of the wave attack. This section explores the possibilities of this system. The first part evaluates the first tests with the system on artificially generated oblique transient flows (waves) by the wave run-up simulator. This flow is thought to have some (but not all) characteristics similar to actual oblique waves. Therefore, it can be assessed if the time lag and corresponding shore-parallel front velocity can be obtained from these signals. The second part considers synthetic measurements, made by taking two virtual laser scanner scan lines from simulations with the numerical wave model SWASH. Based on these simulations, it is examined which characteristics of oblique waves can be obtained from the virtual laser signals. These synthetic measurements can then be compared to the exact quantities as calculated by the model. The section ends with the optimisation of the laser scanner system for future measurements in the field, during storms with oblique wave attack.

6.5.1. TESTS WITH OBLIQUE WAVES GENERATED BY THE WAVE RUN-UP SIMULATOR

WAVE RUN-UP HEIGHTS

First, the wave run-up heights as measured by the laser scanners are compared with video observations, for oblique waves generated by the run-up simulator (see the right panel of Figure 6.1). This is done in order to check if the laser scanners can measure the run-up heights of these oblique waves correctly. Figure 6.9 shows the run-up heights for a test where six 45° oblique waves were repeated three times, for both laser scanners and plotted against the run-up heights derived from videos. The same trends were found as for the perpendicularly incident waves. The data agree well, with most data within the ± 0.05 m bounds, and all but two data points within the ± 0.10 m bounds. Here, both laser scanners gave the same HH value relative to the visually observed data, see the legend of Figure 6.9, and NBI values of approximately -0.01. The differences that did occur between the lasers and video were caused mainly by the interpolation of the visually observed run-up levels between the vertical grid lines that were painted on the grass slope where the run-up was observed, see the right panel of Figure 6.1. The laser lines were located in between these vertical grid lines.

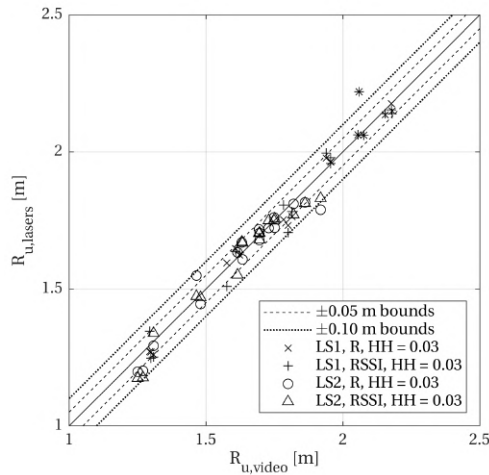


Figure 6.9: Run-up heights from both laser scanners, based on both measured distance (R) and laser reflectance ($RSSI$) versus run-up heights from videos, for a test with obliquely incident waves. Distance between laser lines 1.3 m.

6

TIME LAG AND SHORE-PARALLEL FRONT VELOCITIES

Long-crested obliquely incident waves result in a sinusoidal wave propagating along the length-axis of the dike. Actual storm waves are short-crested at the location of interest, and result in complex wave fronts. During the oblique wave tests with the simulator, it was observed that even though the waves from the simulator did all come from the same direction, as with long-crested waves, the simulator was not wide enough to simulate oblique wave attack over a sufficiently large surface. The volume of water that was released from one point was not the same as a wave crest travelling unaltered along the dike, but more akin to a jet or bore. Hence, the oblique waves as generated by the simulator do not correspond to actual obliquely incident short-crested waves. However, the flow as generated by the simulator is thought to have some characteristics similar to actual oblique waves. During actual storms in the area, sometimes jets or bores occurred that mainly propagated along the length-axis of the dike as well. Such jets were caused by very obliquely incident breaking waves. These jets do roughly correspond to the oblique waves as generated by the simulator. Therefore, it can be assessed if the time lag and corresponding shore-parallel front velocity of these waves can be obtained from the laser scanner signals. The run-up depths and overtopping discharges will not be considered further here, since no validation data were available.

It was possible to determine the time lag in the laser scanner signals. The left panel of Figure 6.10 shows an example of the time lag in the laser scanner signals for one wave. The shore-parallel front velocities (along the y -axis in Figure 6.3) could then be determined from these time lags and the distance between the scan lines. The right panel of Figure 6.10 compares the maximum shore-parallel front velocities based on the laser scanners to video observations for all 18 waves of one oblique test. The results agree reasonably well, with one outlier in the laser scanner data. The HH between laser and video results is

0.13, the NBI is 0.002. The differences that occur are caused mostly by the limited 30 fps framerate of the videos. The maximum velocities of the higher filling levels are approximately equal. Apparently, the simulator generates these larger waves with an approximately constant shore-parallel velocity. Thus, the time lags between the laser signals can potentially be used to determine the shore-parallel velocities of such jets during actual storms in the field.

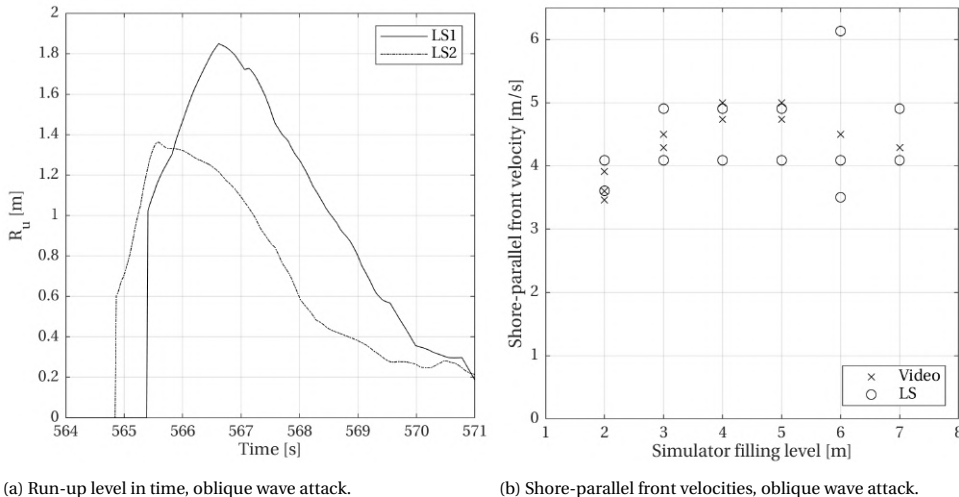


Figure 6.10: Left: Snapshot of run-up level in time for both laser scanners during oblique wave attack. The time lag and different maximum run-up levels are visible. Right: Maximum shore-parallel front velocities determined from laser scanner data (circles) versus video data (crosses). Laser velocities based on the time lags between the laser scanner signals. Distance between laser lines 2.5 m.

6.5.2. NUMERICAL SWASH SIMULATIONS

This section considers the simulations performed with the numerical wave model SWASH. These simulations are used to examine which characteristics of oblique waves can be obtained from synthetic measurements with two virtual laser scanner scan lines. The studied characteristics are the wave peak period, the wave angle of incidence and the wave overtopping discharge. These synthetic measurements can then be compared to the exact quantities as calculated by the model. Finally, the obtained results are used to determine the ideal distance between the laser scanner scan lines.

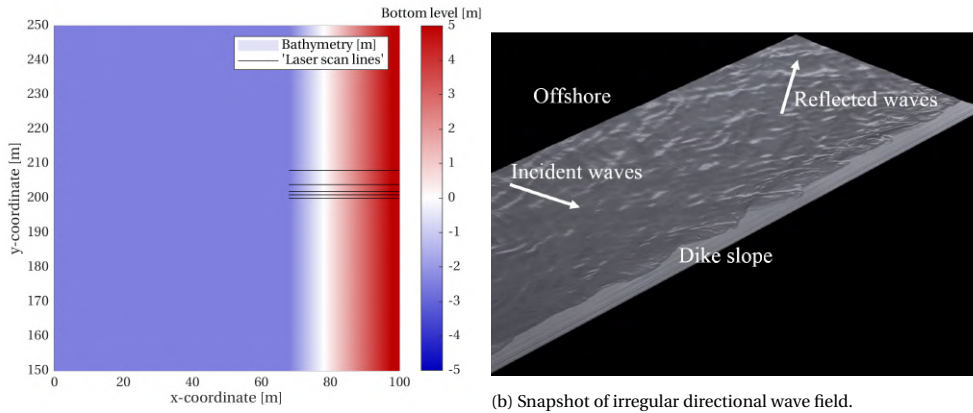
For these simulations, a rectangular basin was used, with dimensions of 100 m cross-shore and 300 m alongshore, and grid cell sizes ranging between 0.10 m and 0.20 m. The waves entered the domain from the west, and either a vertical wall (full reflection) or a 1:4 dike slope (partial reflection) was located at the eastern boundary. The northern and southern boundaries were absorbing and located far enough from the area of interest such that boundary effects did not influence this area of interest. Tests were done for water depths of 10 m and 2.5 m. Both monochromatic waves and irregular short-crested wave fields were applied. Monochromatic waves were chosen, since the analysis method was derived based on monochromatic waves, see below. The irregular short-crested waves

were used, since such conditions represent the conditions at the location of interest, the Eems-Dollard estuary. (Significant) incoming wave heights were set to 1 m, the (peak) period was set to 4 s, angles of incidence ranged from 15° to 60°, roughly corresponding to yearly storm conditions in the area of interest. The irregular wave field was characterised by a standard JONSWAP spectrum (K. Hasselmann et al., 1973), with a directional spreading of 25°.

Test no. [-]	Water depth d [m]	Boundary type [-]	Wave boundary condition [-]	Angle of incidence β [°]
1	10	Vertical wall	Monochromatic	15
2	10	Vertical wall	Monochromatic	45
3	10	Vertical wall	Monochromatic	60
4	2.5	Vertical wall	Monochromatic	15
5	2.5	Vertical wall	Monochromatic	45
6	2.5	Vertical wall	Monochromatic	60
7	2.5	Slope	Monochromatic	15
8	2.5	Slope	Monochromatic	45
9	2.5	Slope	Monochromatic	60
10	2.5	Slope	JONSWAP	15
11	2.5	Slope	JONSWAP	35
12	2.5	Slope	JONSWAP	45

Table 6.2: SWASH simulations that were performed. Angles of incidence β ranging from 15° to 60°, (significant) wave height $H_s = 1$ m for all tests, wave (peak) period $T_p = 4$ s for all tests.

Table 6.2 gives an overview of the SWASH simulations that were performed. Water depth output was obtained along 5 virtual laser scan lines with an output frequency of 50 Hz, at distances of 1 m, 2 m, 4 m and 8 m from the first line, corresponding to the characteristics of the actual laser measurements. On the dike slope, this water depth output is the same as the run-up depth as measured by the laser scanners. Furthermore, for some of the cases discharge output q [m³/s/m] (q -parameter in SWASH, integral of positive flux at a certain virtual crest level) was obtained at several virtual crest levels. Finally, for three cases a (virtual) overtopping box was built into the model for further analysis of the overtopping discharges. The left panel of Figure 6.11 presents part of the 2.5 m deep basin with a dike slope, with the virtual laser lines indicated as well. Refer to <https://youtu.be/cy-VWmV7aUA> for an example wave field, of which the right panel of Figure 6.11 gives a snapshot.



(a) Part of the SWASH model basin.

(b) Snapshot of irregular directional wave field.

Figure 6.11: Left: Part of the 2.5 m deep SWASH basin with a 1:4 dike slope. The virtual laser scan lines are indicated as well. Right: Snapshot of irregular directional wave field, with an angle of incidence of 45° and a directional spreading of 25° . Also refer to <https://youtu.be/cy-VWmV7aUA>.

DATA ANALYSIS

The time lag between both laser scanner signals was shown in Figure 6.10. From this time lag between the two laser signals, the angle of incidence can be obtained. Figure 6.12 shows this schematically, providing the definitions for the analysis method. The solid lines represent an obliquely incident sinusoidal wave, with the wave direction indicated by the arrow, propagating towards the dike, with a phase velocity c [m/s] and a wavelength L [m]. The dike toe and crest are indicated with the thick solid lines. This wave causes a projected wave to travel along the dike, with a velocity c' [m/s] and a wavelength L' [m] (dashed lines). This projected wave is sampled at the two locations LS1 and LS2 (dotted lines), at a distance D [m] from one another.

From the numerical simulations, the run-up was determined in the same way as for the actual laser scanner measurements, by determining the highest location on the slope where the run-up depth was larger than zero. The first step in the further analysis is to determine variance density spectra from the run-up signals of the (virtual) laser scanners, with finite and discrete Fourier transforms (e.g. Bendat & Piersol, 1971):

$$X_j(f, N\Delta t) = \sum_{n=1}^N R_{u,j}(n\Delta t) e^{-i2\pi f n\Delta t} \quad (6.4)$$

with $R_{u,j}$ ($j = 1, 2$) [m] the run-up time signals for the scan lines, f [Hz] the frequency, Δt [s] the sampling interval, n integers and N the window length in samples. Next, the auto-spectral density is determined:

$$S_{jj}(f) = \frac{2}{N\Delta t} E \left[|X_j(f, N\Delta t)|^2 \right] \quad (6.5)$$

with $E[\]$ being an ensemble average over the number of windows. Since these spectra are based on the run-up time series, they do not represent a real wave spectrum, from

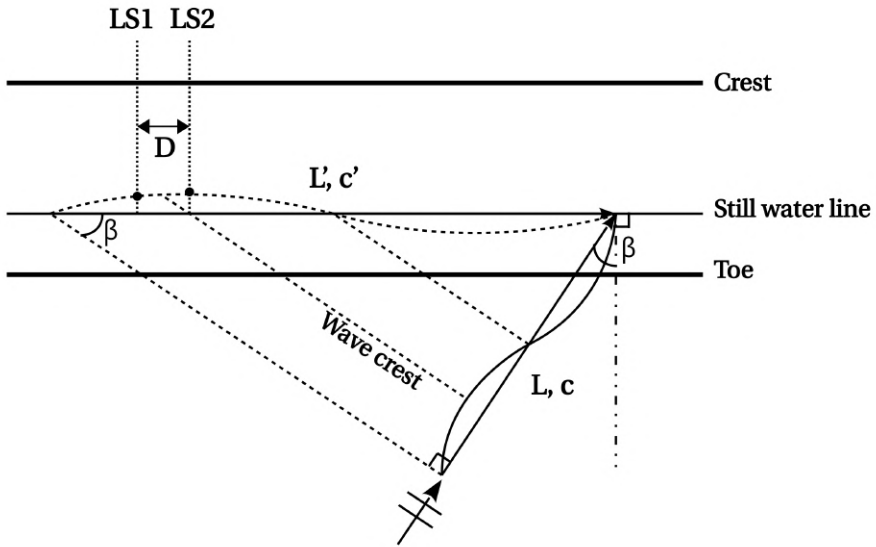


Figure 6.12: Angle of incidence analysis definitions, with an obliquely incident sinusoidal wave (wave direction indicated by the arrow) propagating towards the dike (toe and crest indicated with thick solid lines), with a phase velocity c and a wavelength L . This wave causes a projected wave to travel along the dike, with a velocity c' and a length L' (dashed lines). β is the angle of incidence. Laser scanner scan lines indicated by the dotted lines (LS1 and LS2), with a distance D between them.

6

which e.g. a wave height can be determined. However, from the peak(s) of these spectra, the wave peak frequency f_p [Hz] can be determined. After that, the cross-spectral density is determined from both run-up signals for each pair of virtual laser lines at different distances from one another (1 m, 2 m, 4 m and 8 m apart):

$$S_{12}(f) = \frac{2}{N\Delta t} E[X_1^*(f, N\Delta t) X_2(f, N\Delta t)] \quad (6.6)$$

with X^* the complex conjugate of X . All previous equations in this section are defined for $0 < f < 1/\Delta t$. Martins, Blenkinsopp, and Zang (2016) used a similar approach to determine wave peak periods and celerities based on data as measured by a single laser scanner. The 'time lag spectrum' $\zeta(f)$ is obtained from the cross-spectrum at each frequency, as follows:

$$\zeta(f) = \frac{\arg(S_{12}(f))}{2\pi f} \quad (6.7)$$

From the spectrum of time lags between these virtual laser scanners and the distance between both laser lines D , the phase velocity of the projected waves can be determined at each frequency:

$$c'(f) = \frac{D}{\zeta(f)} \quad (6.8)$$

Next, the incoming wave celerity c is determined at each frequency according to linear

wave theory. Finally, the 'angle of incidence spectrum' $\beta(f)$ can be found with trigonometry, see Figure 6.12 and Figure 6.13:

$$\beta(f) = \sin^{-1} \frac{c}{c'} \quad (6.9)$$

E.g. the peak angle of incidence can then be determined by taking the angle of incidence corresponding to the peak frequency from the angle of incidence spectrum, see Figure 6.13.

The method above was based on monochromatic, sinusoidal waves in deep water, whereby it was assumed that the wave angle of incidence is the same as the angle of the breaking wave on the slope. Next, it will be assessed whether the method performs well for realistic wave conditions of increasing complexity.

WAVE (PEAK) PERIODS

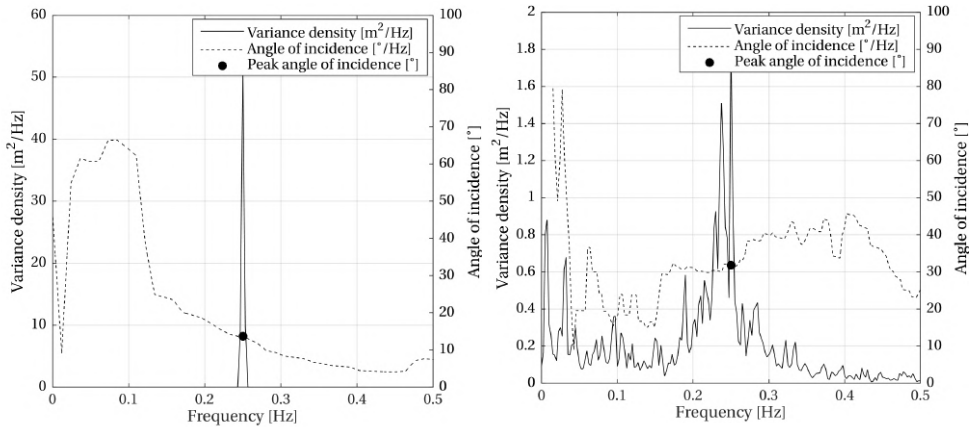
Table 6.2 gives the SWASH simulations that were performed. The wave peak periods were determined from the auto-spectral densities of the run-up signals (Equation 6.5) and compared to the wave peak period of 4 s as applied in SWASH. The overall deviations were very small (HH = 0.006, NBI = 0.01). Hence, with this method a good prediction of the incoming wave period can be determined with a laser scanner, without additional measurements offshore.

ANGLES OF INCIDENCE

The angle of incidence spectra (Equation 6.9) give the angle of incidence for each mode in the spectrum of the measured run-up. Figure 6.13 gives example variance density spectra and angle of incidence spectra of a monochromatic and an irregular short-crested case. Peak angles of incidence are indicated with a circle. Figure 6.14 shows these estimated peak angles of incidence as determined from the virtual laser run-up data for all SWASH simulations. The figure compares them with the modelled angles of incidence.

Generally, the angle of incidence results showed a more constant trend over the entire frequency domain for the monochromatic cases than for the JONSWAP cases. The left panel of Figure 6.13 seems to show larger angles of incidence for the lower frequencies, but note that no energy is present outside the peak frequency. Hence, this likely arose from the data analysis, and was not a physical phenomenon. Around the peak frequency, the angle of incidence lies quite close to the modelled 15°, thus being reliable. The right panel of Figure 6.13 shows more scatter, caused by the shallow water depth and directional spreading of the waves. Larger deviations were expected for the more complex cases, as the analysis method was based on deep water, unidirectional and monochromatic waves. Another likely cause is that the analysis method was based on the assumption that the wave angle of incidence is the same as the angle of the breaking wave on the slope, which could differ somewhat in reality. However, as for the monochromatic case, around the peak frequency a more constant trend occurs, with the estimated angles of incidence quite close to the modelled angle of incidence of 35°. Similar trends were found for the other simulations as well.

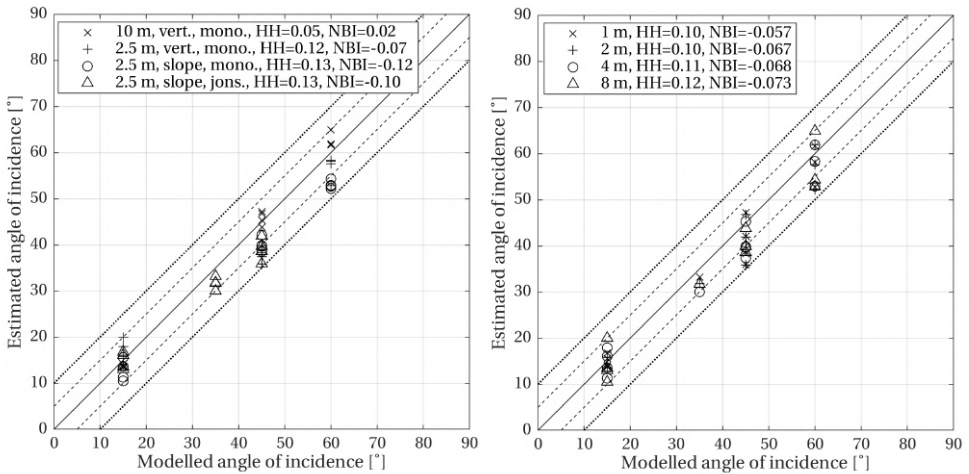
The left panel of Figure 6.14 compares the estimated angles of incidence with the modelled ones. The data were grouped according to the simulation conditions. The data agree quite well, with most values within the $\pm 5^\circ$ error bounds and all values within the $\pm 10^\circ$



(a) Variance density and angle of incidence spectra, monochromatic waves. (b) Variance density and angle of incidence spectra, irregular, short-crested waves.

Figure 6.13: Variance density spectra (solid lines) based on virtual laser line run-up data and angle of incidence spectra (Equation 6.9, dashed lines) for two cases. Left: Angle of incidence of 15°, water depth of 10 m, a vertical wall and monochromatic waves. Right: Angle of incidence of 35°, water depth of 2.5 m, 1:4 dike slope and irregular, short-crested waves. The angle of incidence spectra give the angle of incidence for each mode in the spectrum of the measured run-up. The angle of incidence β was defined according to Figure 6.12. Peak angles of incidence indicated by the circles.

6



(a) Angle of incidence, grouped by wave simulation conditions. (b) Angle of incidence, grouped by distance between scan lines.

Figure 6.14: Wave angle of incidence data for all SWASH simulations, comparing peak angles of incidence as modelled by SWASH with peak angles of incidence derived from virtual laser scanner data (see Figure 6.13). Left: Data grouped according to simulation conditions (water depth 10 m or 2.5 m, vertical wall or 1:4 slope, monochromatic or irregular waves). Right: Data grouped according to distance between the scan lines (1 m, 2 m, 4 m or 8 m). HH and NBI values, and $\pm 5^\circ$ and $\pm 10^\circ$ error bounds (dashed and dotted lines) given as well.

bounds. The results for a water depth of 10 m, a vertical wall and monochromatic waves agree very well ($HH = 0.05$, $NBI = 0.02$). This can be explained by the fact that the analysis method was based on such conditions as well. The HH and NBI values show that generally larger deviations were found with increasing complexity of the modelled conditions. These larger deviations mainly arose from the shallower water depth.

Hence, the method determines the angle of incidence at the peak frequency quite well. The performance could potentially be further improved by lengthening the simulation time, thus obtaining longer timeseries and increased statistical reliability. With this method, an estimate of the incoming peak wave direction could theoretically be determined from the cross-correlation between the two run-up signals, without additional measurements offshore. However, further validation in the field is still recommended.

WAVE OVERTOPPING DISCHARGES

The mean wave overtopping discharges were determined from the virtual SWASH laser lines in the same way as for the actual laser scanner measurements, by determining the maximum volumes above several virtual crest levels by integrating the run-up depths above these crest levels. These overtopping discharges were then compared to the SWASH discharge output parameter q , and to the overtopping discharge as determined from the virtual overtopping box in the model.

Figure 6.15 shows the results for three JONSWAP cases, being tests 10 to 12, with angles of incidence of 15° , 35° and 45° . The agreement between the virtual laser data, the virtual overtopping box and the SWASH output parameter q is important, as agreement between these three shows consistency and reliability of the method used to determine the overtopping discharge from the laser data. This is the case here, since data from all three methods lie quite close to one another. The virtual laser results and the SWASH output parameter q results agree well. The overtopping box results, which were determined at only one crest level, deviate slightly more, but still agree quite well. Hence, the method as used to determine the mean overtopping discharges from the laser data, by integrating run-up depths and determining maximum volumes above the virtual crest, can be considered reliable and consistent with the SWASH q parameter and virtual overtopping box results. Therefore, the method is considered reliable enough to be used with field data from actual storms with oblique wave attack.

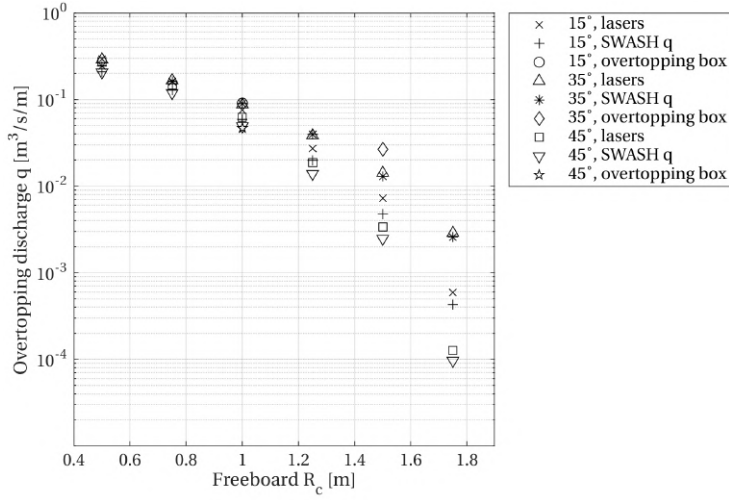


Figure 6.15: Overtopping discharge for several virtual crest levels as determined from the virtual laser scanner data for three SWASH simulations. Tests 10 to 12, with angles of incidence of 15° (crosses), 35° (triangles) and 45° (squares). SWASH discharge parameter q (pluses, asterisks, down-pointing triangles) and virtual overtopping box data (circles, diamonds, pentagrams) plotted as well. Simulations with a 1:4 slope, a JONSWAP spectrum with $H_s = 1$ m and $T_p = 4$ s.

6

PREFERRED DISTANCE BETWEEN LASER SCANNER SCAN LINES

Finally, the preferred distance between the laser lines can be determined, based on the previous analyses of front velocities, wave peak periods, angles of incidence and overtopping discharges. This preferred distance can then be used for future measurements with the system in the field, during actual storms with oblique wave attack.

Around the Nyquist frequency, here $f_{Nyq} = 1/2\Delta t = 25$ Hz, large errors are made when determining a spectrum. Generally, it is recommended to choose the Nyquist frequency four times larger than the mean frequency (e.g. [Holthuijsen, 2007](#)). Hence, the minimum wave period that can be measured with the laser scanners lies around 0.16 s. This minimum wave period lies past the wind waves regime. Thus, this is not really a limitation, as wind waves will be measured with the system.

Furthermore, a balance between the distance between the laser scanner scan lines and the wave period can be derived, based on the aliasing effect. To be able to distinguish the actual wave frequency of a wave passing by the laser scanners, the distance between the laser lines needs to be smaller than $1/4$ of the projected wavelength L' (with $1/2L'$ or L' , the frequency would not be uniquely defined):

$$D_{lasers} \leq 1/4L' \text{ or } L' \geq 4D_{lasers} \quad (6.10)$$

$$D_{lasers} \leq L/(4 \cos \alpha) \text{ or } L \geq \cos \alpha 4D_{lasers} \quad (6.11)$$

From these relations, the maximum distance between the laser scanner scan lines can be determined, to be able to properly measure a certain wave with a certain frequency. As an example, a wave period of 4 s, a water depth of 2.5 m and an angle of incidence of 45° would result in a maximum distance between the laser lines of approximately 7 m.

2.5 m distance between the laser lines ($HH = 0.13$, $NBI = 0.002$) outperformed 1.3 m ($HH = 0.14$, $NBI = -0.017$) and 3.4 m ($HH = 0.22$, $NBI = -0.052$) between the laser lines in estimating the shore-parallel component of the front velocity of the oblique jets as generated by the wave run-up simulator. The scan frequency of 50 Hz is probably the limiting factor for the smaller distance between the laser lines. The limiting factor for the larger distance between the laser lines is a change in the front velocity (and direction) that may occur in between the laser lines.

The estimation of the wave (peak) period does not directly depend on the distance between the laser lines. Hence, no clear preference for an ideal distance between the laser lines could be determined from the wave period results.

The right panel of Figure 6.14 compares the estimated angles of incidence with the modelled ones by SWASH, grouped according to distance between the virtual scan lines. Only small differences were found between the different scan line distances. Overall, 1 m and 2 m distance performed best, with 1 m slightly outperforming 2 m. However, 2 m distance performed best for the JONSWAP cases, the most realistic cases, with $HH = 0.08$ and $NBI = -0.08$. The JONSWAP conditions simulated here roughly correspond to the conditions in the area of interest, the Eems-Dollard estuary. Furthermore, 2.5 m distance between the laser lines performed best for the determination of the shore-parallel component of the front velocity. Therefore, 2 m distance between the laser lines is recommended as the distance for further measurements in the area.

At other locations, the ideal distance might be different. As a rule of thumb for the distance between the laser scanners, $L_p/16$ could be used, with L_p [m] the local peak wavelength at the toe of the structure, but ideally further research should be performed for such cases.

6.6. CONCLUSIONS

This chapter presents the implementation of an innovative system to measure wave run-up and calculate wave overtopping for both perpendicularly and obliquely incident waves, using two coupled laser scanners at a field site. Furthermore, the system can determine the run-up depths and front velocities. Additionally, from the measured run-up signals, the wave (peak) period can be determined, and a reasonable estimate can be given of the wave angle of incidence at the peak frequency. The chapter describes the first calibration tests with the system, with perpendicular and oblique run-up generated by the wave run-up simulator on the grass slope of a dike, as well as numerical simulations with the phase-resolving numerical wave model SWASH to assess the set-up for synthetic but realistic oblique wave attack in more detail.

The measured run-up heights agreed well with the visually observed run-up, for both perpendicularly and obliquely incident waves. Differences of only a few centimetres were found, both for the run-up based on measured distance and based on laser reflectance.

Run-up depths were measured reliably with the laser scanners, at locations higher on the dike slope. Closer to the simulator, the lasers gave too large and unreliable depths due to foam, spray and large turbulence. The advantage compared to the generally used surf boards is that the depth can be determined over the whole slope, not just at a few locations.

Front velocities of perpendicularly incident waves could accurately be determined

from the laser scanner data. The shore-parallel velocity component could be determined reasonably well from the time lag between the laser signals for oblique waves as generated by the simulator. However, further research in the field is recommended.

The overtopping discharges based on maximum volumes agreed well with the [EurO-top \(2018\)](#) equations for perpendicularly incident waves. The discharges based on run-up depths multiplied with front velocities did not agree as well, although with most values within the 90% bounds of the overtopping equations.

To gain more insight in the potential performance of the system during actual oblique wave attack during a storm, numerical simulations were performed, modelling virtual laser scanner scan lines. The method employed here to determine the overtopping discharge, by integrating the run-up depth and determining maximum volumes above the virtual crest, was compared to the SWASH-model discharge output parameter q and a virtual overtopping box built into the model, and can be considered consistent and reliable.

From the virtual laser scanner run-up signals, the incoming wave (peak) period could also be accurately determined. Furthermore, from the cross-correlation between the two run-up signals, a reasonable estimate of the wave angle of incidence at the peak frequency could be determined. Determining these parameters from the run-up signals could alleviate the need of additional measurements offshore. However, measurements of the wave height remain necessary and further validation in the field is required.

For the cases considered here, the wave run-up and run-up depths could be determined as accurately with the laser scanner system as with the conventionally used methods. An advantage of the system is that more insight is gained into certain parameters than with the conventional measurement techniques, e.g. into the depths and velocities, which are measured with high resolution. Since the system is mobile, it can measure at several dike locations by moving the system every few years.

The preferred distance between the laser lines was determined as $L_p/16$, being 2 m for the expected conditions in the Eems-Dollard estuary. Since this calibration was successful, the system will now be placed on the dike in the Eems-Dollard estuary to measure oblique wave run-up and overtopping during severe winter storms for the next 3 years, additional to the measurements with overtopping tanks.¹ The expectation is that measuring during storms and validation with data from the overtopping tanks will lead to new insights in and guidelines on the influence of oblique wave attack on wave overtopping.

ACKNOWLEDGEMENTS

This study was made possible by the inspiring input of the late Gerbrant van Vledder. This chapter was immensely improved by his knowledge, dedication and guidance. We would like to thank the POV Waddenzeedijken for the use of the wave run-up simulator, as well as Gerben van der Meer, Jan Bakker and Frans Roorda for their help with the wave run-up tests. This study was supported by Waterschap Noorderzijlvest and the Hoogwaterbeschermingsprogramma.

¹The system was placed on the dike in the Eems-Dollard estuary in October 2019.

7

FIELD MEASUREMENTS OF VERY OBLIQUE WAVE RUN-UP AND OVERTOPPING WITH LASER SCANNERS

*Progress is made by trial and failure;
the failures are generally a hundred times more numerous than the successes;
yet they are usually left unchronicled.*

William Ramsay

This chapter presents the first field measurements with an innovative laser scanner system, during a severe winter storm. The goal of this chapter is to validate this system for measuring wave run-up and wave overtopping parameters during storms with very oblique wave attack. To this end, the chapter describes the analysis of the data obtained during storm Ciara (10 - 12 February 2020) and validates the results with data from overtopping tanks and video recordings. Storm Ciara was a highly unique and complex storm, with offshore-directed wind and alongshore-directed waves at the dike. This posed large challenges for measuring the front velocities. The wave run-up heights and the overtopping discharges could be measured accurately with the laser scanners. Reasonable results were achieved for the run-up depths. This has led to several new insights into the probability distribution of oblique wave run-up and the run-up depths of up-rushing oblique waves. The 2D front velocities that were derived from laser data deviated more from a

This chapter has been published as **Oosterlo, P.**, Hofland, B., Van der Meer, J.W., Overduin, M., & Steendam, G.J. (2021). Field measurements of very oblique wave run-up and overtopping with laser scanners. *Journal of Coastal and Hydraulic Structures*, 1.

commonly used equation. The wave angle of incidence could not be determined as accurately for storm Ciara, as in previous calibration tests and numerical simulations with less oblique wave attack. This arose from the very oblique wave attack during storm Ciara.

7.1. INTRODUCTION

Wave run-up and wave overtopping measurements in the field are scarce, since they are very difficult to perform. Wave run-up is typically measured in the field using step gauges (e.g. [Wenneker et al., 2016](#)). Other techniques, such as stereo-photogrammetry (e.g. [De Vries et al., 2011](#)), ultrasonic altimeters (e.g. [Matias et al., 2014](#)) and video recordings (e.g. [Vousdoukas, Wziatek, & Almeida, 2012](#)) have also been used. More recent studies (e.g. [Brodie et al., 2012](#); [Vousdoukas et al., 2014](#)) used terrestrial laser scanners (LIDARs) to measure the wave run-up in the field as well. Wave overtopping measurements in the field are performed even less. Recently, a 3D mesh of capacitance wires was used in an attempt to measure wave overtopping in the field ([Pullen et al., 2019](#)). However, typically wave overtopping measurements in the field are performed using overtopping tanks (e.g. [De Rouck et al., 2009](#); [Van der Meer et al., 2019](#); [Wenneker et al., 2016](#)). This is a robust method to measure wave overtopping, but fixed at each location and at a fixed elevation.

[Oosterlo, Hofland, Van der Meer, Overduin, and Steendam \(2021\)](#); [Oosterlo et al. \(2019\)](#) developed an alternative innovative and more flexible solution, using two terrestrial laser scanners. They showed that the system can measure the run-up heights, run-up depths (flow depths, layer thicknesses) and front velocities of up-rushing waves on a dike in field situations with oblique wave attack. From these measurements, also the virtual wave overtopping can be calculated at any height level. Furthermore, an estimate of the (peak) wave period and angle of incidence can be obtained from the data. Determining these two parameters from the run-up signals could alleviate the need for additional measurements offshore. Another advantage of the system is that more insight is gained into certain parameters than with the conventional measurement techniques, e.g. into the depths and velocities, which are measured with high resolution. Since the system is mobile, it can be used to measure at several dike locations by moving the system every few years. The present chapter builds on the system calibration of [Oosterlo et al. \(2021, 2019\)](#).

An extensive field measurement project is being performed in the Eems-Dollard estuary in the north of the Netherlands for a period of 12 years. The measurements started in 2018, measuring wind, water levels, waves, wave run-up and overtopping. The estuary consists of deep channels and shallow tidal flats and is part of the Wadden Sea, a shallow shelf sea (see the left panel of [Figure 7.1](#)). A particular aspect for this area is that the dike design conditions consist of very obliquely incident waves, up to 80° relative to the dike normal. As the reliability of the models as used for the Dutch dike safety assessment has not been sufficiently validated for such conditions, the aim of the measurements is twofold. First, to understand the processes yielding nearshore wave conditions better, ultimately leading to improved numerical prediction models. Second, to understand the processes related to oblique wave run-up and overtopping better, leading to improved prediction methods. In the project, the wave overtopping discharge is measured with four wave overtopping tanks built into dikes at two locations.

The laser scanner system of [Oosterlo et al. \(2021, 2019\)](#) has been updated and upgraded, and is now placed next to two of the overtopping tanks on the dike in the Eems-

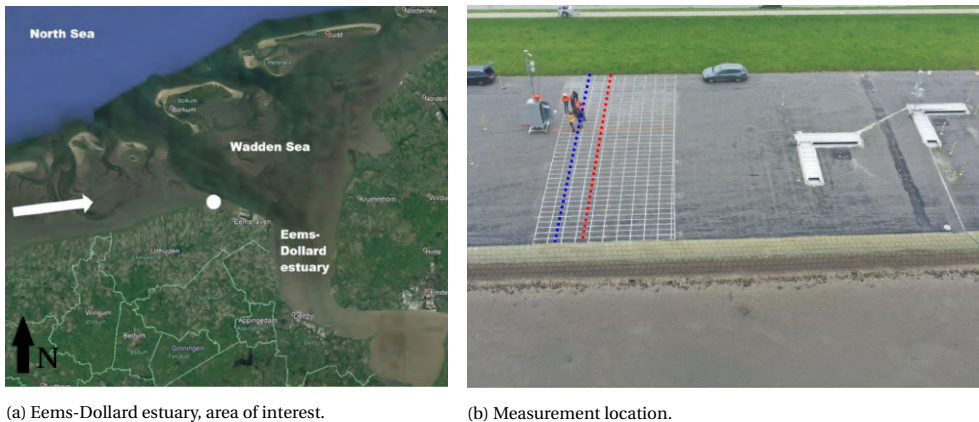


Figure 7.1: Left: The Eems-Dollard estuary in the Netherlands, area of interest of the field measurement project. Laser scanner system location indicated with the white dot. Wind direction during storm Ciara indicated with the arrow. Satellite image: ©2021 GeoBasis-DE/BKG, ©2021 Google. Data: SIO, NOAA, U.S. Navy, NGA, GEBCO. Right: Drone overview of measurement location, with the laser scanner pole (left), the approximate laser scan line locations (blue and red dashed lines), the painted grid on the slope, and two of the overtopping tanks (right).

Dollard estuary, to measure during actual severe winter storms. Previous research measuring wave run-up in the field using laser scanners often used only one laser scanner with a low temporal resolution. To the best of the authors' knowledge, this is the first time that a system using two laser scanners is used to measure these directional parameters in the field, with a high resolution, and during an actual storm with very oblique wave attack.

The goal of this chapter is to validate this innovative system for measuring wave run-up and wave overtopping parameters during an actual severe winter storm with very oblique wave attack. To this end, the present chapter describes the analysis of the data obtained during storm Ciara (10 - 12 February 2020) and validation with data from the overtopping tanks and video recordings. Furthermore, the chapter compares the data as gathered during storm Ciara to the current knowledge on wave overtopping, to gain new insights in the influence of very oblique wave attack on wave overtopping.

The outline of this chapter is as follows. First, the set-up of the new system is described briefly. After that, section 7.3 gives a short description of the measured storm. The next section describes the methods, split into the system calibration, the data processing and the data analysis. This is followed by the results and validation of the measured parameters in section 7.5. The final section gives the conclusions and presents an outlook on the next steps in this research program.

7.2. SYSTEM SET-UP

Oosterlo et al. (2021, 2019) described the first version of the laser scanner system. Recently, an updated version of the system was developed, now using a retractable vertical pole in a cabinet instead of a tripod perpendicular to the dike slope. In October 2019, the new system was placed on the dike at Uithuizerwad in the Eems-Dollard estuary, next to two of the overtopping tanks. See the right panel of Figure 7.1 and Figure 7.2 for an

overview of the measurement location and the system set-up. The retractable pole and cabinet make the system easier to place, set-up and relocate. The waterproof cabinet also contains all the auxiliary devices for the connection of the instruments and the data storage. The present system uses two SICK LMS511pro HR laser scanners, cost-efficient laser scanners with a near-infrared (905 nm) laser beam, which is the newest version of a commonly used laser scanner in previous research (e.g. in Hofland et al., 2015; Streicher et al., 2013). Also, a camera with a framerate of 50 fps is attached to the pole, to further validate the run-up heights and front velocities, see the right panel of Figure 7.2. Furthermore, an accelerometer is attached to the upper laser scanner, to be able to correlate possible outliers with vibrations of the system. The laser scanners measure both the distance R [m] to a surface and the reflected signal intensity RSSI [-] (Received Signal Strength Indicator, a dimensionless value between 0 and 255), which provides information on the type of surface. The scanners have a sampling frequency of 50 Hz, an angular resolution of 0.333° , are synchronised, and detect the last out of five echoes, to reduce the influence of e.g. rain on the data, see Oosterlo et al. (2019). The two laser scanners each scan a line parallel to each other, running from the dike toe to the crest (blue and red dashed lines in the right panel of Figure 7.1). To aid with the video analysis, a 20 m x 10 m grid with a resolution of 0.5 m by 1 m was painted on the slope, also refer to the right panel of Figure 7.1 and the left panel of Figure 7.2.

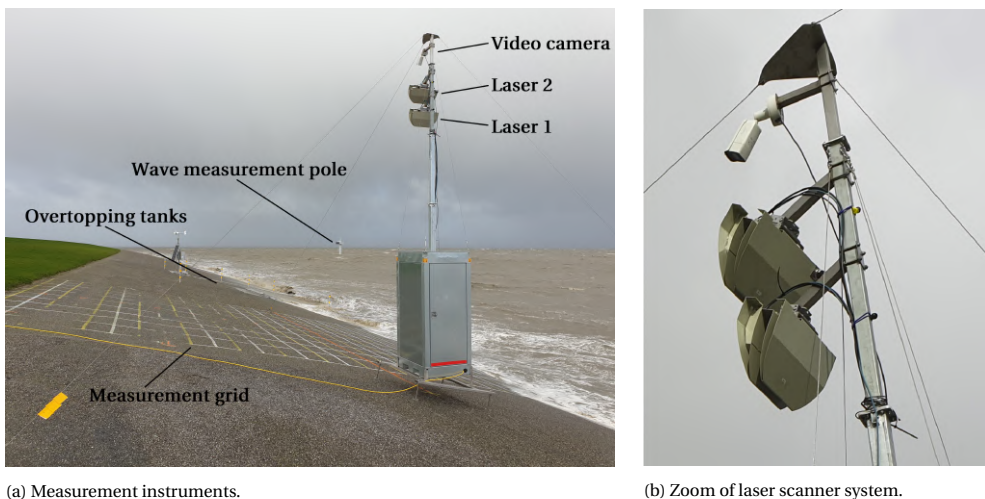


Figure 7.2: Left: New laser scanner system on the dike in the Eems-Dollard estuary, next to the overtopping tanks, during storm Ciara. The Rijkswaterstaat (wave) measurement pole can be seen in the distance. Rijkswaterstaat is the Directorate-General for Public Works and Water Management in the Netherlands. Right: From the bottom to the top, Laser scanner 1, laser scanner 2, video camera.

The local dike slope consists of concrete blocks up to approximately 2 m+NAP (Normaal Amsterdams Peil, Dutch ordnance level, roughly corresponding to mean sea level), asphalt from 2 m+NAP until 6.6 m+NAP and grass from 6.6 m+NAP until approximately 9 m+NAP. The average dike slope at the measurement location is 1:4.5. The cabinet with the laser scanner pole was placed on the asphalt slope at a height of 5 m+NAP. The laser scan-

ners are located at heights of 5.55 m and 6.04 m above the slope, hence at 10.55 m+NAP and 11.04 m+NAP. The distance between the laser scan lines is 1.97 m, which is the optimal spacing (Oosterlo et al., 2021). The resulting slant angles (ϕ_1 and ϕ_2 in Figure 7.7) are 26.0° and 37.6°.

The overtopping tanks are placed inside and flush with the dike slope (see the right panel of Figure 7.1 and Figure 7.3) and collect water through thin openings at elevations of 4.4 m+NAP and 5.3 m+NAP. The tanks are approximately 0.8 m deep and 1.3 m wide, and have a 4 m-wide opening for entering by overtopping waves. The collected volume of water in the tanks is monitored by measuring the water level in the tanks by pressure transducers, and the water can flow out freely through a gate in an outflow channel (Van der Meer et al., 2019).



Figure 7.3: Excavation of the dike slope and placement of the overtopping tanks inside the dike.

7.3. MEASUREMENTS DURING STORM CIARA

The focus of this chapter lies on the measurements performed during storm Ciara. Storm Ciara was an extratropical cyclone, which hit large parts of northern Europe starting on 7 February 2020. Measurements were performed from 10-02-2020 to 12-02-2020. Even though the largest wind velocities occurred on 9 February, the south-southwestern wind direction as present on the 9th did not lead to large water levels or wave heights at the location of interest. This is due to the orientation of the location of interest (see the left panel of Figure 7.1). From 10 to 12 February, the wind direction ranged between west-southwest and west. During these three days, the maximum measured average wind velocity was 21 m/s, the maximum water level h was 3.03 m+NAP, the maximum significant wave height H_{m0} was 0.97 m and the corresponding wave peak period T_p was 4.35 s, also see Table 7.1. Note the unusual ratio of $T_p / T_{m-1,0}$. For a JONSWAP spectrum, this ratio is approximately 1.1. Here, it was approximately 0.9, which indicates a non-standard spectral shape.

The laser scanner system was previously tested for normally and obliquely incident bores (Oosterlo et al., 2021, 2019). Ciara was the first actual storm that was measured with

the system, and immediately tested it to the extreme. Ciara was a highly unique storm, with offshore-directed wind at the measurement location and waves that refracted somewhat to the shallow flats in front of the dike to become almost alongshore-directed waves at the dike, see Figure 7.4. Thus, Ciara caused highly complex conditions at the measurement location with very oblique wave attack with angles of incidence of approximately 70° and more. This poses large challenges for measuring and even just defining, e.g. the 2D front velocities and the overtopping volumes and discharges, also see Figure 7.5. Furthermore, the offshore-directed wind and very obliquely incident waves led to few overtopping waves (≈ 50) and therefore a small overtopping discharge (≈ 0.1 l/s/m) in the lower overtopping tank at 4.4 m+NAP.

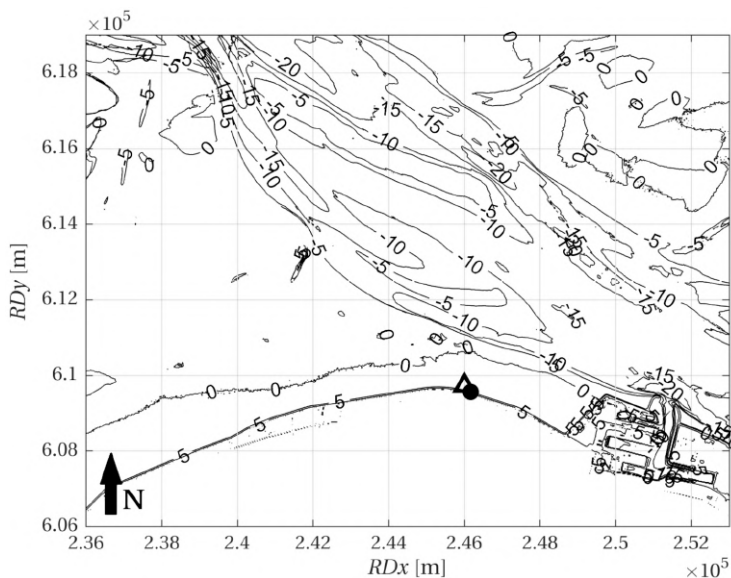


Figure 7.4: Bathymetry of the area of interest, shown as depth contours [m+NAP], with the deep main tidal channel and shallow flats in front of the dike. Laser scanner system (circle) and measurement pole (triangle) locations indicated.

Since the tide at the location of interest is semidiurnal, from 10 to 12 February five high tides were measured. During two of these five high tides more than one wave entered the lower wave overtopping tank. Therefore, these two high tides were selected for further analysis, and from these two high tides two storm peak periods were derived. Table 7.1 and Figure 7.6 present the characteristics of the two storm peaks. Note the positive correlation between water level and wave height, due to the depth-limited conditions at the measurement location.

	Storm peak 1	Storm peak 2	Data source
Date	10-02-2020	11-02-2020	
Start time	11:20	23:50	
Duration [hh:mm]	1:00	1:20	
W_{dir} [°N]	265	260	RWS pole (wind direction meter)
W_{vel} [m/s]	18.5	15.0	RWS pole (wind velocity meter)
h [m+NAP]	2.93	3.03	RWS pole (floaters)
d [m]	2.38	2.48	RWS pole (floaters)
$H_{1/3}$ [m]	1.00	0.95	RWS pole (radar)
H_{m0} [m]	0.97	0.90	RWS pole (radar)
$T_{1/3}$ [s]	4.2	4.15	RWS pole (radar)
T_p [s]	4.35	4.00	RWS pole (radar)
$T_{m-1,0}$ [s]	4.95	4.65	RWS pole (radar)
δ [°N]	312	311	Equation 7.1
β [°]	66	67	Equation 7.1
q_{tank} [l/s/m]	0.130	0.107	Wave overtopping tank
N_{ow} (tank) [-]	57	55	Wave overtopping tank

Table 7.1: Characteristics of considered storm peaks. W_{dir} [°N] is the wind direction, W_{vel} [m/s] the wind velocity, h [m+NAP] the water level, d [m] the water depth, $H_{1/3}$ [m] the significant wave height based on the time signal, H_{m0} [m] the significant wave height based on the spectrum, $T_{1/3}$ [s] the significant wave period based on the time signal, T_p [s] the peak wave period, $T_{m-1,0}$ [s] the wave period based on the moments of the spectrum, δ [°N] the mean wave direction, β [°] the wave angle of incidence relative to the dike normal, q_{tank} [l/s/m] the overtopping discharge as measured by the overtopping tank, N_{ow} [-] the number of overtopping waves in the overtopping tank. RWS pole is the Rijkswaterstaat (wave) measurement pole, see the left panel of Figure 7.2.

Run-up heights and depths and 2D front velocities as measured by the laser scanners during storm Ciara were compared to analysed video recordings and the [EurOtop \(2018\)](#) equations. The (virtual) wave overtopping discharge, as determined from the laser data, was compared to overtopping data from the overtopping tank and the [EurOtop \(2018\)](#) equations. Estimates of the peak wave period were compared to local radar measurements, see Table 7.1. Note that the mean wave direction and angle of incidence were not measured directly, but based on a relation between the mean wind direction and mean wave direction, which was derived based on previous measured storms in the area ([Van der Meer, 2018](#)):

$$\delta = 230^\circ + 0.31 * W_{dir} \quad (7.1)$$

where δ [°N] is wave direction at the measurement location and W_{dir} [°N] is the wind direction at the measurement location. The accuracy of the mean wave direction and thus angle of incidence is estimated to be approximately $\pm 5^\circ$. A short video overview of the measurements can be found at <https://youtu.be/JrItZ58u6GU>.

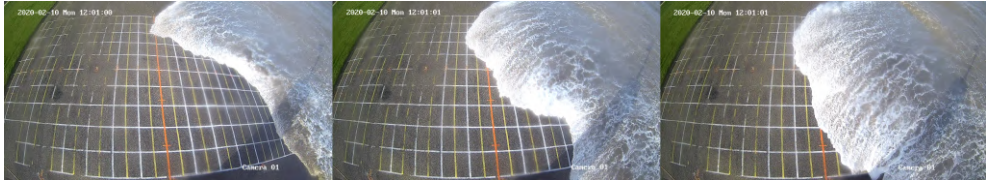
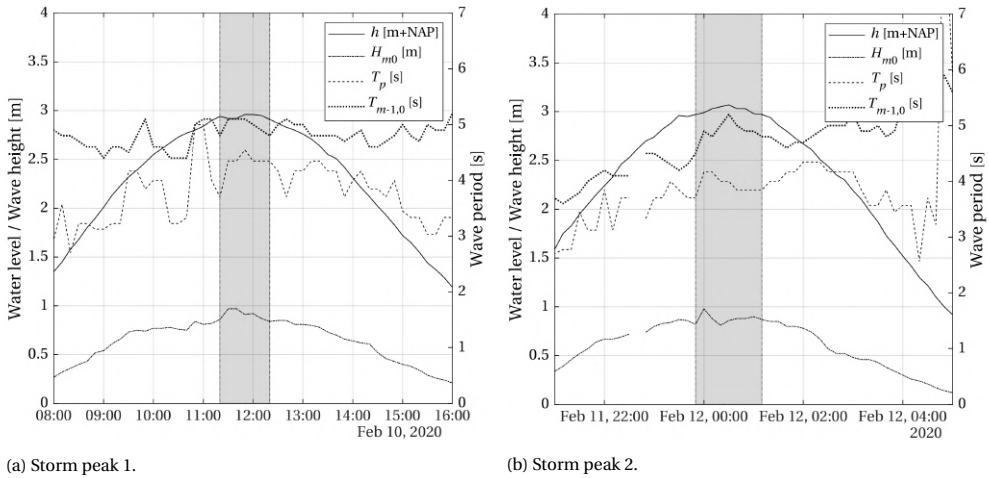


Figure 7.5: Three snapshots taken from the video recordings, showing a very oblique wave running up the slope in a sort of local plunging motion. Note the painted grid as used for the video analysis.



(a) Storm peak 1.

(b) Storm peak 2.

Figure 7.6: Overview of measurements near the toe of the dike around both storm peaks. The shaded regions indicate the considered storm peaks. h [m+NAP] is the water level, H_{m0} the significant wave height [m], T_p the peak wave period [s], $T_{m-1,0}$ the wave period based on the moments of the spectrum.

7.4. METHODS

Oosterlo et al. (2021, 2019) described the calibration and data processing procedures extensively. The same calibration procedures were followed here. With the new version of the laser scanner system, the data processing procedures were updated compared to Oosterlo et al. (2021, 2019) related to several aspects.¹ The measured distances R [m] in polar coordinates were now transformed to x , z and a -coordinates according to Figure 7.7. The x and z -coordinates can be determined directly from the measured distances for a vertical pole, by using:

$$x = x_s + R \sin \theta \tag{7.2}$$

$$z = z_p + h_s - R \cos \theta \cos \phi \tag{7.3}$$

with z [m] being the z -coordinate, x [m] the x -coordinate, x_s [m] the x -coordinate of the laser scanner, z_p [m] the z -coordinate of the laser scanner pole [m], h_s [m] the height of

¹The scripts used for the calibration, data processing and data analysis are open source and can be found at <https://gitlab.com/p-oosterloo/laserscanneranalysis2>.

the laser scanner above the slope, R [m] the measured distance, θ [°] the scan angle and ϕ [°] the slant angle. Generally, a dike slope is not straight, but convex. Furthermore, slight errors in the mounting and orientation of the laser scanners can occur. To account for this, a rotation matrix was applied to the calculated coordinates:

$$M = \begin{bmatrix} \cos \psi & -\sin \psi \\ \sin \psi & \cos \psi \end{bmatrix} \quad (7.4)$$

The correction angle ψ [°] rotates the x - and z -coordinates in the x, z -plane, see Figure 7.7. ψ was determined by fitting the x and z -coordinates resulting from the rotation matrix to the GPS-measured dike slope. The final maximum difference in x -coordinate between the GPS-measured dry slope and the dry slope as calculated from the laser data was 0.04 m, the same order of magnitude as the scan resolution and laser footprint. The maximum difference in z -coordinate between GPS and lasers was 0.05 m, which can be considered accurate, given the convex and irregular shape of the dike slope, the accuracy of the GPS and the maximum accuracy of the mounted laser scanners. The run-up depths can be determined with a higher accuracy. This can be explained as follows: the error in the measurements of the dike slope and water surface is constant. Since the difference between the solid dike slope and the water surface is determined, this error will cancel out. The along-slope a -coordinates were then determined from the x and z -coordinates by using Pythagoras' theorem.

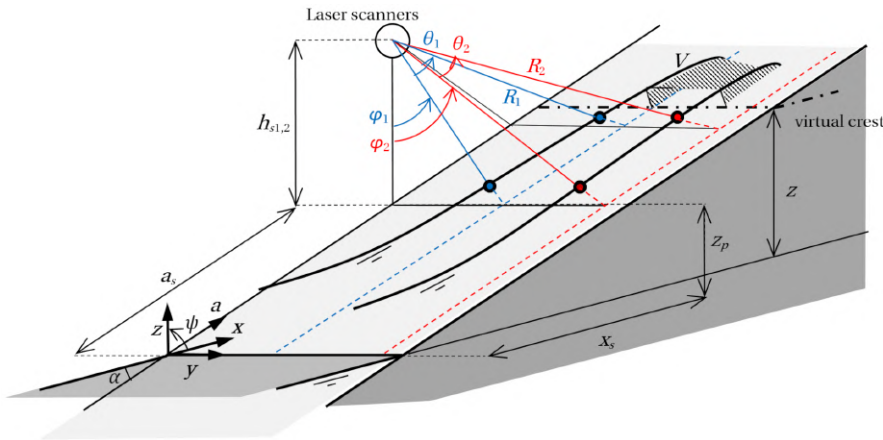


Figure 7.7: Schematised updated set-up with two laser scanners. Scan lines (red and blue dashed lines), scanned points on water surface (red and blue dots) are indicated. x (horizontal), y (perpendicular), z (vertical) and a -coordinate (along the slope) system is also indicated. $R_{1,2}$ [m] are the scanned distances, $\theta_{1,2}$ [°] are the scan angles, $\phi_{1,2}$ [°] the slant angles, x_s [m] are the x -coordinates of the laser scanners, a_s [m] the a -coordinates of the laser scanners, z_p [m] is the z -coordinate of the laser scanner pole, $h_{s1,2}$ [m] are the heights of the laser scanners above the slope, α [°] is the slope angle. V [m³] is a virtual overtopping volume, ψ [°] is the correction angle resulting from the rotation matrix, rotating the x - and z -coordinates in the x, z -plane.

As described in Oosterlo et al. (2021, 2019), the percentage of invalid point measurements at a certain location indicates the quality of the measurement. An invalid measurement means that the magnitude of the laser reflection was too small. These percentages

were very low (of order 0.1%), hence overall the data quality was very good.

After interpolating the data and applying median filters (refer to [Oosterlo et al., 2019](#)), the run-up depths were determined by subtracting the dry slope surface from the measured surface at a certain moment. Run-up depths smaller than a certain threshold, depending on the data quality of the specific laser scanner and storm peak, were removed to remove noise from the signal and prevent the detection of unrealistically high run-up values. Noise in the signal can be caused by e.g. the laser beam reflecting off raindrops, slight inaccuracies in the mounting and orientation of the laser scanners, and the accuracy of the laser scanners themselves, which is in the order of 0.01 m. The threshold is chosen in such a way that realistic and accurate run-up depths and heights are obtained (as verified with video recordings), without extreme outliers. 0.015 m was used for laser scanner 1, 0.030 m and 0.020 m were used for laser scanner 2 for storm peak 1 and 2, respectively. The data were then further corrected by removing depths larger than 1.5 m, and by removing large (>0.5 m) local (in one time or space step) differences in run-up depths, e.g. caused by rain. If an isolated (non-NaN) run-up depth was measured higher on the slope after more than 10 connected invalid measurement points (NaN values), these values were also removed, as they were caused by noise in the data. A similar procedure was followed for the reflectance value, RSSI: a large difference (>100) in one time or space step was removed, a threshold value (1 - 5) was used to prevent unrealistically high run-ups, and valid values after 10 or more straight NaNs were removed.

The wave run-up heights, wave overtopping volumes and discharges, and wave peak periods and angles of incidence were determined in the same way as in [Oosterlo et al. \(2021, 2019\)](#), where the full descriptions can be found. Briefly, this means that for the run-up the highest location on the slope was determined where $z_{\text{run-up}} - z_{\text{dry}} > z_{\text{threshold}}$ OR $RSSI_{\text{run-up}} - RSSI_{\text{dry}} > RSSI_{\text{threshold}}$. Overtopping volumes and discharges were found by integrating the run-up depths between a certain virtual crest level and the run-up level, and then determining the maximum volumes per wave. Wave peak periods were calculated from the variance density spectra of the run-up time signals. The angle of incidence was then determined based on the cross-spectral density of both run-up time signals.

The front velocities were determined from the temporal change in run-up level. To this end, first the time signal of the instantaneous front position was smoothed by applying a median filter with a 0.2 s window, followed by a moving average with a 0.4 s window. After that, the time derivative was taken and the maxima were determined, giving the maximum front velocities during each wave. To validate the laser data, the front velocities were also determined from the videos; by taking the number of video frames it took the front to travel 0.5 m (a somewhat coarser approach).

Estimates of the displacements of the laser lines due to wind vibrations were calculated from the accelerometer data, to be able to correlate possible outliers in the laser data.

[Mentaschi et al. \(2013\)](#) showed that the root-mean-square error RMSE and its variants give smaller values for models affected by negative bias. Hence, these indicators are not always reliable to assess the accuracy of models or measurements. They showed that the HH-indicator as proposed by [Hanna and Heinold \(1985\)](#) provides more reliable information on the accuracy. This HH-indicator was used in [Oosterlo et al. \(2021\)](#) and the present

chapter also uses this indicator. It is defined as:

$$HH = \sqrt{\frac{\sum_{i=1}^N (M_i - O_i)^2}{\sum_{i=1}^N M_i O_i}} \quad (7.5)$$

where M_i is the i th modelled data, O_i is the i th observation and N is the total number of observations. Furthermore, the Normalised Bias Indicator is used:

$$NBI = (\overline{M} - \overline{O}) / \overline{O} \quad (7.6)$$

Both the HH and NBI are dimensionless. These indicators are used to determine the accuracy of the measured laser data, by comparing them to data measured by other instruments and several equations.

7.5. RESULTS

7.5.1. WAVE RUN-UP HEIGHTS

Figure 7.8 presents a typical part of the measured data, showing the run-up signals based on both measured distance R and laser reflectance RSSI for both laser scanners, during a 30-second window. The figure shows the run-up peaks and measured run-up depths as well. The height level of the overtopping tank is indicated with the dotted line. One of the waves shown in the figure caused overtopping in the overtopping tank. Furthermore, the slight delay between the laser scanner signals is visible, where the waves often reached the second laser scanner first with the present wave direction.

Figure 7.9 shows the measured run-up heights for both storm peaks, plotted against the run-up heights observed from the video recordings. The figure shows the run-up heights for both laser scanners, based on both the measured distance R and laser reflectance RSSI data. Figure 7.9 only shows the run-up heights above 4.4 m+NAP, hence the most important waves, as these are the waves that would give overtopping in the overtopping tank. Similar trends were also found for the smaller run-up heights. Note that different numbers of run-up events above the threshold run-up height were found with both laser scanners and the video analysis; due to the very obliquely incident waves, some of the waves reached the threshold run-up height at the location of one of the laser scanners, but not at the other one. These numbers of run-up events and the $R_{u2\%}$ -values have been given in Table 7.2.

Some general observations for both storm peaks can be made. The first one is that both laser scanners generally performed well, as the run-up heights agree quite well with the values as observed from the videos, also visible in the HH and NBI values. Second, the run-up heights based on the measured distances agree better with the video data than the run-up heights based on the RSSI. The RSSI performed quite well for the first storm peak with a few outliers, but gave larger HH and NBI-indicator values for the second storm peak, underestimating the run-up heights. Previous studies Cete (2019); Hofland et al. (2015); Oosterlo et al. (2021, 2019) found that the RSSI performed equal to or better than the measured distance. This can be explained as follows: the RSSI analysis is based on the difference in reflectance between the dry slope and the up-rushing water. The asphalt gives a low reflectance, the water a higher one. However, the paint of the grid on the slope

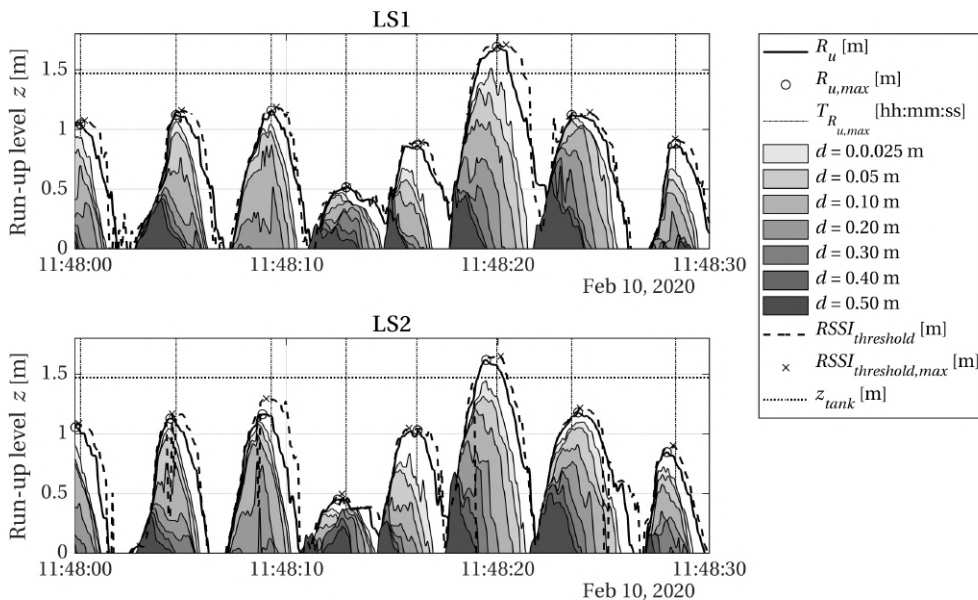


Figure 7.8: Measured run-up heights R_u [m] based on measured distances R (solid lines) and laser reflectance $RSSI$ (dashed lines), as well as measured run-up depths d [m] (contours) for both laser scanners (LS1 and LS2), during a 30 second window. Maximum run-up heights $R_{u,max}$ [m] per wave based on both R (circles) and $RSSI$ (crosses) indicated. Height level of the overtopping tank z_{tank} [m] indicated by the dotted line. Moments of maximum run-up height $T_{R_{u,max}}$ [hh:mm:ss] at LS1 indicated by the dash-dot lines. Note the delay between the signals, where the waves often reached LS2 first with the present wave direction.

7

was very reflective. This thus led to large $RSSI$ values at the grid lines, interfering with the higher $RSSI$ values of the up-rushing waves. This reduced the quality of the present $RSSI$ results.

Also, some storm peak-specific observations can be made. The run-up heights of peak 1 agree well, especially based on the measured distances of laser scanner 1, with almost all values within the ± 0.10 m bounds. Absolute HH and NBI values are at most 0.05, where the run-up based on measured distances shows a slightly negative bias, and the $RSSI$ -based values show a bias close to zero. As the accuracy of the video analysis is estimated to be $a_{Ru} \pm 0.10$ m ($z_{Ru} \pm 0.02$ m), this means that the differences are of the same order of magnitude as the accuracy of the video analysis. The results of laser scanner 2 for storm peak 1 ($HH = 0.05$, $NBI = -0.02$) show somewhat larger deviations than the results of laser scanner 1 ($HH = 0.02$, $NBI = -0.02$). Since the second laser scanner scans a line further from the pole, the measured distances and laser footprint are larger, whereas the laser resolution is lower than of laser scanner 1. Therefore, the data quality of the second laser scanner was somewhat lower and the deviations somewhat larger.

During the analysis, it was observed that the largest deviations of the first storm peak occurred from 11:30 until 11:36, when wind gusts were strongest, which caused stronger vibrations of the system. The accelerometer data were analysed, and the largest displacements of the scan lines indeed occurred between 11:30 and 11:36, being at most a dis-

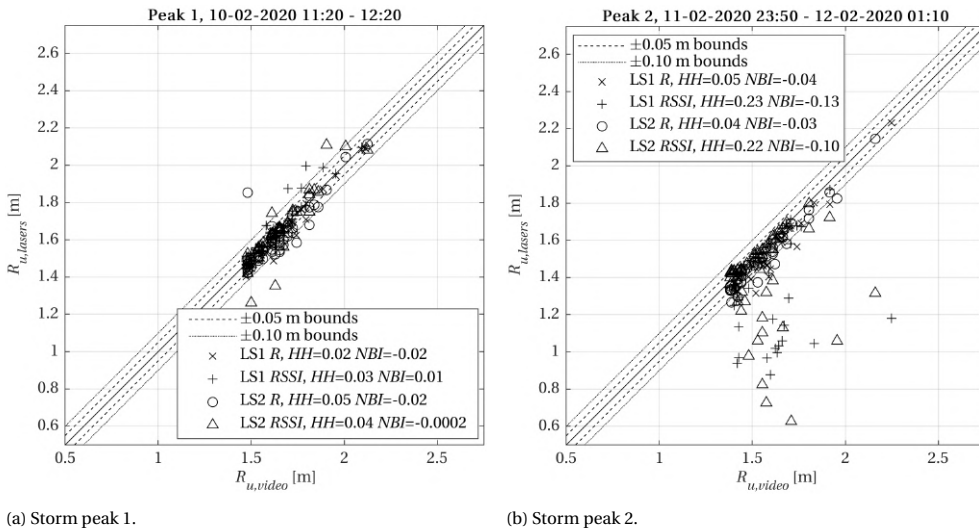


Figure 7.9: Run-up heights above 4.4 m+NAP for both storm peaks for both laser scanners (LS1 and LS2), based on distance R and laser reflectance $RSSI$, compared with run-up heights from video recordings. Left: storm peak 1. Right: storm peak 2. The legend provides the HH and NBI values.

placement of 0.09 m along the y -axis (see Figure 7.7) for laser scanner 2. As the y -axis roughly corresponded to the wind direction, displacements along the a -axis were much smaller. These wind vibrations were also visually observed during the measurements. Therefore, the guywires of the system were tightened more after the first storm peak, to reduce the vibrations during the measurements of the next storm peaks. By doing this, they were reduced to at most 0.06 m in the y -direction for the following storm peaks.

Results based on measured distances also agree well for the second storm peak, showing again a slight negative bias. However, for this storm peak the results based on the $RSSI$ do not agree well at all. Additional to the influence of the painted grid lines, a period of strong wind combined with very heavy rain occurred on 12-02-2020 from 00:34 until 00:37. As described in Oosterlo et al. (2019), the influence of raindrops on the data quality is small when the last echo is used for the laser scanner measurements. This explains the good results of the distance-based run-up heights, despite the rain. However, the combination of strong wind and heavy rain caused raindrops to fly past the laser scanners continuously, whereby the laser beam sometimes reflected off the raindrops, detecting a 'water-like' higher reflectance ($RSSI$) value, when no water was present on the slope. The combined effects of the painted grid lines and very heavy rain thus led to a larger $RSSI$ threshold being necessary during the analysis. This then led to upper parts of the up-rushing waves being filtered out, reducing the $RSSI$ -based data quality. Therefore, the remainder of this chapter will only consider the results based on measured distances. However, note that an extreme value analysis fit through the largest $RSSI$ events would also still be accurate.

The left panel of Figure 7.10 compares the $R_{u2\%}$, the run-up height exceeded by 2% of the waves, based on the laser scanner data of both storm peaks, to the Van der Meer and

Bruce (2014) wave run-up equations, which were later implemented in EurOtop (2018) (and hereafter referred to as such). Note that the influence of oblique wave attack was added to the equations here, by including the influence factor γ_β [-] on the vertical axis. The value of γ_β is 0.85 for the run-up, for the present angles of incidence of 66° and 67°. A dike slope angle of 1:4.2 was used, which is the average slope of the asphalt section of the dike. The data of both storm peaks lie closely together (a result of the similar conditions during both peaks) and fall just above the lower 90%-bound of the EurOtop (2018) equations. EurOtop (2018) gives a 25% larger $R_{u2\%}$, see Table 7.2. However, note that the results are quite sensitive to changes in the angle of incidence and especially the $T_{m-1,0}$ wave period, on which the breaker parameter $\xi_{m-1,0}$ [-] is based. As explained in section 7.3, there exists some uncertainty in the mean wave direction and thus in the angle of incidence, since they were not measured directly, but based on a relation between the wind direction and wave direction. There is also some uncertainty in the $T_{m-1,0}$. A difference in angle of incidence of 5° or a more commonly found ratio of $T_p / T_{m-1,0} = 1.1$, would move the data from the lower 90%-bound to the upper one in Figure 7.10. This highlights the importance of accurately measuring these parameters.

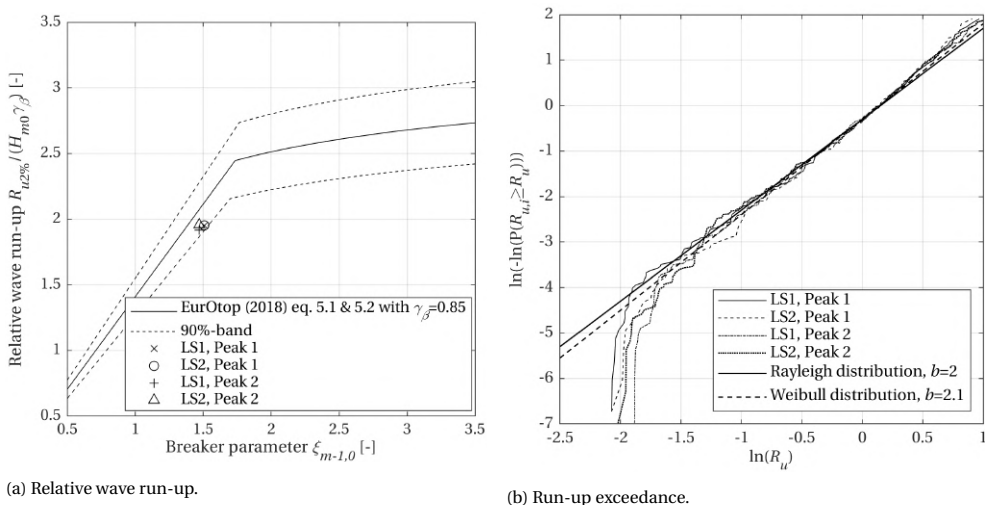


Figure 7.10: Left: Relative wave run-up versus breaker parameter. Figure based on EurOtop (2018). Note the added influence of the oblique wave attack on the vertical axis compared to EurOtop (2018). Data for both laser scanners based on measured distances, and for both storm peaks. Right: Run-up exceedance plots for both laser scanners and both storm peaks, plotted on Weibull scale. A straight line gives a Weibull distribution, a straight line with a slope of 1:2 gives a Rayleigh distribution.

The right panel of Figure 7.10 plots the exceedance probability distributions of the measured run-up heights for both laser scanners and storm peaks on Weibull scale. Here, $P(R_{u,i} \geq R_u)$ [-] is the probability that a certain run-up height $R_{u,i}$ [m] exceeds a specified run-up height R_u [m]. The complementary cumulative distribution function or exceedance function of the Weibull distribution is:

$$P(X \geq x) = e^{-\left(\frac{x}{a}\right)^b} \tag{7.7}$$

where $P(X \geq x)$ is the probability that X is equal to or larger than x [-], b is a non-dimensional shape factor and a is a dimensional scale factor of the distribution. The data have a Weibull distribution if the data show as a straight line in the right panel of Figure 7.10. Deep water waves are Rayleigh-distributed, the Rayleigh distribution is essentially a Weibull distribution with a shape factor b of 2. E.g. Nielsen and Hanslow (1991) determined that the run-up heights on a beach for normally incident waves in deep water also have a Rayleigh distribution. When waves approach shallow water and the highest waves break, the wave height distribution, which first could be described by a Rayleigh-distribution (Weibull distribution with $b = 2$), turns into a Weibull distribution with $b > 2$ (Battjes & Groenendijk, 2000; EurOtop, 2018) or other function with decreased magnitude of low-exceedance events (e.g. Battjes & Groenendijk, 2000). Van der Meer and De Waal (1993) found that if the wave height distribution deviates from a Rayleigh distribution due to shallower water, then the run-up distribution will also deviate with approximately the same amount. The run-up distribution will then also turn into a Weibull distribution with $b > 2$ (Stam, 1989). Stam (1989) also found that the run-up remains approximately Rayleigh-distributed for deep water conditions with limited depth-induced breaking ($d_{toe}/H_{s,toe} \geq 2$ or 3), for rubble mound slopes. The exact run-up distribution on a dike slope of (very) obliquely incident deep or shallow water waves is unknown. However, Van der Meer and De Waal (1990) found that oblique incidence tended to reduce the largest run-up heights more than the smaller run-up heights. This would indicate that the run-up is also Weibull-distributed ($b > 2$) for obliquely incident waves.

Here, the ratio $d_{toe}/H_{s,toe}$ was larger than 2.5, indicating that the run-up would be Rayleigh-distributed ($b = 2$). However, the waves were also very obliquely incident, indicating that the run-up might be Weibull-distributed ($b > 2$). The right panel of Figure 7.10 shows quite similar trends for both storm peaks, where the lower part (smaller run-up heights) shows a different inclination, but the upper part is almost straight. As the focus is mainly on the larger run-up heights, the following only considers the upper part of the graph. Since the upper part is almost straight, the wave run-up heights can be considered Weibull-distributed. Determining the tangent to the curves gives the shape factor b . The scale factor a can be determined by locating the value on the horizontal axis, which corresponds to an exceedance probability of $1 - 0.632 = 0.368$ on the vertical axis. Here, shape factors $b = 2.2$ (laser scanner 1) and $b = 2.4$ (laser scanner 2) were found for the first storm peak, whereas $b = 2.1$ was found for both laser scanners for storm peak 2. The value of the scale factor a was approximately 1.1 m for both storm peaks. The run-up thus follows a Weibull distribution that is quite close to a Rayleigh distribution. These shape factors mean that the larger run-up heights were somewhat smaller than if they were Rayleigh-distributed. This indicates a credible limited influence of the obliquely incident waves on the value of b .

7.5.2. WAVE RUN-UP DEPTHS

The run-up depths as measured by the laser scanners were validated in Oosterlo et al. (2021, 2019), generally showing good results higher on the slope. At those locations, little spray and foam occurred. Larger deviations were found closer to the still water level, where the laser scanners overestimated the run-up depths due to the large amounts of foam and spray which were present there.

For the current measurements, no run-up depth data from other instruments are available. However, Van der Meer (2011) gives the linear relation $d_{2\%} = c_{d2\%}(R_{u2\%} - z)$, which was based on Schüttrumpf (2001); Van Gent (2002). This relation was later included in EurOtop (2018), with $d_{2\%}$ [m] the run-up depth exceeded by 2% of the waves, $c_{d2\%}$ [-] a coefficient depending on the dike slope (see e.g. Van der Meer, 2011), $R_{u2\%}$ [m] the 2% run-up height, and z [m] an arbitrary height on the slope relative to the still water level. Note that these $d_{2\%}$ values are not the run-up depths corresponding to the $R_{u2\%}$ wave, but the 2%-exceedance values of the run-up depth at a certain location on the slope. In other words, the run-up depth at a certain location that is exceeded by 2% of the waves. These values at different locations along the slope may thus also correspond to different waves, as they are based on the statistics of the run-up depths at that specific location on the slope.

No consensus has been reached on the value of the coefficient $c_{d2\%}$ yet. Van der Meer (2011) compared the results of different small and large-scale lab tests where run-up depths were measured. Note that these depths were often measured at the transition between slope and crest, where the wave changes from up-rushing to horizontal. Van der Meer (2011) recommends $c_{d2\%} = 0.20$ for slopes of 1:3 and 1:4, $c_{d2\%} = 0.30$ for a slope of 1:6 and interpolation for slope angles in between these values. The present mean slope of 1:4.5 would then give $c_{d2\%} = 0.23$. However, the research on which Van der Meer (2011) based this recommendation, often found largely differing $c_{d2\%}$ values. All but one small-scale source give $c_{d2\%} = 0.20$ -0.22, all for 1:3 and 1:4 slopes except Schüttrumpf (2001) with a 1:6 slope. On the other side, FlowDike 2 (Lorke et al., 2011) gave $c_{d2\%} = 0.29$, for a 1:6 slope. The only large-scale tests that were considered in Van der Meer (2011), those of Schüttrumpf (2001), were also performed on a 1:6 slope. There, $c_{d2\%} = 0.33$ -0.34 was found. Hence, these discrepancies in $c_{d2\%}$ could either be due to the different slope angles or due to the differences between small and large-scale tests.

Therefore, the left panel of Figure 7.11 shows the relations for both $c_{d2\%} = 0.23$ (recommendation of Van der Meer (2011)) and $c_{d2\%} = 0.34$ (1:6 slope large-scale tests of Schüttrumpf (2001)), comparing them with the laser scanner results. Similar trends as found in Oosterlo et al. (2021, 2019) were found here, with the relation of Van der Meer (2011) giving somewhat larger values than the laser scanners at locations higher on the slope. Since the values in Figure 7.11 were based on the statistics at a certain location, different values were found for both laser scanners. This was caused by the very oblique incidence. However, overall the results of both laser scanners agree well. Better agreement was found with $c_{d2\%} = 0.23$ than with $c_{d2\%} = 0.34$. The legend of the left panel of Figure 7.11 gives the HH and NBI values for $c_{d2\%} = 0.23$. The data of storm peak 1 agree better than the data of storm peak 2, which lie somewhat below the $c_{d2\%} = 0.23$ line. As was explained in sub-section 7.5.1, the data quality of the second storm peak was lower.

The better agreement with $c_{d2\%} = 0.23$ might suggest that the discrepancies found in the literature were caused by the different slope angles, not by the differences between small and large-scale tests. From the video recordings of the present measurements, it was observed that sometimes spray occurred around the still water level, due to breaking waves. This was especially found for the larger waves. Furthermore, some foam and quite some entrained air were present. The right panel of Figure 7.11 gives a snapshot of a large up-rushing wave. The spray could potentially have influenced the results at $z = 0.20$ m, for

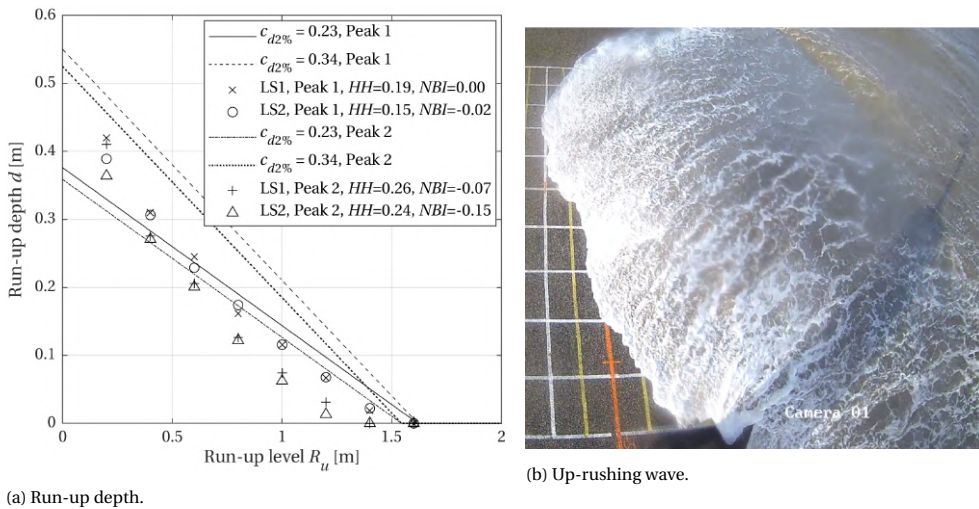


Figure 7.11: Left: Run-up depth at several locations along the dike slope exceeded by 2% of the waves, based on both laser scanners and for both storm peaks. Data compared to linear relation of Van der Meer (2011) for two different values of $c_{d2\%}$. HH and NBI indicator values given for $c_{d2\%} = 0.23$. Right: Snapshot of large up-rushing wave, showing foam and entrained air.

which quite large run-up depths were found. Since the laser beam reflects off the spray and foam, the laser scanners measure run-up depths that include the spray, foam and entrained air. Another potential influence is the laser footprint and resolution. Lower on the slope, the laser footprint is larger and the laser resolution is lower, potentially giving less accurate results lower on the slope. However, the overall results can be deemed reliable.

The reasonable agreement between $c_{d2\%} = 0.23$ and the present data further seems to suggest that the influence of the wave angle of incidence on the run-up depths is small, as the previous research was performed with normally incident waves.

7.5.3. FRONT VELOCITIES

Oosterlo et al. (2021, 2019) measured front velocities of normally incident waves with the laser scanners, and the time lag between the laser signals for obliquely incident waves (see Figure 7.8), and achieved good results. During storm Ciara the waves were very oblique, so these waves had a velocity component along the dike as well. Due to the very oblique incidence and breaking waves, defining a front is very difficult as is determining the 2D front velocities. Furthermore, during the present measurements, it was observed that even if a front was visible initially (lower on the dike slope), this front was then sometimes surpassed by another part of the oblique wave higher on the slope, effectively making that part the new 'front'.

The laser scanners only scan along two transects. The first one lies approximately 7 m from the far edge of the painted measurement grid, the second one lies approximately 9 m from the edge of the grid. Due to the oblique attack, the up-rushing waves travelled across the whole painted measurement grid, also see the right panel of Figure 7.11. Hence, the two laser transects missed quite a large part of the very oblique front running up the slope.

For the laser scanners, front velocities were determined by determining the velocity components along the a -axis (up the slope, along the laser lines, see Figure 7.7) first. These were combined with the delay between the laser signals (cross-correlation, velocity along the slope) to determine a 2D velocity. However, this did not yield good results, as the velocities along the slope were generally determined as being very large (small delay between the laser signals). Potentially, the offshore, but close to along-slope-directed wind played a role here as well. Thus, for the very obliquely incident waves present during storm Ciara, it was not possible to determine the actual 2D front velocities from the laser data accurately.

Therefore, only the highest ten run-ups for each storm peak were considered. Instead of 2D velocities, only the components travelling up the dike slope (along the a -axis) were considered. Results of both laser scanners were averaged and the maxima during each wave were determined. Even though it was not possible to estimate the 2D front velocities based on the laser scanner data, it was possible based on the video recordings. Figure 7.12 compares the 2D front velocities based on the videos and 1D front velocities based on the laser scanners for the ten highest run-ups of each storm peak to the relation:

$$\frac{v_{front}}{\sqrt{gH_{m0}}} = c_u \sqrt{\frac{R_{u,max}}{H_{m0}}} \tag{7.8}$$

Equation 7.8 was taken from EurOtop (2018), where v_{front} [m/s] is the maximum front velocity for an individual wave and c_u [-] is a normally-distributed stochastic parameter with $\mu(c_u) = 1.0$ and $\sigma(c_u) = 0.25$. The figure also includes the FlowDike data (Lorke et al., 2011), to show the scatter.

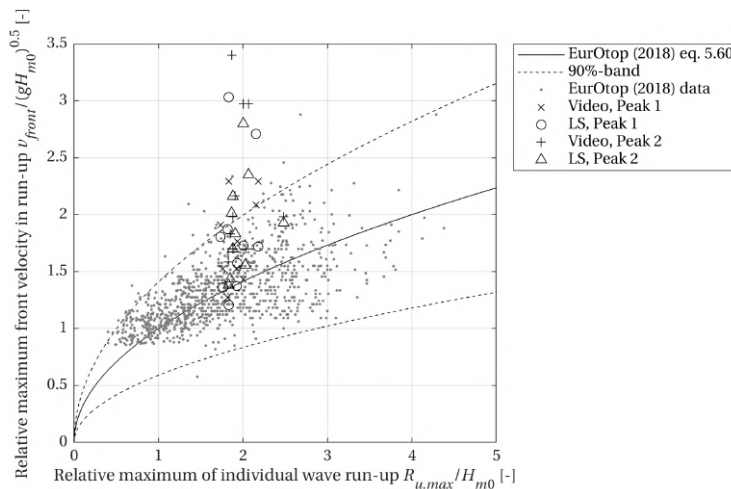


Figure 7.12: Relative maximum front velocity versus relative run-up on the slope. Results based on video analysis (2D velocities) and laser scanners (velocity component in the up-slope direction), compared to Equation 7.8. Figure based on EurOtop (2018), including the FlowDike data (Lorke et al., 2011).

Even these ten largest waves of both storm peaks propagated differently on the dike slope. Some waves had an initial direction mostly up the slope, later turning and becoming more alongslope-directed. Others were already very oblique from the beginning and

travelled mostly along the slope. This again shows that Ciara posed very complicated conditions.

The video results are more reliable than the laser scanner results, since they represent actual 2D velocities. The front velocities as found here are generally larger than the relation that was based on the FlowDike small-scale tests with normally incident waves. One potential explanation for the differences is inaccuracy in determining the front velocities, either for the present measurements or for the FlowDike data. Some other potential explanations could be differences between small-scale tests and actual storms in the field, and differences between normally and obliquely incident waves. It is recommended to determine if improved front velocity results can be achieved with the laser system for future storms with less obliquely incident (but still oblique) waves.

7.5.4. WAVE OVERTOPPING VOLUMES AND DISCHARGES

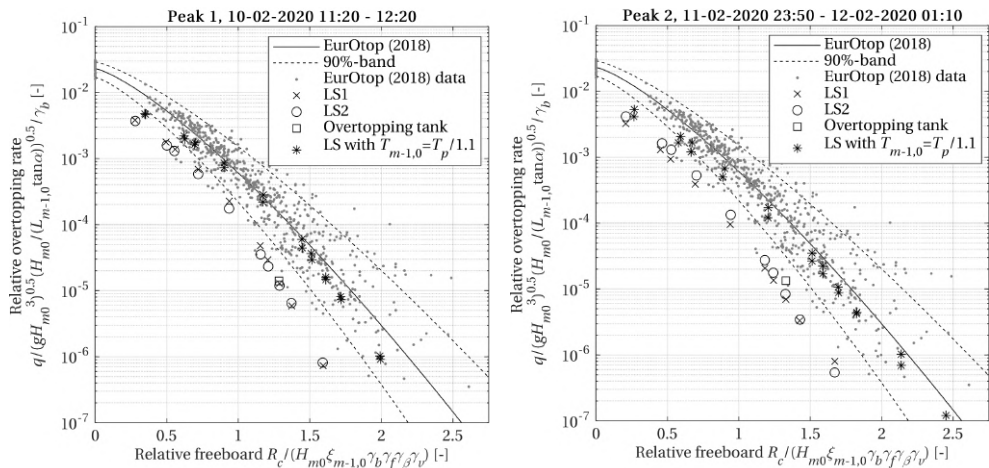
The (virtual) wave overtopping volumes and mean discharges were calculated using the same method as in [Oosterlo et al. \(2021, 2019\)](#), by integrating the run-up depths above a virtual crest level, and taking the maximum value of that volume within a wave period as the overtopping volume for that wave. Several virtual crest levels were considered, where one corresponds to the overtopping tank level (4.4 m+NAP). [Figure 7.13](#) compares the results with the overtopping tank data, the [EurOtop \(2018\)](#) wave overtopping equations and the [EurOtop \(2018\)](#) data, which give an indication of the spread in the data. [Table 7.2](#) gives the overtopping discharges, volumes and number of overtopping waves. With angles of incidence of 66° and 67° , the γ_β for the overtopping is 0.78.

The trend of the laser data in [Figure 7.13](#) agrees quite well with the [EurOtop \(2018\)](#) equations, but both the tank and the laser scanners gave smaller discharges than the equations. [EurOtop \(2018\)](#) predicts a 10 times larger discharge for both storm peaks than measured by the laser scanners and tank, also see [Table 7.2](#). Here, a ratio $T_p/T_{m-1,0} = 0.9$ occurred (as measured by the radar attached to the Rijkswaterstaat pole, see [Table 7.1](#)), while a more common ratio for a JONSWAP spectrum is $T_p/T_{m-1,0} = 1.1$. Therefore, the laser data were also plotted using $T_{m-1,0} = T_p/1.1$ in [Figure 7.13](#). Using this ratio, the lasers, tank and [EurOtop \(2018\)](#) agree much better. See also [Table 7.2](#), where the [EurOtop \(2018\)](#) overtopping volumes and discharges using $T_{m-1,0} = T_p/1.1$ have also been given. Hence, the large deviations in the overtopping discharges mainly seem to stem from the $T_{m-1,0}$ wave period. Large $T_{m-1,0}$ values consistently occur during storms in the area of interest, indicating that low-frequency energy plays a role. The influence of low-frequency energy (and thus $T_{m-1,0}$ wave period) on the overtopping discharge predicted by the [EurOtop \(2018\)](#) equations is generally large (e.g. [Lashley, Bricker, Van der Meer, Altomare, & Suzuki, 2020](#); [Oosterlo, McCall, et al., 2018](#)). However, the low-frequency energy present during storm Ciara apparently did not influence the wave overtopping, as indicated by the much smaller measured wave overtopping discharges than predicted by [EurOtop \(2018\)](#) (with the measured $T_{m-1,0}$). This is contrary to expectations and the [EurOtop \(2018\)](#) equations, since [Van Gent \(1999a, 1999b, 2001\)](#) found that the spectral shape does not affect the wave run-up and overtopping, as long as the $T_{m-1,0}$ is the same. If the measured $T_{m-1,0}$ is correct, this would indicate that the [EurOtop \(2018\)](#) equations may not be fit for use with the complex multi-modal spectra as often present in the Eems-Dollard estuary. Therefore, further research into the measured low-frequency energy and $T_{m-1,0}$ wave period,

and into the influence of low-frequency energy on wave overtopping, is recommended.

	$R_{u2\%}$ [m]	q [l/s/m]	V_{max} [l/m]	N_{ow} [-]
<i>Storm peak 1</i>				
Laser scanner 1	1.62	0.118	100.0	43
Laser scanner 2	1.62	0.109	98.8	52
Video analysis	-	-	-	51 / 48
Overtopping tank	-	0.130	86.1	57
EurOtop (2018)	2.06	1.369 / 0.198	500.5 / 45.3	-
<i>Storm peak 2</i>				
Laser scanner 1	1.47	0.056	106.4	38
Laser scanner 2	1.50	0.067	121.5	39
Video analysis	-	-	-	47 / 50
Overtopping tank	-	0.107	71.2	55
EurOtop (2018)	1.86	0.952 / 0.102	501.5 / 43.8	-

Table 7.2: Run-up and overtopping parameters for both laser scanners, the video recordings, the overtopping tank and EurOtop (2018) equations at 4.4 m+NAP, for both storm peaks. V_{max} [l/m] is the maximum overtopping volume. Note that the table gives two values for several parameters. The two q values for EurOtop (2018) correspond to discharges based on the measured $T_{m-1,0}$ and based on the ratio $T_{m-1,0} = T_p/1.1$. The maximum volumes of EurOtop (2018) correspond to volumes calculated with Equation 7.10 - Equation 7.12, based on the EurOtop (2018) q , a and b values, or based on the laser scanner q , a and b values. The number of overtopping waves according to the video analysis correspond to the number of overtopping waves at the locations of laser lines 1 and 2.



(a) Storm peak 1.

(b) Storm peak 2.

Figure 7.13: Relative overtopping rate for several virtual crest levels, based on both laser scanners (crosses, circles) and the overtopping tank (squares), for both storm peaks. The laser scanner data have also been plotted using the relation $T_{m-1,0} = T_p/1.1$ (asterisks). Results compared to EurOtop (2018) equations (solid and dashed lines) and data (dots). Figure based on EurOtop (2018). R_c [m] is the crest freeboard, $\xi_{m-1,0}$ [-] is the breaker parameter, the different γ parameters [-] are influence factors, see EurOtop (2018).

The discharges as measured by the laser scanners and tank agree well, especially for the first storm peak. The tank gave a 1.5 - 2 times larger discharge than the laser scanners for the second peak. This can be explained using the right panel of Figure 7.9. Due to the somewhat lower data quality, the laser scanners gave a slight negative bias for the run-up heights of the second storm peak. Due to this underestimation of the run-up heights, some of the smaller overtopping waves, which just reached the overtopping tank, were missed, resulting in a somewhat smaller discharge than with the tank.

The percent exceedance distribution of overtopping wave volumes is given by a Weibull distribution (Hughes, Thornton, Van der Meer, & Scholl, 2012):

$$P_{v\%}(V_i \geq V) = \exp \left[- \left(\frac{V}{a} \right)^b \right] \cdot (100\%) \quad (7.9)$$

where $P_{v\%}$ [%] is the percentage of wave volumes that will exceed the specified volume V_i [m³/m]. b is the shape factor and a is the scale factor. The left panel of Figure 7.14 shows the fit for b according to Zanuttigh, Van der Meer, Bruce, and Hughes (2014). A value for b of 0.75 has long been used to describe overtopping of individual wave volumes, but the graph shows that with larger relative discharge the b -value may increase significantly, leading to a gentler distribution of overtopping wave volumes (EurOtop, 2018). b -values were also calculated for the present measurements at several (virtual) crest levels, based on both the laser scanners and the overtopping tank. The laser scanner data follow the trend of the line quite well, but the b -values themselves are smaller. The exact cause of these smaller b -values is unknown. These smaller b -values mean that the distribution of overtopping wave volumes is steeper, meaning that the largest volumes are relatively larger. The overtopping tank data do agree well with the fit.

Table 7.2 also gives the maximum overtopping volumes V_{max} [l/m] for the laser scanners, overtopping tank and EurOtop (2018) equations for both storm peaks. The maximum overtopping volume can be calculated as follows, according to EurOtop (2018):

$$P_{ov} = \frac{N_{ow}}{N_w} \quad (7.10)$$

$$a = \left(\frac{1}{\Gamma(1 + \frac{1}{b})} \right) \left(\frac{qT_m}{P_{ov}} \right) \quad (7.11)$$

$$V_{max} = a [\ln(N_{ow})]^{1/b} \quad (7.12)$$

with N_w [-] the number of incident waves, Γ the mathematical gamma function, P_{ov} [-] the probability of overtopping, T_m [s] the mean wave period and a the scale factor of the Weibull overtopping wave volumes distribution. These maximum volumes generally show more scatter, since they correspond to the maximum of a distribution.

The numbers of overtopping waves agree quite well for all instruments for storm peak 1, see Table 7.2. The laser scanners give fewer overtopping waves for the second storm peak. As explained above, this was caused by the underestimation of the run-up heights by the laser scanners for storm peak 2, leading to fewer run-up heights above the height level of the overtopping tank and thus fewer overtopping waves.

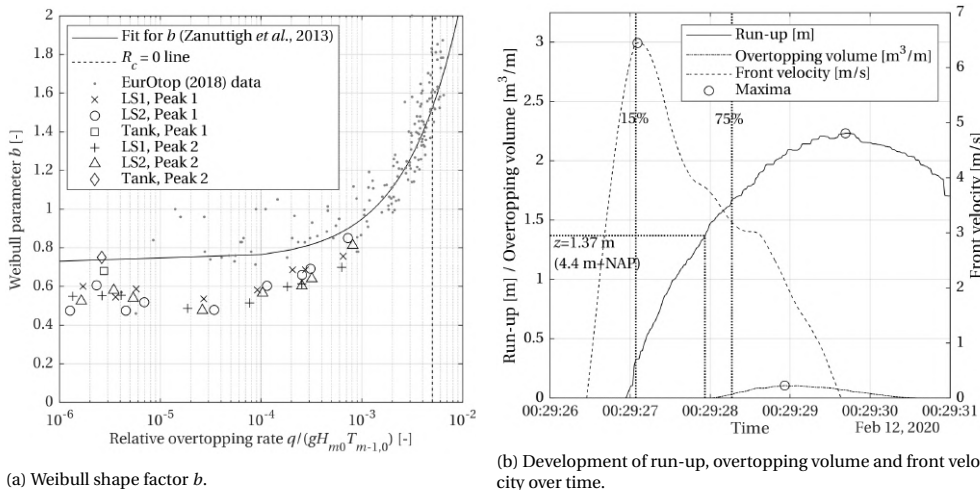


Figure 7.14: Left: Weibull shape factor b for smooth structures and spanning a range of relative freeboards. Laser and overtopping tank data plotted for both storm peaks. Fit for b from Zanuttigh et al. (2014) shown as well. Figure based on EurOtop (2018). Right: Development of run-up, overtopping volume and front velocity over time for one large wave and based on data of one of the laser scanners. The dotted lines indicate the moments that the run-up reaches 15% and 75% of the maximum run-up level, and the moment that the run-up reaches the overtopping tank level.

7

The maximum volumes of both laser scanners and the overtopping tank agree quite well for the first storm peak (15% larger volume with the laser scanners). The results differ more for the second storm peak, where the laser scanners gave a 50% to 70% larger maximum volume than the tank. As was explained above, the laser scanners measure the spray, foam and entrained air, which the overtopping tank does not. No spray was present above the height of the overtopping tank (4.4 m + NAP). However, some foam was present and entrained air was visible at the wave fronts. The volumes as measured with the laser scanners thus include this foam and air, and this can explain the larger maximum volumes as measured by the laser scanners. Since the data quality of the second storm peak was somewhat lower, the maximum volume during the second storm peak might have been slightly overestimated. This was potentially caused by the larger layer thickness threshold that had to be used. However, the influence of the larger threshold is at most a few l/m for the largest overtopping volume and even less for the smaller volumes. Not much is known about the actual air content in up-rushing waves. If the assumption is made that the differences between the maximum volumes were fully caused by the foam and entrained air, then that would mean that approximately 15% of the volume consists of foam and air. This amount seems reasonable when compared to visual observations of the up-rushing waves.

Another explanation that could be proposed is that the laser scanners provide 2D values of the overtopping, along the assumed infinitely thin laser line, whereas the overtopping tank gives overtopping volumes over a width of 4 m. With a large enough number of waves, this influence will average out, and it is therefore expected that this influence was small here.

The [EurOtop \(2018\)](#) equations give 4 to 6 times larger maximum volumes than the lasers and overtopping tank, when using the overtopping discharge q and the a and b -values (scale and shape factors) of the Weibull distribution according to [EurOtop \(2018\)](#) to determine these maximum volumes. The results agree much better, if the q , a and b -values as found with the laser scanners are used instead to determine the maximum volume with Equation 7.10 - Equation 7.12. In that case, the [EurOtop \(2018\)](#) equations give maximum volumes that are 40% - 50% smaller than the volumes found by the laser scanners. Note that the $T_{m-1,0}$ is of influence here as well, as it is included in the [EurOtop \(2018\)](#) equations for both q and b .

The right panel of Figure 7.14 shows the development over time of the run-up height, overtopping volume and up-slope front velocity of one wave based on data of one of the laser scanners. The dotted lines indicate the moments that the run-up reaches 15% and 75% of the maximum run-up level, and the moment that the run-up reaches the overtopping tank level (4.4 m+NAP). For all measured waves that would have caused overtopping, the maximum front velocities were found between 15% to 75% of the maximum run-up height of that specific wave. This is in agreement with [Van der Meer \(2011\)](#). The largest volumes above the virtual crest were generally found just before or at the moment of maximum run-up height.

7.5.5. WAVE PERIODS AND ANGLES OF INCIDENCE

As described in section 7.4, the wave peak periods and angles of incidence were determined with the method as described in [Oosterlo et al. \(2021\)](#). Hence, the wave peak periods were determined from the auto-spectral densities of the run-up signals. The angles of incidence were determined using the cross-spectral density of the run-up signals of both laser scanners, from which the time lag between both laser signals can be determined. The distance between the laser scan lines was then divided by the time lags, to determine the phase velocity of a projected wave travelling past the laser scanners. Using trigonometry and the incident wave celerity based on linear wave theory, the angle of incidence spectrum can be determined, see Figure 7.15. For the full description, refer to [Oosterlo et al. \(2021\)](#).

Figure 7.15 compares the variance density spectra based on the run-up signals $R_u(t)$ during both storm peaks, with variance density spectra as measured by the radar on the Rijkswaterstaat measurement pole (see the left panel of Figure 7.2 and Table 7.1). Note that the spectra based on the run-up signals do not represent a real wave spectrum, from which e.g. a wave height can be determined. The laser-based spectra also show much more variance content than the radar spectra, which are real wave spectra. The main observation is that much low-frequency energy is present in the run-up spectra. Although low-frequency energy is also present in the wave spectra, the low-frequency energy is not as prominent. The exact cause of this apparent large low-frequency energy is unknown, but may have been caused by some type of locally-generated surf-beat. The peak (wind) wave period T_p for storm peak 1 was determined as being 4.5 s, for the second storm peak this was 4.2 s. These values are quite close to the values of 4.35 s and 4.00 s that were derived from the radar measurements near the toe of the dike, see Table 7.1. Hence, quite a good estimate of the incident peak wave period can be obtained from the run-up signals.

The angle of incidence spectra give the angle of incidence β [°] relative to the dike nor-

mal for each mode in the spectra of the measured run-up, and are also given in Figure 7.15. They give a peak angle of incidence of 37° for storm peak 1 and 45° for storm peak 2. These angles of incidence are smaller than the angles of incidence as estimated at the dike toe of 66° and 67°, refer to Table 7.1. Hence, these results do not agree well, even though Oosterlo et al. (2021) achieved good results for angles of incidence up to 45°. A potential explanation for the differences could be that the up-rushing waves turned slightly more towards the dike normal on the shallow flat directly in front of the dike and on the dike slope. Furthermore, there exists some uncertainty in the mean wave direction and thus in the angle of incidence, since they were based on a relation between the wind direction and wave direction (Equation 7.1). However, the differences found here are rather large. This again highlights the complexities of storm Ciara and very obliquely incident waves. Further research is therefore recommended during storms with less oblique (but still oblique) wave attack.

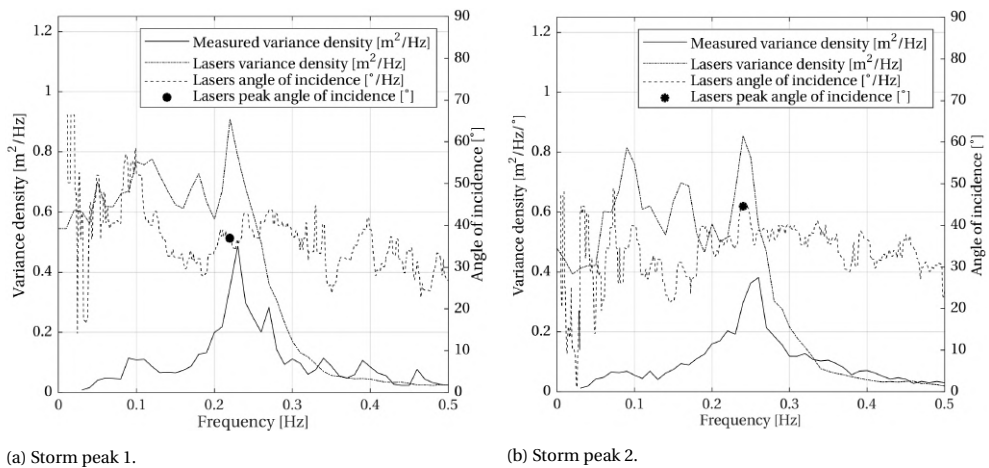


Figure 7.15: Wave variance density spectra based on radar measurements (solid lines), variance density spectra based on laser scanner run-up signals (dash-dot lines) and 'angle of incidence spectra' (dashed lines) for both storm peaks, giving the angle of incidence for each mode in the spectrum. The dots indicate the peak angles of incidence.

7.6. CONCLUSIONS

This chapter presents the first field measurements with an innovative laser scanner system during an actual severe winter storm with very oblique wave attack. The system can measure wave run-up heights, depths and front velocities. From the measured data the wave overtopping, (peak) wave period and angle of incidence can also be calculated. The chapter describes the analysis of the data obtained during storm Ciara (10 - 12 February 2020) and validates the results with data from overtopping tanks and video recordings.

Ciara was a highly unique and complex storm, with offshore-directed wind at the measurement location and waves that refracted somewhat on the shallow flats in front of the dike to become almost alongshore-directed waves at the dike. This posed large challenges

for measuring the 2D front velocities.

The run-up heights based on measured distances agreed well with the run-up observed in video recordings. Run-up heights based on laser reflectance did not agree well, caused by interference of the grid painted on the slope for the video analysis. By removing several of the grid lines good results are expected to be achieved during future storms. The water depth was relatively deep, the waves were breaking and the run-up was very oblique during Ciara. The oblique wave run-up during Ciara was Weibull-distributed ($b = 2.1-2.4$), quite close to a Rayleigh distribution but with somewhat smaller largest run-up heights.

Reasonable agreement between the measured run-up depths and the relation of [Van der Meer \(2011\)](#) with $c_{d2\%} = 0.23$ was found. Discrepancies in the $c_{d2\%}$ -values as found in the literature seem to be caused by the different dike slope angles that were used, rather than caused by differences between small and large-scale tests. The results further seem to suggest that the influence of the wave angle of incidence on the run-up depths is small. However, further research is recommended.

Previous research achieved good results for measuring front velocities of normally incident waves with the laser scanners. Due to the very oblique incidence during storm Ciara, it was very difficult to define a front of the waves, which often ran up the slope in a sort of sideways and local plunging motion, with a larger along-slope-directed velocity higher on the slope. To determine the 2D front velocities based on just the two laser scanner transects was even more complex. It was possible to estimate the 2D front velocities based on the video recordings. The velocities as found here were larger than the relation of [EurOtop \(2018\)](#), which was based on small-scale, normally incident waves. The most likely causes for the differences are inaccuracies in determining the front velocities, differences between small-scale tests and actual storms in the field, and differences between normally and obliquely incident waves.

Overtopping discharges of both the lasers and overtopping tank agreed well. Trends of the calculated overtopping discharges agreed reasonably well with the [EurOtop \(2018\)](#) equations, but the values themselves were smaller than according to the equations. This mainly arose from the $T_{m-1,0}$ wave period, which was relatively large here ($T_p/T_{m-1,0} = 0.9$), indicating that low-frequency energy was present during storm Ciara. Applying $T_p/T_{m-1,0} = 1.1$ of a typical JONSWAP spectrum, resulted in much better agreement between lasers, tank and [EurOtop \(2018\)](#) equations. This would indicate that the low-frequency energy present during storm Ciara did not influence the wave overtopping. This is contrary to expectations and the [EurOtop \(2018\)](#) equations, since [Van Gent \(1999a, 1999b, 2001\)](#) found that the spectral shape does not affect the wave run-up and overtopping. If the measured $T_{m-1,0}$ is correct, this would indicate that the [EurOtop \(2018\)](#) equations may not be fit for use with the complex multi-modal spectra as often present in the Eems-Dollard estuary. Therefore, it is recommended to study the presence of low-frequency energy and the $T_{m-1,0}$ measurements in the area in more detail, and the influence of low-frequency energy on wave overtopping.

b -values of the Weibull distribution of overtopping wave volumes of the laser scanners were smaller than the fit of [Zanuttigh et al. \(2014\)](#), but the trend of the data agreed well. b -values based on the overtopping tank data agreed well with the fit. Maximum overtopping volumes of lasers and tank agreed reasonably well. [EurOtop \(2018\)](#) gave larger maximum volumes based on the q , a and b predicted by [EurOtop \(2018\)](#), but smaller volumes based

on the q , a and b of the laser scanners.

The peak wave period could be determined accurately from the run-up time signals. The angle of incidence of the incoming wave field, based on the laser data, was less oblique than that estimated using an analytical relation, even though good results were achieved using the same method (Oosterlo et al., 2021). Once again, the very oblique, almost coast-parallel, wave attack during Ciara posed large challenges. For further verification of the system, it is recommended to measure in the field at real dikes and during real storms with less oblique (but still oblique) wave attack.

The mobile system will be used at several different locations in the measurement campaign in the area over the coming years. The laser scanners can be installed on any dike; the performance of the system was confirmed for both asphalt and grass dike slopes. Some of the generic results, obtained from the measurements during storm Ciara, are that the wave run-up heights of very obliquely incident breaking waves in relatively deep water are Weibull-distributed, and that the run-up depth equation (Van der Meer, 2011) based on lab measurements also predicts the depths for an actual storm with oblique wave attack quite well. Furthermore, the trend of the EurOtop (2018) equations agrees quite well with measurements of very oblique wave overtopping, but measured discharges were smaller than according to the equations. Accurate measurements of the $T_{m-1,0}$ wave period and angle of incidence are important for further verification of the EurOtop (2018) equations and laser scanner system, and further measurements with the system during storms are expected to provide more insight into both the performance of the system and the understanding of oblique wave run-up and overtopping.

ACKNOWLEDGEMENTS

This study was made possible by the inspiring input of the late Gerbrant van Vledder. We would like to thank Gerben van der Meer, Jan Bakker and Frans Roorda for their help with setting up the laser scanner system, as well as Rik Wegman for his help in analysing the video recordings. This study was supported by Waterschap Noorderzijlvest and the Hoogwaterbeschermingsprogramma.

8

CONCLUSIONS AND RECOMMENDATIONS

If I have seen further it is by standing on the shoulders of Giants.

Isaac Newton

This chapter presents the main conclusions of this dissertation. Section 8.1 answers the main research questions and gives the conclusions. This is followed by section 8.2, which presents the limitations of this study and recommendations for future research. Section 8.3 gives potential applications and extensions of this study for the field measurement campaign in the Eems-Dollard estuary. Finally, appendix E gives an outlook, which discusses some of the implications of this research on the future of the Dutch flood defence safety assessment framework BOI. Potential areas of improvement and recommendations for future research related to BOI are presented as well.

8.1. CONCLUSIONS

The aim of this dissertation was to gain more insight into several uncertain wave propagation processes and (very) oblique wave run-up and overtopping in complex estuaries. This is important for the extreme wave loads on the dikes around the Eems-Dollard estuary. The main focus of the first part of this dissertation was on the modelling of the propagation and transformation of nearshore wind waves with the phase-averaged numerical wave model SWAN. The main focus of the second part of this dissertation was on the measurements of (very) oblique wave run-up and wave overtopping on the dikes in the area. Here, an innovative laser scanner system was developed and applied in the field for the first time, on the slope of a dike during a storm with very oblique wave attack. The six main research questions of this study can now be answered.

8.1.1. PART I: MODELLING WAVE PROPAGATION EFFECTS IN COASTAL WATERS

Mechanisms turning the waves around the corner at the Eemshaven

The first question was: what is the cause of the apparent turning of the waves around the corner at the Eemshaven? More specifically, the aim was to gain more insight in which processes play a role. This question was answered by simulations with the models SWAN, SWASH and REFRAC, using a schematised version of the area around the port Eemshaven and the dike between the Eemshaven and the town Delfzijl. Especially the relatively large-scale simulations with SWASH are considered most realistic, and have provided insight into the relevant processes.

The models predict that the waves indeed turn around the corner at the Eemshaven and become onshore-directed at the dike to the north of Delfzijl during design conditions. With the used bathymetry, the mean wave directions turned 25° to 45° compared to the wind direction, leading to angles of incidence $\beta = 75^\circ - 95^\circ$. A variety of processes play a role in this highly complex estuary and influence the wave conditions at the dike. The main wave propagation processes are wave sheltering, refraction, wave (de)focusing, wave trapping and diffraction. The main wave transformation processes are the triad interactions. The main generative and dissipative processes are depth-induced breaking and wave growth by the wind. These processes create a complex wave field and sometimes directionally multi-peaked spectra at the dike.

Note that these conclusions were not based on measurements, since at the moment of writing no north-westerly storms have been measured within the field measurement campaign in the estuary yet. It is expected that a more definitive analysis of the performance of SWAN in the area can be made after validation with measurements of a storm with a more northerly wind direction (chapter 4).

Performance of SWAN in the estuary and near-dike wave conditions

The second question pertains to the performance of the SWAN model in the estuary and the near-dike wave conditions. More particular, if the wave conditions as predicted by the assessment version of SWAN in the estuary are accurate or not, and if the waves remain as large at the dike as the model predicts. Furthermore, the aim was to gain more insight into whether SWAN can be used safely in this highly complex area, or if the limitations of the underlying modelling concepts of the model are reached or surpassed. This question was

answered using simulations with the SWAN assessment and development versions in the larger area spanning from the North Sea to the Dollard in the south of the Eems-Dollard estuary, and with more detailed simulations with SWAN, SWASH and REFRAC for the area around the corner at the Eemshaven until Delfzijl.

Recommended SWAN settings for the modelling of the wave propagation effects were determined based on simulations with academic refraction and diffraction cases, and with a more detailed model of the area around the Eemshaven and Delfzijl. The here determined recommended settings and the Dutch dike safety assessment (WBI) settings generally outperformed the SWAN default and ST6 settings. It was found that the performance of SWAN related to the directional turning depends on the depth difference per grid cell Δd , the applied turning rate equation, the numerical scheme used to discretise this equation, and the number of directional bins. For narrow-spread waves travelling from deeper towards shallower water, $\Delta d \leq 5$ m is recommended, for waves travelling from shallower towards deeper water, $\Delta d \leq 1$ m, based on the present simulations and conditions considered here. For the refraction of broad-spread seas, the value of Δd influences the results less, but $\Delta d \leq 5$ m is recommended nevertheless. Furthermore, the turning rate equation based on the wave numbers and central differences are recommended for the discretisation. Turning off the rescaling of negative action density may improve the estimation of the directional turning, but may produce negative energy in the spectra. The default SORDUP numerical scheme for the wave propagation is recommended. A high directional resolution is especially relevant for narrow-spread seas, but a higher resolution also outperforms a lower one for broad-spread seas. The refraction limiter of [Van Vledder and Koop \(2009\)](#) can improve the prediction of the wave heights at the dike in the estuary, but comes at the cost of a worse representation of the physics and is therefore only recommended as a mitigation measure. The CCA LTA with $\alpha = 0.05$ for the triads and OCA LTA with $\alpha = 0.1$ performed roughly equal and outperformed other α values, but the first is recommended, as the CCA remains bounded in the unidirectional asymptote. Application of the diffraction approximation can improve the results in certain cases, but application is not recommended, since the approximation is unreliable, unstable and has a grid cell size limitation (chapter 4).

An up to 30% lower H_s and up to 20% lower $T_{m-1,0}$ were found with the SWAN development version compared to the assessment version, at Uithuizerwad and the Twin Dikes. Part of these differences were caused more offshore already, mainly at the transition from the North Sea to the Wadden Sea. While the main focus of this dissertation was on the Eems-Dollard estuary, the main causes for these more offshore differences were still identified, being differences in the refraction formulations of both SWAN versions. The lack of agreement between both SWAN versions and previous field measurements shows that improvements in the understanding of the physics and improvements in the model formulations are still necessary (chapter 3).

SWAN predicted the bulk wave parameters quite well with the recommended settings or WBI settings, for the more realistic schematised case of the area around the Eemshaven and Delfzijl. Whether the wave heights as predicted by SWAN for the Dutch dike safety assessment or the here determined settings are more accurate, depends in a large part on the accuracy of the used wind drag relations. The relation of [Wu \(1982\)](#) as used with the WBI settings gives larger values for the drag coefficient than the relation of [Zijlema](#)

et al. (2012) as used with the recommended settings. Therefore, less wind growth occurs with the recommended settings, and predicted wave heights are 0.4 m lower during design conditions. Which relation is more accurate could not be determined based on the present results and further research is recommended.

Some limitations of SWAN arise in the complex Eems-Dollard estuary. These limitations are related to the omission of diffraction and non-collinear triad wave-wave interactions in SWAN, the overestimation of the transfer to the super-harmonic by the LTA, and the overall worse performance of SWAN for more narrow-spread seas. As a result, SWAN underestimated the wave (de)focusing, overestimated the wave trapping and predicted directionally multi-peaked spectra, even at larger distances from the channel. Hence, the bulk wave parameters are predicted quite well by SWAN, but improvements can still be made related to the representation of the physics and the prediction of the (2D) spectra. Implementation of more advanced triad formulations or better representations for the evolution of the bi-spectrum may significantly improve the results, but come at an increased computational cost.

A wind direction of 330°N seems to be most relevant for the extreme loads on the dike in the estuary, since a direction of 300°N gave wave heights that were 0.4 m - 0.8 m lower during design conditions. This was mainly caused by a reduction of the wave trapping and wave (de)focusing, and an increase of the wave sheltering effect.

An aspect that is not considered in the Dutch dike safety assessment, is the amount of wave energy that is offshore-directed close to the dike. This energy does not contribute to the loads on the dike. For a wind direction of 330°N, 2% - 25% of the wave energy was found to be offshore-directed. For a wind direction of 300°N, this was 10% - 28%, indicating that a significant amount of the energy will not contribute to the loads on the dike. 10% corresponds to 0.2 m, 25% to 0.5 m, with $H_s \approx 2$ m during design conditions at the dike. This may have a large impact on the calculated required crest levels of the dikes in the estuary (chapter 4).

Recommended wave measurement locations

The third question was: where and how should the wave conditions be measured in the Eems-Dollard estuary, to gain further insight into the wave propagation processes in the area? The preferred measurement locations were determined by studying the wave propagation effects with SWAN.

The locations that were determined are the corner of the Eemshaven and the transition area from the deeper channel Bocht van Watum towards the shallow areas in front of the dike in the estuary. Directional wave buoys and an ADCP have since been placed at these locations based on this analysis, amongst others. These measurements are expected to provide more insight in the wave propagation processes and SWAN model performance. Preferably, measurements should be performed with X-band radars as well, since they can provide a 2D image of the waves and their directions as they propagate into the estuary (chapter 3).

8.1.2. PART II: MEASURING WAVE RUN-UP AND OVERTOPPING ON DIKES

Development of technique to measure (very) oblique wave run-up and overtopping in the field during severe winter storms

For the measurement of e.g. the wave overtopping discharge in the field, a flexible, high resolution method was required. Hence, the question arose whether laser scanners can be used to measure (very) oblique wave run-up and overtopping on dikes in the field, during severe winter storms.

This question was answered by designing, setting up, calibrating and validating a system consisting of two synchronised laser scanners. Laser scanners had not been applied to measure run-up and overtopping parameters with a high resolution on the grass slope of a dike in the field before. Another novelty of this system is that two synchronised scanners are used to measure directional information of the waves, compared to previous research which used one laser scanner. Here, this system was used for the first time during an actual severe winter storm with very oblique wave attack. Advantages of the system are that multiple run-up and overtopping parameters can be determined based on the measured data, and that the system can measure these parameters along the whole dike slope and at a large range of (virtual) crest levels. The system is flexible and mobile, it can be placed and relocated easily, without having to dig into the dike (chapters 5, 6 and 7).

Accuracy of laser technique and parameters that can be measured

Obviously, the question arose which parameters the lasers can measure and how accurate the laser technique is in measuring these parameters. This question was answered by calibrating and validating the laser scanner system in the field. The laser scanner technique is highly accurate, provided the correct laser scanner settings are used and a proper calibration of the laser position is performed before the actual measurements are started. Overall, wave run-up and overtopping parameters could be determined as accurately with the laser scanner system as with conventionally used methods.

The laser scanners can be used on different types of slopes; the performance of the system was confirmed for both asphalt and grass dike slopes. However, the influence of varying reflectance of the slope is important. Highly reflective paint of a measurement grid led to large laser reflectance values, which reduced the accuracy of the measured data.

Wave run-up heights could be determined accurately based on both measured distances and laser reflectance, for both normally and obliquely incident waves, with errors of only a few centimetres.

Run-up depths larger than several centimetres could be measured reliably with the lasers. The depths agreed quite well with surf board measurements, at locations higher on the dike slope. Closer to the surf zone, at levels not important for dike design (approximately $R_u \leq H_s/4$), the lasers gave too large and unreliable run-up depths due to foam and spray. The advantage compared to the typically used surf board measurements is that the run-up depth can be determined continuously along the whole slope, not just at a few points on the slope.

Front velocities based on laser scanner data agreed well with front velocities based on video recordings for normally incident waves, and are easier to process automatically and at a higher resolution. 2D front velocities were difficult to determine. The very oblique incidence during the measured storm further complicated this, as the very oblique incid-

ence made it very difficult to define a front. Based on numerical analysis, better performance is expected for less oblique waves. It was observed that very oblique waves in the Ciara storm often ran up the slope in a sort of sideways and local plunging motion, with a larger along-slope-directed velocity higher on the slope. For these complex motions, the developed analysis does not work. Potentially, a manual analysis based on discrete fronts could be done for such motions. Shore-normal components of the front velocities of obliquely incident waves could be determined reasonably well. Shore-parallel velocity components could be determined accurately from the time lag between the laser signals for artificially generated 45° oblique waves by the wave run-up simulator and the SWASH model. These shore-parallel front velocities could not be determined accurately for the measured actual storm, again a result of the very oblique incidence and difficulty in defining a front.

Wave overtopping volumes and discharges based on the laser data agreed well with the Van der Meer and Bruce (2014) equations (later implemented in EurOtop (2018) and hereafter referred to as such), for normally incident waves. Overtopping volumes and discharges during the storm with very obliquely incident waves agreed well with wave overtopping tank measurements. Trends of the calculated discharges agreed reasonably well with the EurOtop (2018) equations, but the equations gave larger volumes and discharges than the lasers and tank. These differences arose mainly from a large measured $T_{m-1,0}$ wave period at the toe of the dike ($T_p/T_{m-1,0} = 0.9$). Large $T_{m-1,0}$ values are consistently measured during storms in the area, indicating that long waves plays a role. Applying $T_p/T_{m-1,0} = 1.1$ of a typical JONSWAP spectrum, resulted in much better agreement between lasers, tank and EurOtop (2018) equations.

Incident peak wave periods could be determined accurately based on the run-up time signals, for both normally and obliquely incident waves. Angles of incidence could be determined accurately for synthetic measurements based on SWASH simulations, with somewhat less oblique wave attack than during the actual storm. The angle of incidence could not be determined as well for the very obliquely incident waves as present during storm Ciara, with mean angles of incidence larger than 65°. Again, the very oblique, almost coast-parallel, wave attack posed large challenges, where waves ran up the slope in a sideways and local plunging motion. Potentially, the linear wave theory assumption on which the analysis method was based, does not hold for these complex conditions with very oblique wave attack (chapters 5, 6 and 7).

Influence of (very) oblique wave attack on wave run-up and overtopping

The final question pertains to the influence of (very) oblique wave attack on wave run-up and overtopping, and the influence on the related (distributions of) run-up heights, depths and velocities, and overtopping volumes and discharges. This question was answered by the verification of the laser scanner system in the field, during the observed severe winter storm Ciara with very oblique wave attack. Note that these conclusions are based on this one storm.

Normally incident deep water wave run-up is Rayleigh-distributed for $d_{toe}/H_{s,toe} \geq 2$ or 3 (Nielsen & Hanslow, 1991; Stam, 1989). Normally incident shallow water wave run-up is Weibull-distributed, with values of the shape factor $b > 2$ (Stam, 1989). Obliquely incident deep water wave run-up is likely Weibull-distributed as well (Van der Meer &

De Waal, 1990). The exact run-up distribution of obliquely incident shallow water wave run-up on a dike slope is unknown. For the present measured storm with very obliquely incident waves and $d_{toe}/H_{s,toe} > 2.5$, the run-up was Weibull-distributed with values of the shape factor b ranging from 2.1-2.4. Hence, quite close to a Rayleigh distribution, but with somewhat smaller largest run-up heights. This confirms that (very) obliquely incident (relatively) deep water wave run-up is indeed Weibull-distributed with a limited influence of the obliquely incident waves on the value of b , in line with the expectations based on previous research.

Reasonable agreement between measured run-up depths and the relation of Van der Meer (2011) with $c_{d2\%} = 0.23$ was found for oblique wave run-up. Discrepancies in $c_{d2\%}$ -values as found in the literature seem to be caused by the different dike slope angles that were used, rather than differences between small and large-scale tests. The results further seem to suggest that the influence of the incident wave angle on the run-up depths is small.

Measured front velocities during the storm seemed larger than the front velocity relation of EurOtop (2018); Van der Meer (2011), which was based on small-scale tests with normally incident waves. These results suggest that the influence of oblique incidence on the front velocities is small as well.

b -values of the Weibull distribution of overtopping wave volumes of the laser scanners were smaller than the fit of Zanuttigh et al. (2014), but the trend of the data agreed reasonably well. These smaller values indicate that the presently measured distribution of overtopping waves was steeper, meaning that the largest volumes are relatively larger. b -values based on the overtopping tank data did agree well with the fit. The exact cause of these differences is unknown, but could be related to the very oblique incidence or the influence of foam, entrained air and spray on the measured run-up depths by the lasers (chapter 7).

8.2. RECOMMENDATIONS

Several aspects were not considered in this study or were only treated briefly. This section presents these aspects and areas for further study, as well as some limitations to the conclusions presented above.

The original scope of this dissertation was to focus on wave measurements and numerical wave modelling in the Eems-Dollard estuary, where the wave measurements would form an important component of analyses and validation data for the models. Since the measurements started quite late in this PhD research, and since storms that are relevant for the area are relatively rare, so far only one storm has been measured with the laser scanners and wave buoys in the estuary. Furthermore, this storm had a (south)westerly wind direction, whereas only northwesterly storms are relevant for the wave penetration into the estuary. Therefore, only measurements at Uithuizerwad became available and not at the Twin Dikes. Measurements during future storms and further validation of measurement techniques, methods and models with measurements are necessary for both topics that were considered in this dissertation.

For the validation of SWAN and SWASH, comparisons with buoy, ADCP and preferably X-band radar measurements of northwestern storms in the area are highly necessary. These measurements are necessary to confirm whether the processes as determined here

indeed play a role, how important their role is, and how well the models can simulate these processes. This study showed that not only the bulk wave parameters should be considered to assess the performance of a numerical wave model, but that it is important to consider the 1D and 2D spectra as well. For the laser scanner system, measurements during a storm with less oblique, but still oblique, wave attack are required. With these measurements, it will be possible to further verify the performance of the system. Certain parameters could not be determined as well from the laser data for the storm with very oblique wave attack, which was considered here. Measurements during a storm with less oblique wave attack can prove whether the system can determine these parameters well for such a storm. Measuring during such a storm can also provide more insight into the influence of e.g. foam, air entrainment and spray on the laser results. Furthermore, more insight can then be gained into the influence of oblique wave attack on wave run-up and overtopping.

Causes were identified for the differences between the assessment and development versions of SWAN in the North Sea and Wadden Sea. Further investigation of the preferred formulations of the physics or the general performance of SWAN in these areas were outside the scope of this study. At the transition from the North Sea to the Wadden Sea, relatively large differences were found in wave heights, due to the different depth-induced breaking formulations. To determine the preferred formulation, further validation with measured spectra is recommended. Comparisons with a more detailed (e.g. phase-resolving) model could aid as well. The same holds for the 2D (non-collinear) triad wave-wave interactions, which likely not only play a role inside the estuary, but around the tidal deltas between the North Sea and Wadden Sea as well. The implementation of refraction in the development version of SWAN is more robust and accurate than the older implementation as used in the assessment version. Use of the refraction limiter of [Van Vledder and Koop \(2009\)](#) can improve the prediction of the wave heights in the estuary, but comes at the cost of a worse representation of the physics and was therefore only recommended as a mitigation measure. More research towards the actual penetration of long North Sea and infragravity waves into the eastern Wadden Sea is therefore still necessary. Finally, further validation of the different wind drag formulations and comparison of SWAN with North Sea and Wadden Sea spectra is necessary.

As a first step to improve the modelling of the triads in SWAN, a proper calibration of the proportionality coefficient α for the CCA LTA is recommended. However, the LTA is a 1D method (it considers only the collinear interactions), which only accounts for the transfer to the super-harmonic. This study showed that transfers by the triads to lower frequencies, 2D (non-collinear) triad interactions and diffraction can play a role around the steep channel slopes in the Eems-Dollard estuary and around the tidal deltas in the Wadden Sea as well. Hence, the LTA only accounts for a part of the physical process. Therefore, future research should preferably focus on the implementation of more advanced (2D) triad formulations (e.g. [Becq et al., 1998](#); [Booij et al., 2009](#); [Eldeberky, 1996](#); [P. A. E. M. Janssen, 2009](#); [Toledo & Agnon, 2012](#); [Van der Westhuysen, 2007](#)), better representations for the evolution of the bi-spectrum (e.g. [T. T. Janssen, 2006](#); [Smit & Janssen, 2016](#); [Vrecica & Toledo, 2016, 2019](#)), and improvement of the modelling of diffraction with phase-averaged models. Further field measurements in the estuary and application of phase-resolving models can aid in reaching these goals.

The focus of this dissertation was on wave propagation processes, where e.g. the dissipative and generative source terms were only treated briefly. Furthermore, processes such as Bragg-scattering were not considered here. Further research should also consider these processes and their role in the area of interest.

The simulations performed in this dissertation used a uniform, stationary wind and neglected the influence of (tidal) currents on e.g. the waves (wave-current interactions were neglected). The influence of local changes in the wind velocity and turning of the wind direction can play a large role, especially in the Eems-Dollard estuary, with complex northwestern storms and the influence of the land mass of the province of Groningen. Due to the tidal inlets in the Wadden Sea and the shape of the Eems-Dollard estuary, tidal current velocities can be large (see e.g. Adema et al., 2014, 2015; Arcadis et al., 2019; Lai, Long, & Huang, 1989; Tolman, 1991). Since the simulations in this dissertation considered the conditions during the peak of a storm, the wind direction and velocity could be considered approximately constant and the tidal current velocities relatively small. However, more research incorporating the effects of dynamics in the wind and wave-current interactions in the Eems-Dollard estuary is still recommended.

So far, the lasers were used to determine the wave run-up heights, run-up flow depths, run-up front velocities, wave overtopping volumes and discharges, wave (peak) periods, and wave angles of incidence. Theoretically, even more parameters can be derived from the laser data. Further research with the laser scanners could e.g. focus on determining the wave directional spreading, the run-up of low-frequency or infragravity waves, or erosion of a dike slope or crest. An estimate can be given of the difficulty and accuracy with which a certain parameter can theoretically be determined from the measured laser data. This depends on how much the given parameter is derived from other parameters. An overview: distance signals, laser reflectance signals → run-up depth (layer thickness) signals, erosion → run-up signals → run-up heights, front velocity signals, wave overtopping volume signals, run-up spectra → wave overtopping discharges, (peak) periods, angles of incidence, directional spreading. This also highlights the importance of applying the correct laser settings and performing a proper system position calibration.

The EurOtop (2018); Van der Meer and Bruce (2014) equations gave larger volumes and discharges than the lasers and tank for storm Ciara. These differences arose mainly from a large measured $T_{m-1,0}$ wave period at the toe of the dike ($T_p/T_{m-1,0} = 0.9$). Large $T_{m-1,0}$ values were consistently measured during storms in the area. The $T_{m-1,0}$ wave period is very sensitive to the low-frequency energy, due to which the $T_{m-1,0}$ can become very large when low-frequency energy is present (Hofland, Chen, Altomare, & Oosterlo, 2017). As a result, the influence of this period and thus the low-frequency energy on the overtopping discharge as calculated with the Van der Meer and Bruce (2014) equations is large, see e.g. Lashley et al. (2020); Lashley, Van der Meer, et al. (2021); Oosterlo, Van der Meer, et al. (2018). Applying a more typical ratio of $T_p/T_{m-1,0} = 1.1$ to the EurOtop (2018) equations resulted in much better agreement between lasers, tank and equations. Therefore, it is recommended to study the presence of low-frequency energy and the $T_{m-1,0}$ measurements in the area in more detail, as well as the influence of low-frequency energy on wave overtopping.

8.3. APPLICATION TO THE MVED FIELD MEASUREMENT CAMPAIGN

This study focused on the Eems-Dollard estuary in the north of the Netherlands. The results of this dissertation can be applied to other locations as well. This section presents some potential applications and extensions of this study.

This dissertation contributes directly to several of the work packages of the MVED field measurement project in the area. Using the results of this dissertation, the measurements in the area can be fine-tuned, with which further calibration and validation of SWAN can be performed. Further validation of SWAN could be performed with simulations with a more detailed model as well, e.g. a phase-resolving model. Added to that, this dissertation has provided points of attention, which can be used for the SWAN storm hindcasts which will be performed within the MVED project. The determined areas of improvement of SWAN are not only relevant for the estuary, but also for other locations where wave sheltering effects or strong refraction effects play a role. Such locations may be narrow inlets, ports, convex coasts or channels with steep slopes.

The laser scanner measurements directly contribute to the MVED project as well. The laser scanner system is currently placed at Uithuizerwad, where it measures during severe winter storms. The system will measure at Uithuizerwad until at least 2022, after which it may be moved to the Twin Dikes location. The laser scanners can be applied at any dike with a smooth slope. Although not validated here, the laser scanners can also be used to measure erosion of the sea-side and land-side slopes of the dike and the crest. The system can aid with future tests with the wave run-up and wave overtopping simulators as well. Further measurements with the system during storms are expected to provide more insight into both the performance of the system and the understanding of oblique wave run-up and overtopping. The present results and insights and those of measurements during future storms can contribute to the further calibration and verification of the cumulative overload method (Van der Meer, 2011; Van der Meer et al., 2010) and to the Dutch safety assessment framework BOI.

Finally, the results of both topics considered in this dissertation contribute to the two main goals of the MVED project: to understand the processes yielding nearshore wave conditions better, ultimately leading to improved numerical prediction models, and to understand the processes related to oblique wave run-up and overtopping better, leading to improved prediction methods. At the end of the MVED project, this will hopefully provide insight in whether the current crest level of the dike between Eemshaven and Delfzijl is sufficiently high.

BIBLIOGRAPHY

- Adema, J., Geleynse, N., & Telenta, B. (2014). *Een rekenexperiment voor de Waddenzee, de storm van 5 & 6 december 2013* (Technical Report C03041.001941.0100 No. december). Zwolle, the Netherlands: Arcadis.
- Adema, J., Geleynse, N., & Telenta, B. (2015). *Een Rekenexperiment voor de Waddenzee, 4 stormen van 2006, 2007, 2013 en 2014* (Technical Report C03041.001941.0200). Zwolle, the Netherlands: Arcadis.
- Allis, M. J., Peirson, W. L., & Banner, M. L. (2011). Application of lidar as a measurement tool for waves. In *The twenty-first international offshore and polar engineering conference*. International Society of Offshore and Polar Engineers. Retrieved from <https://onepetro.org/conference-paper/ISOPE-I-11-402>
- Almeida, L., Masselink, G., Russell, P., & Davidson, M. (2015, jan). Observations of gravel beach dynamics during high energy wave conditions using a laser scanner. *Geomorphology*, 228, 15–27. Retrieved from <https://linkinghub.elsevier.com/retrieve/pii/S0169555X14004279> doi: 10.1016/j.geomorph.2014.08.019
- Arcadis, Deltares, HKV, KNMI, VVC, & Witteveen+Bos. (2019). *POV-Waddenzeedijken. Risicoanalyse HR: Onderzoeksrapportage Fase B* (Technical report OW.11503D / C03011.000625). Zwolle, the Netherlands: Arcadis, Deltares, HKV, KNMI, VVC, Witteveen+Bos.
- Ardhuin, F., Rogers, E., Babanin, A. V., Filipot, J.-F., Magne, R., Roland, A., ... Colard, F. (2010, sep). Semiempirical Dissipation Source Functions for Ocean Waves. Part I: Definition, Calibration, and Validation. *Journal of Physical Oceanography*, 40(9), 1917–1941. Retrieved from <http://journals.ametsoc.org/doi/10.1175/2010JPO4324.1> doi: 10.1175/2010JPO4324.1
- Babanin, A. V., & Young, I. R. (2005). Two-phase behaviour of the spectral dissipation of wind waves. In *Proceedings of the 5th international symposium ocean waves measurement and analysis (waves)* (p. 51). Madrid, Spain. Retrieved from <https://tinyurl.com/e6xrlnxa>
- Battjes, J. A., & Gerritsen, H. (2002, jul). Coastal modelling for flood defence. In D. Cox, J. Hunt, P. Mason, H. Wheeler, & P. Wolf (Eds.), *Philosophical transactions of the royal society of london. series a: Mathematical, physical and engineering sciences* (Vol. 360, pp. 1461–1475). London, England: The Royal Society. Retrieved from <https://royalsocietypublishing.org/doi/10.1098/rsta.2002.1010> doi: 10.1098/rsta.2002.1010
- Battjes, J. A., & Groenendijk, H. W. (2000). Wave height distributions on shallow foreshores. *Coastal Engineering*, 40(3), 161–182. Retrieved from <http://linkinghub.elsevier.com/retrieve/pii/S0378383900000077> doi: 10.1016/S0378-3839(00)00007-7
- Battjes, J. A., & Janssen, J. P. F. M. (1978). Energy loss and set-up due to breaking of random waves. In *Coastal engineering proceedings* (pp. 569–587). Hamburg, Germany:

- American Society of Civil Engineers. Retrieved from <http://journals.tdl.org/icce/index.php/icce/article/view/3294> doi: 10.1061/9780872621909.034
- Beckers, J., Gautier, C., & Groeneweg, J. (2009). *Probabilistic model Wadden Sea: Three alternatives for HBC 2011 and test results. WTI - HR Zout* (Technical Report 1200103-057). Delft, the Netherlands: Deltares. Retrieved from http://publications.deltares.nl/1200103_{ }057.pdf
- Becq, F., Benoit, M., & Forget, P. (1998). Numerical simulations of directionally spread shoaling surface gravity waves. In B. L. Edge (Ed.), *Coastal engineering proceedings*. Copenhagen, Denmark: American Society of Civil Engineers. Retrieved from <https://icce-ojs-tamu.tdl.org/icce/index.php/icce/article/view/5627> doi: 10.9753/icce.v26.%25p
- Becq-Girard, F., Forget, P., & Benoit, M. (1999, oct). Non-linear propagation of unidirectional wave fields over varying topography. *Coastal Engineering*, 38(2), 91–113. Retrieved from <https://linkinghub.elsevier.com/retrieve/pii/S0378383999000435> doi: 10.1016/S0378-3839(99)00043-5
- Bendat, J. S., & Piersol, A. G. (1971). *Random Data Analysis and Measurement Procedures*. New York, New York: John Wiley & Sons.
- Blenkinsopp, C. E., Mole, M., Turner, I., & Peirson, W. (2010, nov). Measurements of the time-varying free-surface profile across the swash zone obtained using an industrial LIDAR. *Coastal Engineering*, 57(11-12), 1059–1065. Retrieved from <https://linkinghub.elsevier.com/retrieve/pii/S0378383910001134> doi: 10.1016/j.coastaleng.2010.07.001
- Blenkinsopp, C. E., Turner, I. L., Allis, M. J., Peirson, W. L., & Garden, L. E. (2012, oct). Application of LiDAR technology for measurement of time-varying free-surface profiles in a laboratory wave flume. *Coastal Engineering*, 68, 1–5. Retrieved from <https://linkinghub.elsevier.com/retrieve/pii/S0378383912000762> doi: 10.1016/j.coastaleng.2012.04.006
- Booij, N. (1998). *Limitations of refraction in SWAN*. Delft, the Netherlands.
- Booij, N., Holthuijsen, L. H., & Bénit, M. P. (2009, aug). A distributed collinear triad approximation in SWAN. In M. Mizuguchi & S. Sato (Eds.), *Proceedings of coastal dynamics 2009* (pp. 1–10). Tokyo, Japan: World Scientific Publishing Company. Retrieved from http://www.worldscientific.com/doi/abs/10.1142/9789814282475_{ }0006 doi: 10.1142/9789814282475_0006
- Booij, N., Ris, R. C., & Holthuijsen, L. H. (1999, apr). A third-generation wave model for coastal regions: 1. Model description and validation. *Journal of Geophysical Research: Oceans*, 104(C4), 7649–7666. Retrieved from <http://doi.wiley.com/10.1029/98JC02622> doi: 10.1029/98JC02622
- Bornschein, A., Pohl, R., Wolf, V., Schüttrumpf, H., Scheres, B., Troch, P., ... Van der Meer, J. W. (2014). Wave Run-up and Wave Overtopping under very oblique wave attack (Cornerdike Project). In *Hydralab iv*. Lisbon, Portugal. Retrieved from <https://hydralab.eu/uploads/proceedings/HyIV-DHI-05.pdf>
- Bouws, E., & Battjes, J. A. (1982). A Monte Carlo approach to the computation of refraction of water waves. *Journal of Geophysical Research*, 87(C8), 5718. Retrieved from <http://doi.wiley.com/10.1029/JC087iC08p05718> doi: 10.1029/JC087iC08p05718

- Brodie, K. L., Slocum, R. K., & McNinch, J. E. (2012, oct). New insights into the physical drivers of wave runup from a continuously operating terrestrial laser scanner. In *2012 oceans* (pp. 1–8). IEEE. Retrieved from <http://ieeexplore.ieee.org/document/6404955/> doi: 10.1109/OCEANS.2012.6404955
- Cavaleri, L., Abdalla, S., Benetazzo, A., Bertotti, L., Bidlot, J. R., Breivik, ... van der Westhuysen, A. J. (2018). Wave modelling in coastal and inner seas. *Progress in Oceanography*, 167(February), 164–233. Retrieved from <https://doi.org/10.1016/j.pocean.2018.03.010> doi: 10.1016/j.pocean.2018.03.010
- Cavaleri, L., & Rizzoli, P. M. (1981). Wind wave prediction in shallow water: Theory and applications. *Journal of Geophysical Research*, 86(C11), 10961. Retrieved from <http://doi.wiley.com/10.1029/JC086iC11p10961> doi: 10.1029/JC086iC11p10961
- Cete, C. (2019). *Quantifying the effect of woody vegetation on the wave loads on a dike using remote sensing. Large scale physical model tests* (MSc Thesis, Delft University of Technology). Retrieved from <http://resolver.tudelft.nl/uuid:88e2b629-efc9-48c8-b438-b250951200de>
- Charnock, H. (1955, oct). Wind stress on a water surface. *Quarterly Journal of the Royal Meteorological Society*, 81(350), 639–640. Retrieved from <http://doi.wiley.com/10.1002/qj.49708135027> doi: 10.1002/qj.49708135027
- Chbab, H., & De Waal, H. (2016). *Achtergrondrapport Hydraulische Belastingen. Wettelijk Beoordelingsinstrumentarium 2017* (Technical Report 1230087-008). Delft, the Netherlands: Deltares. Retrieved from https://www.helpdeskwater.nl/publish/pages/132669/1230087-008-hye-0001_{_}v4-r-achtergrondrapport_{_}hydraulische_{_}belastingen_{_}def.pdf
- Dabbi, E. P., Haigh, I. D., Lambkin, D., Herson, J., Williams, J. J., & Nicholls, R. J. (2015, jun). Beyond significant wave height: A new approach for validating spectral wave models. *Coastal Engineering*, 100, 11–25. Retrieved from <https://linkinghub.elsevier.com/retrieve/pii/S0378383915000538> doi: 10.1016/j.coastaleng.2015.03.007
- De Rouck, J., Verhaeghe, H., & Geeraerts, J. (2009, feb). Crest level assessment of coastal structures — General overview. *Coastal Engineering*, 56(2), 99–107. Retrieved from <https://linkinghub.elsevier.com/retrieve/pii/S0378383908000707> doi: 10.1016/j.coastaleng.2008.03.014
- De Vries, S., Hill, D., de Schipper, M., & Stive, M. (2011, mar). Remote sensing of surf zone waves using stereo imaging. *Coastal Engineering*, 58(3), 239–250. Retrieved from <https://linkinghub.elsevier.com/retrieve/pii/S0378383910001444> doi: 10.1016/j.coastaleng.2010.10.004
- De Waal, J. P. (2003). *Windmodellering voor bepaling van waterstanden en golven. Een analyse van de bouwstenen*. (Technical Report (RIZA werkdocument 2003.118x)). Lelystad, the Netherlands: Rijkswaterstaat RIZA. Retrieved from <http://publicaties.minienm.nl/documenten/windmodellering-voor-bepaling-waterstanden-en-golven-een-analyse>
- De Waal, J. P. (2018). *Basisrapport WBI 2017* (Tech. Rep.). Delft, the Netherlands: Deltares. Retrieved from <https://www.helpdeskwater.nl/onderwerpen/waterveiligheid/primaire/beoordelen/@205809/basisrapport-wbi2017/>

- De Wit, F., & Reniers, A. J. H. M. (n.d.). *Internal presentation on SWASH*. Delft, the Netherlands: Delft University of Technology.
- Den Bieman, J. P., Stuparu, D. E., Hoonhout, B. M., Diermanse, F. L. M., Boers, M., & Van Geer, P. F. C. (2014, oct). Fully probabilistic dune safety assessment using an advanced probabilistic method. In P. J. Lynett (Ed.), *Coastal engineering proceedings* (Vol. 1, p. 9). Seoul, Korea: American Society of Civil Engineers. Retrieved from <https://journals.tdl.org/icce/index.php/icce/article/view/7287> doi: 10.9753/icce.v34.management.9
- Dietrich, J., Zijlema, M., Allier, P.-E., Holthuijsen, L. H., Booij, N., Meixner, J., ... Westerink, J. (2013, oct). Limiters for spectral propagation velocities in SWAN. *Ocean Modelling*, 70, 85–102. Retrieved from <https://linkinghub.elsevier.com/retrieve/pii/S1463500312001655> doi: 10.1016/j.ocemod.2012.11.005
- Donelan, M. A., Babanin, A. V., Young, I. R., & Banner, M. L. (2006, aug). Wave-Follower Field Measurements of the Wind-Input Spectral Function. Part II: Parameterization of the Wind Input. *Journal of Physical Oceanography*, 36(8), 1672–1689. Retrieved from <http://journals.ametsoc.org/doi/10.1175/JPO2933.1> doi: 10.1175/JPO2933.1
- Dusseljee, D., Klopman, G., Van Vledder, G. P., & Riezebos, H. J. (2014, dec). Impact of harbor navigation channels on waves: A numerical modelling guideline. In *Coastal engineering proceedings* (Vol. 1, p. 58). Seoul, Korea: American Society of Civil Engineers. Retrieved from <https://journals.tdl.org/icce/index.php/icce/article/view/7710> doi: 10.9753/icce.v34.waves.58
- Eldeberky, Y. (1996). *Nonlinear transformation of wave spectra in the nearshore zone* (Dissertation, Delft University of Technology). Retrieved from <http://resolver.tudelft.nl/uuid:fa4b60b7-a09e-491a-992e-2dab0a2606fe>
- Eslami Arab, S., Van Dongeren, A., & Wellens, P. (2012, dec). Studying the effect of linear refraction on low-frequency wave propagation (Physical and numerical study). In *Coastal engineering proceedings* (Vol. 1, p. 9). Santander, Spain: American Society of Civil Engineers. Retrieved from <https://icce-ojs-tamu.tdl.org/icce/index.php/icce/article/view/6710> doi: 10.9753/icce.v33.waves.9
- EurOtop. (2007). *EurOtop. Wave Overtopping of Sea Defences and Related Structures: Assessment Manual* (First ed.; T. Pullen, W. Allsop, T. Bruce, A. Kortenhaus, H. F. R. Schüttrumpf, & J. W. Van der Meer, Eds.). Die Küste. Kuratorium für Forschung im Küsteningenieurwesen. Retrieved from <http://www.overtopping-manual.com>
- EurOtop. (2018). *Manual on wave overtopping of sea defences and related structures. An overtopping manual largely based on European research, but for worldwide application* (Second ed.; J. W. Van der Meer et al., Eds.). Retrieved from <http://www.overtopping-manual.com>
- Gautier, C. (2010). *SWAN Calibration and Validation for HBC2011. WTI - HR Zout* (Technical Report 1200103-020). Delft, the Netherlands: Deltares.
- Gautier, C., & Groeneweg, J. (2010). *Aansturingsdocument SWAN voor HR 2011. WTI HR-Zout* (Technical Report 1200103-021). Delft, the Netherlands: Deltares.
- Gautier, C., & Groeneweg, J. (2012). *Achtergrondrapportage hydraulische belasting voor zee en estuaria. WTI - HR2011* (Technical Report 1204143-002). Delft, the Netherlands:

- Deltares. Retrieved from <http://publications.deltares.nl/1204143{ }002.pdf>
- Gautier, C., Van Nieuwkoop, J., & De Ridder, M. (2018). *SWAN-Kuststrook* (Technical Report 11202221-005). Delft, the Netherlands: Deltares.
- Goda, Y., Takayama, T., & Suzuki, Y. (1978, aug). Diffraction Diagrams for Directional Random Waves. In *Coastal engineering proceedings* (pp. 628–650). Hamburg, Germany: American Society of Civil Engineers. Retrieved from <http://ascelibrary.org/doi/10.1061/9780872621909.037> doi: 10.1061/9780872621909.037
- Groeneweg, J., & Gautier, C. (2020). *Generieke methode SWAN modellering voor BOI en andere RWS toepassingen* (Tech. Rep.). Delft, the Netherlands: Deltares.
- Groeneweg, J., Van der Westhuysen, A. J., Van Vledder, G. P., Jacobse, S., Lansen, J., & Van Dongeren, A. (2009, may). Wave modelling in a tidal inlet: Performance of SWAN in the Wadden Sea. In *Coastal engineering proceedings* (pp. 411–423). Hamburg, Germany: World Scientific Publishing Company. Retrieved from <http://www.worldscientific.com/doi/abs/10.1142/9789814277426{ }0035> doi: 10.1142/9789814277426_0035
- Groeneweg, J., Van Gent, M. R. A., Van Nieuwkoop, J., & Toledo, Y. (2015). Wave Propagation into Complex Coastal Systems and the Role of Nonlinear Interactions. *Journal of Waterway, Port, Coastal, and Ocean Engineering*, 141(5), 04015003. Retrieved from <http://ascelibrary.org/doi/10.1061/{ }28ASCE{ }29WW.1943-5460.0000300> doi: 10.1061/(ASCE)WW.1943-5460.0000300
- Groeneweg, J., & Van Vledder, G. P. (2005). Tools for improving wave modeling and field measurements in shallow water. In *Proc. int. symp. on wave measurement and analysis* (pp. 1–10). Madrid, Spain: American Society of Civil Engineers.
- Guenther, G. C., Cunningham, A. G., LaRocque, P. E., & Reid, D. J. (2000). Meeting the accuracy challenge in airborne bathymetry. In *Proceedings of earsel-sig-workshop lidar*. Dresden, Germany. Retrieved from <https://earsel.org/wp-content/uploads/2016/12/01{ }1{ }guenther1.pdf>
- Guzman Mardones, C. (2011). *Impact of access channel geometry on wave penetration in harbours* (MSc Thesis, Delft University of Technology). Retrieved from <http://resolver.tudelft.nl/uuid:1ba13e2e-ba4e-4802-9366-92f7fc00bdfa>
- Hanna, S. R., & Heinold, D. W. (1985). *Development and application of a simple method for evaluating air quality models* (No. 4409). Washington, D.C.: American Petroleum Institute.
- Hashimoto, N., & Kobune, K. (1988, dec). Estimation of Directional Spectrum through a Bayesian Approach. *Coastal Engineering in Japan*, 31(2), 183–198. Retrieved from <https://www.tandfonline.com/doi/full/10.1080/05785634.1988.11924491> doi: 10.1080/05785634.1988.11924491
- Hasselmann, K., Barnett, T. P., Bouws, E., Carlson, H., Cartwright, D. E., Enke, K., ... Walden, H. (1973). Measurements of wind-wave growth and swell decay during the Joint North Sea Wave Project (JONSWAP). *Deutsches Hydrographisches Zeitschrift*, 8(12), 1–95. Retrieved from <http://resolver.tudelft.nl/uuid:f204e188-13b9-49d8-a6dc-4fb7c20562fc>
- Hasselmann, S., & Hasselmann, K. (1985, nov). Computations and Parameterizations of the Nonlinear Energy Transfer in a Gravity-Wave Spectrum. Part

- I: A New Method for Efficient Computations of the Exact Nonlinear Transfer Integral. *Journal of Physical Oceanography*, 15(11), 1369–1377. Retrieved from [http://journals.ametsoc.org/doi/10.1175/1520-0485\(1985\)015{ }3C1369:CAPOTN{ }3E2.0.CO;2](http://journals.ametsoc.org/doi/10.1175/1520-0485(1985)015{ }3C1369:CAPOTN{ }3E2.0.CO;2) doi: 10.1175/1520-0485(1985)015<1369:CAPOTN>2.0.CO;2
- Hasselmann, S., Hasselmann, K., Allender, J. H., & Barnett, T. P. (1985, nov). Computations and Parameterizations of the Nonlinear Energy Transfer in a Gravity-Wave Spectrum. Part II: Parameterizations of the Nonlinear Energy Transfer for Application in Wave Models. *Journal of Physical Oceanography*, 15(11), 1378–1391. Retrieved from [http://journals.ametsoc.org/doi/10.1175/1520-0485\(1985\)015{ }3C1378:CAPOTN{ }3E2.0.CO;2](http://journals.ametsoc.org/doi/10.1175/1520-0485(1985)015{ }3C1378:CAPOTN{ }3E2.0.CO;2) doi: 10.1175/1520-0485(1985)015<1378:CAPOTN>2.0.CO;2
- Herbers, T. H. C., Elgar, S., & Guza, R. T. (1995). Generation and propagation of infragravity waves. *Journal of Geophysical Research*, 100(C12), 24863. Retrieved from <http://doi.wiley.com/10.1029/95JC02680> doi: 10.1029/95JC02680
- Hofland, B., Chen, X., Altomare, C., & Oosterlo, P. (2017, may). Prediction formula for the spectral wave period $T_{m-1,0}$ on mildly sloping shallow foreshores. *Coastal Engineering*, 123, 21–28. Retrieved from <https://linkinghub.elsevier.com/retrieve/pii/S037838391630237X> doi: 10.1016/j.coastaleng.2017.02.005
- Hofland, B., Diamantidou, E., Van Steeg, P., & Meys, P. (2015, dec). Wave runup and wave overtopping measurements using a laser scanner. *Coastal Engineering*, 106, 20–29. Retrieved from <https://linkinghub.elsevier.com/retrieve/pii/S0378383915001519> doi: 10.1016/j.coastaleng.2015.09.003
- Holthuijsen, L. H. (2007). *Waves in oceanic and coastal waters*. Cambridge, United Kingdom: Cambridge University Press.
- Holthuijsen, L. H., Herman, A., & Booij, N. (2003, oct). Phase-decoupled refraction–diffraction for spectral wave models. *Coastal Engineering*, 49(4), 291–305. Retrieved from <https://linkinghub.elsevier.com/retrieve/pii/S0378383903000656> doi: 10.1016/S0378-3839(03)00065-6
- Hughes, S. A., Thornton, C. I., Van der Meer, J. W., & Scholl, B. N. (2012, oct). Improvements in describing wave overtopping processes. In *Coastal engineering proceedings* (Vol. 1, p. 35). Santander, Spain: ASCE. Retrieved from <https://icce-ojs-tamu.tdl.org/icce/index.php/icce/article/view/6684> doi: 10.9753/icce.v33.waves.35
- Hwang, P. A. (2011, mar). A Note on the Ocean Surface Roughness Spectrum. *Journal of Atmospheric and Oceanic Technology*, 28(3), 436–443. Retrieved from <http://journals.ametsoc.org/doi/10.1175/2010JTECH0812.1> doi: 10.1175/2010JTECH0812.1
- Janssen, P. A. E. M. (2009, oct). On some consequences of the canonical transformation in the Hamiltonian theory of water waves. *Journal of Fluid Mechanics*, 637, 1–44. Retrieved from https://www.cambridge.org/core/product/identifier/S0022112009008131/type/journal_{ }article doi: 10.1017/S0022112009008131
- Janssen, T. T. (2006). *Nonlinear surface waves over topography* (Dissertation, Delft University of Technology). Retrieved from <http://resolver.tudelft.nl/uuid:>

- [Of2c9d56-d2eb-4dc7-961e-61733a384c09](https://doi.org/10.1175/1520-0485(1984)014<1271:OTEOAF>2.0.CO;2)
- Johnson, D. (2002). *DIWASP, a directional wave spectra toolbox for MATLAB: User Manual*. (User Manual). Perth, Australia: Centre for Water Research, University of Western Australia; MetOcean Solutions Ltd. Retrieved from <https://github.com/metocean/diwasp>
- Jongejan, R. (2013). *Vaststellen uitgangspunten definitieve kalibratie. WTI 2017, Cluster Raamwerk* (Technical Report 1207803-001). Delft, the Netherlands: Deltares.
- Klein, M. D., & Kroon, J. (2011). *Productieberekeningen Waddenzee voor WTI-2011 : rapportage fase 1* (Technical Report PR1872.10). Lelystad, the Netherlands: Svasek, HKV.
- Komen, G. J., Hasselmann, K., & Hasselmann, K. (1984, aug). On the Existence of a Fully Developed Wind-Sea Spectrum. *Journal of Physical Oceanography*, 14(8), 1271–1285. Retrieved from [http://journals.ametsoc.org/doi/10.1175/1520-0485\(1984\)014<1271:OTEOAF>2.0.CO;2](http://journals.ametsoc.org/doi/10.1175/1520-0485(1984)014<1271:OTEOAF>2.0.CO;2) doi: 10.1175/1520-0485(1984)014<1271:OTEOAF>2.0.CO;2
- Lai, R. J., Long, S. R., & Huang, N. E. (1989). Laboratory studies of wave-current interaction: Kinematics of the strong interaction. *Journal of Geophysical Research*, 94(C11), 16201. Retrieved from <http://doi.wiley.com/10.1029/JC094iC11p16201> doi: 10.1029/JC094iC11p16201
- Lashley, C. H., Bricker, J. D., Van der Meer, J. W., Altomare, C., & Suzuki, T. (2020, sep). Relative Magnitude of Infragravity Waves at Coastal Dikes with Shallow Foreshores: A Prediction Tool. *Journal of Waterway, Port, Coastal, and Ocean Engineering*, 146(5), 04020034. Retrieved from [http://ascelibrary.org/doi/10.1061/\(ASCE\)WW.1943-5460.0000576](http://ascelibrary.org/doi/10.1061/(ASCE)WW.1943-5460.0000576) doi: 10.1061/(ASCE)WW.1943-5460.0000576
- Lashley, C. H., Jonkman, S. N., Van der Meer, J. W., Bricker, J. D., & Vuik, V. (2021). The Influence of Infragravity Waves on the Safety of Coastal Defences: A Case Study of the Dutch Wadden Sea. *Natural Hazards and Earth System Sciences Discussions*(July), 1–40. Retrieved from <https://nhess.copernicus.org/preprints/nhess-2021-211/nhess-2021-211.pdf> doi: 10.5194/nhess-2021-211
- Lashley, C. H., Van der Meer, J. W., Bricker, J. D., Altomare, C., Suzuki, T., & Katsuya, H. (2021). Formulating wave overtopping at vertical and sloping structures with very shallow foreshores using deep-water wave characteristics. *Journal of Waterway, Port, Coastal, and Ocean Engineering*, *In press*.
- Liu, J. (2009). *Swell propagation in a natural coastal channel in the SWAN model* (MSc Thesis, Delft University of Technology). Retrieved from <http://resolver.tudelft.nl/uuid:5daeaa85-556a-408c-8a70-d3c3498d1ba2>
- Lopez de la Cruz, J. (2010). *The evolution of storms on the Wadden Sea* (Technical Report 1200264-004-HYE-0012). Delft, the Netherlands: Deltares. Retrieved from https://puc.overheid.nl/rijkswaterstaat/doc/PUC_{_}155186_{_}31/
- Lorke, S., Brüning, A., Van der Meer, J. W., Schüttrumpf, H., Bornschein, A., Gilli, S., ... Schlütter, F. (2011, feb). On the effect of current on wave run-up and wave overtopping. In *Coastal engineering proceedings* (Vol. 1, p. 13). Shanghai, China: ASCE. Retrieved from <https://icce-ojs-tamu.tdl.org/icce/index.php/icce/article/view/1388> doi: 10.9753/icce.v32.structures.13

- Magne, R., Belibassakis, K. A., Herbers, T. H. C., Arduin, F., O'Reilly, W. C., & Rey, V. (2007, jan). Evolution of surface gravity waves over a submarine canyon. *Journal of Geophysical Research*, 112(C01002), 1–12. Retrieved from <http://doi.wiley.com/10.1029/2005JC003035> doi: 10.1029/2005JC003035
- Martins, K., Blenkinsopp, C. E., & Zang, J. (2016). Monitoring Individual Wave Characteristics in the Inner Surf with a 2-Dimensional Laser Scanner (LiDAR). *Journal of Sensors*, 2016, 1–11. Retrieved from <http://www.hindawi.com/journals/js/2016/7965431/> doi: 10.1155/2016/7965431
- Maslov, D. V., Fadeev, V. V., & Lyashenko, A. I. (2000). A shore-based lidar for coastal seawater monitoring. In *Proc. earsel-sig-workshop lidar* (Vol. 1, pp. 46–52). Dresden, Germany. Retrieved from <https://citeseerx.ist.psu.edu/viewdoc/download?doi=10.1.1.573.9310&rep=rep1&type=pdf>
- Matias, A., Blenkinsopp, C. E., & Masselink, G. (2014, apr). Detailed investigation of overwash on a gravel barrier. *Marine Geology*, 350, 27–38. Retrieved from <https://linkinghub.elsevier.com/retrieve/pii/S0025322714000292> doi: 10.1016/j.margeo.2014.01.009
- Mentaschi, L., Besio, G., Cassola, F., & Mazzino, A. (2013, dec). Problems in RMSE-based wave model validations. *Ocean Modelling*, 72, 53–58. Retrieved from <https://linkinghub.elsevier.com/retrieve/pii/S1463500313001418> doi: 10.1016/j.ocemod.2013.08.003
- Ministerie van Infrastructuur en Milieu. (2016a). *Regeling veiligheid primaire waterkeringen 2017. Bijlage III Sterkte en veiligheid* (Technical Report No. april 2016). Den Haag, the Netherlands: Ministerie van Infrastructuur en Milieu. Retrieved from <https://www.helpdeskwater.nl/onderwerpen/waterveiligheid/primaire/beoordelen/@205740/regeling-veiligheid-1/>
- Ministerie van Infrastructuur en Milieu. (2016b). *Regeling veiligheid primaire waterkeringen 2017. Bijlage II Voorschriften bepaling hydraulische belasting primaire waterkeringen* (Technical Report). Den Haag, the Netherlands: Ministerie van Infrastructuur en Milieu. Retrieved from <https://www.helpdeskwater.nl/onderwerpen/waterveiligheid/primaire/beoordelen/@205739/regeling-veiligheid-0/>
- Ministerie van Infrastructuur en Milieu. (2016c). *Regeling veiligheid primaire waterkeringen 2017. Bijlage I Procedure* (Tech. Rep.). Den Haag, the Netherlands: Ministerie van Infrastructuur en Milieu. Retrieved from <https://www.helpdeskwater.nl/onderwerpen/waterveiligheid/primaire/beoordelen/@205738/regeling-veiligheid/>
- Ministerie van Infrastructuur en Milieu. (2016d). *Schematiseringshandleiding grasbekleding. WBI 2017* (Tech. Rep.). Den Haag, the Netherlands: Ministerie van Infrastructuur en Milieu. Retrieved from <https://www.helpdeskwater.nl/@205746/grasbekleding-wbi/>
- Misra, S. K., Driscoll, A. M., Kirby, J. T., Cornett, A., Lomonaco, P., Sayao, O., & Yavary, M. (2008, may). Surface gravity wave interactions with deep-draft navigation channels - Physical and numerical modeling case studies. In *Coastal engineering proceedings* (pp. 2786–2798). Hamburg, Germany: World Scientific Publishing Company. Retrieved from <http://www.worldscientific.com/doi/abs/10.1142/>

- 9789814277426{ }0230 doi: 10.1142/9789814277426_0230
- Nicolai, R., Klein, M., Kroon, A., Kallen, M.-J., & Verkaik, J. (2011). *Productieberekeningen Waddenzee voor WTI-2011: rapportage fase 3* (Technical Report PR1872.14). Lelystad, the Netherlands: HKV Lijn in Water & Svasek Hydraulics.
- Nielsen, P., & Hanslow, D. J. (1991). Wave runup distributions on natural beaches. *Journal of Coastal Research*, 7(4), 1139–1152. Retrieved from <https://www.jstor.org/stable/4297933>
- Oosterlo, P. (2015). *A method to calculate the probability of dike failure due to wave overtopping, including the infragravity waves and morphological changes* (MSc Thesis, Delft University of Technology). Retrieved from <http://resolver.tudelft.nl/uuid:4c139e62-cc55-4013-844f-ad5d5ab62e29>
- Oosterlo, P., Hofland, B., Van der Meer, J. W., Overduin, M., & Steendam, G. J. (2021). Calibration and preparation of field measurements of oblique wave run-up and overtopping on dikes using laser scanners. *Coastal Engineering*, 167(103915), 1–13. Retrieved from <https://linkinghub.elsevier.com/retrieve/pii/S0378383921000752> doi: 10.1016/j.coastaleng.2021.103915
- Oosterlo, P., Hofland, B., Van der Meer, J. W., Overduin, M., Steendam, G. J., Nieuwenhuis, J.-W., ... Reneerkens, M. (2019). Measuring (Oblique) Wave Run-Up and Overtopping with Laser Scanners. In *Proc. coastal structures* (pp. 442–452). Hannover, Germany: Bundesanstalt für Wasserbau. Retrieved from <https://hdl.handle.net/20.500.11970/106657> doi: 10.18451/978-3-939230-64-9_045
- Oosterlo, P., McCall, R., Vuik, V., Hofland, B., Van der Meer, J. W., & Jonkman, S. (2018, may). Probabilistic Assessment of Overtopping of Sea Dikes with Foreshores including Infragravity Waves and Morphological Changes: Westkapelle Case Study. *Journal of Marine Science and Engineering*, 6(2), 48. Retrieved from <http://www.mdpi.com/2077-1312/6/2/48> doi: 10.3390/jmse6020048
- Oosterlo, P., Van der Meer, J. W., Hofland, B., & Van Vledder, G. (2018). Wave modelling in a complex estuary: Study in preparation of field measurement campaign Eems-Dollard estuary. In P. Lynett (Ed.), *Coastal engineering proceedings* (Vol. 1, p. 66). Baltimore, Maryland: American Society of Civil Engineers. Retrieved from <https://journals.tdl.org/icce/index.php/icce/article/view/8356> doi: 10.9753/icce.v36.papers.66
- Oppenheimer, M., Glavovic, B., Hinkel, J., van de Wal, R., Magnan, A. K., Abd-Elgawad, A., ... Sebesvari, Z. (2019). *Sea Level Rise and Implications for Low-Lying Islands, Coasts and Communities*. IPCC Special Report on the Ocean and Cryosphere in a Changing Climate (Tech. Rep.). IPCC. Retrieved from <https://www.ipcc.ch/srocc/chapter/chapter-4-sea-level-rise-and-implications-for-low-lying-islands-coasts-and-communities/>
- Pallares, E., Sánchez-Arcilla, A., & Espino, M. (2014, sep). Wave energy balance in wave models (SWAN) for semi-enclosed domains—Application to the Catalan coast. *Continental Shelf Research*, 87, 41–53. Retrieved from <https://linkinghub.elsevier.com/retrieve/pii/S0278434314001022> doi: 10.1016/j.csr.2014.03.008
- Penney, W. G., Price, A. T., Martin, J. C., Moyce, W. J., Penney, W. G., Price, A. T., & Thornhill, C. K. (1952, mar). Part I. The diffraction theory of sea waves and the shelter afforded by breakwaters. *Philosophical Transactions of the Royal Society of London. Series A*,

- Mathematical and Physical Sciences*, 244(882), 236–253. Retrieved from <https://royalsocietypublishing.org/doi/10.1098/rsta.1952.0003> doi: 10.1098/rsta.1952.0003
- Pullen, T., Silva, E., Brown, J., Yelland, M., Pascal, R., Pinnell, R., ... Jones, D. (2019). WireWall–laboratory and field measurements of wave overtopping. In *Proc. coastal structures* (pp. 1170–1179). Hannover, Germany: Bundesanstalt für Wasserbau. Retrieved from <https://hdl.handle.net/20.500.11970/106615> doi: 10.18451/978-3-939230-64-9_117
- Ris, R. C., Holthuijsen, L. H., & Booij, N. (1999, apr). A third-generation wave model for coastal regions: 2. Verification. *Journal of Geophysical Research: Oceans*, 104(C4), 7667–7681. Retrieved from <http://doi.wiley.com/10.1029/1998JC900123> doi: 10.1029/1998JC900123
- Rogers, W. E., Babanin, A. V., & Wang, D. W. (2012, sep). Observation-Consistent Input and Whitecapping Dissipation in a Model for Wind-Generated Surface Waves: Description and Simple Calculations. *Journal of Atmospheric and Oceanic Technology*, 29(9), 1329–1346. Retrieved from <http://journals.ametsoc.org/doi/10.1175/JTECH-D-11-00092.1> doi: 10.1175/JTECH-D-11-00092.1
- Rogers, W. E., Hwang, P. A., & Wang, D. W. (2003, feb). Investigation of Wave Growth and Decay in the SWAN Model: Three Regional-Scale Applications*. *Journal of Physical Oceanography*, 33(2), 366–389. Retrieved from [http://journals.ametsoc.org/doi/10.1175/1520-0485\(2003\)033<0366:IOWGAD-%7D3E2.0.CO;2](http://journals.ametsoc.org/doi/10.1175/1520-0485(2003)033<0366:IOWGAD-%7D3E2.0.CO;2) doi: 10.1175/1520-0485(2003)033<0366:IOWGAD>2.0.CO;2
- Rogers, W. E., & Van Vledder, G. P. (2013, oct). Frequency width in predictions of windsea spectra and the role of the nonlinear solver. *Ocean Modelling*, 70, 52–61. Retrieved from <https://linkinghub.elsevier.com/retrieve/pii/S1463500312001710> doi: 10.1016/j.ocemod.2012.11.010
- Salmon, J. E. (2016). *Surf Wave Hydrodynamics in the Coastal Environment* (Dissertation, Delft University of Technology). Retrieved from <https://doi.org/10.4233/uuid:b038f8a2-d2db-46fc-8419-3141f21faa1c>
- Salmon, J. E., & Holthuijsen, L. H. (2015, nov). Modeling depth-induced wave breaking over complex coastal bathymetries. *Coastal Engineering*, 105, 21–35. Retrieved from <https://linkinghub.elsevier.com/retrieve/pii/S0378383915001301> doi: 10.1016/j.coastaleng.2015.08.002
- Salmon, J. E., Holthuijsen, L. H., Zijlema, M., Van Vledder, G. P., & Pietrzak, J. D. (2015, mar). Scaling depth-induced wave-breaking in two-dimensional spectral wave models. *Ocean Modelling*, 87, 30–47. Retrieved from <https://linkinghub.elsevier.com/retrieve/pii/S146350031400198X> doi: 10.1016/j.ocemod.2014.12.011
- Salmon, J. E., Smit, P. B., Janssen, T. T., & Holthuijsen, L. H. (2016, aug). A consistent collinear triad approximation for operational wave models. *Ocean Modelling*, 104, 203–212. Retrieved from <https://linkinghub.elsevier.com/retrieve/pii/S1463500316300609> doi: 10.1016/j.ocemod.2016.06.009
- Schüttrumpf, H. F. R. (2001). *Wellenüberlaufströmung bei See-deichen. Experimentelle und theoretische Untersuchungen* (Dissertation, Technischen Universität Carolo-Wilhelmina zu Braunschweig). doi: 10.24355/dbbs.084-200511080100-46

- Schüttrumpf, H. F. R., & Van Gent, M. R. A. (2004). Wave Overtopping at Seadikes. In *Proc. coastal structures 2003* (pp. 431–443). Portland, Oregon: American Society of Civil Engineers. Retrieved from <http://ascelibrary.org/doi/10.1061/40733{ }28147{ }2936> doi: 10.1061/40733(147)36
- Smit, P. B., & Janssen, T. T. (2013, aug). The Evolution of Inhomogeneous Wave Statistics through a Variable Medium. *Journal of Physical Oceanography*, 43(8), 1741–1758. Retrieved from <http://journals.ametsoc.org/doi/10.1175/JPO-D-13-046.1> doi: 10.1175/JPO-D-13-046.1
- Smit, P. B., & Janssen, T. T. (2016, feb). The Evolution of Nonlinear Wave Statistics through a Variable Medium. *Journal of Physical Oceanography*, 46(2), 621–634. Retrieved from <https://journals.ametsoc.org/view/journals/phoc/46/2/jpo-d-15-0146.1.xml> doi: 10.1175/JPO-D-15-0146.1
- Smit, P. B., Janssen, T. T., & Herbers, T. H. C. (2015, apr). Stochastic Modeling of Coherent Wave Fields over Variable Depth. *Journal of Physical Oceanography*, 45(4), 1139–1154. Retrieved from <https://doi.org/10.1175/JPO-D-14-0219.1> doi: 10.1175/JPO-D-14-0219.1
- Sommerfeld, A. (1896, jun). Mathematische Theorie der Diffraction. *Mathematische Annalen*, 47(2-3), 317–374. Retrieved from <http://link.springer.com/10.1007/BF01447273> doi: 10.1007/BF01447273
- Spore, N. J., Brodie, K. L., & Swann, C. (2014). Automated Feature Extraction of Foredune Morphology from Terrestrial Lidar Data. In *American geophysical union, fall meeting 2014*. American Geophysical Union. Retrieved from <https://ui.adsabs.harvard.edu/abs/2014AGUFMEP31B3558S/abstract>
- Stam, C. (1989). *Taluds van losgestorte materialen. Golfploop op statisch stabiele stortsteen taluds onder golfaanval. Deel III, verslag modelonderzoek* (Technical Report M1983 deel III). Delft, the Netherlands: Waterloopkundig Laboratorium/WL. Retrieved from <https://puc.overheid.nl/rijkswaterstaat/doc/PUC{ }155294{ }31/>
- Steendam, G. J., Van der Meer, J. W., Van Hoven, A., & Labrujere, A. (2017, jun). Wave run-up simulations on real dikes. In *Coastal engineering proceedings* (Vol. 1, p. 42). Antalya, Turkey: American Society of Civil Engineers. Retrieved from <https://icce-ojs-tamu.tdl.org/icce/index.php/icce/article/view/8248> doi: 10.9753/icce.v35.structures.42
- Stijnen, J., & Kallen, M. (2010). *Diepwaterrandvoorwaarden WTI-2011 (ELD, EUR, YM6, SCW, SON)* (Technical Report PR1759.10). Lelystad, the Netherlands: HKV.
- Streicher, M., Hofland, B., & Lindenbergh, R. C. (2013). Laser Ranging for Monitoring Water Waves in the New Deltares Delta Flume. In *Isprs annals of the photogrammetry, remote sensing and spatial information sciences* (Vol. 2, pp. 271–276). Antalya, Turkey: ISPRS. Retrieved from <http://www.isprs-ann-photogramm-remote-sens-spatial-inf-sci.net/II-5-W2/271/2013/> doi: 10.5194/isprsannals-II-5-W2-271-2013
- The REFRAC team. (2019). *REFRAC User Manual. REFRAC version 20.02* (Manual). Delft, the Netherlands: Delft University of Technology.
- The SWAN team. (2017a). *SWAN Scientific and Technical Documentation. SWAN Cycle III version 41.10AB* (Tech. Rep.). Delft, the Netherlands: Delft University of Technology.

- Retrieved from <http://swanmodel.sourceforge.net/>
- The SWAN team. (2017b). *SWAN User Manual. SWAN Cycle III version 41.10AB* (Tech. Rep.). Delft, the Netherlands: Delft University of Technology. Retrieved from <http://swanmodel.sourceforge.net/>
- The SWAN team. (2019a). *SWAN Scientific and Technical Documentation. SWAN Cycle III version 41.31* (Technical Report). Delft, the Netherlands: Delft University of Technology. Retrieved from <http://swanmodel.sourceforge.net/>
- The SWAN team. (2019b). *SWAN User Manual. SWAN Cycle III version 41.31* (Technical Report). Delft, the Netherlands: Delft University of Technology. Retrieved from <http://swanmodel.sourceforge.net/>
- The SWASH team. (2019a). *SWASH Implementation Manual. SWASH version 6.01* (Manual). Delft, the Netherlands: Delft University of Technology. Retrieved from <http://swash.sourceforge.net/>
- The SWASH team. (2019b). *SWASH User Manual. SWASH version 6.01* (Tech. Rep.). Delft, the Netherlands: Delft University of Technology. Retrieved from <http://swash.sourceforge.net/>
- Toledo, Y. (2013, jan). The oblique parabolic equation model for linear and nonlinear wave shoaling. *Journal of Fluid Mechanics*, 715, 103–133. Retrieved from https://www.cambridge.org/core/product/identifier/S0022112012005022/type/journal_article doi: 10.1017/jfm.2012.502
- Toledo, Y., & Agnon, Y. (2012, jul). Stochastic evolution equations with localized nonlinear shoaling coefficients. *European Journal of Mechanics - B/Fluids*, 34, 13–18. Retrieved from <https://linkinghub.elsevier.com/retrieve/pii/S0997754612000088> doi: 10.1016/j.euromechflu.2012.01.007
- Tolman, H. L. (1991, jun). Effects of Tides and Storm Surges on North Sea Wind Waves. *Journal of Physical Oceanography*, 21(6), 766–781. Retrieved from [http://journals.ametsoc.org/doi/10.1175/1520-0485\(1991\)021%3C0766:EOTASS%3E2.0.CO;2](http://journals.ametsoc.org/doi/10.1175/1520-0485(1991)021%3C0766:EOTASS%3E2.0.CO;2) doi: 10.1175/1520-0485(1991)021<0766:EOTASS>2.0.CO;2
- Tolman, H. L. (2009). *User manual and system documentation of WAVEWATCH III version 3.14*. (Technical Note 276). NOAA/NWS/NCEP/MMAB.
- Van der Meer, J. W. (2002). *Technical Report Wave Run-up and Wave Overtopping at Dikes* (Technical Report). Delft, the Netherlands: Technical Advisory Committee on Flood Defence (TAW). Retrieved from <http://www.overtopping-manual.com/assets/downloads/TRRunupOvertopping.pdf>
- Van der Meer, J. W. (2011). *The Wave Run-up Simulator. Idea, necessity, theoretical background and design* (Technical Report vdm11355). Heerenveen, the Netherlands: Van der Meer Consulting B.V. Retrieved from http://www.vandermeerconsulting.nl/downloads/stability_a/2011_wave_run_up_simulator.pdf
- Van der Meer, J. W. (2018). *Meerjarige Veldmetingen Eems-Dollard. Te verwachten stormomstandigheden en bepalen hoogte van de golfoverslagbakken in de dijk bij Uithuizerwad* (Tech. Rep.). Akkrum, the Netherlands: Van der Meer Consulting B.V.
- Van der Meer, J. W., & Bruce, T. (2014, nov). New Physical Insights and Design Formulas on Wave Overtopping at Sloping and Vertical Structures. *Journal of*

- Waterway, Port, Coastal, and Ocean Engineering*, 140(6), 04014025. Retrieved from <http://ascelibrary.org/doi/10.1061/{%}28ASCE{%}29WW.1943-5460.0000221> doi: 10.1061/(ASCE)WW.1943-5460.0000221
- Van der Meer, J. W., & De Waal, J. P. (1990). *Invloed van scheve inval en richtingspreiding op golfploop en overslag. Verslag modelonderzoek* (Technical Report H638). Delft, the Netherlands: Waterloopkundig Laboratorium/WL. Retrieved from <http://resolver.tudelft.nl/uuid:45507b56-d20a-475c-854f-522782d6b3da>
- Van der Meer, J. W., & De Waal, J. P. (1993). *Waterbeweging op taluds. Invloed van berm, ruwheid, ondiep voorland en scheve lang- en kortkammige golfaanval*. (Technical Report H1256-B). Delft, the Netherlands: Waterloopkundig Laboratorium/WL. Retrieved from <http://resolver.tudelft.nl/uuid:c86b42fc-cc86-4d59-ae06-0612549bd674>
- Van der Meer, J. W., Nieuwenhuis, J.-W., Steendam, G. J., Reneerkens, M., Steetzel, H., & Van Vledder, G. P. (2019). Wave Overtopping Measurements at a Real Dike. In *Proc. coastal structures* (pp. 1107–1117). Hannover, Germany: Bundesanstalt für Wasserbau. Retrieved from <https://hdl.handle.net/20.500.11970/106609> doi: 10.18451/978-3-939230-64-9_111
- Van der Meer, J. W., Schrijver, R., Hardeman, B., van Hoven, A., Verheij, H., & Steendam, G. J. (2010). Guidance on erosion resistance of inner slopes of dikes from three years of testing with the Wave Overtopping Simulator. In *Proceedings of the ice, coasts, marine structures and breakwaters* (pp. 2: 460–473). Edinburgh, Scotland: Thomas Telford Ltd. Retrieved from <http://www.icevirtuallibrary.com/doi/10.1680/cmsb.41318.0044> doi: 10.1680/cmsb.41318.0044
- Van der Meer Consulting, Arcadis, Deltares, Etrometa, Infram-Hydrén, TU Delft, & Unesco-IHE. (2017). *Plan van aanpak Meerjarige veldmetingen Eems-Dollard* (Tech. Rep. No. 2.0). Groningen, the Netherlands: Waterschap Noorderzijlvest.
- Van der Reijden, I. M. (2020). *Modelling refraction of waves over tidal channels. A numerical study focusing on the performance of spectral wave models with respect to bottom refraction* (MSc thesis, Delft University of Technology). Retrieved from <http://resolver.tudelft.nl/uuid:f89e52d0-009d-4a69-9b06-f4216cc065db>
- Van der Westhuysen, A. J. (2007). *Advances in the spectral modelling of wind waves in the nearshore* (Dissertation, Delft University of Technology). Retrieved from <http://resolver.tudelft.nl/uuid:1c87b2fc-a5e5-4058-b0f4-3de07c49b41e>
- Van der Westhuysen, A. J. (2010, jan). Modeling of depth-induced wave breaking under finite depth wave growth conditions. *Journal of Geophysical Research*, 115(C1), C01008. Retrieved from <http://doi.wiley.com/10.1029/2009JC005433> doi: 10.1029/2009JC005433
- Van der Westhuysen, A. J., Van Dongeren, A. R., Groeneweg, J., Van Vledder, G. P., Peters, H., Gautier, C., & van Nieuwkoop, J. C. C. (2012, nov). Improvements in spectral wave modeling in tidal inlet seas. *Journal of Geophysical Research: Oceans*, 117(C11), n/a–n/a. Retrieved from <http://doi.wiley.com/10.1029/2011JC007837> doi: 10.1029/2011JC007837
- Van der Westhuysen, A. J., Zijlema, M., & Battjes, J. A. (2007, feb). Nonlinear saturation-based whitecapping dissipation in SWAN for deep and shallow water. *Coastal Engineering*, 54(2), 151–170. Retrieved from <https://linkinghub.elsevier.com/>

- [retrieve/pii/S037838390600127X](#) doi: 10.1016/j.coastaleng.2006.08.006
- Van Dongeren, A., Van der Westhuysen, A. J., Groeneweg, J., Van Vledder, G. P., Lansens, J., Smale, A., ... Wenneker, I. (2011, jan). Spectral wave modelling in tidal inlet seas: Results from the SBW Wadden Sea Project. *Coastal Engineering Proceedings*, 1(32), 44. Retrieved from <https://icce-ojs-tamu.tdl.org/icce/index.php/icce/article/view/970> doi: 10.9753/icce.v32.waves.44
- Van Gent, M. R. A. (1999a). *Physical model investigations on coastal structures with shallow foreshores: 2D model tests with single and double-peaked wave energy spectra* (Tech. Rep.). Delft, the Netherlands: WL | Delft Hydraulics. Retrieved from <http://resolver.tudelft.nl/uuid:1b4729de-2e86-4b8a-98d5-48d8e07d5902>
- Van Gent, M. R. A. (1999b). *Wave run-up and wave overtopping for double-peaked wave energy spectra* (Tech. Rep.). Delft, the Netherlands: WL | Delft Hydraulics. Retrieved from <http://resolver.tudelft.nl/uuid:05632d4d-6823-4570-a8af-7adbe2598e8e>
- Van Gent, M. R. A. (2001). Wave Runup on Dikes with Shallow Foreshores. *Journal of Waterway, Port, Coastal, and Ocean Engineering*, 127(5), 254–262. Retrieved from <http://ascelibrary.org/doi/10.1061/{%}28ASCE{%}290733-950X{%}282001{%}29127{%}3A5{%}28254{%}29> doi: 10.1061/(ASCE)0733-950X(2001)127:5(254)
- Van Gent, M. R. A. (2002). *Low-exceedance wave overtopping events: Measurements of velocities and the thickness of water-layers on the crest and inner slope of dikes* (Technical Report DC030202/H3803). Delft: WL | Delft Hydraulics. Retrieved from <http://resolver.tudelft.nl/uuid:e71289dd-f6aa-471e-856c-832071a83753>
- Van Nieuwkoop, J., & Gautier, C. (2015). *Validation of SWAN wave directions* (Technical Report 1220082-007). Delft: Deltares. Retrieved from https://puc.overheid.nl/rijkswaterstaat/doc/PUC_{ }148599_{ }31/1/
- Van Nieuwkoop, J., & Groeneweg, J. (2014). *Modelling of wave penetration in complex areas: analysis of hindcast data* (Technical Report 1209433-007). Delft, the Netherlands: Deltares. Retrieved from https://puc.overheid.nl/rijkswaterstaat/doc/PUC_{ }146803_{ }31/
- Van Reen, M. J. (2013). *Veiligheid Nederland in Kaart 2: Overstromingsrisico Dijkkring 6 Friesland en Groningen* (Technical Report HB 1838722). Lelystad, the Netherlands: Consortium Albicom. Retrieved from https://www.helpdeskwater.nl/publish/pages/135876/dijkkring_{ }6_{ }web_{ }1r.pdf
- Van Vledder, G. P. (2015). *Stappenplan aanpassing hydraulische randvoorwaarden op basis van nieuwe inzichten winddrag* (Technical Report VVC55M1R3). Olst, the Netherlands: Van Vledder Consulting. Retrieved from https://puc.overheid.nl/PUC/Handlers/DownloadDocument.ashx?identificer=PUC_{ }154265_{ }31{ }&versienummer=1
- Van Vledder, G. P., & Koop, O. (2009). *Analysis of wave penetration into the Eastern Wadden Sea* (Technical Report A2302). Marknesse, the Netherlands: Alkyon. Retrieved from https://puc.overheid.nl/rijkswaterstaat/doc/PUC_{ }155190_{ }31/1/
- Vieira Leite, J. P., Van der Meer, J. W., Franco, L., Romano, A., Pepi, Y., Bruce, T., ... Menendez, M. (2019). Distribution of Overtopping Wave Volumes Caused by Crossing Seas. In *Proc. coastal structures* (pp. 1130–1140). Hannover, Germany: Bundesanstalt für

- Wasserbau. Retrieved from <https://hdl.handle.net/20.500.11970/106611>
doi: 10.18451/978-3-939230-64-9_113
- Voort, L. (2018). *Personal communication*.
- Vosselman, G., & Maas, H.-G. (2010). *Airborne and terrestrial laser scanning*. Dunbeath, Scotland, UK: Whittles Publishing.
- Vousdoukas, M. I., Kirupakaramoorthy, T., Oumeraci, H., De la Torre, M., Wübbold, F., Wagner, B., & Schimmels, S. (2014, jan). The role of combined laser scanning and video techniques in monitoring wave-by-wave swash zone processes. *Coastal Engineering*, 83, 150–165. Retrieved from <https://linkinghub.elsevier.com/retrieve/pii/S0378383913001695> doi: 10.1016/j.coastaleng.2013.10.013
- Vousdoukas, M. I., Wziatek, D., & Almeida, L. P. (2012, jan). Coastal vulnerability assessment based on video wave run-up observations at a mesotidal, steep-sloped beach. *Ocean Dynamics*, 62(1), 123–137. Retrieved from <http://link.springer.com/10.1007/s10236-011-0480-x> doi: 10.1007/s10236-011-0480-x
- Vrecica, T., & Toledo, Y. (2016, may). Consistent nonlinear stochastic evolution equations for deep to shallow water wave shoaling. *Journal of Fluid Mechanics*, 794, 310–342. Retrieved from https://www.cambridge.org/core/product/identifiser/S0022112015007508/type/journal_{_}article doi: 10.1017/jfm.2015.750
- Vrecica, T., & Toledo, Y. (2019, oct). Consistent nonlinear deterministic and stochastic wave evolution equations from deep water to the breaking region. *Journal of Fluid Mechanics*, 877, 373–404. Retrieved from https://www.cambridge.org/core/product/identifiser/S0022112019005251/type/journal_{_}article doi: 10.1017/jfm.2019.525
- Vrouwenvelder, A. C. W. M., & Steenbergen, H. M. G. M. (2003). *Theoriehandleiding PC-RING. Deel C: Rekentechnieken* (Technical Report 003-CI-R0022). Delft, the Netherlands: TNO. Retrieved from https://puc.overheid.nl/rijkswaterstaat/doc/PUC_{_}130481_{_}31/1/
- Vuik, V. (2019). *Building safety with nature: Salt marshes for flood risk reduction* (Dissertation, Delft University of Technology). doi: 10.4233/uuid:9339474c-3c48-437f-8aa5-4b908368c17e
- Wenneker, I., & Gautier, C. (2016). *Overzicht van SWAN modellen in gebruik binnen de RWS primaire processen* (Technical Report 1230072-002). Delft, the Netherlands: Deltares.
- Wenneker, I., Spelt, B., Peters, H., & De Ronde, J. (2016, mar). Overview of 20 years of field measurements in the coastal zone and at the Petten sea dike in the Netherlands. *Coastal Engineering*, 109, 96–113. Retrieved from <https://linkinghub.elsevier.com/retrieve/pii/S0378383915002276> doi: 10.1016/j.coastaleng.2015.12.009
- Wu, J. (1982). Wind-stress coefficients over sea surface from breeze to hurricane. *Journal of Geophysical Research: Oceans*, 87(C12), 9704. Retrieved from <http://doi.wiley.com/10.1029/JC087iC12p09704> doi: 10.1029/JC087iC12p09704
- Wübbold, F., Hentschel, M., Vousdoukas, M. I., & Wagner, B. (2012). Application of an autonomous robot for the collection of nearshore topographic and hydrodynamic measurements. In *Coastal engineering proceedings* (Vol. 1, p. 53). Sant-

- ander, Spain. Retrieved from <https://icce-ojs-tamu.tdl.org/icce/index.php/icce/article/view/6688> doi: 10.9753/icce.v33.management.53
- Yan, L. (1987). *An improved wind input source term for third generation ocean wave modeling*. De Bilt, the Netherlands: KNMI. Retrieved from <https://library.wur.nl/WebQuery/hydrotheek/263563>
- Young, I. R., & Babanin, A. V. (2006, mar). Spectral Distribution of Energy Dissipation of Wind-Generated Waves due to Dominant Wave Breaking. *Journal of Physical Oceanography*, 36(3), 376–394. Retrieved from <http://journals.ametsoc.org/doi/10.1175/JPO2859.1> doi: 10.1175/JPO2859.1
- Zanuttigh, B., Van der Meer, J. W., Bruce, T., & Hughes, S. (2014). Statistical characterisation of extreme overtopping wave volumes. In *Coasts, marine structures and breakwaters 2013* (pp. 442–451). Edinburgh, Scotland: ICE Publishing. Retrieved from <https://www.icevirtuallibrary.com/doi/abs/10.1680/fsts.59757.048> doi: 10.1680/fsts.59757.048
- Zijderveld, A., & Peters, H. (2009, may). Measurement programme Dutch Wadden Sea. In *Coastal engineering proceedings* (pp. 404–410). Hamburg, Germany: World Scientific Publishing Company. Retrieved from http://www.worldscientific.com/doi/abs/10.1142/9789814277426_{_}0034 doi: 10.1142/9789814277426_0034
- Zijlema, M. (2019). *Personal communication*. Delft, the Netherlands.
- Zijlema, M. (2020). *On grid dependence of refraction in SWAN*. Delft, the Netherlands.
- Zijlema, M., Stelling, G., & Smit, P. B. (2011, oct). SWASH: An operational public domain code for simulating wave fields and rapidly varied flows in coastal waters. *Coastal Engineering*, 58(10), 992–1012. Retrieved from <https://linkinghub.elsevier.com/retrieve/pii/S0378383911000974> doi: 10.1016/j.coastaleng.2011.05.015
- Zijlema, M., Van Vledder, G. P., & Holthuijsen, L. H. (2012, jul). Bottom friction and wind drag for wave models. *Coastal Engineering*, 65, 19–26. Retrieved from <https://linkinghub.elsevier.com/retrieve/pii/S0378383912000440> doi: 10.1016/j.coastaleng.2012.03.002
- Zwamborn, J., & Grieve, G. (1974, jun). Wave Attenuation and Concentration Associated with Harbour Approach Channels. In *Coastal engineering proceedings* (pp. 2068–2085). Copenhagen, Denmark: American Society of Civil Engineers. Retrieved from <http://ascelibrary.org/doi/10.1061/9780872621138.123> doi: 10.1061/9780872621138.123



DETERMINATION OF CHARACTERISTIC STORMS

This appendix determines the expected storm conditions in the Eems-Dollard estuary, corresponding to storms with several return periods and based on the 2017 Dutch dike safety assessment framework WBI. Furthermore, wave conditions, overtopping discharges and required crest levels corresponding to these storm conditions and return periods are presented for the Uithuizerwad (UHW) and Twin Dikes (TD) locations. Finally, two characteristic storms are determined based on these conditions. These characteristic storms are used to determine e.g. which wave heights and periods can be expected during the measurement campaign in the area, and are used for analyses throughout this dissertation.

Hydra-NL ('HYDraulische RANdvoorwaarden', hydraulic boundary conditions) is the probabilistic model that was used to assess the coastal flood defences in the Netherlands within WBI 2017. Hydra-NL performs probabilistic calculations, using the WBI SWAN databases with wave conditions at the flood defences as input, amongst others.

Hydra-NL is used here to determine the wind conditions, water levels and wave conditions corresponding to return periods of 1, 10, 100, 1,000, 3,000, 10,000 and 100,000 years at UHW and TD. Furthermore, the required crest levels are determined for each of these return periods, for which the mean overtopping discharge is at most 5 l/s/m (based on [EurOtop, 2018](#), grass covered crest and landward slope; maintained and closed grass cover; $H_{m0} = 1 \text{ m} - 3 \text{ m}$). Finally, the mean wave overtopping discharges corresponding to the actual crest levels of the dikes at UHW and TD are determined for each of these return periods.

The dike profiles at UHW and TD¹ were schematised for use in Hydra-NL. The dike orientation at UHW is approximately 20°N. The dike at UHW consists of asphalt on the lower slope until 6.38 m+NAP and grass at the upper slope, until the crest level at 8.92

¹The old Twin Dikes location dike profile was used here. Recently, a resting and breeding island for birds was constructed directly in front of this location. Therefore, the final measurement location at TD was shifted somewhat towards the north.

m+NAP. For UHW, the slope roughness factor γ_f in the overtopping equations was set to 1.0 for both the lower and upper slopes, according to [EurOtop \(2018\)](#). The orientation of the dike normal at TD is approximately 45°N. The dike at TD consists of basalt at the lower part of the slope and grass at the upper part of the slope. The basalt runs until approximately 3.5 m+NAP, the crest level is 8.5 m+NAP. For the Twin Dikes, the roughness was set to 0.9 for the lower slope and to 1.0 for the upper slope.

Table [A.1](#) and [A.2](#) give the results for UHW. Table [A.3](#) and [A.4](#) give the results for TD. Table [A.1](#) and [A.3](#) give the results when using the WBI 2017 settings in Hydra-NL. Table [A.2](#) and [A.4](#) use the same settings, but without taking the model uncertainties in the H_{m0} wave height ($\mu = -0.01$, $\sigma = 0.19$) and $T_{m-1,0}$ wave period ($\mu = -0.04$, $\sigma = 0.11$) as prescribed by WBI into account. The model uncertainties are estimates of the uncertainty in these parameters as predicted by SWAN over the whole coastal region. Hence, these values do not indicate the actual uncertainties in the SWAN results at UHW and TD. WBI 2017 did not use model uncertainties for the water levels in the coastal region.

The norm probabilities of flooding prescribed by law at UHW and TD are 1,000 year⁻¹ and 3,000 year⁻¹, respectively (expressed as return periods). The tables show that both dike sections can be considered safe if a mean overtopping discharge of 5 l/s/m is allowed (the required crest level is lower than the actual crest level). Note that this would hold if only wave overtopping would be considered as a dike failure mechanism. In reality, many failure mechanisms are considered within WBI, for which the combined (total) probability of flooding needs to be smaller than the norm probability (see chapter 2). The tables show several differences between UHW and TD. The conditions at both UHW and TD are characterised by a wind direction of 300°N for the less extreme conditions (return periods of 1-100 years). For the larger return periods, the conditions at UHW are still characterised by a wind direction of 300°N, whereas the conditions at TD are characterised by a 330°N wind direction. The calculated water levels at TD are larger, which they are in reality as well. Wave heights at TD are smaller, $T_{m-1,0}$ wave periods are much smaller. Apparently, low-frequency (North Sea) waves do not reach the Twin Dikes location in the SWAN simulations underlying the Hydra-NL model. Angles of incidence are similar at both UHW and TD for the less extreme conditions, but become smaller at TD during the extreme conditions. Overall, this results in required crest levels that are on average 1 m lower at TD than at UHW.

P [year]	W_{dir} [°N]	W_{vel} [m/s]	h [m+NAP]	H_{m0} [m]	$T_{m-1,0}$ [s]	δ [°N]	β [°]	Req. crest level [m+NAP]	q actual crest level [l/s/m]
1	300	18.5	2.73	0.79	3.60	319.4	60.6	3.60	<0.1
10	300	22.5	3.59	1.22	4.78	323.6	56.4	5.13	<0.1
100	300	27.0	4.37	1.57	5.48	324.3	55.7	6.44	<0.1
1,000	300	29.9	4.85	2.19	5.90	324.8	55.2	7.61	0.19
3,000	300	30.5	4.95	2.24	6.76	325.0	55.0	8.15	0.69
10,000	300	32.7	5.31	2.44	7.05	324.8	55.2	8.67	2.42
100,000	300	36.7	5.95	2.81	7.60	325.2	54.8	9.64	21.53

Table A.1: Hydra-NL results at Uithuizerwad using the WBI 2017 settings. P [year] is the return period, W_{dir} [°N] the wind direction, W_{vel} [m/s] the potential wind velocity, h [m+NAP] the water level, H_{m0} [m] the significant wave height, $T_{m-1,0}$ [s] the spectral wave period, δ [°N] the mean wave direction, β [°] the wave angle of incidence. The last two columns give the required crest levels for which the mean overtopping discharge is at most 5 l/s/m and the mean overtopping discharge q [l/s/m] with the actual crest level of the dike.

P [year]	W_{dir} [°N]	W_{vel} [m/s]	h [m+NAP]	H_{m0} [m]	$T_{m-1,0}$ [s]	δ [°N]	β [°]	Req. crest level [m+NAP]	q actual crest level [l/s/m]
1	300	18.5	2.73	0.80	3.76	319.4	60.6	3.66	<0.1
10	300	22.4	3.57	1.23	4.96	323.6	56.4	5.19	<0.1
100	300	26.5	4.29	1.56	5.64	324.3	55.7	6.42	<0.1
1,000	300	30.7	4.98	1.87	6.26	325.0	55.0	7.59	0.16
3,000	300	32.7	5.30	2.03	6.50	324.9	55.1	8.03	0.57
10,000	300	34.9	5.65	2.19	6.77	325.0	55.0	8.57	1.77
100,000	300	39.1	6.32	2.50	7.26	325.1	54.9	9.51	16.06

Table A.2: Hydra-NL results at Uithuizerwad using the WBI 2017 settings, without taking the model uncertainties in the H_{m0} wave height and $T_{m-1,0}$ wave period into account.

P [year]	W_{dir} [°N]	W_{vel} [m/s]	h [m+NAP]	H_{m0} [m]	$T_{m-1,0}$ [s]	δ [°N]	β [°]	Req. crest level [m+NAP]	q actual crest level [l/s/m]
1	300	18.3	2.99	0.63	2.10	341.2	63.8	3.28	<0.1
10	300	22.8	3.95	0.88	2.62	347.3	57.7	4.43	<0.1
100	300	27.2	4.78	1.14	2.90	347.6	57.4	5.42	<0.1
1,000	330	31.3	5.07	1.82	3.84	6.7	38.3	6.36	<0.1
3,000	330	33.3	5.38	1.99	3.98	6.5	38.5	6.83	<0.1
10,000	330	35.5	5.71	2.19	4.13	6.4	38.6	7.32	<0.1
100,000	330	39.7	6.34	2.60	4.40	6.5	38.5	8.22	1.66

Table A.3: Hydra-NL results at the Twin Dikes using the WBI 2017 settings.

P [year]	W_{dir} [°N]	W_{vel} [m/s]	h [m+NAP]	H_{m0} [m]	$T_{m-1,0}$ [s]	δ [°N]	β [°]	Req. crest level [m+NAP]	q actual crest level [l/s/m]
1	300	18.3	2.98	0.63	2.19	341.2	63.8	3.30	<0.1
10	300	22.8	3.95	0.89	2.73	347.3	57.7	4.45	<0.1
100	300	27.2	4.77	1.15	3.02	347.5	57.5	5.44	<0.1
1,000	300	31.6	5.52	1.43	3.26	347.4	57.6	6.38	<0.1
3,000	330	33.1	5.34	1.99	4.12	6.5	38.5	6.84	<0.1
10,000	330	35.0	5.65	2.17	4.27	6.4	38.6	7.31	<0.1
100,000	330	39.2	6.26	2.58	4.55	6.5	38.5	8.20	1.47

Table A.4: Hydra-NL results at the Twin Dikes using the WBI 2017 settings, without taking the model uncertainties in the H_{m0} wave height and $T_{m-1,0}$ wave period into account.

The calculations with WBI 2017 settings and with WBI settings without model uncertainties give fairly similar results at UHW for the less extreme conditions (return periods of 1-100 years). The WBI settings give 5%-10% smaller wind velocities and water levels than the calculations without model uncertainties, for the more extreme conditions. Furthermore, the WBI settings give a 10% larger H_{m0} and a 5% larger $T_{m-1,0}$ for the extreme conditions at UHW. Apparently, the increase in H_{m0} and $T_{m-1,0}$ when including model uncertainties, leads to a decrease in the wind velocity and water level within the model, for the larger return periods. This behaviour was probably caused by interpolation within the model. Differences in mean wave direction are negligible. Overall, this leads to differences in crest levels of up to 15 cm for the extreme conditions, due to inclusion of the model uncertainties.

At TD, again very similar results are found with the WBI 2017 settings and with the WBI settings without model uncertainties, for the less extreme conditions. For the 1,000-year return period, a 330°N wind direction was found with the WBI settings, whereas the calcu-

lation without model uncertainties still gave 300°N. Now, the WBI settings give a 1% larger wind velocity and water level, compared to the calculations without model uncertainties and for the more extreme conditions. The H_{m0} does not differ much between the calculations with and without model uncertainties. The $T_{m-1,0}$ actually becomes 3%-4% smaller with model uncertainties included, potentially again due to interpolation, but the exact cause is unknown. Differences in mean wave direction are negligible again. This results in differences in required crest levels between calculations including and excluding model uncertainties of at most a few centimetres.

Two characteristic storms were determined based on the previous results. The first is a more extreme storm that can be expected during the field measurement campaign in the area (return period of 1-100 years). The second one is a design storm, which represents the extreme conditions with which the dikes are designed and assessed (return periods of 1,000-10,000 years). These conditions can e.g. be used for (numerical) modelling of the extreme conditions in the area. Table A.5 gives both the offshore and expected nearshore conditions at UHW and TD. Note that these values are thus based on the SWAN simulations underlying Hydra-NL within WBI, performed with the WBI version of SWAN and with the WBI settings for the physics and numerics, see Appendix D.

	Field measurements (1-100 years)	Design (1,000-10,000 years)
Offshore		
W_{dir} [°N]	300	330
W_{vel} [m/s]	20	35
h [m+NAP]	4	6
UHW		
H_{m0} [m]	1.2	2.3
$T_{m-1,0}$ [s]	5	7
δ [°N]	320	325
β [°]	60	55
TD		
H_{m0} [m]	0.9	2.2
$T_{m-1,0}$ [s]	2.5	4.2
δ [°N]	345	6
β [°]	60	40

Table A.5: Two characteristic storms for the Eems-Dollard estuary. An extreme storm with a return period of 1-100 years, to be expected during the field measurement campaign in the area. A design storm with a return period of 1,000-10,000 years, which represents the conditions with which the dikes are designed. Offshore conditions and nearshore conditions at UHW and TD given. Conditions based on WBI SWAN simulations with the WBI SWAN version and WBI SWAN settings.

B

REFRACTION IN SWAN

This appendix provides further details on the implementation of refraction within SWAN, which is based on Snel's law. The following was based on [The SWAN team \(2019a\)](#). A case with parallel depth contours is considered, see the left panel of Figure B.1. Here, grid point (i, j) lies in shallower water. The grid points $(i - 1, j)$ and $(i, j - 1)$ are in deeper water. Let n be the coordinate along the wave rays. Then, according to Snel's law:

$$\frac{d\theta}{dn} = \frac{1}{c} \frac{dc}{dn} \tan\theta \quad (\text{B.1})$$

where θ will be of the order of 45° , giving:

$$\frac{d\theta}{dn} = \frac{1}{c} \frac{dc}{dn} \quad (\text{B.2})$$

The slope at grid point (i, j) determines the value of $\frac{d\theta}{dn}$. In shallow water $c = \sqrt{gd}$ with d [m] the water depth, so:

$$\frac{d\theta}{dn} = \frac{1}{2d} \frac{dd}{dn} \quad (\text{B.3})$$

which can be approximated as:

$$\frac{d\theta}{dn} = \frac{1}{2d_{i,j}} \frac{d_* - d_{i,j}}{\Delta n} \quad (\text{B.4})$$

with d_* [m] the water depth in one of the neighbouring grid points $(i - 1, j)$ and $(i, j - 1)$. In the numerical procedure $\frac{d\theta}{dn}$ is constant over a spatial step, so the change in direction over a step is:

$$\frac{d\theta}{dn} \Delta n = \frac{d_* - d_{i,j}}{2d_{i,j}} \quad (\text{B.5})$$

In order to maintain stability, the change of direction must remain below 90° . Consequently, it is obtained that:

$$d_* - d_{i,j} \leq \pi d_{i,j} \quad (\text{B.6})$$

Within SWAN, the factor π has been replaced by a user-determined factor β . Hence, the depths in surrounding grid points are reduced to $\beta d_{i,j}$ if they are larger than this value. This treatment is similar to the one used by WaveWatch III (Tolman, 2009), in that the effective reduction in bottom slope allows long waves to propagate in shallow water. Note that the limiter is not enabled by default. This limiter was implemented in SWAN up to and including version 41.01. However, based on experience, this approach was not effective enough.

Another potential issue is the accuracy with which the directional turning rate is computed for large water depth differences between two grid points (large Δd). In SWAN, the turning rate c_θ in rad/m or rad/s used to be computed as (the following was again based on The SWAN team, 2019a):

$$c_\theta = \frac{\sigma}{\sinh 2kd} \left(\frac{\partial d}{\partial x} \sin \theta - \frac{\partial d}{\partial y} \cos \theta \right) \quad (\text{B.7})$$

with k [rad/m] the wave number, σ [-] the relative frequency and x and y coordinates [m]. Here, wave refraction can only be caused by depth variation. This equation can be chosen in SWAN by providing the command `NUM DIR DEP`. As an alternative, the turning rate can be formulated in terms of phase velocity (wave number):

$$c_\theta = -\frac{c_g}{c} \frac{\partial c}{\partial m} \quad (\text{B.8})$$

with m [m] the coordinate along the wave crests, or:

$$c_\theta = \frac{c_g}{c} \left(\frac{\partial c}{\partial x} \sin \theta - \frac{\partial c}{\partial y} \cos \theta \right) \quad (\text{B.9})$$

An advantage of this equation is that refraction due to a non-rigid seafloor can be included. This equation has been implemented in SWAN since version 41.01 and is enabled by default, or could be set with the command `NUM DIR WNUM`. Although these equations seem identical, they differ in result due to the numerics. Equation B.7 tends to be inaccurate for larger values of Δd , e.g. for relatively coarse grids with steep bottom slopes.

Considering these numerics, until version 41.01A, the derivatives $\frac{\partial d}{\partial x}$ or $\frac{\partial c}{\partial x}$ were approximated using a first order backward difference scheme. This approximation also seemed to be inaccurate for larger Δd . Moreover, it could lead to non-physical asymmetry in turning rate, and therefore wave energy. Therefore, since version 41.01AB, second order central differences are applied. Hence, the 'refraction velocity' (Equation B.9) is approximated in SWAN as:

$$c_\theta = \frac{c_{g,i,j}}{c_{i,j}} \left(\frac{c_{i+1,j} - c_{i-1,j}}{2\Delta x} \sin \theta - \frac{c_{i,j+1} - c_{i,j-1}}{2\Delta y} \cos \theta \right) \quad (\text{B.10})$$

Note that the division by $c_{i,j}$ in Equation B.10 is technically not correct, i.e. not consistent with Snell's law (Van der Reijden, 2020; Zijlema, 2020). Consider the three grid points in the right panel of Figure B.1, where one point lies in deeper water, and two points in shallower water. Following the wave ray, consistent with Snell's law, gives:

$$c_\theta \approx -\frac{1}{c_1} \frac{c_2 - c_1}{\Delta n} \tan \Delta \theta_1 \quad (\text{B.11})$$

Hence, using Snel's law, the value of c_1 is used in the term $1/c_1$. However, c_1 lies somewhere on the wave ray. SWAN cannot compute this c_1 , as it does not lie on a grid point. To solve this problem, SWAN uses c_2 in the second grid point instead. This leads to Equation B.12 for Snel's law and Equation B.13 for SWAN:

$$\Delta\theta = -\frac{1}{c_1} (c_2 - c_1) \tan\theta_1 \quad (\text{B.12})$$

$$\Delta\theta = -\frac{1}{c_2} (c_2 - c_1) \tan\theta_1 \quad (\text{B.13})$$

Hence, if point 2 is located in shallower water, c_2 will be smaller than c_1 and the resulting $\Delta\theta$ will be larger, leading to stronger refraction with SWAN than according to Snel's law.

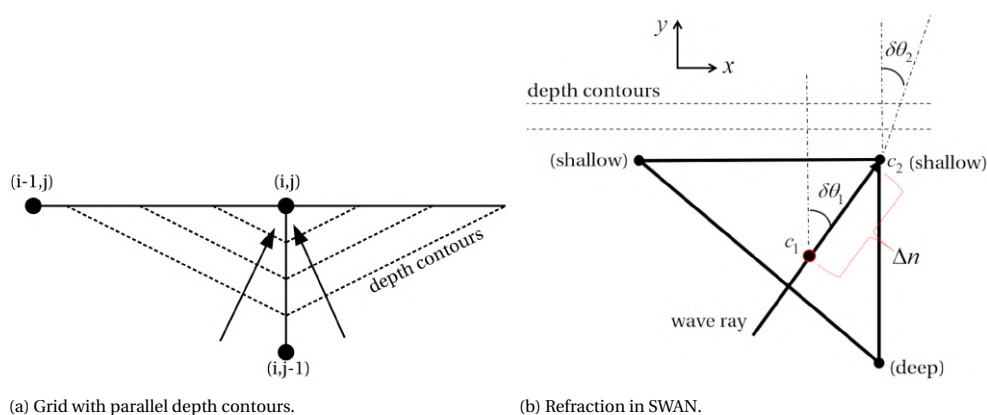


Figure B.1: Left: Geographic grid with parallel depth contours, after [Booij \(1998\)](#). Right: SWAN refraction situation sketch. Definitions of variables given in the main text. Figure after [Zijlema \(2020\)](#).

Experience shows that for waves propagating from deeper to shallower water, the turning rate can indeed be overestimated for larger values of Δd (see Table 4.1 or [Van der Reijden \(2020\)](#); [Zijlema \(2020\)](#)). In turn, for waves propagating from shallower to deeper water, the turning rate can be underestimated. With large Δd , the errors may become exceptionally large, so that wave energy may turn over more than one directional bin. This justified the use of a refraction limiter ([Dietrich et al., 2013](#)):

$$|c_\theta| = \alpha_\theta \Delta\theta \left(\frac{|c_x|}{\Delta x} + \frac{|c_y|}{\Delta y} \right) \quad (\text{B.14})$$

This restriction on the turning rate and, in turn, safety margin on the CFL condition, prevents wave energy changing over more than some directional bins or even over the whole directional sector. As of SWAN version 40.91, this limiter has been implemented in SWAN, replacing the limiter of [Booij \(1998\)](#) (after version 41.01). Note once again that the limiter is not enabled by default.

Finally, [Van Vledder and Koop \(2009\)](#) proposed a 'refraction limiter' as a workaround setting to improve the modelling of low-frequency waves into the interior of the Wadden

Sea, as underestimations of low-frequency energy were found there. This limiter was not based on any physics and consists of turning off the refraction for frequencies lower than 0.2 Hz. In SWAN it can be set with the command `REFRL`.

C

GUIDELINES FOR PARALLEL SIMULATIONS WITH SWASH

This appendix describes some of the experiences of the author with respect to the application of the SWASH model on the Dutch national supercomputer Cartesius. Furthermore, some guidelines for parallel simulations with SWASH are presented.

C.1. COMPILING SWASH

Compiling SWASH on the Cartesius system was necessary, since SWASH had not been used on the system before. Experience taught that the 2016 version of the Intel toolchain is necessary for the correct compilation and running of SWASH on Cartesius. SWASH does not work correctly (yet) with newer versions of the toolchain. Since Cartesius uses Intel MPI, a change in the `Platform.pl` file of the source code of SWASH was necessary, to call Intel MPI with `mpiiFort` instead of the default `mpif90`.

C.2. RUNNING SWASH

Cartesius uses the SLURM batch system. Hence, directly using `swashrun` or using `swashrun` in a job script does not work on Cartesius. Therefore, the SWASH executable needs to be called directly. An example of a job script is:

```
1  #!/bin/bash
2  #SBATCH -t 0-12:00:00 -n 64
3
4  module load pre2019
5  module load intel/2016b
6
7  ln -s YOURFILENAME.sws INPUT
8
9  export I_MPI_INTRANODE_EAGER_THRESHOLD=10485760
10
11 srun swash.exe
```

This job script sets the maximum run duration to 12 hours and uses 64 computational cores. Next, two modules (toolchains) are loaded and the SWASH input file `YOURFILENAME.sws` is linked to a file called `INPUT`. The `export` command increases the buffer size to 1 MB, also see section C.5. Finally, SWASH is called.

C.3. PARALLEL SIMULATIONS

By default, SWASH decomposes the computational grid into sub-domains in a strip-wise manner. The size of the resulting sub-domains depends on the total computational grid size and the number of computational cores that are used. If these sub-domains become too small, the results will become inaccurate or the calculation will crash. This is related to the communication between the sub-domains. For this communication, each sub-domain is surrounded by an auxiliary layer of three grid points, the halo. Hence, the lower limit for the length of a sub-domain in any direction is $3 + 1 + 3 = 7$ grid cells. However, sub-domains of only seven grid cells in a certain direction would lead to a domain with only one 'independent' grid cell. A better lower limit would thus be of the order of 10 grid cells. In practice, such small sub-domains should preferably be avoided. With a small sub-domain, the number of computations may be reduced for each core, but the amount of communication between the larger number of sub-domains is increased. For each computational cluster or system, there is a fundamental limitation on how much speed-up can be achieved, and there exists an optimum in the number of cores that leads to the most speed-up (Amdahl's law).

C.4. MODEL SETTINGS

For more stable calculations for cases with multiple layers, it is recommended to impose some background viscosity, for the coupling of the vertical layers (to 'glue' the layers together). The command `BREAK` should only be used when shallow water is present in the bathymetry, hence when depth-induced breaking is actually expected, otherwise this could lead to the calculation crashing. The maximum number of (output) file names in SWASH is set to 99 by default. If one requests many output files, then this limit can be extended by editing the file `swashinit` and changing the highest file ref. number to a higher number.

C.5. COMMUNICATION BETWEEN PROCESSES DURING PARALLEL COMPUTATIONS

Two computational processes on a cluster communicate with each other at the same time through 'blocking', with a blocking send and a blocking receive. Generally, one process waits until another process can receive the information, the blocking. SWASH is written in such a way that all processes send at the same time, and then all receive at the same time. Cartesius uses the first implementation, which can lead to problems when using SWASH on Cartesius. Processes can end up waiting for each other endlessly, a so-called deadlock. 'Eager' allows a send operation to complete without acknowledgement from a matching receive. Hence, different processes can first simultaneously send, and then receive. The eager send buffer is set to 256 kilobytes by default on Cartesius. For larger models, the amount of data to be sent is larger, and a deadlock can occur. A solution for this problem is to increase the buffer, e.g. by setting the environment before calling SWASH, with `export I_MPI_INTRANODE_EAGER_THRESHOLD=1048576`, which is 1 megabyte (Voort, 2018). Another possible solution is to adjust the buffer size in SWASH, by changing the value of the parameter `MAXBUF` in the file `m_parallel.ftn` and then re-compiling SWASH Zijlema (2019). This issue was solved and implemented in SWASH version 7.01.

C.6. DIVISION OF GRID OVER THE DIFFERENT COMPUTATIONAL CORES WHEN USING EXCEPTION VALUES IN THE MODEL

An issue with parallel calculations and SWASH version 5.01 occurred when exception values (permanently dry grid cells) were used in a model. In these situations, something went wrong in the determination of how the calculation domain was cut and divided over the different computational cores. In some cases, they expressed themselves in segmentation faults, in less fortunate cases in SWASH model errors. As described, the default option in SWASH to decompose the computational grid into sub-domains is in a strip-wise matter (see The SWASH team, 2019a). If the grid is not easily divisible, then the orthogonal recursive bisection (ORB) method can be used instead. This method can aid in situations with small numbers of cores, but with the present model set-up and a larger number of cores, the ORB method ran endlessly, and the calculations never actually started. This issue was solved and implemented in SWASH version 7.01A.

C.7. RESONANCE-LIKE BEHAVIOUR IN SPONGE LAYERS

In some cases, with parallel computations and using SWASH version 5.01 with sponge layers, resonance-like behaviour occurred inside the sponge layers. Monotonic increasing water level oscillations started to occur in a sponge layer, after which the calculation crashed. In some cases, these problems could be solved by adding a radiation boundary condition at the end of the sponge layer as a mitigation measure. Part of this issue was fixed and implemented in SWASH version 6.01. This issue was fully fixed and implemented in SWASH version 7.01.

C.8. MERGING MODEL OUTPUT

If increases in the time step occur during a parallel calculation, the output time series are not merged properly at the end of the calculation. With a strongly decreasing time step during the calculation, the same issue arose. Hence, one has to be careful in choosing the right initial time step based on the CFL criterion. Furthermore, this problem occurred when requesting output located on different sub-domains (different computational cores). This issue was fixed and implemented in SWASH version 7.01A.

D

SWAN MODEL SETTINGS

Table [D.1](#) presents the SWAN model settings as used for the Dutch dike safety assessment WBI, using SWAN version 40.72ABCDE. Furthermore, the table gives the current SWAN default settings of the development version 41.31. Table [D.2](#) gives the ST6 model settings of [Rogers et al. \(2012\)](#) (the international state of the art) as used in this dissertation (settings partly based on [Gautier et al., 2018](#)), with the SWAN development version 41.31. The table also gives the in this dissertation determined recommended settings for the modelling of wave propagation effects in the Eems-Dollard estuary with the development version. Refer to [The SWAN team \(2019b\)](#) for further explanations of the different parameters.

SWAN version & model settings	SWAN Dutch safety assessment WBI (40.72ABCDE)	SWAN development default (41.31)
Directional resolution	36 10° bins	36 10° bins
Frequency resolution	44 bins, 0.015 Hz - 1 Hz	36 bins, 0.03 Hz - 1 Hz
Third-generation mode	Van der Westhuysen et al. (2012) GEN3 WESTH	Komen et al. (1984) GEN3 KOM
Linear wind growth	Cavaleri and Rizzoli (1981) (disabled)	Cavaleri and Rizzoli (1981) (disabled)
Exponential wind growth	Yan (1987)	Komen et al. (1984)
Wind drag formulation	Wu (1982)	Zijlema et al. (2012)
Swell dissipation	-	-
White-capping	Van der Westhuysen et al. (2007) WCAP WESTH [cds2]=5e-5 [br]=0.00175 [p0]=4 [powst]=0 [powk]=0 [nldisp]=0 [cds3]=0.8 [powfsh]=1	Komen et al. (1984) ; Pallares et al. (2014) ; Rogers et al. (2003) WCAP KOM [delta]=1
Quadruplet wave-wave interactions	Explicit DIA per sweep (S. Hasselmann & Hasselmann, 1985 ; S. Hasselmann et al., 1985) QUAD [iquad]=2	Explicit DIA per sweep (S. Hasselmann & Hasselmann, 1985 ; S. Hasselmann et al., 1985) QUAD [iquad]=2
Bottom friction	JONSWAP (K. Hasselmann et al., 1973) FRIC JON CON [cfjon]=0.038	JONSWAP (K. Hasselmann et al., 1973) FRIC JON CON [cfjon]=0.038
Depth-induced breaking	Van der Westhuysen (2010) BREA WESTH [alpha]=0.96 [pown]=2.5 [bref]=-1.3963 [shfac]=500	Battjes and Janssen (1978) or Salmon, Holthuijsen, Zijlema, Van Vledder, and Pietrzak (2015) BREAK CON OR BREAK BKD
Triad wave-wave interactions	OCA LTA (Eldeberky, 1996) TRIAD [itriad]=1 [trfac]=0.1 (in 40.72ABCDE) TRIAD [itriad]=11 [trfac]=0.1 (in 41.31)	CCA LTA (Eldeberky, 1996 ; Salmon et al., 2016) TRIAD [itriad]=1 [trfac]=0.8 or OCA LTA (Eldeberky, 1996) TRIAD [itriad]=11 [trfac]=0.05

Refraction	c_θ based on depth-gradients and using first-order backward differences NUM DIR DEP; Limiter on excessive directional turning based on Tolman (2009) (disabled); Limiter, disabling refraction for low frequencies (Van Vledder & Koop, 2009) (enabled) REFRL 0.2 2	c_θ based on gradient in wave number and using second order central differences (The SWAN team, 2019a) NUM DIR WNUM; Limiter on excessive directional turning based on Dietrich et al. (2013) (disabled)
Quadruplet and action limiter	LIM	LIM
Numerical propagation scheme	SORDUP	SORDUP
Stop criterion	NUM STOPC [dabs]=0.00 [drel]=0.01 [curvat]=0.001 [npnts]=99. STAT [mxitst]=80 [alfa]=0.001	NUM STOPC [dabs]=0.005 [drel]=0.01 [curvat]=0.005 [npnts]=99.5 STAT [mxitst]=50 [alfa]=0.00

Table D.1: SWAN model settings as used for the Dutch dike safety assessment WBI (version 40.72ABCDE) and default settings of the SWAN development version 41.31. Refer to The SWAN team (2019b) for further explanations of the different parameters.

SWAN version & model settings	SWAN development (41.31)	SWAN development recommended (41.31)
Directional resolution	45 8° bins	360 1° bins
Frequency resolution	36 bins, 0.03 Hz - 1 Hz	36 bins, 0.03 Hz - 1 Hz
Third-generation mode	Rogers et al. (2012) GEN3 ST6 [a1sds]=5.6e-6 [a2sds]=17.5e-5 VECTAU U10P [windscaling]=31 AGROW SSWELL	Komen et al. (1984) GEN3 KOM
Linear wind growth	Cavaleri and Rizzoli (1981) (by including AGROW above)	Cavaleri and Rizzoli (1981) (disabled)
Exponential wind growth	Donelan, Babanin, Young, and Banner (2006)	Komen et al. (1984)
Wind drag formulation	Hwang (2011)	Zijlema et al. (2012)
Swell dissipation	Ardhuin et al. (2010) (by including SSWELL above)	-
White-capping	Babanin and Young (2005); Young and Babanin (2006)	Komen et al. (1984); Pallares et al. (2014); Rogers et al. (2003) WCAP KOM [delta]=1
Quadruplet wave-wave interactions	Explicit DIA per iteration (S. Hasselmann & Hasselmann, 1985; S. Hasselmann et al., 1985) QUAD [iquad]=3	Explicit DIA per sweep (S. Hasselmann & Hasselmann, 1985; S. Hasselmann et al., 1985) QUAD [iquad]=2
Bottom friction	JONSWAP (K. Hasselmann et al., 1973) FRIC JON CON [cfjon]=0.038	JONSWAP (K. Hasselmann et al., 1973) FRIC JON CON [cfjon]=0.038
Depth-induced breaking	Battjes and Janssen (1978) BREAK CON	Battjes and Janssen (1978) or Salmon et al. (2015) BREAK CON or BREAK BKD
Triad wave-wave interactions	OCA LTA (Eldeberky, 1996) TRIAD [itriad]=11 [trfac]=0.05	CCA LTA (Eldeberky, 1996; Salmon et al., 2016) TRIAD [itriad]=1 [trfac]=0.05

Refraction	c_θ based on gradient in wave number and using second order central differences (The SWAN team, 2019a) NUM DIR WNUM; Limiter on excessive directional turning based on Dietrich et al. (2013) (disabled)	c_θ based on gradient in wave number and using second order central differences (The SWAN team, 2019a) NUM DIR WNUM; Limiter on excessive directional turning based on Dietrich et al. (2013) (disabled)
Quadruplet and action limiter	-	LIM
Numerical propagation scheme	BSBT	SORDUP
Stop criterion	NUM STOPC [dabs]=0.005 [drel]=0.01 [curvat]=0.005 [npnts]=99.5 STAT [mxitst]=50 [alfa]=0.00	NUM STOPC [dabs]=0.00 [drel]=0.003 [curvat]=0.001 [npnts]=99.5 STAT [mxitst]=160 [alfa]=0.00

Table D.2: SWAN model settings as used for the ST6 settings ([Rogers et al., 2012](#)) with the SWAN development version 41.31, and recommended settings for the modelling of refraction and diffraction in the Eems-Dollard estuary with the SWAN development version 41.31. ST6 settings partly based on [Gautier et al. \(2018\)](#). Refer to [The SWAN team \(2019b\)](#) for further explanations of the different parameters.

E

OUTLOOK

This appendix discusses some of the implications of this research on the future of the Dutch flood defence safety assessment framework BOI. Potential areas of improvement and future research are presented as well. The focus lies on the flood defences in the coastal region, of which the required crest levels are determined with BOI. More specifically, the main focus lies on the eastern Wadden Sea and Eems-Dollard estuary and the determination of the wave loads with SWAN. The listed implications, potential areas of research and potential improvements are not only based on the results of this dissertation, but on the available literature, experiences of the author during this PhD research and his personal vision and opinions as well. Estimates of the required effort and potential influence on the calculated required crest levels with BOI for the Dutch coastal region are given for each aspect. Here, a small required effort is defined as estimated to require up to 1 year, medium up to 3 years and large more than 3 years. The influence on the required crest levels is split into a small influence, medium influence and large influence as well. No exact numbers can be given, but a distinction is made between an expected increase or decrease in the required crest levels. It is expected that many of the described topics will be studied further and ultimately implemented in BOI 2023 or BOI 2035. Finally, this appendix gives a long-term vision for the future of the BOI safety assessment framework, again mainly focused on the determination of the wave loads in the coastal region. Overviews of the current limitations, challenges and potential future improvements in wave modelling in general can be found in [Cavaleri et al. \(2018\)](#). Present limitations, challenges and potential future improvements for (the SWAN modelling in) BOI have also been described by [Arcadis et al. \(2019\)](#) and [Groeneweg and Gautier \(2020\)](#).

E.1. IMPLICATIONS, POTENTIAL IMPROVEMENTS AND FUTURE AREAS OF RESEARCH RELATED TO BOI

Wind

The statistics of the wind, which are used for the eastern Wadden Sea in BOI, are based on the station at West-Terschelling. However, this location is located in the western Wadden Sea, where patterns in wind direction and velocity tend to be different compared to the Eastern Wadden Sea and especially the Eems-Dollard estuary (e.g. Adema et al., 2014, 2015). There, the influence of the surrounding land mass of the province of Groningen and the shape of the estuary itself lead to different wind velocities and directions. For Terschelling, wind data are available since 1968. There are two wind stations in the eastern Wadden sea, Huibertgat, which measures since 1980, and Nieuw Beerta, which measures since 1990. Even though these data sets have a shorter length, they can still provide valuable insights in the differences in wind velocities and directions outside and inside the estuary. Arcadis et al. (2019) analysed and compared wind data of historic severe storms at these two locations with West-Terschelling, to gain more insight into the influence of the land mass of Groningen. They found that for wind velocities larger than 15 m/s, the wind velocity is approximately 25% smaller inside the Eems-Dollard estuary than at Terschelling. The influence of the land roughness is currently not taken into account in BOI. Inclusion of this effect would likely lead to smaller and more realistic wind velocities in the estuary. This effect may play a role at other locations as well. The required effort related to this aspect is estimated as being medium, the impact on the calculated required crest levels is estimated as being a medium reduction in crest levels (potentially a large influence at certain locations, e.g. Eems-Dollard estuary, a negligible influence at others, e.g. North Sea coast).

BOI uses a standard trapezoidal storm development profile for the eastern Wadden Sea, which was determined based on data from a wind station in the western Wadden Sea. As described above, the situation in the Eems-Dollard is largely different from the western Wadden Sea. Arcadis et al. (2019) showed that the currently used storm development profile is not representative for storms that lead to large water levels in the Wadden Sea. Local storms can have a strong peak and quick turning in direction. However, the longer lasting storms, which turn from west to northwest, cause the largest water level set-up in the Wadden Sea. In such storms, the wind velocity exceeds 70% of the maximum wind velocity in the storm for more than 45 hours. This is much longer than the storm profile that is used in BOI, where the 70% wind velocity value is only exceeded for 16 hours. Therefore, reassessment of the storm development profile for the eastern Wadden Sea and Eems-Dollard estuary is recommended. The required effort related to this aspect is estimated as being small, the impact on the crest levels is estimated as being a medium increase in crest levels (potentially a large influence in the eastern Wadden Sea and Eems-Dollard estuary, but a relatively small influence at other locations such as the North Sea coast).

BOI presently uses the uncapped wind drag relation of Wu (1982). This relation gives larger values for the drag coefficient than the relations of Zijlema et al. (2012) and Hwang (2011). As consensus seems to have been reached on the capping of the wind drag, an expression that accounts for this capping should be used in BOI. This could be the capped version of the expression of Wu (1982) or the expressions of Zijlema et al. (2012) and

Hwang (2011), as long as the uncertainty in the expressions is accounted for as well. Since the flood defences are assessed with extreme conditions, including the newest insights in the wind drag in BOI will lead to differences in the required crest levels of the flood defences. Van Vledder (2015) already proposed several options for adjusting the wind statistics in BOI. One of the solutions that was proposed, was to use a pseudo-wind, to adjust the wind velocity which has a certain probability of occurrence, without having to adjust the data internally (in the databases). A more consistent and robust solution would be to recalculate the BOI simulations using the new wind drag formulation in all models. Especially consistency in the wind drag relations between the atmospheric, flow and wave models is necessary. An ideal solution would be to remove the wind drag from the models, and to directly use the wind stresses. However, in order to achieve this, significant changes in the models may be required. Depending on the measure that is chosen, the required effort related to this aspect is estimated as being medium to large. The influence on the crest levels is estimated as being large (of influence in the whole coastal region) and probably leading to reductions in required crest levels.

Water levels

The water level statistics in BOI are based on triangular interpolation, using data of three different water level measurement stations. Using interpolation means that the statistics are not based on a physical relation. In reality, the water level set-up is partly caused by the wind. This physical relation between wind and water level is currently not explicitly included in BOI. However, the influence of the wind is implicitly included in the statistical series of the measurement stations. No (numerical) model is used to determine the water level at a nearshore location. Water levels and flow fields are calculated with the WAQUA model, but they are only used as input for the SWAN simulations that determine the wave conditions, not for the statistics of the water levels themselves. In other words, there is no direct coupling between the waves and water level (statistics). Since the water level depends on the wind, tide and waves, the water level should preferably be removed as a stochastic variable from BOI, and should be determined by numerical modelling. Ideally, two-way coupling between the models would be used. However, this would require a significant effort and redesign of both the probabilistic and numerical model set-up. Furthermore, large uncertainties still exist regarding the wave-dependent wind drag. The existing formulations give widely varying results and measurements are scarce. The required effort is estimated as being large, the influence on the crest levels is estimated as being medium. This could lead to either an increase or reduction in the required crest levels, depending on the location.

Offshore wave conditions

BOI uses SWAN to determine the wave conditions at the flood defences. At the offshore boundaries of the SWAN Wadden Sea model, wave boundary conditions are applied. These consist of 1.5D spectra, determined based on the ratio between SWAN results and measurements at two measurement stations in the North Sea. Stijnen and Kallen (2010) determined the ratio between the wave parameters as determined by SWAN and the measured parameters at these stations, after which these ratios were used to correct the spectra at the model boundaries. Applying such a correction could lead to wave parameters, which are already incorrect at the boundary of the Wadden Sea grid, which will then

propagate into the model and potentially influence the parameters at the flood defences. An example of a potential issue with this method is the following: the measured data are extrapolated to extreme return periods that have not been measured. If the measured data are extrapolated to a return period of, e.g. 10,000 years, then potentially a wave height could be obtained that cannot exist at the local water depth. A more thorough assessment of the influence of this correction method is therefore recommended. A quick remedy could be to impose a certain upper limit on these extrapolated wave heights, e.g. based on a certain maximum ratio between wave height and water depth. A better solution would be to remove this extreme extrapolation and only use the measured spectra at the stations for validation. Using a redesigned and recalibrated model set-up, the wave boundary conditions at the Wadden Sea grid could then follow directly from large-scale atmospheric, flow and wave models with a higher (spatial and temporal) resolution wind as the only input. Depending on the measure that is chosen, the required effort ranges from small to large. The estimated influence on the crest levels is a small reduction in required crest levels, as the influence of a potential overestimation in the wave height is expected to be reduced at the coast, due to e.g. depth-induced breaking.

E**SWAN version**

BOI currently uses SWAN version 40.72ABCDE. The most recent version is 41.31. Version 41.31 includes the new implementation of refraction (which is more accurate and robust) and the consistent collinear (CCA) LTA for the triads, which 40.72ABCDE does not. Therefore, it is recommended to switch to the newest version for BOI. On the other side, BOI presently uses the [Van der Westhuysen et al. \(2012\)](#) settings. These settings are not included in version 41.31 any longer. Therefore, further thorough comparison and validations of the [Van der Westhuysen et al. \(2012\)](#), [Komen et al. \(1984\)](#) and ST6 ([Rogers et al., 2012](#)) settings is necessary first, to determine which settings are preferred. The required effort is estimated as being medium, the influence on the crest levels is estimated as being small or medium, depending on how many of the formulations for the physics will be changed compared to the present settings. Less uncertainty in the predicted wave conditions might lead to either increases or reductions in required crest levels, depending on the location.

SWAN computational grids and grid resolution

BOI uses curvilinear grids with a maximum resolution of approximately 20 m x 80 m in the Eems-Dollard estuary. However, it was determined here that such a resolution may not be sufficient in areas where strong refraction or diffraction play a role. Furthermore, oscillations in the $T_{m-1,0}$ and H_s were found in the results of the WBI 2017 simulations at the dikes in the eastern Wadden Sea (see chapter 3). These oscillations extend from the tidal inlets towards the dikes and are related to the sweep mechanism, which is used for curvilinear grids in SWAN. It was confirmed that this effect does not occur if a rectilinear grid is used. However, curvilinear grids allow local refinements, which rectilinear grids do not. The resolution of the current curvilinear grids could be increased to allow better modelling of refraction, but a disadvantage of local refinements in curvilinear grids is that these refinements have to span the whole horizontal or vertical distance of the grid, increasing the resolution in areas where this increase is not required, thus increasing computational costs. In the future, potentially unstructured grids could be used

instead. Unstructured grids allow local refinements without having to increase the resolution throughout the grid, saving computational resources. Local refinements could be based on e.g. local depth gradients. However, such grids would need to be thoroughly validated first. The required effort of changing to unstructured grids is estimated as being large. Theoretically, the influence on the crest levels should be small, but improved modelling of e.g. refraction due to the use of finer grids might have an influence, either resulting in increases or decreases.

SWAN directional resolution

The SWAN simulations of BOI use 36 directional bins, which is sufficient for most situations. However, the present study confirmed that this number of directions may be too small at locations where wave sheltering effects or strong refraction occur. BOI uses 96 directional bins in the Europoort area, since a 'radiation problem' occurs in this area when less directional bins are used. A similar problem was observed for certain conditions and model settings in the present study. Sometimes all wave energy was assigned to one directional bin in the first time step at the tidal deltas in the eastern Wadden Sea, at the relatively narrow inlets between the barrier islands. This energy did not diffuse out of this bin during subsequent iterations. This seemed to be related to the first guess and number of directional bins. At present, this effect can be identified visually, and removed by manually altering the grid or initial settings. Potentially, increasing the number of directional bins at such locations may improve the results. Based on the results found in this dissertation, it is recommended to at least double the directional resolution in areas with narrow inlets, and to preferably quadruple the resolution in areas where wave sheltering or strong refraction effects occur. The required effort is estimated as being small, the influence on the crest levels is estimated as being small as well and could be either an increase or decrease.

SWAN refraction

BOI uses the refraction limiter of [Van Vledder and Koop \(2009\)](#) on the SWAN grid that covers the eastern part of the Wadden Sea and the Eems-Dollard estuary. As described before, the refraction limiter proved to work, but it is not a very elegant solution, since it was not based on any physics. Furthermore, the newest SWAN version includes a new implementation of the refraction, which is more accurate and robust. This work showed that SWAN is able to model the refraction effects in the Eems-Dollard estuary reasonably well, provided the grid resolution is high enough (or better: Δd is small enough). The present maximum resolution of 20 m x 80 m in the Eems-Dollard estuary within BOI is rather coarse, and a higher resolution will improve the modelling of refraction. More research towards the actual refraction and penetration of long North Sea and infragravity waves into the eastern Wadden Sea is necessary still, as well as the modelling of this penetration with SWAN. These refraction-related aspects should preferably be considered together with what is described under 'SWAN computational grids and grid resolution', 'SWAN triad wave-wave interactions' and 'SWAN infragravity waves'. The required effort of these topics combined is estimated as being large, the impact on the crest levels is estimated as being large as well. The influence of refraction and triads can lead to either increases or decreases in required crest levels. Especially the influence of infragravity waves may lead to increases in required crest levels.

SWAN diffraction

SWAN includes a phase-decoupled refraction-diffraction approximation, but BOI does not use this approximation. It was determined here that the approximation is often unstable. For most locations, diffraction effects will be small and largely local. However, e.g. inside harbours or in areas where wave sheltering effects occur, diffraction can play a significant role. Future research could focus on the improvement of the modelling of diffraction with phase-averaged models, but an inherent limitation of these models is that they do not include phase information. Recently, [Smit and Janssen \(2013\)](#) and [Smit, Janssen, and Herbers \(2015\)](#) have developed a generalised evolution equation for the transport of the complete second order wave statistics of the surface elevation, including cross-correlation. The equation generalises the action balance equation by including the evolution of the cross-correlation terms. Using this equation might improve the modelling of e.g. wave interference and diffraction. An alternative would be to use a different model, e.g. phase-resolving, in areas where diffraction is deemed important. The required effort is estimated as being medium, the influence on the crest levels is estimated as being small. Using the analogy of the semi-infinite breakwater: in the shadow zone an increase in the required crest levels, a decrease in the areas under direct wave attack.

E

SWAN triad wave-wave interactions

Currently, SWAN includes 1D triad formulations only. Furthermore, the SWAN BOI simulations use the original collinear approximation (OCA) LTA for the triad wave-wave interactions, which contains inconsistencies ([Salmon et al., 2016](#)). The newest SWAN version includes the CCA LTA, which solved these inconsistencies. However, the LTA is still only 1D (it only considers the collinear interactions) and only considers the self-self interaction (transfer to the super-harmonic). It was shown that 2D (non-collinear) interactions and transfers to lower frequencies can play a role as well (see also e.g. [Groeneweg et al., 2015](#); [Herbers, Elgar, & Guza, 1995](#); [Toledo, 2013](#)). These interactions can broaden the spectra and influence the refraction. Furthermore, the (relative) influence of the triads can increase strongly for more narrow-spread seas. Therefore, the development and implementation of 2D formulations for the triads is considered highly beneficial, even if such formulations come at a larger computational cost. [Salmon \(2016\)](#) presents several suggestions, such as 2D source terms (e.g. [Becq et al., 1998](#)) or better representations of the evolution of the bi-spectrum (e.g. [T. T. Janssen, 2006](#); [Smit & Janssen, 2016](#); [Vrecica & Toledo, 2016, 2019](#)). This might finally lead to 'third-generation' source terms which take the spectral energy balance at each frequency and directional component into account. An intermediate solution may be to develop hybrid models, which enable a compromise between computing all frequency interactions and only the self-self interactions. This may be achieved by only considering interactions between frequency components over a characteristic frequency bandwidth, determined by the frequency width of the primary spectral peak ([Salmon, 2016](#)). As a first solution, [Salmon \(2016\)](#) suggested modifying the form of the directional function in the CCA LTA. Preferably, these aspects should be considered together with the aspects described under depth-induced breaking, refraction and diffraction. Furthermore, the influence and modelling of Bragg-scattering should be studied in more detail. Depending on which avenue is chosen, the estimated required effort ranges from small to large. The potential influence on the crest levels of these aspects combined is estimated as being large. The influence of refraction and triads can lead to

either increases or decreases in required crest levels. Especially the influence of infragravity waves may lead to increases in required crest levels.

SWAN depth-induced breaking

The formulation of [Van der Westhuysen \(2010\)](#) was chosen for the depth-induced breaking in the SWAN simulations of BOI, since this formulation outperformed the one of [Battjes and Janssen \(1978\)](#) in the Wadden Sea. The formulation of [Battjes and Janssen \(1978\)](#) limited the wave growth over flat bottoms. [Salmon and Holthuijsen \(2015\)](#) found that the formulation of [Salmon et al. \(2015\)](#) performed equal to or better than the other two formulations for several considered cases. Based on the simulations performed for this dissertation, no preference for one of the formulations could be given yet. Therefore, it is recommended to further assess and validate the performance of the different formulations, especially since the formulation of [Van der Westhuysen \(2010\)](#) is not present in the newest SWAN version any longer. The estimated required effort is small to medium, the estimated influence on the crest levels is small to medium as well, depending on the location. Both increases and decreases in wave heights have been found in the literature, when using the formulation of [Salmon et al. \(2015\)](#) instead of the one of [Van der Westhuysen \(2010\)](#). Hence, no clear indication can be given yet of resulting increases or decreases in required crest levels.

SWAN wind growth

In this dissertation, large differences were found between the results of the SWAN assessment and development versions, which were related to the used wind drag formulations. The wind drag was treated under 'wind' already. As described, consistency between the different models in the applied drag relations is necessary. Preferably, the wind stresses would be used directly in SWAN, but this will require a significant effort in adapting the model. Wind drag and wind growth-related aspects in SWAN should be considered together with the white-capping and quadruplet wave-wave interactions, as these source terms influence one another. The estimated required effort is medium, the influence on the crest levels is estimated as being medium to large (of influence in the whole coastal region), probably leading to reductions in required crest levels.

SWAN infragravity waves

Currently, SWAN does not model infragravity wave energy. Infragravity or long wave energy plays an important role at many locations. An example is the penetration of long North Sea and infragravity waves into the eastern Wadden Sea and Eems-Dollard estuary. Infragravity waves can be generated locally as well, such as on shallow foreshores. The inclusion of infragravity waves in SWAN is considered highly important, since this energy may have a large impact on the wave conditions, wave overtopping and required crest levels of the flood defences (see e.g. [Hofland et al., 2017](#); [Lashley et al., 2020](#); [Lashley, Van der Meer, et al., 2021](#); [Oosterlo, Van der Meer, et al., 2018](#)). Therefore, it is recommended to study if an 'infragravity source term' could be implemented in SWAN. These infragravity wave-related aspects should preferably be treated together with what was described under 'SWAN refraction', 'SWAN triad wave-wave interactions' and 'Wave run-up and overtopping'. The required effort is estimated as being large, the potential impact on

the crest levels is estimated as being large as well (potentially large increases in required crest levels at locations where significant amounts of low-frequency energy are present).

SWAN convergence

In this dissertation, it was observed that SWAN has difficulties converging in a highly complex area such as the Eems-Dollard estuary. BOI uses a maximum of 80 iterations. However, in the present simulations of the estuary, varying numbers of computational points had not yet converged after 80 iterations. This mainly influenced the mean wave direction and directional spreading, since they converge slower than the wave height and wave period. Therefore, a stricter stop criterion with a maximum number of iterations of 160 was used for many of the simulations performed in this dissertation. A careful assessment of the convergence behaviour in the simulations as used for BOI is recommended, after which potentially a stricter criterion could be chosen. The required effort is estimated as being small, as is the estimated influence on the crest levels (slight changes in wave direction may lead to slight increases or decreases in required crest levels).

Directional broadness of spectra

Bulk wave parameters such as the significant wave height, wave peak period and mean wave direction are used often to characterise the wave conditions at a specific location. BOI also uses these parameters, and uses the $T_{m-1,0}$ wave period, mean wave direction and total (significant) wave height as input for wave overtopping calculations. 1D and 2D spectra and the first four moments of the directional distribution provide much more detailed insight than bulk wave parameters, see also e.g. [Cavaleri et al. \(2018\)](#); [Dabbi et al. \(2015\)](#); [Rogers and Van Vledder \(2013\)](#). The 2D spectra of the present calculations showed that, while the mean wave direction may be onshore-directed, quite a large part of the energy in the spectrum may be offshore-directed. This energy does not contribute to the loads on the dike. Hence, using the mean wave direction and the total wave height may lead to overestimations of the wave overtopping and required crest levels. The use of wave spectra instead of bulk wave parameters is not just recommended for BOI, but for any wave measuring or modelling study. For BOI, a first solution could be to simply use the amount of directional spreading as a measure to determine if the spectrum is directionally broad. At locations with directionally broad spectra, 2D spectra could be generated with SWAN at the dikes. Furthermore, the orientation of the dike normal could be included in the BOI calculations. With this information, the bulk wave parameters could be determined based on the onshore-directed part of the spectrum only. Added to this, inclusion of a model uncertainty in the wave direction might be beneficial, especially for directionally broad spectra. On the other side, it may be difficult to determine a value for this uncertainty, as wave direction measurements are generally rare. The required effort is estimated as being small, the influence on the crest levels is estimated as being small to medium (potentially a medium reduction in required crest levels at certain locations, a negligible influence at other locations).

Number of SWAN and WAQUA simulations

BOI uses discrete values for the wind velocity, wind direction, wind set-up, phase difference and time relative to the peak of the storm as input for SWAN simulations (1800 combinations in total). Furthermore, 8 peak wind directions, 5 wind velocities, 3 phase dif-

ferences and 3 offshore wind surges are combined for runs with the WAQUA model (360 combinations). The wind surges are 0 m+NAP, 2 m+NAP and 4 m+NAP. In an area where very large water levels occur, e.g. the Eems-Dollard estuary, extrapolation is used within the probabilistic calculations. It has to be determined, if using only three different values for the surge is enough to describe the extreme conditions accurately in such areas. As described before, the preferred solution would be to completely remove the water level as a stochastic variable. In that way, the local water level would solely be determined by the wind and hydrodynamic simulations. Depending on the measure that is chosen (e.g. adding surge levels or redesigning the framework of models), the required effort is estimated as being small or large. The influence on the crest levels is estimated as being small and could either be an increase or decrease in the required crest levels.

Interpolation of SWAN results in databases

BOI uses an extensive procedure to interpolate the SWAN results onto so-called 'probabilistic calculation grids' and store them in databases. These grids are essentially matrices and are used for inter- and extrapolation within the probabilistic calculations. The interpolation procedure reduces the 1800 SWAN simulations in the databases to 280, effectively eliminating the potential difference in time relative to the peak of the storm, difference in storm surge level and difference in phase relative to the tide (see chapter 2). For the interpolation of the data at each SWAN output point, eight different probabilistic calculation grids are used, one for each of the eight wind directions that are considered in BOI. These eight grids each have a maximum of 35 grid points, corresponding to seven different water levels and five wind velocities. To fill these grids, the local water levels and wind velocities at the SWAN output points at the dikes are used, which can vary relative to the peak of the storm. However, the offshore wind direction (at the peak of the storm) at one of the measurement stations is used for the grids, not the varying wind direction at the SWAN output points. Hence, the wind velocities and water levels in the grids can correspond to other moments in time, but the wind direction in the grids is always the direction at the peak. In this way, this procedure might fail to incorporate the dynamic character of the storm.

Based on another extensive procedure, certain grid points of the probabilistic calculation grids are selected to be either included or excluded in the probabilistic calculations. This procedure is not based on any physical background or relation. Grid points are selected using a rectangular 'mask' with a certain size. All grid points within the rectangle are included in the inter- and extrapolation procedure. However, the SWAN results often show a triangular or trapezoidal shape, because of the physical relations and correlations between wind, water levels and waves. For example, onshore wind directions tend to lead to large water levels. This means that combinations of large wind velocities from onshore wind directions and lower water levels tend to be scarce. The same holds for offshore wind directions, which mainly lead to low water levels. This also holds for the correlation between water levels and wave heights; a small water depth leads to small wave heights, whereas a large water depth can lead to either small wave heights or large wave heights, depending on the wind conditions.

The selection of grid points with the rectangle thus leads to 35 or less grid points (data for at most seven different water levels and five wind velocities). The probabilistic model uses extrapolation for values that lie outside these grid points. The maximum water level

in the grids is 7 m+NAP. However, water levels occur in the SWAN results for the Eems-Dollard estuary that are over 10 m+NAP for certain conditions. Since the grids for the probabilistic calculations only include values up until 7 m+NAP, this means that (wave) data points that are actually available are neglected, and that the probabilistic model will extrapolate for water levels larger than 7 m+NAP instead.

Hence, the procedure of inter- and extrapolation should likely be improved, to make it more consistent with the actual physical relations between the different parameters. A first step would be to include all available values in the SWAN databases, e.g. for water levels larger than 7 m+NAP. In this way, extrapolation is not necessary as often. A more extensive solution would again be to redesign and expand the probabilistic model. The estimated required effort ranges from medium to large, the influence on the crest levels is estimated as being small to medium (negligible at certain locations, small to medium influence at others, either being increases or reductions).

Wave run-up and overtopping

The mean wave overtopping discharge was used for the dike safety assessment in WBI 2017. The [Van der Meer \(2002\)](#) equations, later implemented in [EurOtop \(2007\)](#), were used to determine the wave overtopping discharge. The cumulative overload method could be used as well, for a more detailed assessment. It is expected that the cumulative overload method will replace the mean overtopping discharge within BOI in the future. For the cumulative overload method, information on e.g. front velocities of the overtopping flow and information on the strength of the dike (grass) cover are necessary. Further calibration and verification of this method is required for use in BOI, especially for (very) oblique wave attack during actual storms. E.g. further measurements with the laser scanners are expected to provide more insight into this.

Furthermore, it is currently not well-known how to quantify wave overtopping for a combination of wind waves and infragravity waves. In theory, the $T_{m-1,0}$ wave period should account for this ([Van Gent, 1999a, 1999b, 2001](#)). As this period is very sensitive to the low-frequency energy, the $T_{m-1,0}$ can become very large when low-frequency energy is present ([Hofland et al., 2017](#)). The influence of low-frequency energy on the overtopping discharge as calculated by the [Van der Meer and Bruce \(2014\)](#) equations is large, see e.g. [Lashley et al. \(2020\)](#); [Lashley, Van der Meer, et al. \(2021\)](#); [Oosterlo, Van der Meer, et al. \(2018\)](#).

However, the results of this dissertation suggest that the low-frequency energy as present at Uithuizerwad during storm Ciara did not influence the wave overtopping. Recently, [Lashley, Jonkman, Van der Meer, Bricker, and Vuik \(2021\)](#) found that the equation of [Van Gent \(1999a, 1999b, 2001\)](#), which was developed for shallow water conditions, is much less sensitive to the $T_{m-1,0}$ wave period and thus low-frequency energy. However, [EurOtop \(2018\)](#) presently only recommends use of this equation for values of the breaker parameter $\xi_{m-1,0} > 7$. These results suggest that the [EurOtop \(2018\)](#) approach may be incorrect for locations where low-frequency energy plays a role and that the equation of [Van Gent \(1999a, 1999b, 2001\)](#) may be a better alternative for such conditions, even if $\xi_{m-1,0} < 7$.

Therefore, it is recommended to study the presence of low-frequency energy and the $T_{m-1,0}$ measurements in the area in more detail, as well as the influence of low-frequency energy on wave overtopping. These aspects should preferably be considered together with

what was described under 'SWAN infragravity waves' as well. The required effort is estimated as being medium, the potential impact on the crest levels is estimated as being large (direct influence on wave overtopping and thus on required crest levels, at many locations). The influence of infragravity waves will likely lead to increases in required crest levels. Further research on (very) oblique wave attack may lead to increases or decreases in required crest levels, depending on the found influence of this oblique wave attack on the wave overtopping. Further measurements in the field and tests with the overtopping simulator, as well as use of the cumulative overload method, may lead to changes in the allowed overtopping volumes or discharges, directly influencing the required crest levels.

Probabilistic methods

BOI contains many of the most commonly used probabilistic calculation techniques. One of these techniques is FORM (First Order Reliability Method). FORM linearises the reliability function in the design point and approximates the probability distribution of each variable by a standard normal distribution (or sometimes a log-normal distribution). While FORM generally needs less evaluations to determine the probability of flooding, there are limits to the shape of the limit state and the method relies on consistent derivatives to be able to locate the design point. Hence, this approach is troubled by limit states with multiple (near) design points (Den Bieman et al., 2014; Oosterlo, 2015). Monte Carlo sampling is another method that is included in BOI. This method consists of generating random numbers from a uniform probability density function. The probability of failure can be estimated by repeating this procedure many times, by determining the frequency with which these drawings occur in the failure space. However, Monte Carlo sampling requires many realisations, which further increase with increasing numbers of stochastic variables. It might be beneficial to implement an alternative probabilistic calculation method, if more stochastic variables and model uncertainties would be included in BOI, or if more complex limit state functions would be implemented. An example of such a method is Adaptive Directional Importance Sampling (ADIS), see e.g. Oosterlo, McCall, et al. (2018). ADIS is a fully probabilistic method, like Monte Carlo sampling, and can cope with large numbers of stochastic variables and complex limit state functions. The main advantage of ADIS is that it greatly reduces the number of calculations necessary, since it combines aspects of both directional sampling and importance sampling. The estimated required effort is medium. Theoretically, the influence on the crest levels should be small, as the chosen probabilistic method should not influence the required crest levels.

E.2. LONG-TERM VISION FOR WAVE MODELLING IN BOI

This sub-section presents a long-term vision for the future of the Dutch safety assessment framework BOI, with the main focus being on the wave modelling. It is assumed that the computational requirements do not form a limitation. In this ideal future scenario, the whole framework of probabilistic, numerical and analytical models of BOI would be updated. An efficient fully probabilistic model would be used for the probabilistic calculations. The probabilistic model would only use the wind and the tide as 'base' (off-shore) stochastic variables, the water level would be removed as such. Furthermore, more model uncertainties would be included for the (wave) parameters at the flood defences, and these uncertainties would be determined more accurately.

Beckers et al. (2009) already presented a method to improve the probabilistic model in BOI, such that the wind dynamics and tide can be included in the probabilistic model. They provided a new set of stochastic variables: the wind direction (either non-changing, slowly changing or fast changing), the wind velocity (slowly or fast increasing and decreasing), the tidal phase (phase difference between storm peak and tide), and the tidal amplitude. In this way, the local water level could be determined by hydrodynamic simulations and would no longer be a stochastic variable itself.

The numerical modelling would start with a large-scale world or ocean model with the tides and wind as only input. I.e., without currents, waves or other boundary conditions, they would be generated fully within the models. The world or ocean model would be two-way coupled to a continental shelf or North Sea model. This model would in turn be two-way coupled to more local models, e.g. for the Wadden Sea. The two-way coupling, e.g. by (radiation) stresses, allows for the interaction between the different models, such as the interactions between wind, water levels, currents and waves (see e.g. Adema et al., 2014, 2015). The wind would be included by using the stresses directly, without the necessity of a wind drag relation. All models could be nested or run separately from one another. With the ever increasing computational capacities (e.g. supercomputers) and the development of models that can use unstructured grids, it might even be feasible to merge these models into one large-scale world model in the future, with local refinements wherever needed. Currently, the models are run with a uniform wind, possibly somewhat including the effect of a turning wind, as in the Wadden Sea. Ideally, characteristic (global) pressure, wind and storm patterns (in space and time) would be defined, which could serve as input for the atmospheric, SWAN and D-Hydro models. This would require all models to run in the non-stationary mode. Non-stationary runs are further required, because the largest wind velocities, water levels and waves do not always occur at the same time.

The latest SWAN version would be used, with consistent and best available settings, including the newest insights in the physics. With new developments regarding the formulations of the physics and future increases in computational power, several of the source terms could be determined (near-)exact, e.g. the triad and quadruplet wave-wave interactions. SWAN would not only be able to model wind waves, but would be able to cope with infragravity waves as well. Unstructured grids would be used. The unstructured grids would allow for more detail, without the limitation of curvilinear grids that local refinements extend throughout the whole computational domain, which would save computational resources. The local refinements would be fine enough for e.g. refraction to be modelled accurately, even at locations with very large depth gradients. Perhaps, the possibility would be added to BOI to use a more detailed model locally, at locations where SWAN currently does not perform well. Such areas could be ports, estuaries, or locations with (very) shallow foreshores, where e.g. diffraction, reflections or infragravity waves play a role. This more detailed model could be a phase-resolving model and use the output from SWAN simulations as input.

As Salmon (2016) described, it is unlikely that phase-resolving models will replace phase-averaged models in the near future, especially in the safety assessment frameworks and operational models. This is due to the present exclusion of the wind growth in such models, due to their computational demand, and due to the instabilities that sometimes still occur. However, they can be applied in smaller complex domains where phase-averaged

models are not (yet) sufficient enough. Furthermore, they can be used to improve the understanding of the physics, which could in turn lead to new formulations for the phase-averaged models. If the growth of the waves by the wind can be added to phase-resolving models in the future, then these models might become available for use at larger scales as well. With further increases in computational power, phase-resolving models may then potentially replace phase-averaged models in areas such as the Eems-Dollard estuary or even the whole Wadden Sea.

Finally, BOI would mainly use 2D wave spectra instead of bulk wave parameters. A better coupling would be made between the hydraulic loads and the strength of the defences. An example is the transition from a mean wave overtopping discharge towards the cumulative overload method. The influence of infragravity waves and multi-modal spectra on wave overtopping would be characterised in more detail and taken into account, as well as the influence of oblique to very oblique wave attack on wave overtopping. To reach this ideal future scenario, it is highly important that field measurements - such as the ones performed in the MVED project in the Eems-Dollard estuary - keep on being performed in the future, as they can strongly contribute to the development of the BOI framework.

LIST OF SYMBOLS

ROMAN LETTERS

a	Dimensional scale factor of Weibull distribution	
b	Non-dimensional shape factor of Weibull distribution	-
c	Wave phase velocity	m/s
c_d	Van der Meer (2011) coefficient in run-up depth equation, dependent on the dike slope	-
c_θ	Directional turning rate	rad/s, rad/m
c_u	EurOtop (2018) coefficient in run-up front velocity equation	-
D	Test/storm duration, distance between laser scanner scan lines	s, m
d	Water depth, run-up depth	m
f	Frequency	Hz
f_p	Peak frequency	Hz
h	Water level	m
$H_{1/3}$	Significant wave height, based on the mean of the highest one-third of the waves in a wave record	m
H_{m0}	Significant wave height, based on spectral analysis	m
H_{rel}	Relative wave height	m
H_s	Significant wave height	m
h_s	Height of laser scanner above dike slope	m
k	Wave number	rad/m
L	Wavelength	m
L_p	Wavelength, corresponding to wave peak period	m
M	Model data	
N	Normal distribution, number of waves in record, number of observations, window length used for Fourier transform	-

N_{ow}	Number of overtopped waves	-
N_w	Number of incident waves	-
O	Observation data	
P	Average return period	year
P_{ov}	Probability of overtopping	-
$P_{v\%}$	Percentage of wave volumes that exceed a specified volume V_i	%
q	Mean wave overtopping discharge	l/s/m
R	Distance measured by laser scanner	m
R_u	Run-up height	m
$R_{u2\%}$	Run-up height, exceeded by 2% of the number of incoming waves	m
$T_{1/3}$	Significant wave period, based on the mean of the highest one-third of the waves in a wave record	s
T_m	Mean wave period	s
$T_{m-1,0}$	Spectral wave period, based on the moments of the spectrum, defined as m_{-1}/m_0	s
T_p	Wave peak period, based on spectral analysis	s
U	Ursell number, defined as $H_{m0}L_p^2/d^3$	-
U_p	Potential wind velocity, defined as the hourly averaged wind speed at 10 m above homogeneous open terrain with a roughness length of 0.03 m	m/s
V	(Virtual) overtopping volume	m ³ /m
v_{front}	Run-up front velocity	m/s
V_{max}	Maximum (virtual) overtopping volume during a certain period of time	m ³ /m
V_{peak}	Maximum (virtual) overtopping volume per wave	m ³ /m
W	Weibull distribution	
W_{dir}	Wind direction	°N
W_{vel}	Wind velocity	m/s
x_s	x-coordinate of laser scanner	m
z_p	z-coordinate of laser scanner pole	m

GREEK LETTERS

Γ	Mathematical gamma function	
α	Calibration coefficient of the LTA for the triad wave-wave interactions (Eldeberky, 1996), dike slope angle	-, °
β	Wave angle of incidence, wave angle of incidence spectrum	°, °/Hz
δ	(Mean) wave direction relative to north	°N
γ_β	EurOtop (2018) influence factor for angle of wave attack	-
γ_f	EurOtop (2018) influence factor for roughness and permeability	-
μ	Mean value of normally distributed parameter	
ϕ	Slant angle of laser scanner	°
ψ	Correction angle, rotating laser scanner coordinate system	°
ζ	Time lag spectrum	s/Hz
$\xi_{m-1,0}$	Iribarren number, breaker parameter, surf similarity, based on the spectral wave steepness $s_{m-1,0}$	-
σ	Standard deviation of normally-distributed parameter, relative frequency	-
σ_δ	Wave directional spreading (wave direction relative to north)	°
σ_θ	Wave directional spreading (wave direction relative to normal to depth contours)	°
θ	(Mean) wave direction relative to normal to depth contours, scan angle of laser scanner	°
θ_{crit}	Angle relative to normal to depth contours, for which the wave direction becomes parallel to the depth contours due to refraction	°

ABBREVIATIONS AND ACRONYMS

ADCP	Acoustic Doppler Current Profiler
ADIS	Adaptive Directional Importance Sampling
BDM	Bayesian Direct Method for spectral estimation (Hashimoto & Kobune, 1988)
BOI	Beoordelings- en OntwerpInstrumentarium, Dutch flood defence safety assessment framework

BSBT	Backward in Space, Backward in Time numerical scheme
BVW	Bocht Van Watum
CCA	Consistent Collinear Approximation for the triad wave-wave interactions (Salmon et al., 2016)
CFL	Courant-Friedrichs-Lewy condition
CSM	Continental Shelf Model
DCSM	Dutch Continental Shelf Model
DIA	Discrete Interaction Approximation for the quadruplet wave-wave interactions (S. Hasselmann & Hasselmann, 1985 ; S. Hasselmann et al., 1985)
DIWASP	Directional WAVE SPECTRA toolbox (Johnson, 2002)
DLD	DoLLarD, southern part of Eems-Dollard estuary
EMSH	EeMSHaven
FORM	First Order Reliability Method
GPS	Global Positioning System
HH	Hanna and Heinold (1985) indicator
Hydra	HYDraulische RAndvoorwaarden (Hydraulic boundary conditions), probabilistic model used for the Dutch flood defence safety assessment
JONSWAP	JOint North Sea WAVE Project (K. Hasselmann et al., 1973)
LIDAR	Laser Imaging Detection And Ranging
LS	Laser Scanner
LTA	Lumped Triad Approximation for the triad wave-wave interactions (Eldeberky, 1996)
MATLAB	MATrix LABoratory
MPI	Message Passing Interface
MVED	Meerjarige Veldmetingen Eems-Dollard (Multi-year field measurements Eems-Dollard)
NaN	Not a Number
NAP	Normaal Amsterdams Peil, Dutch ordnance level
NBI	Normalised Bias Indicator

OCA	Original Collinear Approximation for the triad wave-wave interactions
ORB	Orthogonal Recursive Bisection method for the division of a computational grid over multiple computational cores
OWEZ	Oude WesterEems Zuid
REFRAC	REFRACTION (The REFRAC team, 2019)
RMSE	Root-Mean-Square Error
RSSI	Received Signal Strength Indicator
SLURM	Simple Linux Utility for Resource Management or Slurm Workload Manager
SORDUP	Second ORDER UPwind numerical scheme
SPB	Stochastic Parametric Boussinesq model for the triad wave-wave interactions (Becq-Girard et al., 1999)
ST6	Observation-consistent wind input and white-capping (ST6 physics of Rogers et al., 2012)
SWAN	Simulating WAVes Nearshore (Booij et al., 1999)
SWASH	Simulating WAVes till SHore (Zijlema et al., 2011)
TD	Twin Dikes
UHW	Uithuizerwad
WAQUA	WATER beweging en water QUALity modellering
WBI	Wettelijk BeoordelingsInstrumentarium, Dutch flood defence safety assessment framework
ZUNO	ZUIDelijke NOordzee model (Southern North sea model)

PROBABILITY DISTRIBUTIONS

The following notations are used for the Normal and Weibull distributions:

$$N(\mu;\sigma)$$

$$W(a;b)$$

where μ is the mean, σ the standard deviation, a a dimensional scale factor, b a non-dimensional shape factor.

LIST OF FIGURES

1.1	Area of interest. The square indicates the Eems-Dollard estuary. Parts of the North Sea, the Wadden Sea and the north of the Netherlands shown as well. Bathymetrical data from Rijkswaterstaat six-yearly bathymetrical surveys, blue is deeper, yellow is shallower.	2
1.2	Eems-Dollard estuary, with the port Eemshaven (red area), the town Delfzijl (blue area), the deep main tidal channel (number 1), the secondary channel the Bocht van Watum (number 2), the dike section of interest (black line) and the two locations of interest for the field measurements, Uithuizerwad (UHW) and the Twin Dikes (TD). Bathymetrical data from Rijkswaterstaat six-yearly bathymetrical surveys, blue is deeper, yellow is shallower.	3
1.3	Outline of the dissertation. The set-up with two main parts is given, as well as the interactions between the different components.	7
1.4	Dissertation focus from three different points of view. Top: Protection against flooding. Middle: Physics of water surface waves. Bottom: Measuring and modelling of water surface wave processes. Hatched areas are main focuses, dashed areas are outside the scope of the dissertation. Figures inspired by Vuik (2019).	9
1.5	Eems-Dollard estuary with measurement instruments as of the end of 2020. See Table 1.1 for the definitions of the numbers and further details on the instruments. Bathymetrical data from Rijkswaterstaat six-yearly bathymetrical surveys.	11
1.6	Top: Dike at Uithuizerwad (UHW), with two of the overtopping tanks and the laser scanner system in the background. Bottom: Twin Dikes location (TD), with two of the overtopping tanks being built into the dike.	12
2.1	Top: Average (indicated by all directions) and schematised (indicated by trapezium) profile for the development of the wind velocity in time (Beckers et al., 2009). Bottom: Average (lines with circles) and schematised (solid lines) profiles for the development of the wind direction in time for several directional sectors (after Gautier & Groeneweg, 2012).	20
2.2	Overview of the WBI SWAN grids used to determine the wave conditions in the Wadden Sea (after Klein & Kroon, 2011).	21
3.1	Bathymetry of the area of interest. The square indicates the Eems-Dollard estuary. Parts of the North Sea, the Wadden Sea and the north of the Netherlands are shown as well. Blue is deeper, orange is shallower (after Zijdeveld & Peters, 2009).	31

3.2	Eems-Dollard estuary, with the deep main tidal channel (number 1), the secondary channel the Bocht van Watum (number 2), the dike section of interest (black line), the two locations of interest for setting up the first measurements, Uithuizerwad (UHW) and the Twin Dikes (TD), and the wind direction during extreme conditions (arrow). Blue is deeper, orange is shallower.	32
3.3	Left: The five computational grids as used for the SWAN simulations. Right: Zoom of the most detailed grids. Uithuizerwad (UHW) and the Twin Dikes (TD) indicated in the right panel.	34
3.4	Left: SWAN model bathymetry as used for the quantification of propagation effects and the comparison of the two SWAN versions, with the area around the Eemshaven indicated by the rectangle. Right: Bathymetry of the schematised model of the area around the Eemshaven, including the shallow area in front of the dike and a 1:10 slope. The western boundary ($y = 0$ m until $y = 1500$ m) is closed off, representing the dike (thick black line). Mean wave direction indicated with the arrow.	37
3.5	Results for return periods of 1 year, 10 years and 100,000 years. Left: SWAN model bathymetry and mean wave direction vectors. Right: Absolute gradient in mean wave direction. Bottom contours drawn at -3 m, -15 m and -25 m.	39
3.6	Model bathymetry (contours), Twin Dikes location (black dot) and recommended measurement locations (rectangles).	40
3.7	In clockwise direction: SWAN bathymetry with output locations around UHW and TD. Significant wave height H_s at the output locations for the three different cases, during design conditions. Mean wave direction (δ , nautical, coming from) at the output locations. Here, north is 360° , northwest $< 360^\circ$, northeast $> 360^\circ$. Spectral wave period $T_{m-1,0}$ at the output locations.	41
3.8	Ursell number $U = H_{m0}L_p^2/d^3$ during design conditions and 2D spectra output locations. Location 1 is located in the North Sea, location 2 on the tidal delta, location 3 just behind the tidal delta in the main tidal channel and location 4 is located further inside the main tidal channel. -3 m, -15 m and -25 m depth contours shown as well.	42
3.9	2D variance density spectra at locations of Figure 3.8 during design conditions, as found by SWAN 40.72ABCDE with WBI settings (A cases), SWAN 41.10AB with default settings (B cases), and combination of 40.72ABCDE and 41.10AB (C cases). Contour lines plotted at 0.99, 0.9, $1/2$, $1/4$, $1/8$, $1/16$, $1/32$, $1/64$ and $1/128$ times the local maximum variance density. Spectra plotted using Nautical convention (coming from).	44
3.10	Significant wave height H_s during design conditions for the case with a 1:10 slope, using the safety assessment version. Gradients in the wave height occur, resembling diffraction patterns, without inclusion of diffraction in the model. Spectral output locations (asterisks) and mean wave direction (arrow) shown as well.	46
3.11	2D spectra for the case with a 1:10 west-east slope, using both the SWAN assessment and development versions.	47

4.1	Top: Area of interest. The square indicates the Eems-Dollard estuary. Parts of the North Sea, the Wadden Sea and north of the Netherlands shown as well. Bathymetrical data from Rijkswaterstaat 2014 bathymetrical survey. Bottom: Area of interest around the Eemshaven in the Eems-Dollard estuary (rectangle), with the deep tidal channels (1 and 2) and shallow flats clearly visible. The black line indicates the dike of interest. TD (Twin Dikes) indicates the overtopping measurement location in the area of interest.	55
4.2	Left: Definition of incident angle θ [°] and critical angle θ_{crit} [°], relative to the normal to the depth contours, based on Snel's law. The dashed line is the channel axis. Right: Waves propagating in three different directions over a channel. Longitudinally (1), at an angle smaller than the critical angle (2) and at the critical angle (3). Figure after Guzman Mardones (2011); Zwamborn and Grieve (1974).	58
4.3	Bathymetries of the academic refraction (first two panels) and diffraction (third panel) models. Model (2D spectra) output locations shown with circles, range of angles of incidence θ shown in middle panel.	63
4.4	Detailed model, schematised based on the area of interest (see lower panel of Figure 4.1). The model includes the main tidal channel, the secondary channel Bocht van Watum and the shallow flats. Model output locations indicated as well (circles).	64
4.5	First two rows: Relative wave heights H_{rel} [-] of REFRAC, SWAN and SWASH for waves travelling from shallower towards deeper water, with $\theta = 48^\circ$ and $\theta = 60^\circ$ (318°N and 330°N). Bottom row: SWASH surface elevation η [m] for both angles of incidence.	70
4.6	2D spectra at three locations for regular waves travelling from shallower to deeper water with $\theta = 48^\circ$ (318°N). Top row: SWASH with non-linear waves ($H_s = 1$ m). Middle row: SWASH with linear waves ($H_s = 0.1$ m). Bottom row: SWAN with non-linear waves ($H_s = 1$ m). Variance density of each model normalised and colour-scaled with the maximum variance density at the offshore (80,1500) location.	71
4.7	Diffraction for semi-infinite breakwater case with regular waves coming from 270°N. SWASH (left), SWAN (middle) and SWAN with diffraction approximation enabled (right), compared to analytical solution of Penney et al. (1952); Sommerfeld (1896) (black dashed lines). The thick black line indicates the dike.	74
4.8	2D spectra at three locations for irregular, narrow spread waves travelling from shallower to deeper water with $\theta = 48^\circ$ (318°N). Top row: SWASH. Second row: SWAN with the recommended settings for the numerics (see sub-section 4.5.1 and appendix D) and the default settings for the physics (see appendix D). Third row: SWAN with the same settings, but with $\alpha = 0.05$ instead of $\alpha = 0.8$. Bottom row: SWAN with the same settings, $\alpha = 0.05$, 20 m grid cells and the diffraction approximation enabled. Variance density of each model normalised and colour-scaled with the maximum variance density at the offshore (80,1500) location.	76

- 4.9 Diffraction for semi-infinite breakwater case with irregular, narrow-spread waves coming from 270°N. SWASH (left), SWAN with recommended settings (middle) and SWAN with recommended settings, diffraction approximation and 20 m grid cells (right), compared to analytical solution of Penney et al. (1952); Sommerfeld (1896) (black dashed lines). The thick black line indicates the dike. 79
- 4.10 2D spectra at three locations for irregular, broad-spread waves travelling from shallower to deeper water with an angle of incidence of 48° (318°N). Top row: SWASH. Middle row: SWAN with the recommended settings, with no wind imposed on the model. Bottom row: SWAN with the same settings, but with a 35 m/s wind coming from 318°N imposed. Variance density of each model normalised and colour-scaled with the maximum variance density at the offshore (80,1500) location. 81
- 4.11 2D spectra at three locations for irregular, broad-spread waves travelling from shallower to deeper water with an angle of incidence of 48° (318°N) and a 35 m/s wind coming from 318°N imposed. Top row: SWAN with default settings. Second row: SWAN with WBI settings. Third row: SWAN with ST6 settings. Bottom row: SWAN with recommended settings, with 20 m grid cells and the diffraction approximation enabled. Variance density of each model normalised and colour-scaled with the maximum variance density at the offshore (80,1500) location. 84
- 4.12 Diffraction for semi-infinite breakwater case with irregular, broad-spread waves coming from 270°N. SWASH (left), SWAN (without diffraction approximation) without wind imposed on the model (middle) and SWAN with wind imposed (right), compared to analytical solution of Goda et al. (1978) (black dashed lines). The thick black line indicates the dike. 86
- 4.13 Diffraction for semi-infinite breakwater case with irregular, broad-spread waves. SWAN with WBI settings (left), SWAN with ST6 settings (middle) and SWAN with recommended settings, diffraction approximation and 20 m grid cells (right). The black dashed lines indicate the analytical solution of Goda et al. (1978), the thick black line indicates the dike. 87
- 4.14 2D variance density spectra [$\text{m}^2/\text{Hz}/^\circ$] from Dutch dike safety assessment WBI database at the Twin Dikes (TD) overtopping measurement location in the area of interest (left panel), at a location several hundred metres to the southeast of TD (middle panel), and from the present SWAN model using the WBI settings (right panel). Water depth d [m], significant wave height H_s [m], wave peak period T_p [s], wave direction δ [°N] and directional spreading σ [°] given as well. 88
- 4.15 REFRAC wave rays for the detailed model. The mean wave direction and 30° directional spreading are represented by wave rays from 330°N, 315°N and 345°N. Several wave propagation effects occur: Relatively unaltered propagation onto shallow flats (2 and 6), relatively unaltered propagation into channel (5), wave defocusing on channel slopes (4), refraction out of channel (3), and wave reflection off the channel slope or wave trapping (1). 89

4.16	Left: SWASH snapshot of steady-state surface elevation and four areas of interest. Directional narrowing and reduction of wave energy, due to wave sheltering, diffraction, depth-induced breaking and refraction from the deep channel to the shallow flat (1). Directional narrowing and slight increase of wave energy, due to wave sheltering, wave (de)focusing and wave reflection or trapping (2). Reduction in wave sheltering, diffraction and wave (de)focusing (3). Directional narrowing and reduction in wave energy, due to wave (de)focusing (4). Right: Relative wave height H_{rel} [-] and mean wave direction δ [°N] along three y -transects at $x = 80$ m, $x = 600$ m and $x = 1000$ m.	90
4.17	SWASH 2D spectra at several locations. Variance density normalised and colour-scaled with the maximum variance density at the offshore (80,1750) location.	92
4.18	2D SWAN spectra at several locations. First two rows: SWAN with recommended settings, without wind imposed. Bottom two rows: SWAN with recommended settings, with wind. Variance density normalised and colour-scaled with the maximum variance density at the offshore (80,1750) location.	94
4.19	2D SWAN spectra at several locations. First two rows: SWAN with WBI settings, with wind imposed. Bottom two rows: SWAN with recommended settings, diffraction approximation, 20 m grid cells and with wind. Variance density normalised and colour-scaled with the maximum variance density at the offshore (80,1750) location.	96
5.1	Left: Laser scanner system (red circle) and run-up simulator (black rectangle) during tests with normally incident waves. Right: Top view during obliquely incident waves. Scan lines indicated by blue and red lines.	105
5.2	Schematised set-up with two laser scanners. Set-up based on Hofland et al. (2015), but with two laser scanners. Scan lines (blue and red dashed lines), scanned points on water surface (blue and red dots) indicated. R [m] is the scanned distance, θ [°] the scan angle, ϕ [°] the slant angle, β [°] a correction in case the scanned line does not run straight along the slope. h_s [m] the laser scanner heights, x_s [m] the x -coordinate of the laser scanners, α [°] the slope angle. V [m ³ /m] is a virtual overtopping volume.	107
5.3	Left: Simulation of rain with garden sprinklers. Right: Laser scanners with guywires and accelerometer (circle).	109
5.4	Left: Run-up data for test 1 from both laser scanners and based on both distance and $RSSI$ versus run-up heights from video data. Right: Run-up data for test 1a from both laser scanners and based on both distance and $RSSI$, as well as Rayleigh distribution from wave run-up simulator filling level formula. The x -axis on Rayleigh scale, the dike crest level is indicated with the horizontal dashed line.	110
5.5	Left: Run-up depths at $z = 1.42$ m for test 1 as measured with both laser scanners, a surf board and from visual estimations, compared with equation from Van der Meer (2011). Right: Run-up depth in time at the same location for a filling level of 7 m and for both laser scanners and the surf board.	112

5.6	Left: Front velocities from laser data compared to video and paddle wheel (PW) data. Right: Run-up and front velocity time signals of one of the laser scanners and front velocity time signal from video analysis for a wave with a filling level of 5 m of test 1. Dotted lines indicate percentages of the maximum run-up level.	113
5.7	Left: Relative overtopping rate for several virtual crest levels for test 1a and based on maximum volumes or run-up depth multiplied with front velocity, compared to EurOtop (2018) equations. Right: Distribution of individual overtopping volumes, compared to EurOtop (2018). R_c [m] is the crest free-board, $\xi_{m-1,0}$ [-] is the breaker parameter, the different γ parameters [-] are influence factors, see EurOtop (2018).	115
5.8	Snapshot of run-up level in time for both laser scanners during oblique wave attack. The time lag and different maximum run-up levels are visible.	116
6.1	System overview during perpendicular (left panel) and obliquely (right panel) incident waves. Laser scanners (white circle), run-up simulator (white rectangle), laser scanner scan lines (blue and red lines), up-slope direction (arrows) and 45° angle indicated.	122
6.2	Left: Side view of system set-up and instrumentation. x -coordinates horizontal, z -coordinates vertical, y -coordinates perpendicular to the figure. α [°] is the slope angle. LS pole is the laser scanner pole, LS1 the lower laser scanner, LS2 the upper laser scanner. PW are the 6 paddle wheels; SB the five surf boards. Right: Example of surf board (white rectangle) and paddle wheel (white circle). Up-slope direction indicated by the arrow.	123
6.3	System set-up as used for the conversion of measured distances (R_1 [m] and R_2 [m], blue and red lines) in polar coordinates to cartesian x , y , z -coordinates [m] according to the coordinate system as shown. Dike slope α [°], laser scan lines (blue and red dashed lines), scanned points on water surface (blue and red dots), virtual crest level z_{crest} [m], run-up depths d_1 [m] and d_2 [m], and virtual overtopping volume V [m ³] indicated.	124
6.4	Determination of run-up levels R_u [m] (circles) and virtual overtopping volumes V [m ³ /m] (shaded regions) based on the run-up depths d (solid, dashed and dash-dot lines), for three different waves and at three different virtual crest levels (dotted lines). The waves are plotted for the moment that the volume above the virtual crest line (the shaded area) is maximum for that specific wave. The assumption is that this would be the overtopped volume that would have overtopped if the crest was located at this virtual level.	125
6.5	Left: Run-up heights derived from both laser scanners (LS1 and LS2), based on distance (R) and laser reflectance ($RSSI$), compared with run-up heights from videos, for a test with 21 perpendicularly incident waves. The HH-indicator values are shown as well. Right: Run-up heights for test with 100 randomly generated perpendicularly incident waves for both laser scanners, as well as Rayleigh distribution derived from wave run-up simulator filling level formula (dashed line). The horizontal axis is plotted on Rayleigh scale, the dike crest level is indicated with the horizontal dotted line.	127

- 6.6 Left: Run-up depths as measured with both laser scanners (LS1 and LS2), the third surf board (SB3) and as estimated from videos at $z = 1.42$ m, compared with the relation of Van der Meer (2011) (Equation 6.3). Right: Run-up depths in time at the same location for a single wave, for both laser scanners and the third surf board. 129
- 6.7 Left: Front velocities determined from laser scanner data versus paddle wheel (PW) and video data. Velocities based on front travelling from one paddle wheel to the next. Right: Run-up (dash-dot) and front velocity (dashed) time signals of laser scanner 1 and front velocity time signal (solid line) from video analysis for a single wave. The dotted vertical lines indicate percentages of the maximum run-up level. 131
- 6.8 Left: Relative overtopping rate at different virtual crest heights based on maximum volumes (crosses, circles) or run-up depth multiplied with front velocity (pluses, triangles) for a test with 100 random perpendicularly incident waves, compared to EurOtop (2018) equations (solid and dashed lines). Right: Distribution of overtopping volumes for three different crest freeboards, compared to EurOtop (2018). R_c [m] is the crest freeboard, $\xi_{m-1,0}$ [-] the breaker parameter, the different γ [-] parameters are influence factors, see EurOtop (2018). 132
- 6.9 Run-up heights from both laser scanners, based on both measured distance (R) and laser reflectance ($RSSI$) versus run-up heights from videos, for a test with obliquely incident waves. Distance between laser lines 1.3 m. 134
- 6.10 Left: Snapshot of run-up level in time for both laser scanners during oblique wave attack. The time lag and different maximum run-up levels are visible. Right: Maximum shore-parallel front velocities determined from laser scanner data (circles) versus video data (crosses). Laser velocities based on the time lags between the laser scanner signals. Distance between laser lines 2.5 m. 135
- 6.11 Left: Part of the 2.5 m deep SWASH basin with a 1:4 dike slope. The virtual laser scan lines are indicated as well. Right: Snapshot of irregular directional wave field, with an angle of incidence of 45° and a directional spreading of 25° . Also refer to <https://youtu.be/cy-VWmV7aUA>. 137
- 6.12 Angle of incidence analysis definitions, with an obliquely incident sinusoidal wave (wave direction indicated by the arrow) propagating towards the dike (toe and crest indicated with thick solid lines), with a phase velocity c and a wavelength L . This wave causes a projected wave to travel along the dike, with a velocity c' and a length L' (dashed lines). β is the angle of incidence. Laser scanner scan lines indicated by the dotted lines (LS1 and LS2), with a distance D between them. 138

- 6.13 Variance density spectra (solid lines) based on virtual laser line run-up data and angle of incidence spectra (Equation 6.9, dashed lines) for two cases. Left: Angle of incidence of 15° , water depth of 10 m, a vertical wall and monochromatic waves. Right: Angle of incidence of 35° , water depth of 2.5 m, 1:4 dike slope and irregular, short-crested waves. The angle of incidence spectra give the angle of incidence for each mode in the spectrum of the measured run-up. The angle of incidence β was defined according to Figure 6.12. Peak angles of incidence indicated by the circles. 140
- 6.14 Wave angle of incidence data for all SWASH simulations, comparing peak angles of incidence as modelled by SWASH with peak angles of incidence derived from virtual laser scanner data (see Figure 6.13). Left: Data grouped according to simulation conditions (water depth 10 m or 2.5 m, vertical wall or 1:4 slope, monochromatic or irregular waves). Right: Data grouped according to distance between the scan lines (1 m, 2 m, 4 m or 8 m). HH and NBI values, and $\pm 5^\circ$ and $\pm 10^\circ$ error bounds (dashed and dotted lines) given as well. 140
- 6.15 Overtopping discharge for several virtual crest levels as determined from the virtual laser scanner data for three SWASH simulations. Tests 10 to 12, with angles of incidence of 15° (crosses), 35° (triangles) and 45° (squares). SWASH discharge parameter q (pluses, asterisks, down-pointing triangles) and virtual overtopping box data (circles, diamonds, pentagrams) plotted as well. Simulations with a 1:4 slope, a JONSWAP spectrum with $H_s = 1$ m and $T_p = 4$ s. 142
- 7.1 Left: The Eems-Dollard estuary in the Netherlands, area of interest of the field measurement project. Laser scanner system location indicated by white dot. Wind direction during storm Ciara indicated with the arrow. Satellite image: ©2021 GeoBasis-DE/BKG, ©2021 Google. Data: SIO, NOAA, U.S. Navy, NGA, GEBCO. Right: Drone overview of measurement location, with the laser scanner pole (left), the approximate laser scan line locations (blue and red dashed lines), the painted grid on the slope, and two of the overtopping tanks (right). 147
- 7.2 Left: New laser scanner system on the dike in the Eems-Dollard estuary, next to the overtopping tanks, during storm Ciara. The Rijkswaterstaat (wave) measurement pole can be seen in the distance. Rijkswaterstaat is the Directorate-General for Public Works and Water Management in the Netherlands. Right: From the bottom to the top, Laser scanner 1, laser scanner 2, video camera. 148
- 7.3 Excavation of the dike slope and placement of the overtopping tanks inside the dike. 149
- 7.4 Bathymetry of the area of interest, shown as depth contours [m+NAP], with the deep main tidal channel and shallow flats in front of the dike. Laser scanner system (circle) and measurement pole (triangle) locations indicated. 150
- 7.5 Three snapshots taken from the video recordings, showing a very oblique wave running up the slope in a sort of local plunging motion. Note the painted grid as used for the video analysis. 152

7.6 Overview of measurements near the toe of the dike around both storm peaks. The shaded regions indicate the considered storm peaks. h [m+NAP] is the water level, H_{m0} the significant wave height [m], T_p the peak wave period [s], $T_{m-1,0}$ [s] the wave period based on the moments of the spectrum. . . . 152

7.7 Schematised updated set-up with two laser scanners. Scan lines (red and blue dashed lines), scanned points on water surface (red and blue dots) are indicated. x (horizontal), y (perpendicular), z (vertical) and a -coordinate (along the slope) system is also indicated. $R_{1,2}$ [m] are the scanned distances, $\theta_{1,2}$ [°] are the scan angles, $\phi_{1,2}$ [°] the slant angles, x_s [m] are the x -coordinates of the laser scanners, a_s [m] the a -coordinates of the laser scanners, z_p [m] is the z -coordinate of the laser scanner pole, $h_{s1,2}$ [m] are the heights of the laser scanners above the slope, α [°] is the slope angle. V [m³] is a virtual overtopping volume, ψ [°] is the correction angle resulting from the rotation matrix, rotating the x - and z -coordinates in the x,z -plane. 153

7.8 Measured run-up heights R_u [m] based on measured distances R (solid lines) and laser reflectance $RSSI$ (dashed lines), as well as measured run-up depths d [m] (contours) for both laser scanners (LS1 and LS2), during a 30 second window. Maximum run-up heights $R_{u,max}$ [m] per wave based on both R (circles) and $RSSI$ (crosses) indicated. Height level of the overtopping tank z_{tank} [m] indicated by the dotted line. Moments of maximum run-up height $T_{R_{u,max}}$ [hh:mm:ss] at LS1 indicated by the dash-dot lines. Note the delay between the signals, where the waves often reached LS2 first with the present wave direction. 156

7.9 Run-up heights above 4.4 m+NAP for both storm peaks for both laser scanners (LS1 and LS2), based on distance R and laser reflectance $RSSI$, compared with run-up heights from video recordings. Left: storm peak 1. Right: storm peak 2. The legend provides the HH and NBI values. 157

7.10 Left: Relative wave run-up versus breaker parameter. Figure based on EurOtop (2018). Note the added influence of the oblique wave attack on the vertical axis compared to EurOtop (2018). Data for both laser scanners based on measured distances, and for both storm peaks. Right: Run-up exceedance plots for both laser scanners and both storm peaks, plotted on Weibull scale. A straight line gives a Weibull distribution, a straight line with a slope of 1:2 gives a Rayleigh distribution. 158

7.11 Left: Run-up depth at several locations along the dike slope exceeded by 2% of the waves, based on both laser scanners and for both storm peaks. Data compared to linear relation of Van der Meer (2011) for two different values of $c_{d2\%}$. HH and NBI indicator values given for $c_{d2\%} = 0.23$. Right: Snapshot of large up-rushing wave, showing foam and entrained air. 161

7.12 Relative maximum front velocity versus relative run-up on the slope. Results based on video analysis (2D velocities) and laser scanners (velocity component in the up-slope direction), compared to Equation 7.8. Figure based on EurOtop (2018), including the FlowDike data (Lorke et al., 2011). 162

- 7.13 Relative overtopping rate for several virtual crest levels, based on both laser scanners (crosses, circles) and the overtopping tank (squares), for both storm peaks. The laser scanner data have also been plotted using the relation $T_{m-1,0} = T_p/1.1$ (asterisks). Results compared to EurOtop (2018) equations (solid and dashed lines) and data (dots). Figure based on EurOtop (2018). R_c [m] is the crest freeboard, $\xi_{m-1,0}$ [-] is the breaker parameter, the different γ parameters [-] are influence factors, see EurOtop (2018). 164
- 7.14 Left: Weibull shape factor b for smooth structures and spanning a range of relative freeboards. Laser and overtopping tank data plotted for both storm peaks. Fit for b from Zanuttigh et al. (2014) shown as well. Figure based on EurOtop (2018). Right: Development of run-up, overtopping volume and front velocity over time for one large wave and based on data of one of the laser scanners. The dotted lines indicate the moments that the run-up reaches 15% and 75% of the maximum run-up level, and the moment that the run-up reaches the overtopping tank level. 166
- 7.15 Wave variance density spectra based on radar measurements (solid lines), variance density spectra based on laser scanner run-up signals (dash-dot lines) and 'angle of incidence spectra' (dashed lines) for both storm peaks, giving the angle of incidence for each mode in the spectrum. The dots indicate the peak angles of incidence. 168
- B.1 Left: Geographic grid with parallel depth contours, after Booij (1998). Right: SWAN refraction situation sketch. Definitions of variables given in the main text. Figure after Zijlema (2020). 205

LIST OF TABLES

1.1	Overview of instruments MVED field measurement campaign. See Figure 1.5 for the locations of the instruments in the estuary. BVW indicates the channel Bocht van Watum, OWEZ indicates Oude WesterEems Zuid, the location of a Rijkswaterstaat directional Waverider buoy. The WaveDroid is located next to this buoy for validation. DLD indicates the southern part of the Eems-Dollard estuary, EMSH is the Eemshaven. TBD is To Be Determined. D indicates Developed in this dissertation, LB indicates Location Based on information in this dissertation, U is Used in this dissertation, NU is Not Used. ¹ Approximate location. ² WaveDroid might be relocated after the first year.	13
2.1	Combinations of stochastic variables as used in WBI WAQUA and SWAN simulations, to determine the nearshore wave loads for the Wadden Sea. After Gautier and Groeneweg (2010).	19
3.1	Storm conditions as used for quantification of propagation effects.	33
3.2	SWAN model settings as used for the Dutch dike safety assessment WBI (version 40.72ABCDE) and default settings of the SWAN development version 41.10AB. Refer to The SWAN team (2017b) for further explanations of the different parameters.	36
3.3	Design conditions as used in the SWAN simulations with the schematised model of the area around the Eemshaven.	37
4.1	Directional turning rates for a 1:10 slope and a wave with $T = 10$ s and initial $\theta = 30^\circ$. Results for several grid cell sizes according to Snel's law, SWAN Equation B.7 (based on the water depths) and SWAN Equation B.9 (based on the wave numbers). Δx [m] is the grid cell size, d_1 and d_2 [m] are water depths, Δd [m] is the difference in water depth over one grid cell, $\Delta\theta_{\text{Snel}}$ [°] the directional turning rate according to Snel's law, $\Delta\theta_{\text{SWAN,DEP}}$ [°] the SWAN turning rate using Equation B.7 and $\Delta\theta_{\text{SWAN,WNUM}}$ [°] the SWAN turning rate using Equation B.9.	61
4.2	Directional turning rate $\Delta\theta_{\text{SWAN}}$ [°] as calculated by SWAN, relative to the incident wave direction and relative to the directional turning rate as calculated by Snel's law, for several combinations of grid cell size Δx [m] or depth difference per grid step Δd [m], turning rate equation, numerical scheme used to discretise this equation and rescaling of negative action density.	68
6.1	HH and NBI values, comparing the run-up depths as measured by different instruments. SB3 is the third surf board, LS1 is laser scanner 1, LS2 is laser scanner 2.	130

6.2	SWASH simulations that were performed. Angles of incidence β ranging from 15° to 60° , (significant) wave height $H_s = 1$ m for all tests, wave (peak) period $T_p = 4$ s for all tests.	136
7.1	Characteristics of considered storm peaks. W_{dir} [$^\circ$ N] is the wind direction, W_{vel} [m/s] the wind velocity, h [m+NAP] the water level, d [m] the water depth, $H_{1/3}$ [m] the significant wave height based on the time signal, H_{m0} [m] the significant wave height based on the spectrum, $T_{1/3}$ [s] the significant wave period based on the time signal, T_p [s] the peak wave period, $T_{m-1,0}$ [s] the wave period based on the moments of the spectrum, δ [$^\circ$ N] the mean wave direction, β [$^\circ$] the wave angle of incidence relative to the dike normal, q_{tank} [l/s/m] the overtopping discharge as measured by the overtopping tank, N_{ow} [-] the number of overtopping waves in the overtopping tank. RWS pole is the Rijkswaterstaat (wave) measurement pole, see the left panel of Figure 7.2.	151
7.2	Run-up and overtopping parameters for both laser scanners, the video recordings, the overtopping tank and EurOtop (2018) equations at 4.4 m+NAP, for both storm peaks. V_{max} [l/m] is the maximum overtopping volume. Note that the table gives two values for several parameters. The two q values for EurOtop (2018) correspond to discharges based on the measured $T_{m-1,0}$ and based on the ratio $T_{m-1,0} = T_p/1.1$. The maximum volumes of EurOtop (2018) correspond to volumes calculated with Equation 7.10 - Equation 7.12, based on the EurOtop (2018) q , a and b values, or based on the laser scanner q , a and b values. The number of overtopping waves according to the video analysis correspond to the number of overtopping waves at the locations of laser lines 1 and 2.	164
A.1	Hydra-NL results at Uithuizerwad using the WBI 2017 settings. P [year] is the return period, W_{dir} [$^\circ$ N] the wind direction, W_{vel} [m/s] the potential wind velocity, h [m+NAP] the water level, H_{m0} [m] the significant wave height, $T_{m-1,0}$ [s] the spectral wave period, δ [$^\circ$ N] the mean wave direction, β [$^\circ$] the wave angle of incidence. The last two columns give the required crest levels for which the mean overtopping discharge is at most 5 l/s/m and the mean overtopping discharge q [l/s/m] with the actual crest level of the dike.	199
A.2	Hydra-NL results at Uithuizerwad using the WBI 2017 settings, without taking the model uncertainties in the H_{m0} wave height and $T_{m-1,0}$ wave period into account.	199
A.3	Hydra-NL results at the Twin Dikes using the WBI 2017 settings.	200
A.4	Hydra-NL results at the Twin Dikes using the WBI 2017 settings, without taking the model uncertainties in the H_{m0} wave height and $T_{m-1,0}$ wave period into account.	200

A.5	Two characteristic storms for the Eems-Dollard estuary. An extreme storm with a return period of 1-100 years, to be expected during the field measurement campaign in the area. A design storm with a return period of 1,000-10,000 years, which represents the conditions with which the dikes are designed. Offshore conditions and nearshore conditions at UHW and TD given. Conditions based on WBI SWAN simulations with the WBI SWAN version and WBI SWAN settings.	201
D.1	SWAN model settings as used for the Dutch dike safety assessment WBI (version 40.72ABCDE) and default settings of the SWAN development version 41.31. Refer to The SWAN team (2019b) for further explanations of the different parameters.	213
D.2	SWAN model settings as used for the ST6 settings (Rogers et al., 2012) with the SWAN development version 41.31, and recommended settings for the modelling of refraction and diffraction in the Eems-Dollard estuary with the SWAN development version 41.31. ST6 settings partly based on Gautier et al. (2018). Refer to The SWAN team (2019b) for further explanations of the different parameters.	215

CURRICULUM VITÆ

PATRICK OOSTERLO

21-01-1991 Born in Heerenveen, the Netherlands

EDUCATION

2003–2009 Gymnasium, OSG Sevenwolden, Heerenveen

2009–2013 BSc, Civil Engineering, Delft University of Technology, Delft

2013–2015 MSc, Civil Engineering, Delft University of Technology, Delft

2016–2021 PhD, Civil Engineering, Delft University of Technology, Delft

EXPERIENCE

2014–2015 Student assistant, Section of Hydraulic Structures and Flood Risk, Faculty of Civil Engineering and Geosciences, Delft University of Technology, Delft

2015–2016 Researcher, Section of Hydraulic Structures and Flood Risk, Faculty of Civil Engineering and Geosciences, Delft University of Technology, Delft

2016–2021 PhD researcher, Section of Hydraulic Structures and Flood Risk, Faculty of Civil Engineering and Geosciences, Delft University of Technology, Delft

2021–present Advisor hydraulic loads and data, Section of Flood Defences, Unit of Water, Transport and Environment (WVL), Rijkswaterstaat, Utrecht and Lelystad

AWARDS

2019 3rd place, Student paper competition, Coastal Structures 2019 conference, Hannover, Germany, Ports and Harbors Committee, COPRI, ASCE

LIST OF PUBLICATIONS

PEER-REVIEWED JOURNAL PAPERS

- Oosterlo, P.**, Hofland, B., Van der Meer, J.W., Overduin, M., & Steendam, G.J. (2021). Field measurements of very oblique wave run-up and overtopping with laser scanners. *Journal of Coastal and Hydraulic Structures, 1*. <https://journals.open.tudelft.nl/jchs/article/view/5779>
doi: 10.48438/jchs.2021.0006
- Oosterlo, P.**, Hofland, B., Van der Meer, J.W., Overduin, M., & Steendam, G.J. (2021). Calibration and preparation of field measurements of oblique wave run-up and overtopping on dikes using laser scanners. *Coastal Engineering, 167*, 103915. <https://linkinghub.elsevier.com/retrieve/pii/S0378383921000752>
doi: 10.1016/j.coastaleng.2021.103915
- Lashley, C.H., Zanuttigh, B., Bricker, J.D., Van der Meer, J.W., Altomare, C., Suzuki, T., ... & **Oosterlo, P.** (2020). Benchmarking of numerical models for wave overtopping at dikes with shallow mildly sloping foreshores: Accuracy versus speed. *Environmental Modelling & Software, 130*, 104740. <https://linkinghub.elsevier.com/retrieve/pii/S1364815220303789>
doi: 10.1016/j.envsoft.2020.104740
- Oosterlo, P.**, McCall, R.T., Vuik, V., Hofland, B., Van der Meer, J.W., & Jonkman, S.N. (2018). Probabilistic Assessment of Overtopping of Sea Dikes with Foreshores including Infragravity Waves and Morphological Changes: Westkapelle Case Study. *Journal of Marine Science and Engineering, 6*(2), 48. <http://www.mdpi.com/2077-1312/6/2/48>
doi: 10.3390/jmse6020048
- Hofland, B., Chen, X., Altomare, C., & **Oosterlo, P.** (2017). Prediction formula for the spectral wave period $T_{m-1,0}$ on mildly sloping shallow foreshores. *Coastal Engineering, 123*, 21-28. <https://linkinghub.elsevier.com/retrieve/pii/S037838391630237X>
doi: 10.1016/j.coastaleng.2017.02.005

CONFERENCE CONTRIBUTIONS

- Oosterlo, P.**, Hofland, B., Van der Meer, J.W., Overduin, M., & Steendam, G.J. (2020). Field measurements of very oblique wave run-up and overtopping with laser scanners. *Coastal Engineering Proceedings, 36v*, 20. <https://www.youtube.com/watch?v=TwSwJuxb-Yo>
doi: 10.9753/icce.v36v.waves.20

- Oosterlo, P.**, Van Vledder, G.Ph., Hofland, B., Van der Meer, J.W., Geleynse, N., Renneerens, M., Steendam, G.J., Veendorp, M. (2019). Wave modelling and field measurements in a complex estuary. *International Workshop on Waves, Storm Surges and Coastal Hazards 2019*. http://www.waveworkshop.org/16thWaves/Presentations/QQ4%20Presentation_WW2019_v1.pdf
- Oosterlo, P.**, Hofland, B., Van der Meer, J.W., Overduin, M., Steendam, G.J., Nieuwenhuis, J.W., ... & Renneerens, M. (2019). Measuring (oblique) wave run-up and overtopping with laser scanners. *Proc. Coastal Structures 2019*, 442-452. <https://hdl.handle.net/20.500.11970/106657>
doi: 10.18451/978-3-939230-64-9_045
- Oosterlo, P.**, Van der Meer, J.W., Hofland, B., & Van Vledder, G.Ph. (2018). Wave modelling in a complex estuary: Study in preparation of field measurement campaign Eems-Dollard estuary. *Coastal Engineering Proceedings*, 1(36), 66. <https://journals.tdl.org/icce/index.php/icce/article/view/8356>
doi: 10.9753/icce.v36.papers.66

BOOKS, CHAPTERS AND EDITORIAL WORK

- Oosterlo, P.**, McCall, R.T., Vuik, V., Hofland, B., Van der Meer, J.W., & Jonkman, S.N. (2018). Probabilistic Assessment of Overtopping of Sea Dikes with Foreshores including Infragravity Waves and Morphological Changes: Westkapelle Case Study. *Climate Change, Coasts and Coastal Risk*, Ranasinghe, R., & Jongejan, R. (Eds.). <http://www.mdpi.com/2077-1312/6/2/48>
doi: 10.3390/jmse6020048
- Jonkman, S.N., Nillesen, A.L., **Oosterlo, P.**, & De Kort, R.P.J. (2016). Bouwen aan de delta: Gerealiseerde waterbouwkundige werken, Inzendingen prof.dr.ir. J.F. Agemaprijs 2015. <http://resolver.tudelft.nl/uuid:79cdeb29-42b6-45bb-85b3-fa01f36fc0c5>

PROFESSIONAL JOURNALS AND MEDIA

- Oosterlo, P.**, Hofland, B., & Van der Meer, J.W. (2020). Verlangen naar stevige storm. *Land+Water*, 6/7, 2020. <https://research.tudelft.nl/en/clippings/verlangen-naar-stevige-storm>
- Oosterlo, P.**, Hofland, B., & Van der Meer, J.W. (2020). Waiting for the perfect storm. *Stories of Science, Technische Universiteit Delft*. <https://www.tudelft.nl/en/ceg/research/stories-of-science/waiting-for-the-perfect-storm>
- Oosterlo, P.**, Hofland, B., & Van der Meer, J.W. (2020). Nearshore waves in complex estuaries and related wave overtopping. Meerjarige Veldmetingen Eems-Dollard. *ExtraCT*, 23(1). <https://online.fliphtml5.com/emngs/smvq>

